

DISTRIBUTION STATEMENT A
Approved for Public Release
Distribution Unlimited

MATERIALS RESEARCH SOCIETY
SYMPOSIUM PROCEEDINGS VOLUME 746

Magnetoelectronics and Magnetic Materials—Novel Phenomena and Advanced Characterization

Symposium held December 1–5, 2002, Boston, Massachusetts, U.S.A.

EDITORS:

Shufeng Zhang

University of Missouri-Columbia
Columbia, Maryland, U.S.A.

Michael R. Fitzsimmons

Los Alamos National Laboratory
Los Alamos, New Mexico, U.S.A.

Wolfgang Kuch

Max-Planck-Institut f. Mikrostrukturphysik
Halle, Germany

Ivan K. Schuller

University of California-San Diego
La Jolla, California, U.S.A.

Gernot Güntherodt

RWTH Aachen
Aachen, Germany

Jeffrey B. Kortright

Lawrence Berkeley National Laboratory
Berkeley, California, U.S.A.

Collin Broholm

Johns Hopkins University
Baltimore, Maryland, U.S.A.

Teruya Shinjo

International Institute for Advanced Studies
Kyoto-fu, Japan

Andrew D. Kent

New York University
New York, New York, U.S.A.

Yimei Zhu

Brookhaven National Laboratory
Upton, New York, U.S.A.



Materials Research Society
Warrendale, Pennsylvania

20030812 224

This work was supported in part by the Army Research Office under Grant Number DAAD19-02-1-0445. The views, opinions, and/or findings contained in this report are those of the author(s) and should not be construed as an official Department of the Army position, policy, or decision, unless so designated by other documentation.

This work was supported in part by the Office of Naval Research under Grant Number N00014-03-1-0202. The United States Government has a royalty-free license throughout the world in all copyrightable material contained herein.

Single article reprints from this publication are available through
University Microfilms Inc., 300 North Zeeb Road, Ann Arbor, Michigan 48106

CODEN: MRSPDH

Copyright 2003 by Materials Research Society.
All rights reserved.

This book has been registered with Copyright Clearance Center, Inc. For further information, please contact the Copyright Clearance Center, Salem, Massachusetts.

Published by:

Materials Research Society
506 Keystone Drive
Warrendale, PA 15086
Telephone (724) 779-3003
Fax (724) 779-8313
Web site: <http://www.mrs.org/>

Manufactured in the United States of America

**Magnetoelectronics and Magnetic
Materials—Novel Phenomena
and Advanced Characterization**

**This document contains
blank pages that were
not filmed.**

CONTENTS

Preface.....	ix
Materials Research Society Symposium Proceedings.....	x
* Origin of the Magnetic Proximity Effect.....	1
Miguel Kiwi	
* Simulations of the Domain State Model.....	13
U. Nowak, A. Misra, and K.D. Usadel	
Exchange Bias and Training Effect in Polycrystalline Antiferromagnetic/Ferromagnetic Bilayers.....	25
Markus Kirschner, Dieter Suess, Thomas Schrefl, and Josef Fidler	
Rotating Anisotropies Without Superparamagnetic Grains in Exchange Bias Systems	31
T.C. Schulthess	
Interdiffusion, Crystallinity and Exchange Bias in Mn_xPt_{1-x}/Co Bilayers.....	37
Erie H. Morales, Yikuan Wang, and D. Lederman	
Crystal-Field Effect on Magnetic Moment and Exchange-Coupling for $Fe/W(100)$ and $Fe/W(110)$	43
X. Qian and W. Hübner	
Correlation Between Magnetic Property and Cation Distribution in Z-Type Hexagonal Barium-Ferrite ($Ba_3Co_{2-x}Fe_{24+x}O_{41}$) by Neutron Diffraction	49
Yukio Takada, Takeshi Tachibana, Takashi Nakagawa, Takao A. Yamamoto, Takeshi Shimada, and Shinji Kawano	
Nonstoichiometry of Epitaxial $FeTiO_{3+\delta}$ Films	55
Tatsuo Fujii, Makoto Sadai, Masakazu Kayano, Makoto Nakanishi, and Jun Takada	
Microstructure and Magnetic Property of L1o $CoPt-20\text{ at.}\% C$ Magnetic Thin Film	61
D.Y. Oh and J.K. Park	

*Invited Paper

* Role of Spin Momentum Current in Magnetic Non-Local Damping of Ultrathin Film Structures	67
G. Woltersdorf, R. Urban, and B. Heinrich	
Study of the Low Field Microwave Response in Yttrium Aluminates Dilutely Doped With Manganese	75
Rakhim R. Rakhimov, David E. Jones, and George B. Loutts	
Domain Wall Magnetoresistance and Complex Magnetic Response in Antiferromagnetically Coupled Fe/Cr Multilayers	81
F.G. Aliev, R. Villar, R. Schad, and J.L. Martinez	
Annealing of $\text{Co}_x\text{Cu}_{1-x}/\text{Cu}$ Multilayers	89
Jörg Ebert, Mohammad Ghafari, Branko Stahl, and Horst Hahn	
Magnetoresistance and Hall Effect Characterization on Magnetic Thin Films Multilayers	95
Jenica Neamtu and Marius Volmer	
Ab Initio Study of CPP Transport in Fe/Cr/Fe Trilayers: Influence of Transition Metal Impurities	101
Heike C. Herper, Peter Entel, Laszlo Szunyogh, and Peter Weinberger	
* Ab Initio Theory of CPP Transport	107
P. Weinberger	
In-Plane Transport of Doped Manganite Trilayers	127
Lisa Berndt Alldredge and Y. Suzuki	
Complex Magnetic Response in Magnetic Tunnel Junctions Determined via Magnetic and Transport Measurements	133
R. Guerrero, V.V. Pryadun, F.G. Aliev, R. Villar, J.L. Martinez, and J. Moodera	
Bistable Memory Effect in Chromium Oxide Junctions	139
A. Sokolov, C.-S. Yang, E. Ovtchenkov, L. Yuan, S.-H. Liou, and B. Doudin	
Nanoscale Analysis of a Co-SrTiO_3 Interface in a Magnetic Tunnel Junction	145
J.-L. Maurice, F. Pailloux, D. Imhoff, J.-P. Contour, A. Barthélémy, M. Bowen, C. Colliex, and A. Fert	

*Invited Paper

Observation of the Verwey Transition in Fe₃O₄ Nanocrystals	151
Gil Markovich, Teipi Fried, Pankaj Poddar, Amos Sharoni, David Katz, Tommer Wizansky, and Oded Millo	
Double Quantum Wire Magnetic Response	157
Anatoly Yu. Smirnov, Lev G. Mourokh, and Norman J.M. Horing	
Ferromagnetic Single-Electron Transistor With RC Gate	163
Jun-ichi Shirakashi and Yasushi Takemura	
Metal/Self-Assembled Monolayer/Metal Junctions for Magnetoelectronic Applications	169
Y.A. Ovchikov, Chunjuan Zhang, J. Redepenning, and B. Doudin	
* Recent Developments in Magnetic Recording Heads	175
Atsushi Tanaka and Mitsumasa Oshiki	
Micromagnetic Simulation of Thermal Effects in Magnetic Nanostructures	183
Rok Dittrich, Thomas Schrefl, Vassilios Tsiantos, Hermann Forster, Dieter Suess, Werner Scholz, and Josef Fidler	
* Precessional Strategies for the Ultrafast Switching of Soft and Hard Magnetic Nanostructures	189
T. Devolder, M. Belmeguenai, H.W. Schumacher, C. Chappert, and Y. Suzuki	
Inert Gas Condensation of Iron and Iron-Oxide Nanoparticles	201
C. Baker, S. Ismat Shah, S.K. Hasanain, B. Ali, L. Shah, G. Li, T. Ekiert, and K.M. Unruh	
Chemically Functional Alkanethiol Derivatized Magnetic Nanoparticles.....	207
David A. Fleming, Michael Napolitano, and Mary Elizabeth Williams	
Magnetic Properties of Ni Nanoparticles Embedded in Amorphous SiO₂	213
Fabio C. Fonseca, Gerardo F. Goya, Renato F. Jardim, Reginaldo Muccillo, Neftalí L.V. Carreño, Elson Longo, and Edson R. Leite	

*Invited Paper

A Small Angle Polarized Neutron Scattering Investigation of Magnetic Correlations in Nanocrystalline Fe₈₉Zr₇B₃Cu₁	219
Enrico Agosti, Oscar Moze, John Cadogan, Kiyonori Suzuki, Andre Heinemann, and Armen Hoell	
Mössbauer Characterization of Iron Oxide Nanoclusters Grown Within Aluminosilicate Matrices	225
Georgia C. Papaefthymiou, A. Bustamante Dominguez, and Rosa B. Scorzelli	
* Half-Integer Spin Molecular Nanomagnets	231
David N. Hendrickson, George Christou, Wolfgang Wernsdorfer, Stephen O. Hill, Núria Aliaga-Alcade, Sumit Bhaduri, Rachel S. Edwards, Sheila M.J. Aubin, and Ziming Sun	
* Defects, Tunneling, and EPR Spectra of Single-Molecule Magnets	241
Kyungwha Park, M.A. Novotny, N.S. Dalal, S. Hill, P.A. Rikvold, S. Bhaduri, G. Christou, and D.N. Hendrickson	
* Single Crystal High Frequency Cavity-Based EPR Spectroscopy of Single Molecule Magnets	253
S. Hill, R.S. Edwards, S.I. Jones, S. Maccagnano, J.M. North, N. Aliaga, E.-C. Yang, N.S. Dalal, G. Christou, and D.N. Hendrickson	
* Quantum Computing: From Bragg Reflections to Decoherence Estimates	265
Peter Pfeifer and Chen Hou	
Author Index	277
Subject Index	279

*Invited Paper

PREFACE

The papers in this volume are drawn from Symposium Q, "Magnetoelectronics—Novel Magnetic Phenomena in Nanostructures," and Symposium R, "Advanced Characterization of Artificially Structured Magnetic Materials," which were held December 1–5 at the 2002 MRS Fall Meeting in Boston, Massachusetts. The common focus of interest was on artificially engineered nanostructured magnetic systems. The two symposia discussed new phenomena in such systems that are interesting for magnetoelectronic applications, their preparation, and advanced methodology for characterization.

Interest in nanomagnetism has been catalyzed by advances in two fields of research:

(i) Advances in materials synthesis of structures whose length scales transcend magnetic length scales and open the possibility for creating materials with new magnetic properties. Such structures include interfaces, superlattices, tunneling devices, nanostructures, and single-molecule magnets. (ii) Advances in sample characterization techniques for nanomagnetism allow detailed exploration of structure-property relationships in nanostructured magnetic systems. The symposia reviewed current trends in both fields, and provided a forum for discussions about the outlook for further advances and new capabilities.

The symposia were sponsored by the Army Research Office, the Advanced Technology Institute Foundation of Japan, the Office of Naval Research, the National Science Foundation, the Advanced Light Source, the Advanced Photon Source, JEOL USA Inc., the Los Alamos Neutron Science Center, the National High Magnetic Field Laboratory, the NIST Center for Neutron Research, and the ORNL Spallation Neutron Source. We are very grateful for their generous financial support.

Symposium Q

Shufeng Zhang
Gernot Güntherodt
Andrew D. Kent
Teruya Shinjo
Ivan K. Schuller

Symposium R

Wolfgang Kuch
Michael R. Fitzsimmons
Jeffrey B. Kortright
Collin Broholm
Yimei Zhu

January 2003

MATERIALS RESEARCH SOCIETY SYMPOSIUM PROCEEDINGS

- Volume 715— Amorphous and Heterogeneous Silicon-Based Films—2002, J.R. Abelson, J.B. Boyce, J.D. Cohen, H. Matsumura, J. Robertson, 2002, ISBN: 1-55899-651-6
- Volume 716— Silicon Materials—Processing, Characterization and Reliability, J. Veteran, D.L. O'Meara, V. Misra, P. Ho, 2002, ISBN: 1-55899-652-4
- Volume 717— Silicon Front-End Junction Formation Technologies, D.F. Downey, M.E. Law, A. Claverie, M.J. Rendon, 2002, ISBN: 1-55899-653-2
- Volume 718— Perovskite Materials, K. Poeppelmeier, A. Navrotsky, R. Wentzcovitch, 2002, ISBN: 1-55899-654-0
- Volume 719— Defect and Impurity Engineered Semiconductors and Devices III, S. Ashok, J. Chevallier, N.M. Johnson, B.L. Sopori, H. Okushi, 2002, ISBN: 1-55899-655-9
- Volume 720— Materials Issues for Tunable RF and Microwave Devices III, S.C. Tidrow, J.S. Horwitz, J. Levy, X. Xi, 2002, ISBN: 1-55899-656-7
- Volume 721— Magnetic and Electronic Films—Microstructure, Texture and Application to Data Storage, P.W. DeHaven, D.P. Field, S.D. Harkness IV, J.A. Sutliff, J.A. Szpunar, L. Tang, T. Thomson, M.D. Vaudin, 2002, ISBN: 1-55899-657-5
- Volume 722— Materials and Devices for Optoelectronics and Microphotonics, R.B. Wehrspohn, S. Noda, C. Soukoulis, R. März, 2002, ISBN: 1-55899-658-3
- Volume 723— Molecularly Imprinted Materials—Sensors and Other Devices, K.J. Shea, M.J. Roberts, M. Yan, 2002, ISBN: 1-55899-659-1
- Volume 724— Biological and Biomimetic Materials—Properties to Function, J. McKittrick, J. Aizenberg, C. Orme, P. Vekilov, 2002, ISBN: 1-55899-660-5
- Volume 725— Organic and Polymeric Materials and Devices—Optical, Electrical and Optoelectronic Properties, G.E. Jabbour, N.S. Sariciftci, S.T. Lee, S. Carter, J. Kido, 2002, ISBN: 1-55899-661-3
- Volume 726— Organic/Inorganic Hybrid Materials—2002, R.M. Laine, C. Sanchez, S. Yang, C.J. Brinker, 2002, ISBN: 1-55899-662-1
- Volume 727— Nanostructured Interfaces, G. Duscher, J.M. Plitzko, Y. Zhu, H. Ichinose, 2002, ISBN: 1-55899-663-X
- Volume 728— Functional Nanostructured Materials through Multiscale Assembly and Novel Patterning Techniques, Steven C. Moss, 2002, ISBN: 1-55899-664-8
- Volume 729— BioMEMS and Bionanotechnology, L.P. Lee, J.T. Borenstein, R.P. Manginell, M. Okandan, P.J. Hesketh, 2002, ISBN: 1-55899-665-6
- Volume 730— Materials for Energy Storage, Generation and Transport, G. Ceder, S.A. Ringel, R.B. Schwarz, 2002, ISBN: 1-55899-666-4
- Volume 731— Modeling and Numerical Simulation of Materials Behavior and Evolution, V. Tikare, E.A. Olefsky, A. Zavaliangos, 2002, ISBN: 1-55899-667-2
- Volume 732E—Chemical-Mechanical Planarization, S.V. Babu, R. Singh, N. Hayasaka, M. Oliver, 2002, ISBN: 1-55899-668-0
- Volume 733E—Polymer Nanocomposites, S. Nutt, R. Vaia, W. Rodgers, G.L. Hagnauer, G.W. Beall, 2002, ISBN: 1-55899-669-9
- Volume 734— Polymer/Metal Interfaces and Defect Mediated Phenomena in Ordered Polymers, E.D. Manias, G.G. Malliaras, 2003, ISBN: 1-55899-671-0
- Volume 735— Bioinspired Nanoscale Hybrid Systems, G. Schmid, U. Simon, S.J. Stranick, S.M. Arrivo, S. Hong, 2003, ISBN: 1-55899-672-9
- Volume 736— Electronics on Unconventional Substrates—Electrotextiles and Giant-Area Flexible Circuits, M.S. Shur, P. Wilson, D. Urban, 2003, ISBN: 1-55899-673-7
- Volume 737— Quantum Confined Semiconductor Nanostructures, J.M. Buriak, D.D.M. Wayner, F. Priolo, B. White, V. Klimov, L. Tsybeskov, 2003, ISBN: 1-55899-674-5
- Volume 738— Spatially Resolved Characterization of Local Phenomena in Materials and Nanostructures, D.A. Bonnell, J. Piqueras, A.P. Shreve, F. Zypman, 2003, ISBN: 1-55899-675-3
- Volume 739— Three-Dimensional Nanoengineered Assemblies, T.M. Orlando, L. Merhari, K. Ikuta, D.P. Taylor, 2003, ISBN: 1-55899-676-1
- Volume 740— Nanomaterials for Structural Applications, C. Berndt, T.E. Fischer, I. Ovid'ko, G. Skandan, T. Tsakalakos, 2003, ISBN: 1-55899-677-X

MATERIALS RESEARCH SOCIETY SYMPOSIUM PROCEEDINGS

- Volume 741— Nano- and Microelectromechanical Systems (NEMS and MEMS) and Molecular Machines, A.A. Ayon, T. Buchheit, D.A. LaVan, M. Madou, 2003, ISBN: 1-55899-678-8
- Volume 742— Silicon Carbide 2002—Materials, Processing and Devices, S.E. Sadow, D.J. Larkin, N.S. Saks, A. Schoener, 2003, ISBN: 1-55899-679-6
- Volume 743— GaN and Related Alloys—2002, E.T. Yu, C.M. Wetzel, J.S. Speck, A. Rizzi, Y. Arakawa, 2003, ISBN: 1-55899-680-X
- Volume 744— Progress in Semiconductors II—Electronic and Optoelectronic Applications, B.D. Weaver, M.O. Manasreh, C.C. Jagadish, S. Zollner, 2003, ISBN: 1-55899-681-8
- Volume 745— Novel Materials and Processes for Advanced CMOS, M.I. Gardner, J-P. Maria, S. Stemmer, S. De Gendt, 2003, ISBN: 1-55899-682-6
- Volume 746— Magnetoelectronics and Magnetic Materials—Novel Phenomena and Advanced Characterization, S. Zhang, W. Kuch, G. Guentherodt, C. Broholm, A. Kent, M.R. Fitzsimmons, I. Schuller, J.B. Kortright, T. Shinjo, Y. Zhu, 2003, ISBN: 1-55899-683-4
- Volume 747— Crystalline Oxide-Silicon Heterostructures and Oxide Optoelectronics, D.S. Ginley, S. Guha, S. Carter, S.A. Chambers, R. Droopad, H. Hosono, D.C. Paine, D.G. Schlom, J. Tate, 2003, ISBN: 1-55899-684-2
- Volume 748— Ferroelectric Thin Films XI, D. Kaufman, S. Hoffmann-Eifert, S.R. Gilbert, S. Aggarwal, M. Shimizu, 2003, ISBN: 1-55899-685-0
- Volume 749— Morphological and Compositional Evolution of Thin Films, N. Bartelt, M.J. Aziz, I. Berbezier, J.B. Hannon, S. Hearne, 2003, ISBN: 1-55899-686-9
- Volume 750— Surface Engineering 2002—Synthesis, Characterization and Applications, A. Kumar, W.J. Meng, Y-T. Cheng, J. Zabinski, G.L. Doll, S. Veprek, 2003, ISBN: 1-55899-687-7
- Volume 751— Structure-Property Relationships of Oxide Surfaces and Interfaces II, X. Pan, K.B. Alexander, C.B. Carter, R.W. Grimes, T. Wood, 2003, ISBN: 1-55899-688-5
- Volume 752— Membranes—Preparation, Properties and Applications, V.N. Burganos, R.D. Noble, M. Asaeda, A. Ayril, J.D. LeRoux, 2003, ISBN: 1-55899-689-3
- Volume 753— Defect Properties and Related Phenomena in Intermetallic Alloys, E.P. George, H. Inui, M.J. Mills, G. Eggeler, 2003, ISBN: 1-55899-690-7
- Volume 754— Supercooled Liquids, Glass Transition and Bulk Metallic Glasses, A.L. Greer, T. Egami, A. Inoue, S. Ranganathan, 2003, ISBN: 1-55899-691-5
- Volume 755— Solid-State Chemistry of Inorganic Materials IV, M. Greenblatt, M.A. Alario-Franco, M.S. Whittingham, G. Rohrer, 2003, ISBN: 1-55899-692-3
- Volume 756— Solid-State Ionics—2002, P. Knauth, J-M. Tarascon, E. Traversa, H.L. Tuller, 2003, ISBN: 1-55899-693-1
- Volume 757— Scientific Basis for Nuclear Waste Management XXVI, R.J. Finch, D.B. Bullen, 2003, ISBN: 1-55899-694-X
- Volume 758— Rapid Prototyping Technologies, A.S. Holmes, A. Piqué, D.B. Dimos, 2003, ISBN: 1-55899-695-8
- Volume 759— Granular Material-Based Technologies, S. Sen, M.L. Hunt, A.J. Hurd, 2003, ISBN: 1-55899-696-6
- Volume 760E—The Undergraduate Curriculum in Materials Science and Engineering, E.P. Douglas, O.D. Dubón Jr., J.A. Isaacs, W.B. Knowlton, M. Stanley Whittingham, 2003, ISBN: 1-55899-697-4
- Volume 761E—Molecular Electronics, M-I. Baraton, E.L. Garfunkel, D.C. Martin, S.S.P. Parkin, 2003, ISBN: 1-55899-698-2

Prior Materials Research Society Symposium Proceedings available by contacting Materials Research Society

ORIGIN OF THE MAGNETIC PROXIMITY EFFECT

Miguel Kiwi

Facultad de Física, Pontificia Universidad Católica de Chile,

Casilla 306, Santiago, Chile 6904411

(Dated: January 16, 2003)

Abstract

The magnetic proximity effect (MPE) has attracted the attention of theorists and experimentalists for at least three decades. Lately, the relevance of the effect for the development of nanodevices has revived interest on the subject. Here we review how the field has evolved, centering our attention on metal-metal and metal-insulator systems. We describe, and critically compare, the different theoretical approaches that have been put forward, as well as their limitations. An evaluation of the relationship between existing theories and available experimental results is also attempted.

1. INTRODUCTION

Almost 30 years ago Zuckermann [1], in a pioneer work, showed theoretically that a system formed by a thin film of a weak itinerant ferromagnet (FM), in atomic contact with a thick film of an enhanced paramagnetic metal (PM), can exhibit a nonzero Curie temperature. Shortly thereafter this theory was extended to a system formed by a ferromagnet in contact with an antiferromagnet [2]. The technique that was used consisted in solving a simplified version of the integral equation derived from the Landau-Ginzburg theory of phase transitions. This equation reads as follows:

$$M(\vec{r}) = \int d^3r' U(\vec{r}) \chi_T(\vec{r} - \vec{r}'; 0) M(\vec{r}') - U(\vec{r}) M^3(\vec{r}) \sum_{\omega} G_p^0(\omega), \quad (1.1)$$

where $M(\vec{r})$ is the local magnetization at point \vec{r} , $U(\vec{r})$ the Hubbard exchange constant, $\chi_T(\vec{r}; 0)$ the static \vec{r} -dependent magnetic susceptibility of the non-interacting conduction electrons and $G_p^0(\omega)$ the propagator for these momentum p conduction electrons.

The above equation was analyzed using the procedure set forth by Werthamer [3], for the proximity effect between two superconductors. This way the integral equation 1.1 is transformed into a differential equation. The solution of this equation was obtained by matching the superconducting order parameter and its slope at the interface. However, this procedure is not reliable when applied to magnetic interfaces. First, with the possible exception of very weak magnets, the coherence length of the magnetic order parameter $M(\vec{r})$ is smaller than a typical lattice parameter, which excludes a continuous differential equation as a valid description. In addition, there is no *a priori* reason for requiring that the slope of $M(\vec{r})$ be continuous across an interface. For all these reasons a difference equation formulation seems to be appropriate.

On the other hand, in 1978 Bergmann [4] published experimental results on very thin film magnetization of Ni, Co and Fe deposited on a PM metallic substrate (Pb₃Bi). He interpreted his measurements to imply that the magnetization of the first few FM layers, closest to the PM, was substantially different from the bulk value. Moreover, he concluded that Ni did not develop a magnetic moment in films thinner than three monolayers. This in itself is an interesting fact, since magnetic dead layers at the surface of bulk Ni had first been reported and later disproved. Thus, Bergmann's measurements are relevant to the basic problem of the relation of magnetism and dimensionality, since in the crossover

from zero dimensions (a single magnetic Ni atom) to three-dimensional magnetic bulk Ni, the intermediate stage of a two-dimensional ultrathin Ni film deposited on a PM substrate turns out to be non-magnetic.

Bergmann's measurements constitute, to the best of my knowledge, the first experimental verification of the magnetic proximity effect (MPE); they also show unequivocally that the coherence length of $M(\vec{r})$ is of the order of magnitude of 0.1 nm.

2. METALLIC SYSTEMS

2.1. Early theories

Bergmann's experiments provided strong additional motivation for the formulation of a proper difference equation treatment of the problem. Not surprisingly shortly thereafter (1979), Cox *et al.* [5] put forward such a theoretical model to describe this experiment. Since Ni is clearly a typical example of an itinerant electron FM they suggested a treatment on the basis of a single band Hubbard model. Essentially it can be formulated as follows:

$$H = H_{FM} + H_{FM/PM} + H_{PM}, \quad (2.1)$$

where H_{FM} , H_{PM} and $H_{FM/PM}$ represent the ferromagnet, paramagnet and the coupling between them, respectively. They can be specified as

$$H_{FM} = \epsilon_{FM} \sum_{j,\sigma} c_{j,\sigma}^\dagger c_{j,\sigma} + t_{FM} \sum_{\langle i,j \rangle} \sum_{\sigma} [c_{i,\sigma}^\dagger c_{j,\sigma} + c_{j,\sigma}^\dagger c_{i,\sigma}] + U \sum_i \sum_{\sigma} \hat{n}_{i,\sigma} \hat{n}_{i,-\sigma}, \quad (2.2)$$

$$H_{PM} = \epsilon_{PM} \sum_{j,\sigma} c_{j,\sigma}^\dagger c_{j,\sigma} + t_{PM} \sum_{\langle i,j \rangle} \sum_{\sigma} [c_{i,\sigma}^\dagger c_{j,\sigma} + c_{j,\sigma}^\dagger c_{i,\sigma}], \quad (2.3)$$

$$H_{FM/PM} = t_{FM/PM} \sum_{\langle i,j \rangle} \sum_{\sigma} [c_{i,\sigma}^\dagger c_{j,\sigma} + c_{j,\sigma}^\dagger c_{i,\sigma}]. \quad (2.4)$$

Above $c_{j,\sigma}^\dagger$ and $c_{j,\sigma}$ are the spin σ electron creation and destruction operators at lattice site j , respectively. ϵ_{FM} and ϵ_{PM} are the FM and PM band centers, $\langle i, j \rangle$ denotes only nearest neighbor summation. t_{FM} , t_{PM} and $t_{FM/PM}$ are the hopping matrix elements for the FM, PM and across the FM/PM interface, respectively, and U is the Hubbard exchange constant.

In the preceding formulation it was assumed, in order to make the problem tractable, that the interface between the FM and the PM is flat, free of defects and that the crystal structures of the FM and PM match perfectly. However, the solution of this single-band problem is non-trivial, even after the preceding simplifications are adopted. The first major difficulty that has to be overcome is the charge transfer across the interface, to which the results are extremely sensitive. In Ref. [5] this was approximated by the addition of a spin independent potential Δ added to each PM site, in order to simulate a step like dipole at the interface; next, Δ was determined self-consistently. In this way semi-quantitative conclusions on the behavior of very thin FM films deposited on a PM substrate were obtained.

The main trends that the model of Cox *et al.* [5] established are that the magnitude of the magnetic moments depend mainly on the degree of band hybridization at the interface $t_{FM/PM}/t_{PM}$ and the band filling of the FM film itself. For a monolayer, and a plausible set of hopping parameters, the model yields a loss of the Ni magnetic moment, but not so for Co or Fe. However, its major weakness is the treatment of the charge transfer across the interface.

2.2. Interface charge transfer

Not long thereafter Mata *et al.* [6] reexamined the problem carrying out a more detailed calculation of several additional physical quantities, like charge transfer and layer by layer magnetization. The system treated was a single Ni, Co or Fe atomic layer deposited on Pb_3Bi , as the typical PM. However, the major improvement introduced by Mata *et al.* was in the interfacial charge transfer treatment. This was achieved using a generalized version of the Friedel sum rule, put forward by Toulouse [7], in which the charge rearrangements are related to the scattering phase shifts. This issue is quite crucial, since small charge transfers have large physical effects. Analytically, the generalized Friedel sum rule reads as follows:

$$\Delta N = \frac{1}{\pi N} \sum_{\vec{k}} \eta(\epsilon, \vec{k}_F) = - \frac{1}{\pi N} \sum_{\vec{k}} \arg \det(\mathbf{I} - \mathbf{V} G_0), \quad (2.5)$$

where ΔN is the difference between the nominal bulk electron occupation N and the FM film occupations, \mathbf{I} is the unit matrix, G_0 the bulk Greens function of the PM and \mathbf{V} the difference between the Hamiltonian 2.1 and the one which describes the infinite PM. The main conclusions, reached on the basis of the treatment of Ref. [6], were that both the charge

transfer and the magnetization are only significant for the FM and PM atomic layers closest to the interface.

This study was extended, using the same charge transfer treatment, to FM slabs of up to 50 monolayers thick, by Altbir *et al.* [8]. They were able to establish that for relatively weak ferromagnets, that is for $U/t_{PM} \leq 10$, the magnetization of the FM film was substantially modified, but that hardly any magnetization spread into the paramagnetic substrate was observable, not even close to the interface. These results are qualitatively independent of the filling of the single FM band.

2.3. Multiple bands

Tersoff and Falicov [9] reformulated the problem by changing the system: instead of considering a FM film on a semi-infinite PM bulk, they studied the behavior of a thin PM (3 monolayer Cu film) on a semi-infinite FM (Ni). This system has several advantages: the lattice parameters of Cu and Ni are quite similar, and both have the same crystal structure, and furthermore Cu grows well on Ni. Moreover, their treatment is more realistic, since they generalized the single band model described by Eq. 2.4, incorporating the 3d, 4s and 4p bands of Cu and Ni. A reduction to 0.33 and 0.13 μ_B of the Ni bulk magnetization (0.62 μ_B) for the nearest and second nearest layers to a (100) interface, respectively, was obtained. However, similar calculations indicated that Ni is paramagnetic (or nearly so) on the (111) face of Cu [10, 11]. Moreover, and in agreement with previous work, no appreciable penetration of the magnetization into the Cu did result.

Other authors have also explored the same ideas using closely related procedures. Mathon *et al.* [12] investigated the exchange coupling between Co and Cu, on the basis of a method put forward by Mathon [13]. Hasegawa and Herman [14] extended the calculations in two aspects: i) they studied, in a band theory formulation, the cobalt-chromium FM/AF interface, in contrast with a FM/PM one; and, ii) they included finite temperature effects.

On the experimental side of the aisle Frydman and Dynes [15], as recently as 1999, measured the magnetoresistance of granular ferromagnets suggesting that their observations could be interpreted as reflecting the existence of a magnetic proximity effect (MPE). More precisely, they measured the magnetoresistance of films of isolated Ni grains covered by different non-magnetic overlayers. They explored both the superparamagnetic to FM tran-

sition, and the impact of the different overlayers on the magnetic coupling between the Ni grains. The observation that a strong correlation of hysteresis with magnetic overlayer susceptibility does exist lead Frydman and Dynes [15] to suggest that, in high quality samples, the proximity effect may be dominant in the short distance scale. Just a few months ago Åkerman *et al.* [16] extracted, from Brillouin light scattering experiments, an upper bound for the magnetic thickness of Fe films. This upper bound turned out to be less than 1 Å for Fe/X/ZnF₂ and X/Fe/ZnF₂ systems, where X= Al and Pd, which constitutes an indication of the weakness of the MPE in metallic systems.

3. METAL-INSULATOR FM/AF INTERFACES

As a consequence of the interest that the exchange bias (EB) phenomenon [17] has attracted during the last years the interface between metallic FM's and AF insulators has become a subject of intensive research. In this context the electronic band theory models described above are replaced by a Heisenberg-like Hamiltonian descriptions of localized magnetic moments [18, 19]. Without going into specifics of the EB problem, on which we refer the reader to several recent experimental and theoretical reviews [17, 19, 20], here we will focus our attention on the difficulties related to the MPE issue that have to be overcome in the theoretical treatment of the interface. In close analogy with Eq. 2.1 the Hamiltonian that is applied in this context reads

$$\mathcal{H} = \mathcal{H}_{AF} + \mathcal{H}_{FM/AF} + \mathcal{H}_{FM} . \quad (3.1)$$

where \mathcal{H}_{AF} , $\mathcal{H}_{F/AF}$ and \mathcal{H}_{FM} describe the AF substrate, interface coupling and the F slab, respectively. For the single magnetic cell, partially represented in Fig. 1, and in sharp contrast with 2.4, the localized spin Heisenberg description takes the form

$$\begin{aligned} \mathcal{H}_{AF} = & - J_{AF} [S \hat{e}_{AF} \cdot (\vec{S}^{(\alpha)} - \vec{S}^{(\beta)}) + 2\vec{S}^{(\alpha)} \cdot \vec{S}^{(\beta)}] \\ & - \frac{1}{2} K_{AF} [(\vec{S}^{(\alpha)} \cdot \hat{e}_{AF})^2 + (\vec{S}^{(\beta)} \cdot \hat{e}_{AF})^2] - \frac{1}{2} \mu_B g (\vec{S}^{(\alpha)} + \vec{S}^{(\beta)}) \cdot \vec{H} , \end{aligned} \quad (3.2)$$

$$\mathcal{H}_{FM/AF} = - J_{F/AF} (\vec{S}^{(\alpha)} + \vec{S}^{(\beta)}) \cdot \vec{S}_1 , \quad (3.3)$$

$$\mathcal{H}_{FM} = - 2J_F \sum_{k=1}^{N-1} \vec{S}_k \cdot \vec{S}_{k+1} - \sum_{k=1}^N [\frac{K_F}{H^2} (\vec{S}_k \cdot \vec{H})^2 + \mu_B g \vec{S}_k \cdot \vec{H}] . \quad (3.4)$$

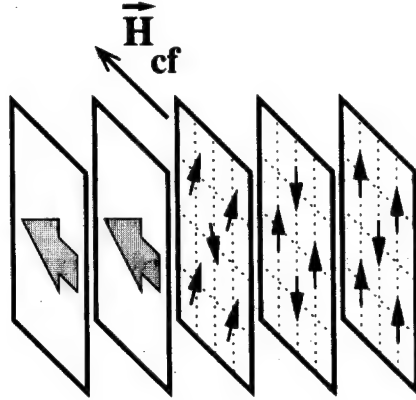


FIG. 1: Illustration of the perpendicular FM and AF magnetic interface configuration, with spin canting in the first AF layer.

Above $S = |\vec{S}|$ and N is the number of FM layers. μ_B and g denote the Bohr magneton and the Fe gyromagnetic ratio, respectively, while \vec{H} is the external applied magnetic field. J_μ denotes the Heisenberg exchange parameter and K_μ the uniaxial anisotropy. In Eq. 3.2 the unit vector \hat{e}_{AF} defines the AF uniaxial anisotropy direction, $\vec{S}^{(\alpha)}$ and $\vec{S}^{(\beta)}$ are canted spin vectors in the AF interface, belonging to the α - and β -AF sub-lattices.

The illustration of Fig. 1 stresses the fact, pointed out by Koon [18], that the ground state configuration corresponds to *perpendicular* orientation of the bulk FM moments relative to the AF magnetic easy axes direction. Moreover, Koon also showed that the magnetic moments in the AF interface layer exhibit canting; in fact, the minimum energy is achieved with the AF spins adopting a relatively small canting angle ($\theta < 10^\circ$) relative to the AF bulk easy axis, with a component opposite to the cooling field \vec{H}_{cf} direction. However this canting, which is the manifestation of the MPE, has a significant magnitude only in the AF layer closest to the interface [21–23].

The theoretical treatment outlined above actually is quite rudimentary. It assumes perfect crystallographic and magnetic order of the FM and the AF all the way to the interface, and moreover assumes perfect crystal structure matching across a flat interface. Since the MPE is only appreciable in the interface vicinity this is a rather strong assumption. Moreover, since the elastic energy related to symmetry breaking is in general so much larger than the

magnetic energies, this adds significant difficulties to a reliable treatment. Weissmann *et al.* [27], in view of the fact that both the FM and AF interface characteristics (geometry and physical parameters) are hard to determine experimentally and complicated to estimate theoretically, recently adopted two alternative interface configurations to obtain upper and lower bounds for the computed values of the exchange coupling across the interface between metallic Fe and insulating FeF₂, derived on the basis of *ab-initio* density functional theory calculations implemented for a periodic supercell. They yield values of $J_{FM/AF}$ that are quite close to each other and of the correct order of magnitude, which corresponds to ~ 1 meV. However, more realistic first principle computations of non-collinear and/or rough interfaces do not seem feasible at present.

Experimentally the MPE of metal-insulator FM/AF systems has recently received a great deal of attention. Here we limit ourselves to pointing out a few of these measurements, that are directly related to the model discussed above. Manago *et al.* [24] and Hoffmann *et al.* [25] investigated the magnetic proximity effect in NiO/Pd superlattices, with conflicting results. While the former suggested that a ferromagnetic moment of $0.59 \mu_B$ developed per Pd atom, Hoffmann *et al.* used polarized neutron reflectometry to directly observe the Pd magnetic moment and to characterize its spatial dependence (*i.e.* the magnetization profile of the heterostructure), but without finding evidence of Pd magnetization. In addition, Hoffmann *et al.* [26] just reported neutron reflectometry results on another metal-insulator FM/AF system: Co/LaFeO₃, where a net magnetic moment is observed to develop in the AF layer closest to the interface. More remarkably, this AF magnetization remains constant when the magnetic field is cycled and is coupled antiferromagnetically to the FM. These experimental observations are fully compatible with the exchange bias model put forward in Refs. [21–23].

4. SPIN INJECTION

The renewed interest in the MPE is certainly related to spintronics. In fact, a century plus since the discovery of the electron, and after extensive exploitation of charge related effects, the electron spin is only now being explored for application in devices. In this context another related avenue, spin injections into semiconductors has received much attention [28, 29]. However, the physical mechanisms related to spin injection are completely different to the ones discussed above. While in the conventional MPE quantum mechanics is the governing

ingredient, spin injection is a diffusive non-equilibrium process in which electrons tunnel through a barrier at the heterojunction. The barrier is essential since otherwise, and for the reasons outlined in the preceding sections, spin injections turns out to be very weak for FM contacts with typical metallic resistivity. Present theories [28, 29] allow to conclude that spin-dependent tunneling can be employed to achieve spin injection, but that the spin injection efficiency does not exceed 2% at a temperature of 3 K [30].

Another recently explored road to spin coherence in a semiconductor is reflection off a FM. In fact, Epstein *et al.* [31] observed spontaneous spin coherence induced by FM proximity in a Mn based hybrid ferromagnet/*n*-GaAs heterostructure, while Ciuti *et al.* [32] analyzed theoretically the non-equilibrium spin dynamics of carriers reflected from a FM interface.

5. SUMMARY AND CONCLUSION

In summary, we have outlined the evolution of the understanding of the magnetic proximity effect (MPE), as it has developed over the last 30 years. Two fundamentally different physical systems were considered: i) a FM metal in contact with a PM metal; and, ii) a FM metal on an AF insulator. Completely distinct theoretical treatments yield, for both cases, a rather short ranged MPE. For ferromagnets on paramagnets the effect is strongest on the FM side, while for a FM on an antiferromagnet it is the AF magnetization close to the interface that is more strongly affected.

Lately, and in relation to spintronics, a different but closely related phenomenon has received much attention: the spin injection of polarized electrons into a semiconductor. This is a non-equilibrium diffusive process, of a different nature from the quantum mechanical phenomenon known as MPE. A full understanding of both, MPE and spin injection, are relevant for the exciting and challenging problem of achieving successful manipulation of electron spin in practical devices.

Acknowledgments

Work supported by the *Fondo Nacional de Desarrollo Científico y Tecnológico* (FONDECYT, Chile) under grant #8990005.

- [1] M. J. Zuckermann, Solid State Comm. **12**, 745 (1973).
- [2] M. Kiwi and M. J. Zuckermann, "The Proximity Effect for Weak Itinerant Ferro- and Antiferro-Magnets", Proc. of the 19-th Conf. on Magnetism and Magnetic Materials, **18**, 347 (1973).
- [3] N. R. Werthamer, Phys. Rev. **132**, 2440 (1963).
- [4] G. Bergman, Phys. Rev. Lett. **41**, 264 (1978).
- [5] B. N. Cox, R. A. Tahir-Kheli and R. J. Elliot, Phys. Rev. **B20**, 2864 (1979).
- [6] G. J. Mata, E. Pestana and M. Kiwi, Phys. Rev. **B26**, 3841 (1982).
- [7] G. Toulouse, Solid State Comm. **4**, 593 (1966).
- [8] D. Altbir, M. Kiwi, G. Martínez and M. J. Zuckermann, Phys. Rev. **B40**, 6963 (1989).
- [9] J. Tersoff and L. M. Falicov, Phys. Rev. **B25**, 2959 (1982).
- [10] J. Tersoff and L. M. Falicov, Phys. Rev. **B26**, 459 (1982).
- [11] J. Tersoff and L. M. Falicov, Phys. Rev. **B26**, 6186 (1982).
- [12] J. Mathon *et al.*, Phys. Rev. Lett. **74**, 3696 (1995).
- [13] J. Mathon, J. Phys. Cond. Matter **1**, 2505 (1989).
- [14] H. Hasegawa and F. Herman, Phys. Rev. **B38**, 4863 (1988).
- [15] A. Frydman and R. C. Dynes, Solid State Comm. **110**, 485 (1999).
- [16] J. J. Åkerman, I. Guedes, C. Leighton, M. Grimsditch and I. K. Schuller, Phys. Rev. **B65**, 104432 (2002).
- [17] J. Nogués and I. K. Schuller, J. Magn. Magn. Mater. **192**, 203 (1999), and references therein.
- [18] N. C. Koon, Phys. Rev. Lett. **78**, 4865 (1997).
- [19] M. Kiwi, J. Magn. Magn. Mater., **234/3**, 584 (2001), and references therein.
- [20] R. L. Stamps, J. Phys. D: Appl. Phys. **33**, R247 (2000).
- [21] M. Kiwi, J. Mejía-López, R. D. Portugal and R. Ramírez, Europhysics Letters **48**, 573 (1999).
- [22] M. Kiwi, J. Mejía-López, R. D. Portugal and R. Ramírez, Appl. Phys. Lett. **75**, 3995 (1999).
- [23] M. Kiwi, J. Mejía-López, R. D. Portugal and R. Ramírez, Solid State Comm. **116**, 315 (2000).
- [24] T. Manago, H. Miyajima, K. Kawaguchi, M. Sohma and I. Yamaguchi, J. Magn. Magn. Mater., **177/181**, 1191 (1998).
- [25] A. Hoffmann, M. R. Fitzsimmons, J. A. Dura and C. F. Majkrzak, Phys. Rev. **B65**, 024428 (2001).

- [26] A. Hoffmann, J. W. Seo, M. R. Fitzsimmons, H. Siegwart, J. Fompeyrine, J. P. Loquet, J. A. Dura and C. F. Majkrzak, accepted for publication in Phys. Rev. B.
- [27] M. Weissmann, A. M. Lois and M. Kiwi, J. Mag. Mag. Mat., **234/1**, 19 (2001).
- [28] D. L. Smith and R. N. Silver, Phys. Rev. **B64**, 045323 (2001).
- [29] A. Fert and H. Jaffrès, Phys. Rev. **B64**, 184430 (2001).
- [30] Z. G. Yu and M. E. Flatté, Phys. Rev **B66**, 201202 (2002).
- [31] R. J. Epstein *et al.*, Phys. Rev **B65**, 121202 (2002).
- [32] C. Ciuti, J. P. McGuire and L. J. Sham, Phys. Rev. Lett. **89**, 156601 (2002).

Simulations of the Domain State Model

U. Nowak¹, A. Misra², and K. D. Usadel¹

¹ Theoretische Physik, Gerhard-Mercator-Universität Duisburg
47048 Duisburg, Germany

² Dept. of Physics and MINT Center, University of Alabama
Box 870209, AL 35487, USA

ABSTRACT

The domain state model for exchange bias consists of a ferromagnetic layer exchange coupled to an antiferromagnetic layer. In order to model a certain degree of disorder within the bulk of the antiferromagnet, the latter is diluted throughout its volume. Extensive Monte Carlo simulations of the model were performed in the past. Exchange bias is observed as a result of a domain state in the antiferromagnetic layer which develops during the initial field cooling, carrying a remanent domains state magnetization which is partly irreversible during hysteresis. A variety of typical effects associated with exchange bias like, e. g., its dependence on dilution, positive bias, temperature and time dependences as well as the dependence on the thickness of the antiferromagnetic layer can be explained within this model.

INTRODUCTION

For compound materials consisting of a ferromagnet (FM) in contact with an antiferromagnet (AFM) a shift of the hysteresis loop along the magnetic field axis can occur which is called exchange bias (EB). Often, this shift is observed after cooling the entire system in an external magnetic field below the Néel temperature T_N of the AFM. Although EB is well known since many years [1, 2] its microscopic origin is still discussed controversially. For a review of the vast literature on EB the reader is referred to an article by Nogués and Schuller [3].

In the approach of Malozemoff [4, 5, 6] EB is attributed to the formation of domain walls in the AFM, perpendicular to the FM/AFM interface due to interface roughness. These domain walls are supposed to occur during cooling in the presence of the magnetized FM and to carry a small net magnetization at the FM/AFM interface. This interface magnetization is furthermore supposed to be stable during the reversal of the FM, consequently shifting the hysteresis loop. However, the formation of domain walls in the AFM only due to interface roughness is energetically unfavorable and its occurrence and stability has never been proven.

Because of these difficulties other approaches have been developed. In a model introduced by Koon [7] EB is obtained through a mechanism in which a domain wall forms in the AFM parallel to the interface while the magnetization of the FM rotates. This mechanism has been proposed earlier by Mauri et al. [8]. Nevertheless it was shown by Schulthess and Butler [9, 10] that in this model EB vanishes if the motion of the spins in the AFM is not restricted to a plane parallel to the film as was done in Koon's work. To

obtain EB Schulthess and Butler assumed uncompensated AFM spins at the interface. However, their occurrence and stability during a magnetic hysteresis loop is not *explained*, neither in their model nor in other models [11, 12] although uncompensated AFM spins were observed experimentally [13, 14].

In a recent experiment Miltényi et al. [15] showed that it is possible to strongly influence EB in Co/CoO bilayers by diluting the antiferromagnetic CoO layer, i. e. by inserting non-magnetic substitutions ($\text{Co}_{1-x}\text{Mg}_x\text{O}$) or defects (Co_{1-y}O) not at the FM/AFM interface, but rather throughout the volume part of the AFM. In the same letter it was shown that a corresponding theoretical model, the domain state model, investigated by Monte Carlo simulations shows a behavior very similar to the experimental results. It was argued that EB has its origin in a domain state (DS) in the AFM which triggers the spin arrangement and the FM/AFM exchange interaction at the interface. Later it was shown that a variety of experimental facts associated with EB can be explained within this DS model [16, 17, 18, 19, 20].

The importance of defects for the EB effect is also confirmed by recent experiments on $\text{Fe}_x\text{Zn}_{1-x}\text{F}_2/\text{Co}$ bilayers [21] and by experiments [22, 23] where it was shown that it is possible to modify EB by means of irradiating an FeNi/FeMn system by He ions in presence of a magnetic field. Depending on the dose of the irradiation and the magnetic field present at the time of irradiation, it was possible to manipulate both the magnitude and even the direction of the EB field. Further support for the relevance of domains in EB systems is given by a direct spectroscopic observation of AFM domains [24, 25].

DOMAIN STATE MODEL

The domain state model [15] for EB consists of t_{FM} monolayers of FM and t_{AFM} monolayers of diluted AFM. The FM is exchange coupled to the topmost layer of the AFM. The geometry of the model is sketched in Fig. 1 for $t_{\text{FM}} = 1$ and $t_{\text{AFM}} = 3$.

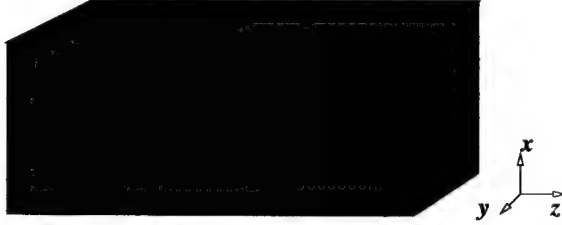


Figure 1: Sketch of the DS model with one FM layer and three diluted AFM layers. The dots mark defects. The easy axis of both, FM and AFM is the z - axis.

The system is described by a classical Heisenberg model with nearest neighbor exchange on a simple cubic lattice with exchange constants J_{FM} and J_{AFM} for the FM and the AFM respectively, while J_{INT} stands for the exchange constant between FM and AFM. For the nearest neighbor-exchange constant J_{AFM} of the AFM which mainly determines its

Néel temperature we set $J_{\text{AFM}} = -J_{\text{FM}}/2$. For simplicity, we assume the same value for the interface coupling, but with positive sign ($J_{\text{INT}} = -J_{\text{AFM}}$). Also, we assume that the values of the magnetic moments of FM and AFM are identical (included in the magnetic field energy B). The Hamiltonian of our system is thus,

$$\begin{aligned} \mathcal{H} = & -J_{\text{FM}} \sum_{\langle i,j \rangle} \vec{S}_i \cdot \vec{S}_j - \sum_i (d_z S_{iz}^2 + d_x S_{ix}^2 + \vec{S}_i \cdot \vec{B}) \\ & -J_{\text{AFM}} \sum_{\langle i,j \rangle} \epsilon_i \epsilon_j \vec{\sigma}_i \cdot \vec{\sigma}_j - \sum_i \epsilon_i (k_z \sigma_{iz}^2 + \vec{\sigma}_i \cdot \vec{B}) \\ & -J_{\text{INT}} \sum_{\langle i,j \rangle} \epsilon_j \vec{S}_i \cdot \vec{\sigma}_j, \end{aligned} \quad (1)$$

where \vec{S}_i denote normalized spins at sites of the FM layer and $\vec{\sigma}_i$ denote normalized spins at sites of the AFM.

The first line of the Hamiltonian describes the energy of the FM with the z -axis as its easy axis (anisotropy constant $d_z = 0.02J_{\text{FM}}$). d_z sets the Stoner-Wohlfarth limit of the coercive field, i. e., the zero temperature limit for magnetization reversal by coherent rotation ($B_c = 2d_z$, in our units, for a field parallel to the easy axis). The dipolar interaction is approximated by an additional anisotropy term (anisotropy constant $d_x = -0.1J_{\text{FM}}$) which includes the shape anisotropy, leading to a magnetization which is preferentially in the $y-z$ -plane. We checked, however, that its value does not influence our results, as far as the EB is concerned. The second line is the contribution from the AFM also having its easy axis along z direction. The AFM is diluted, i. e., a fraction p of sites is left without a magnetic moment ($\epsilon_i = 0$) while the other sites carry a moment ($\epsilon_i = 1$). The last term describes the interaction of the FM with the interface AFM monolayer.

Eq. 1 suggests a simple ground state argument for the strength of the bias field.

Assuming that all spins in the FM remain parallel during field reversal and that some net magnetization of the interface layer of the AFM remains constant during the reversal of the FM a simple calculation gives the usual estimate for the bias field,

$$t_{\text{FM}} B_{\text{EB}} = J_{\text{INT}} m_{\text{INT}}, \quad (2)$$

where m_{INT} is that stable part of the interface magnetization of the AFM (per spin) which is responsible for the EB. For an ideal uncompensated and totally stable interface one would expect $m_{\text{INT}} = 1$. As is well known, this estimate leads to a much too high bias field, while for an ideal compensated interface, on the other hand, one would expect $m_{\text{INT}} = 0$ and, hence, $B_{\text{EB}} = 0$. Experimentally, however, often there is on the one hand no big difference between compensated and uncompensated interfaces and on the other hand it is found that B_{EB} is much smaller than $J_{\text{INT}}/t_{\text{FM}}$, rather of the order of a few percent of it. The solution of this puzzle is that m_{INT} is neither constant during field reversal nor is it a simple known quantity [19, 18] and we will discuss this in detail in the following.

RESULTS

Monte Carlo methods are used with a heat-bath algorithm and single-spin flip dynamics [26] for the simulation of the model explained above. The trial step of the spin update consists of two steps: first it is a small variation within a cone around the initial spin direction, followed, second, by a total spin flip. This twofold spin update is ergodic and symmetric [27] and can take care of a broad range of anisotropies, from very soft spins up to the high anisotropy (Ising) limit. We perform up to 40000 Monte Carlo steps (MCS) for a complete hysteresis loop.

To observe the domain structure of the AFM we have to guarantee that typical length scales of the domain structure fit into our system. In the following we show results for systems of lateral extension $L \times L$ with $L = 64$ or 128 and a thickness of $t_{\text{FM}} = 1$ and t_{AFM} ranging from 3 to 9. We use periodical boundary conditions within the film plane and open boundary conditions perpendicular to it.

The main quantities which we monitor are the thermal averages of the z -component of the magnetic moment for each individual monolayer normalized to the magnetic moment of the saturated monolayer. In our simulations the system is cooled from above to below the ordering temperature of the AFM. During cooling the FM is initially magnetized along the easy z axis resulting in a nearly constant exchange field for the AFM monolayer at the interface. Also, the system is cooled in the presence of an external magnetic field, the cooling field. In addition to the exchange field from the ordered FM this field acts also on the AFM. When the desired final temperature is reached a magnetic field along the easy axis is applied and reduced in small steps down to a certain minimum value and afterwards raised again up to the initial value. This corresponds to one cycle of the hysteresis loop.

Typical hysteresis loops are depicted in Fig. 2. Shown are results for the magnetization of the FM (upper figure) as well as that of the AFM interface monolayer (lower figure). An EB is observed clearly and we determine the corresponding EB field as $B_{\text{EB}} = (B^+ + B^-)/2$ where B^+ and B^- are those fields of the hysteresis loop branches for increasing and decreasing field, where the easy axis component of the magnetization of the FM becomes zero.

An analysis of the magnetization curve of the interface layer gives an interesting insight into the nature of EB. After the field cooling procedure the AFM interface carries a magnetization (m_I). A part of this AFM interface magnetization is stable during hysteresis and leads to the fact that the magnetization curve of the interface layer of the AFM is shifted upwards. This irreversible part of the interface magnetization of the AFM acts as an additional effective field on the FM, resulting in EB. Note that the interface magnetization of the AFM also displays hysteresis, following the exchange coupling to the FM. This means that the whole interface magnetization of the AFM consists of a reversible part leading to an enhanced coercivity and an irreversible part leading to EB.

In experiments usually the magnetization of the whole FM/AFM bilayer is measured. The corresponding sample magnetization loop might not only be shifted horizontally but also vertically. The vertical shift contains contributions from the volume part of the AFM as well as from its interface. The volume magnetization of the AFM is induced by the cooling field and hence not shifted when the cooling field is zero and shifted upwards when it is finite. The interface contribution depends on the sign of the interface coupling and

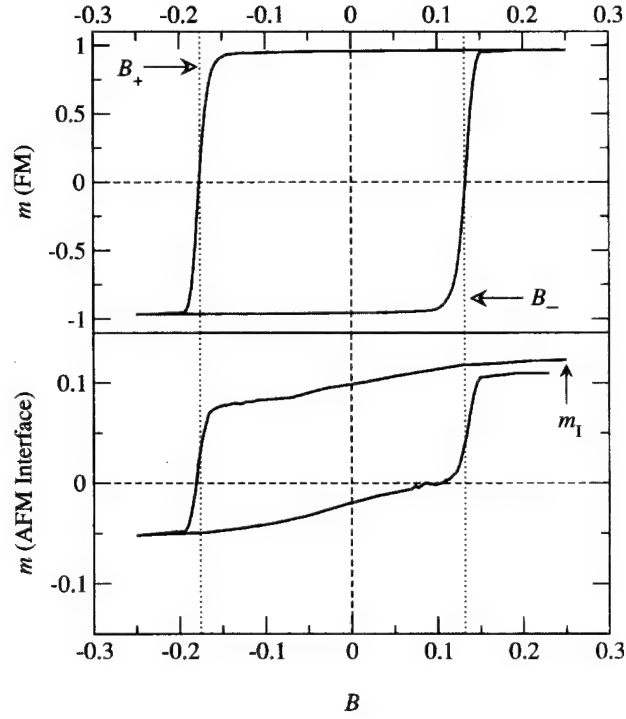


Figure 2: Simulated hysteresis loops of the DS model as explained in the text. Dilution $p = 0.4$, $k_B T = 0.1 J_{\text{FM}}$, positive interface coupling, $J_{\text{INT}} = |J_{\text{AFM}}|$. AFM anisotropy $k_z = J_{\text{FM}}/2$. The cooling field was $B_c = 0.25 J_{\text{INT}}$. Shown is the magnetic moment of the FM and the interface monolayer of the AFM (normalized to its saturation value.)

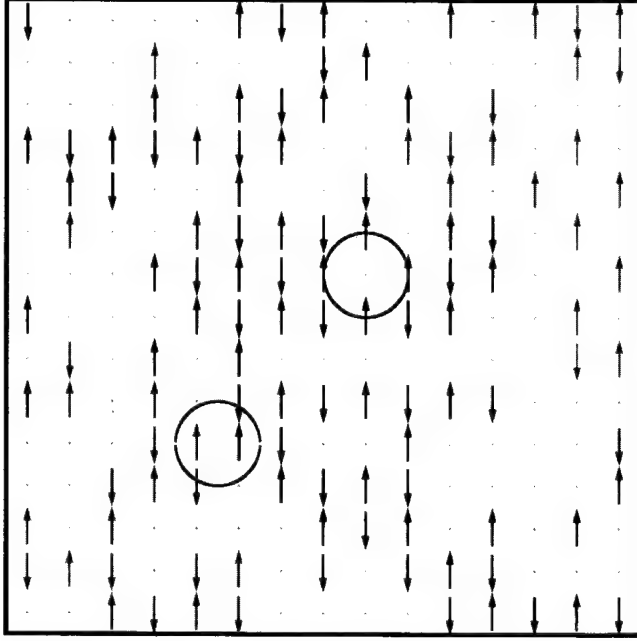


Figure 3: Snapshot of a spin configuration in a small portion of the interface monolayer of the AFM after field cooling ($B_c = 0.25J_{\text{FM}}$). The color coding distinguishes different AFM domains. The circles mark sources of magnetization. The external field and the FM magnetization are pointing up.

may be positive, as in our calculation, or even negative for negative interface coupling (see also [28, 19, 18]).

With the following two sketches we want to illustrate on a more microscopic basis where the interface magnetization of the AFM and its partitioning in reversible and irreversible parts comes from. Figure 3 shows spin configurations in a small portion of the interface monolayer of the AFM after field cooling. The simulated system size is $64 \times 64 \times 10$ with only one FM monolayer. For simplicity, this simulation was performed in the Ising limit for the AFM ($k_z \rightarrow \infty$). The dilution p of the AFM is 50 %, nevertheless the spins are much more connected than it appears from the sketch via the third dimension.

Obviously, the AFM is in a domain state. The reason for the domain formation and, consequently, for the lack of long-range order is the interface magnetization which couples to the exchange field coming from the FM and the external field (both pointing up) lowering the energy of the system. The interface magnetization follows from two contributions. Examples for both are indicated via the circles.

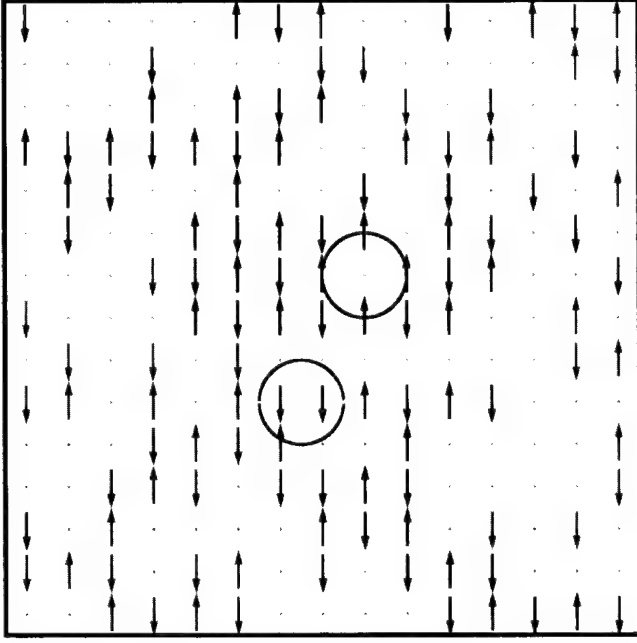


Figure 4: Snapshot of the same portion of the AFM interface monolayer after reversal of the FM ($B = -0.25J_{\text{INT}}$). The circles mark once again sources of magnetization where the domain wall magnetization is reversed while the volume magnetization is unchanged. The external field and the FM magnetization are now pointing down.

One contribution comes from parallel spin pairs in the domain walls, all pointing up in our example, i. e. into the direction of the exchange field of the FM and the external field. We will call this part in the following *domain wall magnetization*. A second contribution comes from an imbalance of the number of defects of the two antiferromagnetic sublattices. We will call this contribution in the following *volume magnetization*. The imbalance of the number of defects of the two antiferromagnetic sublattices also leads to a net magnetization within a domain which couples to the exchange field of the FM and the external field. The reason for the imbalance is that the domain structure is not random. Rather, it is an optimized structure arising during the initial cooling procedure with as much magnetization as possible coupling to the exchange field of the FM and the external field, following the energy minimization principle.

However, an AFM interface magnetization alone cannot lead to EB. Only the irreversible part of it (during hysteresis) may lead to EB. Figure 4 shows for comparison spin configurations in the same portion of the interface monolayer of the AFM after

reversal of the FM. Clearly, the bigger parts of the domain structure did not change during reversal of the FM. However, there are rearrangements on smaller length scales, leading mainly to the fact that the domain wall magnetization changes its sign. In Figure 4 all of the spin pairs within domain walls are pointing down following the reversed FM and the external field.

However, the volume magnetization coming from the defects remains frozen. The stability of the domain structure stems from the fact that the domain walls are pinned at defects sites as well as between pairs of spins which are aligned with the field. Hence, during a movement of the domain wall energy barriers may have to be overcome by thermal activation. This explains why a large domain in general will stay in a metastable state on exponentially long time scales, while rearrangements on a shorter length scale are possible, of course depending on the temperature and the material parameters of the AFM.

Many of the essential properties of diluted AFMs, the occurrence of domain states, metastability, remanent magnetization and slow relaxation, among others, have been investigated before, even though not in the context of EB (for reviews on diluted AFMs see [29, 30], for a detailed discussion of the connection between diluted AFMs and EB systems see [18]).

An important property of diluted AFMs is the slow relaxation of the remanent magnetization, i. e., the magnetization obtained after switching off the cooling field. Here it is known that the remanent magnetization of the DS relaxes non-exponentially on extremely long time scales after the field is switched off [31, 32, 33] or even within the applied field [34, 35, 36]. In the DS model EB is related to this remanent magnetization. This implies a decrease of EB due to slow relaxation of the AFM DS. Especially, the reason for the so-called training effect can be understood from Figs. 2, where it is shown that the hysteresis loop of the AFM interface layer is not closed on the right hand side. This implies that the DS magnetization is lost partly during the hysteresis loop due to a rearrangement of the AFM domain structure. This loss of magnetization clearly leads to a reduction of the EB for the next loop.

CONCLUSIONS

It was shown both, experimentally [15, 19] and by Monte Carlo simulations [15, 18], that diluting the AFM in the volume part away from the FM/AFM interface significantly enhances EB. This dilution supports the formation of domains in the volume of the AFM which carry magnetization. The DS of the AFM is to some extent frozen during hysteresis and this irreversible part of the DS magnetization at the AFM interface leads to EB.

In the domain state model, domain formation is crucial for the existence of EB. Without domain formation there would be no EB for compensated and a much too high EB for uncompensated interfaces. Defects in the AFM favor domain formation and thus make the distinction between compensated and uncompensated interfaces to a large extent obsolete. Also, it should be noted that the occurrence of a DS with an irreversible surplus magnetization is not restricted to diluted AFMs. Spin glasses, for instance, show similar features and it is known that the EB effect occurs also in compounds of FM and spin glass [3]. In these systems we believe the same mechanism leading to EB in our DS model is also

at work.

Important features of EB systems found experimentally [19] have their counterpart in the simulations [18], such as the order of magnitude of EB fields, the shape of hysteresis curves, the dilution dependence of EB, its temperature dependence, the training effect, and the occurrence of positive EB. The dependence of EB on thickness of the AFM is further discussed in [16], the dependence on the anisotropy of the AFM in [17].

Recent experiments [22, 23] which showed that EB can be modified by means of ion irradiating, i. e., by inducing defects in the bulk of the AFM underline the importance of defects for the understanding of EB. The DS model for EB in which the ion irradiation is modeled as a second dilution of the AFM after the initial cooling procedure explains the experimental facts in terms of domain rearrangements caused by diluting the system within an applied field [20].

In conclusion, our simulations strongly suggest that the existence of a DS in the AFM enhanced by defects or any other mechanism reducing the energy necessary to form domains in the volume part of the AFM, is a common feature of FM/AFM compounds showing a significant EB.

ACKNOWLEDGMENT

This work has been supported by the Deutsche Forschungsgemeinschaft through SFB 491. The authors thank B. Beschoten and G. Güntherodt for a fruitful cooperation.

References

- [1] W. H. Meiklejohn and C. P. Bean, Phys. Rev. **102**, 1413 (1956).
- [2] W. H. Meiklejohn and C. P. Bean, Phys. Rev. **105**, 904 (1957).
- [3] J. Nogués and I. K. Schuller, J. Magn. Magn. Mat. **192**, 203 (1999).
- [4] A. P. Malozemoff, Phys. Rev. B **35**, 3679 (1987).
- [5] A. P. Malozemoff, J. Appl. Phys. **63**, 3874 (1988).
- [6] A. P. Malozemoff, Phys. Rev. B **37**, 7673 (1988).
- [7] N. C. Koon, Phys. Rev. Lett. **78**, 4865 (1998).
- [8] D. Mauri, H. C. Siegmann, P. S. Bagus, and E. Kay, J. Appl. Phys. **62**, 3047 (1987).
- [9] T. C. Schulthess and W. H. Butler, Phys. Rev. Lett. **81**, 4516 (1998).
- [10] T. C. Schulthess and W. H. Butler, J. Appl. Phys. **85**, 5510 (1999).
- [11] M. D. Stiles and R. D. McMichael, Phys. Rev. B **59**, 3722 (1999).
- [12] M. Kiwi, J. Mejía-López, R. D. Portugal, and R. Ramírez, Europhys. Lett. **48**, 573 (1997).

- [13] K. Takano, R. H. Kodama, A. E. Berkowitz, W. Cao, and G. Thomas, Phys. Rev. Lett. **79**, 1130 (1997).
- [14] K. Takano, R. H. Kodama, A. E. Berkowitz, W. Cao, and G. Thomas, J. Appl. Phys. **83**, 6888 (1998).
- [15] P. Miltényi, M. Gierlings, J. Keller, B. Beschoten, G. Güntherodt, U. Nowak, and K. D. Usadel, Phys. Rev. Lett. **84**, 4224 (2000).
- [16] U. Nowak, A. Misra, and K. D. Usadel, J. Appl. Phys. **89**, 7269 (2001).
- [17] U. Nowak, A. Misra, and K. D. Usadel, J. Magn. Magn. Mat. **240**, 243 (2002).
- [18] U. Nowak, K. D. Usadel, P. Miltényi, J. Keller, B. Beschoten, and G. Güntherodt, Phys. Rev. B **66**, 14430 (2002).
- [19] J. Keller, P. Miltényi, B. Beschoten, G. Güntherodt, U. Nowak, and K. D. Usadel, Phys. Rev. B **66**, 14431 (2002).
- [20] A. Misra, U. Nowak, and K. D. Usadel, J. Appl. Phys. in press (2003).
- [21] H. T. Shi, D. Lederman, and E. E. C. Fullerton, J. Appl. Phys. **91**, 7763 (2002).
- [22] T. Mewes, R. Lopusnik, J. Fassbender, B. Hillebrands, M. Jung, D. Engel, A. Ehresmann, and H. Schmoranz, Appl. Phys. Lett. **76**, 1057 (2000).
- [23] A. Mougin, T. Mewes, M. Jung, D. Engel, A. Ehresmann, H. Schmoranz, J. Fassbender, and B. Hillebrands, Phys. Rev. B **63**, 60409 (2001).
- [24] F. Nolting, A. Scholl, J. Stöhr, J. W. Seo, J. Fompeyrine, H. Siegwart, J.-P. Locquet, S. Anders, J. Lüning, E. E. Fullerton, M. F. Toney, M. R. Scheinfein, and H. A. Padmore, Nature **405**, 767 (2000).
- [25] H. Ohldag, A. Scholl, F. Nolting, S. Anders, F. U. Hillebrecht, and J. Stöhr, Phys. Rev. Lett. **86**, 2878 (2001).
- [26] K. Binder and D. W. Heermann, in *Monte Carlo Simulation in Statistical Physics*, edited by P. Fulde (Springer-Verlag, Berlin, 1997).
- [27] U. Nowak, in *Annual Reviews of Computational Physics IX*, edited by D. Stauffer (World Scientific, Singapore, 2001), p. 105.
- [28] J. Nogués, C. Leighton, and I. K. Schuller, Phys. Rev. B **61**, 1315 (2000).
- [29] W. Kleemann, Int. J. Mod. Phys. B **7**, 2469 (1993).
- [30] D. P. Belanger, in *Spin Glasses and Random Fields*, edited by A. P. Young (World Scientific, Singapore, 1998).
- [31] S.-J. Han, D. P. Belanger, W. Kleemann, and U. Nowak, Phys. Rev. B **45**, 9728 (1992).

- [32] U. Nowak, J. Esser, and K. D. Usadel, *Physica A* **232**, 40 (1996).
- [33] M. Staats, U. Nowak, and K. D. Usadel, *Phase Transitions* **65**, 159 (1998).
- [34] J. Villain, *Phys. Rev. Lett.* **52**, 1543 (1984).
- [35] P. Pollak, W. Kleemann, and D. P. Belanger, *Phys. Rev. B* **38**, 4773 (1988).
- [36] U. Nowak and K. D. Usadel, *Phys. Rev. B* **39**, 2516 (1989).

Exchange Bias and Training Effect in Polycrystalline Antiferromagnetic/Ferromagnetic Bilayers

Markus Kirschner, Dieter Suess, Thomas Schrefl and Josef Fidler
Solid State Physics, Vienna University of Technology,
Wiedner Haupstr. 8-10/138, A-1040 Vienna, Austria

ABSTRACT

Exchange bias and training effect are simulated for IrMn/NiFe bilayers. As a function of the thickness of the antiferromagnet the bias field shows a maximum for a thickness of 22 nm. For decreasing antiferromagnetic thickness the domain wall energy approaches zero. For large thicknesses the high anisotropy energy hinders switching of the antiferromagnetic grains resulting in weak bias. Starting from the field cooled state as initial configuration a bias field of about 8 mT is obtained assuming a antiferromagnetic layer thickness of 20 nm, a ferromagnetic layer thickness of 10 nm, and a grain size of 10 nm. The next hysteresis cycle shows a reduction of the bias field by about 65%. Exchange bias and training effect in fully compensated antiferromagnet/ferromagnet bilayers are explained with a simple micromagnetic model. The model assumes no defects except for grain boundaries, and coupling is due to spin flop at a perfect interface. The simulations show that a weak exchange interaction between randomly oriented antiferromagnetic grains and spin flop coupling at a perfectly compensated interface are sufficient to support exchange bias.

INTRODUCTION

The phenomena of exchange anisotropy and exchange bias, particularly, were discovered in the year 1956 by Meiklejohn and Bean [1] when studying Co particles surrounded with antiferromagnetic oxide (CoO). They found that the field required to switch the ferromagnet from the field cooled state into the reversed state is larger than that to rotate the ferromagnet back to its original direction. Since the introduction of the Giant Magnetic Resistance (GMR) head in magnetic recording [2] the bias effect has been used widely in modern technology. The pinned layer of a spin valve sensor is stabilized through coupling to an antiferromagnet. A common system used in GMR reading heads are IrMn/NiFe bilayers [3]. Despite the application of exchange bias in magnetic field sensors, the physical mechanisms that lead to the hysteresis shift are still a field of discussion. Various theories explain particular aspects of the bias effect [4]. Nevertheless many issues remain to be solved [5]. One of the most striking experimental facts is the presence of exchange bias at fully compensated antiferromagnetic (AF) interfaces [6,7] in which the net spin averaged over a microscopic length scale is zero. Intuitively, one might expect that for compensated interfaces the bias effect vanishes, as the spins pinning the ferromagnetic cancel. Therefore various models of exchange bias assume partly uncompensated interfaces [4].

In this paper we propose a mechanism for exchange bias at fully compensated interfaces. The numerical results obtained for IrMn/NiFe bilayers are compared with experimental data from the recent literature [8,9]. The simulations on a mesoscopic length scale show that a weak exchange interaction between randomly oriented AF grains and spin flop coupling at a perfectly compensated interface are sufficient to support exchange bias.

Originally, Koon [10] proposed a mechanism for exchange bias at fully compensated interfaces. Using an atomistic model Koon showed that a fully compensated antiferromagnetic interface will lead to a 90° coupling between the antiferromagnet and the ferromagnet. Indeed 90° coupling has been observed experimentally [6,7]. In Koon's model a weak canting of the antiferromagnetic spins close to the interface provide a small net magnetic moment parallel to the ferromagnetic magnetization direction. The antiferromagnet near the interface thus aligns perpendicular to the ferromagnet (spin flop coupling). Under the assumption that the antiferromagnetic spins are restricted to planes parallel to the interface, Koon was able to predict exchange bias. The loop shift can be attributed to partial domain walls wound up in the antiferromagnet. Allowing full three dimensional rotations of the antiferromagnetic spins, Schulthess and Butler [11] showed that the domain walls are unstable due to out of plane rotations of the antiferromagnetic spins. They conclude that spin flop coupling at compensated interfaces enhances the coercivity but does not lead to exchange bias. Stiles and McMichael [12] drew a similar conclusion introducing spin flop coupling in their model for polycrystalline ferromagnetic-antiferromagnetic bilayers.

Nowak and co-workers [13] proposed the so-called domain state model for exchange bias. In their model the antiferromagnet breaks up into magnetic domains due to domain wall pinning at random defects. The domains may carry a remanent surplus magnetization. This small net magnetic moment provides coupling across the interface. The authors find a bias shift for directions parallel to the antiferromagnetic anisotropy axis for spins in a single crystal lattice.

In our model we assume a perfectly compensated interface. The antiferromagnet is not a single crystal but a collection of grains with randomly oriented anisotropy direction. In contrast to the model of Stiles and McMichael [12] we assume weak exchange coupling between the grains. Using a finite element simulation with subgrain discretization, Suess and co-workers [14] showed that a perfectly compensated interface will lead to spin flop coupling which in turn causes exchange bias. Weak exchange interactions between the AF grains were essential: (1) They partly suppress out of plane rotations of the antiferromagnetic moments and (2) provide the wall energy between lateral antiferromagnetic domains. The simulation show that the reversal of the ferromagnet causes the formation of domains within the antiferromagnet: Some of the AF grains switch irreversibly when the ferromagnet reverses, whereas another part of the AF grains remain stable. After reversal of the ferromagnet the system stores energy in antiferromagnetic domain walls perpendicular to the interface, which in turn gives rise to the observed loop shift. The finite element approach showed that the magnetization configurations in the AF grains remain almost uniform during the reversal of the ferromagnet. Therefore, a granular model where the magnetization is actually uniform within the AF grains should yield very similar results but allows to simulate larger systems with the great advantage of avoiding possible finite size effects.

INTERACTING GRAIN MODEL

Let us consider a thin ferromagnetic film spin flop coupled to a polycrystalline antiferromagnet with randomly oriented easy axes. The magnetization configuration within the AF grains are assumed to be uniform. This is a good approximation for small grain sizes and low intergrain exchange coupling within the antiferromagnet. Due to the spin flop coupling the antiferromagnetic spins are not fully antiparallel near the interface. Since the deviation is small and relaxes very rapidly to the spin structure of the bulk we neglect the tilting of the spins. Thus,

for the simplest case of two sublattices the magnetic state of each AF grain can be described by a single vector of one sublattice. The magnetization vector of the other sublattice points exactly antiparallel. This means that as long as the applied field is not larger than the antiferromagnetic exchange, as is the case in most experiments, magnetic surface and volume charges cancel in the antiferromagnet. Any remaining contributions to magnetostatic energy for individual magnetic sublattices in the antiferromagnet can be taken into account through the anisotropy constant, K_1 . Shape effects for the ferromagnetic film are approximated with an in plane anisotropy energy in the ferromagnet.

The interacting grain model takes into account the intergrain exchange energy, the spin flop coupling energy [12,15], the anisotropy energy in the antiferromagnet, the demagnetization energy of the ferromagnet, and the Zeeman energy in an external field. The total energy of the ferromagnet (F) / antiferromagnet (AF) bilayer system per grain j is

$$E^j = \sum_{i=1}^{nV} \left[-J_F S^2 n_F t_F l (\mathbf{u}_F^i \cdot \mathbf{u}_F^j) - J_{AF} S^2 n_{AF} t_{AF} l (\mathbf{u}_{AF}^i \cdot \mathbf{u}_{AF}^j) \right] \\ - J_{AF-F} S^2 n_l l^2 (\mathbf{u}_{AF}^j \cdot \mathbf{u}_F^j)^2 - K_1 t_{AF} l^2 (\mathbf{k}_{AF}^j \cdot \mathbf{u}_{AF}^j)^2 \\ - \frac{J_s^2}{\mu_0} t_F l^2 (\mathbf{k}_F^j \cdot \mathbf{u}_F^j)^2 - J_s t_F l^2 (\mathbf{H} \cdot \mathbf{u}_F^j). \quad (1)$$

The sum over i is carried out only over the nearest neighbor grains in the antiferromagnet and ferromagnet, respectively. Here \mathbf{u} is the unit of the magnetization, J is the exchange integral, S is the average total spin quantum number, \mathbf{k} is the a unit vector parallel to the uniaxial anisotropy axis, t is the layer thickness, l is the grain size, \mathbf{H} is the external field, and J_s is the spontaneous magnetic polarization of the ferromagnet. The indices AF, F, and AF-F (or I) denote the antiferromagnet, the ferromagnet, and the antiferromagnetic/ferromagnetic interface, respectively. For simple cubic lattices with lattice constant a we find for the number of spins per unit area: $n_F = n_{AF} = n_l = 1/a^2$ and for the spontaneous polarization $J_s = \mu_0 g \mu_B S/a^3$. Here μ_B is the Bohr magneton and g is the Landé factor.

Calculations are performed by first choosing the magnetocrystalline anisotropy axes of the AF grains randomly in space and then initializing the system by simulating field cooling. Afterwards, the evolution of the magnetization configuration with changing external field is investigated. A Metropolis Monte Carlo algorithm similar to that introduced by Hinzke and Nowak [16] is used to simulate field cooling. The hysteresis loops are calculated quasistatically: An equilibrium configuration is obtained by the numerical integration of the Landau-Lifshitz Gilbert equation at value of the external field. The field step was 2 mT.

RESULTS AND DISCUSSION

Experimentally, the exchange bias field is inversely proportional to ferromagnetic layer thickness, t_F . This relation breaks down for small t_F [5]. The thickness of the antiferromagnetic film has to exceed a certain critical thickness to find exchange bias. H_{eb} decreases abruptly for small t_{AF} . For large antiferromagnetic thickness two different effects are found. In most systems the bias field remains constant for $t_{AF} > 20$ nm. However, in some systems the thickness of H_{eb} is reduced for large t_{AF} . In addition in some systems, as t_{AF} is reduced, $H_{eb}(t_{AF})$ shows a pronounced

peak before the main decrease [5]. Van Driel and co-workers [9] measured the dependence of H_{eb} on antiferromagnetic layer for textured and randomly oriented IrMn/Ni bilayers. They found that the maximum of the peak is shifted towards smaller t_{AF} in the $\langle 111 \rangle$ textured film.

In the following we present the results for the thickness dependence of the exchange bias field for IrMn/NiFe bilayers. In addition we compare the computed magnetization structure in the ferromagnet with magnetic images obtained by transmission electron microscopy [8]. IrMn for exchange biased bilayer systems is used in the disordered fcc (γ) phase. The average spins on each (002) plane are aligned parallel along the c-axis with alternating signs on neighboring (002) planes [4]. In terms of magnetic anisotropies, a $\langle 111 \rangle$ texture corresponds to an average angle of 54.74° between the easy axes and the interface normal. We calculated $H_{eb}(t_{AF})$ for randomly oriented IrMn grains and for $\langle 111 \rangle$ textured films assuming a Gaussian distribution of the magnetocrystalline anisotropy direction with a standard deviation of 20° . The material parameters used for the simulations were $J_F = 0.43$ meV, $J_{AF} = 0.023$ meV, $J_{AF-F} = 0.043$ meV, $K_1 = 10^5$ J/m³, $l = 10$ nm, and $J_s = 1$ T.

Figure 1 gives the calculated dependence of the bias field and of the coercivity on the ferromagnetic layer thickness and shows the influence of texture on $H_{eb}(t_{AF})$. The bias field is proportional to $1/t_F$ as long as $t_F \geq 10$ nm. The bias field as a function of t_{AF} shows a maximum. The maximum bias field of about 9 mT is reached for t_{AF} between 20 nm and 30 nm for the randomly oriented bilayer. The maximum is shifted towards 15 nm for the $\langle 111 \rangle$ textured IrMn/NiFe bilayer. Detailed investigations showed that there is a clear correlation between the number of switched AF grains and the bias field. As the ferromagnet is reversed a small fraction of the AF grains switches irreversible. The large antiferromagnetic domains which are formed during field cooling break up into smaller domains. The reversed state stores some additional domain wall energy which in turn leads to exchange bias. The wall energy depends on the pattern of switched AF grains. The bias field was found to be proportional to the ratio C/C_{max} , where C is the circumference of the pattern of switched AF grains and C_{max} is the maximum possible circumference. The relation $H_{eb} \propto (C/C_{max}) t_{AF}$ holds for the entire thickness range which confirms that exchange bias is associated with the domain wall energy stored in the lateral AF domains.

King and co-workers [8] observed 360° wall loops during the reversal of the ferromagnet in IrMn/NiFe bilayers. Such loops, once formed, were remarkably stable and remained up to fields of about 300 Oe. Beyond this, the ferromagnetic film appeared saturated.

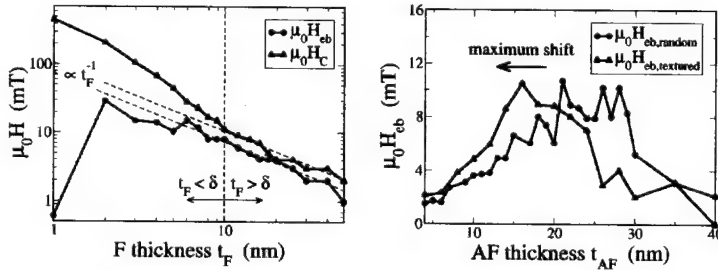


Figure 1. Calculated thickness dependence of the bias field of an IrMn/NiFe bilayer. Left hand side: H_{eb} and H_c as a function of the ferromagnetic layer thickness, $t_{AF} = 20$ nm. Right hand side: H_{eb} as a function of the antiferromagnetic layer thickness, $t_F = 10$ nm for randomly oriented and textured IrMn grains.

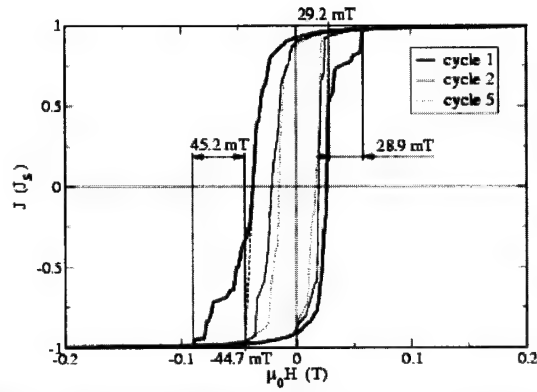


Figure 2. Calculated hysteresis loops for a $J_F = 0.129$ meV, $J_{AF} = 0.023$ meV, $J_{AF-F} = 0.043$ meV, $K_1 = 10^5$ J/m³, $l = 10$ nm, $t_F = 10$ nm, $t_{AF} = 20$ nm and $J_s = 1$ T. The knee in the hysteresis loop is due to the formation and annihilation of a 360° domain wall loop.

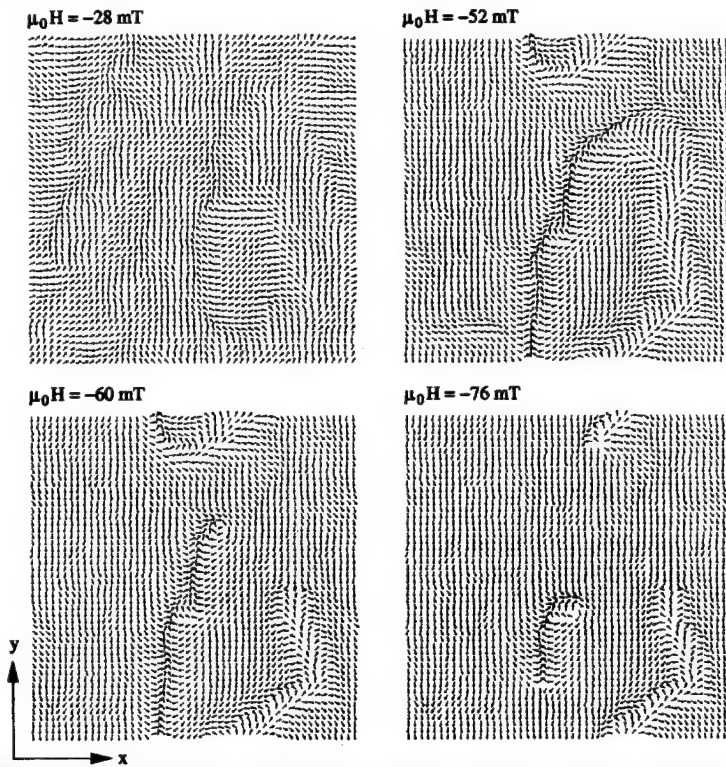


Figure 3. Formation and annihilation of a 360° domain wall loop in the ferromagnet.

To ensure their annihilation a substantially high external field had to be applied. Repetition of the hysteresis cycle showed a similar behavior, but the locations of these loops tended to vary.

In our simulations stable 360° wall loops or lines appeared primarily for $J_F = 0.129$ meV. Figure 2 shows the calculated hysteresis loops. At $\mu_0 H = 40$ mT domain walls move together and, rather than annihilating, form a 360° wall loop as shown in figure 3. This configuration is stable due to the pinning effect of the antiferromagnetic layer, leading to a distinct knee in the hysteresis curve.

In addition figure 2 shows a training effect, the decrease of the loop shift and of the coercivity with increasing number of hysteresis cycles. When the ferromagnet is switched back the antiferromagnetic domain structure that was formed after field cooling is not fully recovered. Each cycle through the magnetization loop brings the antiferromagnet closer to a type of dynamic equilibrium in which the coercive field no longer changes with each additional cycle and the loop area remains constant. In our simulations, this equilibrium appeared after about four cycles.

ACKNOWLEDGEMENTS

The authors thank R. L. Stamps, J. V. Kim (University of Western Australia) and J. N. Chapman (University of Glasgow) for helpful discussion.

This work was supported by the Austrian Science Fund (Y-132 PHY).

REFERENCES

1. W. H. Meiklejohn and C. P. Bean, *Phys. Rev.* **102**, 1413 (1956)
2. C. Tsang, R. E. Fontana, R.E.; T. Lin; D. E. Heim, V. S. Speriosu, B. A. Gurney and M. L. Williams, *IEEE Trans. Magn.* **30**, 3801 (1994).
3. J. R. Childress, M. J. Carey, R. J. Wilson, N. Smith, C. Tsang, M. K. Ho, K. Carey, S. A. MacDonald, L. M. Ingall and B. A. Gurney, *IEEE Trans. Magn.* **37**, 1745 (2001).
4. A. E. Berkowitz, K. Takano, *J. Magn. Magn. Mater.* **200**, 552 (1999).
5. J. Nogués, I. K. Schuller, *J. Magn. Magn. Mater.* **192**, 203 (1999).
6. Y. Ijiri, J. A. Borchers, R. W. Erwin, S.-H. Lee, P. J. van der Zaag and R. M. Wolf, *Phys. Rev. Lett.* **80**, 608 (1998).
7. J. Nogués, T. J. Moran, D. Lederman and Ivan K. Schuller, *Phys. Rev. B* **59**, 6984 (1999).
8. J.P. King, J.N. Chapman, M.F. Gillies and J.C.S. Kools, *J. Phys. D: Appl. Phys.*, **34**, 528 (2001)
9. J. van Driel, F. R. de Boer, K.-M. H. Lenssen and R. Coehoorn, *J. Appl. Phys.* **88**, 975 (2000)
10. N.C. Koon, *Phys. Rev. Lett.* **78**, 4865 (1997).
11. T.C. Schulthess and W.H. Butler, *Phys. Rev. Lett.* **81**, 4516 (1998).
12. M.D. Stiles and R.D. McMichael, *Phys. Rev. B* **59**, 3722 (1999).
13. U. Nowak, A. Misra and K.D. Usadel, *J. Appl. Phys.* **89**, 7269 (2001)
14. D. Suess, T. Schrefl, W. Scholz, J.-V. Kim, R. L. Stamps, J. Fidler, *IEEE Trans. Magn.* **38**, 2397 (2002).
15. R. L. Stamps, *J. Phys. D: Appl. Phys.* **33**, 247 (2000).
16. D. Hinzke and U. Nowak, *Phys. Rev. B* **58**, 265 (1998).

Rotating Anisotropies Without Superparamagnetic Grains in Exchange Bias Systems

T. C. Schulthess

Center for Computational Sciences and Computer Science and Mathematics Division
Oak Ridge National Laboratory
Oak Ridge, TN 37831-6114, U. S. A.

ABSTRACT

We introduce a random field model with anisotropic interfacial exchange for ferromagnet / antiferromagnet bilayers and calculate average coupling energies and coupling directions for different grain or domain sizes. The model is shown to reconcile Malozemoff's random field Ising model for exchange bias with the spinflop coupling mechanism. Furthermore, we find that for small and mid size domains, the average coupling direction strongly varies between different interfacial configurations. We show how this behavior can lead to rotating anisotropies in systems with very strong magnetocrystalline anisotropies, where the use of superparamagnetic grains or domains in the antiferromagnet is not justified.

INTRODUCTION

The most frequently discussed effects in ferromagnetic (FM) / antiferromagnet (AFM) bilayers is the shift in the magnetization curve that can be observed when the system has been cooled in an external field[1]. The magnitude of the shift is inversely proportional to the thickness of the FM layer which implies that the effect is directly related to the interfacial exchange between the FM and AFM and the effect is thus referred to as *exchange anisotropy* or *exchange bias* [2, 3]. The temperature below which the exchange bias is observed is called blocking temperature (T_B), it is typically equal or somewhat smaller than the Neel temperature (T_N) of the AFM. It is commonly believed that the bias sets in when the AFM spins order and a sufficient number of domains in the AFM are blocked such that the AFM spins do not reverse when the FM magnetization is inverted during the measurement of the magnetization curve.

In most cases, hysteretic effects such as a strong increase in coercivity are observed along with the onset of exchange bias[4-6]. Most models to explain these effects are based on an idea of Fulcommer and Charap [7], where, assuming that the FM couples in some form to the AFM, magnetic structure of smaller grains or domains in the AFM will be dragged along irreversibly with the FM magnetization and lead to hysteresis, while the larger grains, in which the magnetic order is locked in, will lead to the bias effect. Stiles and McMichael [8] introduced the notion of a *rotating anisotropy* which follows the FM magnetization when the external field is rotated and is attributed to magnetically "loose" grains in the AFM. With this model they were able to explain a direction independent shift in the resonance field of ferromagnetic resonance experiments.

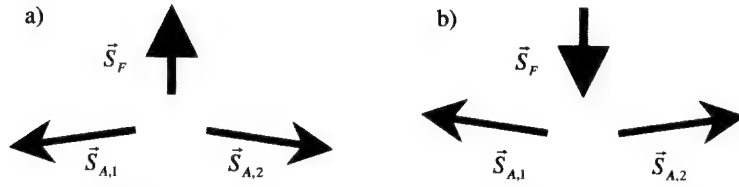


Figure 1: Model of three spins where the F-A part of the exchange energy is given by

$$E_{exch}^{F-A} = - \sum_{i=1,2} J_i \vec{S}_F \cdot \vec{S}_{A,i} + \sum_{i=1,2} \vec{D}_i \cdot (\vec{S}_F \times \vec{S}_{A,i}).$$

While the concept of a superparamagnetic structure in smaller grains or domains in the AFM is reasonable for systems with weak magnetocrystalline anisotropy such as NiO, it is not clear why it should apply to an AFM like CoO where the anisotropy energy is of the same order as the exchange energy[9]. In the present contribution we show that within the random field model a variable effective coupling direction that arises from adjustment of the walls in smaller and mid-sized AFM domains will lead to a rotating anisotropy. In this picture most AFM moments are frozen and dissipative effects are due to irreversible motion of domain walls.

RANDOM FIELD MODEL WITH ANISOTROPIC EXCHANGE

In order to understand how the net coupling direction of the FM to an AFM domain can vary without rotating the AFM domains, we first have to investigate the microscopic coupling mechanisms between the AFM and the FM moment. For interfaces with compensated exchange between the FM and the AFM, i.e. where the FM spins couple equally to all AFM sublattices[10], the following two models are typically discussed in the literature[11, 12]:

1. The random field model [13-15], in which the AFM is assumed to break up into domains. The finite area of these domains will result in a net interfacial exchange which scales as $(1/\sqrt{N})$ if N is the number of AFM-FM pairs. In this model the FM and AFM spins are assumed to be collinear which leads to a change in exchange energy $\Delta E = 2J/\sqrt{N}$ when the FM spins are reversed. The random field model is commonly used to explain the net unidirectional coupling between the FM and individual AFM domains (or grains).
2. The spin-flop coupling model [16, 17], which assumes Heisenberg spins and where the frustrated exchange across the interface leads to a slight canting to the AFM moments and a net coupling of the FM that is perpendicular to the AFM easy axis. In contrast to the random field Ising model the coupling is uniaxial and does not lead to exchange bias [18, 19]. Furthermore, the coupling strength is independent of the AFM domain / grain size.

The collinearity required by the random field Ising model is only justified for small domains in the AFM. For most realistic domain/grain sizes, the spin-flop mechanisms will dominate [8] leaving the origin of the unidirectional coupling as a puzzle. We will now show that spin-flop coupling can have a unidirectional component when the

anisotropic Dzyaloshinsky-Moriya (DM) term is added to the exchange, i.e. the exchange energy between two moments on sites i and j has the form

$$E_{ij} = -J_{ij} \vec{s}_i \cdot \vec{s}_j + \vec{D}_{ij} (\vec{s}_i \times \vec{s}_j). \quad (1)$$

In cases where the crystal structure has a center of inversion at the point bisecting the line between i and j , \vec{D}_{ij} can be shown to vanish [20, 21]. While this symmetry condition holds in most bulk system, it is never satisfied at the AFM/FM interface[22] and the DM term thus has to be included to properly describe interfacial exchange. The consequence of the DM term is that the difference in exchange energy upon reversal of the FM spins is different from zero in the spin-flop coupling state. This is best illustrate by considering three spins (see Figure 1), \vec{S}_F , $\vec{S}_{A,1}$, and $\vec{S}_{A,2}$, in the spin-flop coupling states. The energy difference when \vec{S}_F is reversed (Figures 1a and 1b) is $\Delta E_{chg} = 2(D_{1,z} + D_{2,z})$.

In order to estimate the magnitude of the unidirectional term in the case of a FM/AFM bilayer, we perform a calculation using the random field model with anisotropic interfacial exchange. We consider a bilayer with bcc type lattice and a (110) interface with nearest neighbor exchange J in the FM and $-J$ in the AFM. In the AFM we further assume uniaxial anisotropy along the (001) direction with $K/J=1$. For the interfacial exchange we use Eq. (1) with $J_{ij} = Jr$ and

$D_{ij} = Dr'(\sin \vartheta \cos \varphi, \sin \vartheta \sin \varphi, \cos \vartheta)$, where $r \in [-1,1]$, $r' \in [-1,1]$, $\vartheta \in [0, \pi]$, and $\varphi \in [0, 2\pi)$ are uniform random variables. These random fluctuations are usually justified with the large variation of the interfacial bond lengths that results from the large lattice mismatch between the FM and AFM in systems like CoO/Permally or FeF2/Fe. The particular system we consider here consists of 5 layers in the AFM and 10 layers in the FM. We use periodic boundary conditions parallel to the interface with variable unit cell

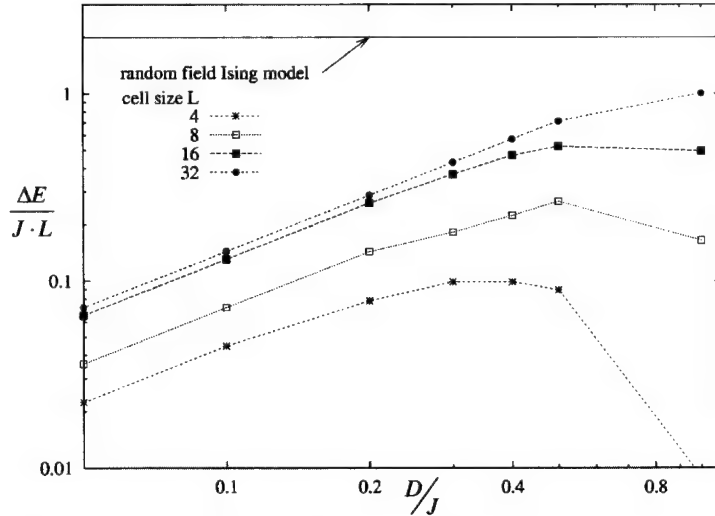


Figure 2: Energy change due to reversal of the FM spins for AFM-FM bilayers (see text for details) for Heisenberg spins with random anisotropic interfacial exchange and different sizes of the computational cell (symbols) compared to expected result from the random field Ising model (solid line)

size consisting of L by L primitive cells ($L = 2, 4, 8, 16$, and 32). The effect of the magnetostatic interaction is treated as an effective hard axis in the FM perpendicular to the interface. We seek to calculate AFM/FM coupling energies as a function of domain size, where we equate the unit cell size of our model to the domains size. For this we have to suppress the formation of further domains within the unit cell. We have therefore prepared an ordered AFM spin configuration and randomized FM spins as an initial condition and subsequently minimized the energy using the Landau Lifshitz equations (see [19] for details). When the energy minimum is reached, the FM spins are inverted and the energy is again minimized. For all but the smallest unit cells this procedure always yields two distinct states. Their energy differences, averaged over 40 random configurations, are plotted in Figure 2 and compared to the result of the random field Ising model. While the unidirectional anisotropy due to the DM term is systematically smaller than that of the random field Ising model, it has nevertheless comparable order or magnitude provided D/J is not too small. Moria [21] estimated $D/J \sim 0.1$ in bulk AFM but values that are as large as 0.5 have been reported for systems with lower symmetry [23].

EFFECTIVE COUPLING DIRECTION AND ROTATING ANISOTROPIES

In the previous section we have determined energy differences averaged over many random configurations of the interfacial exchange interactions. The direction of the FM magnetization with regard to the AFM easy axis for each of these configurations is plotted in Figure 3. By choosing appropriate initial conditions for the minimization procedure discussed above, the system can always be prepared in a way that the global

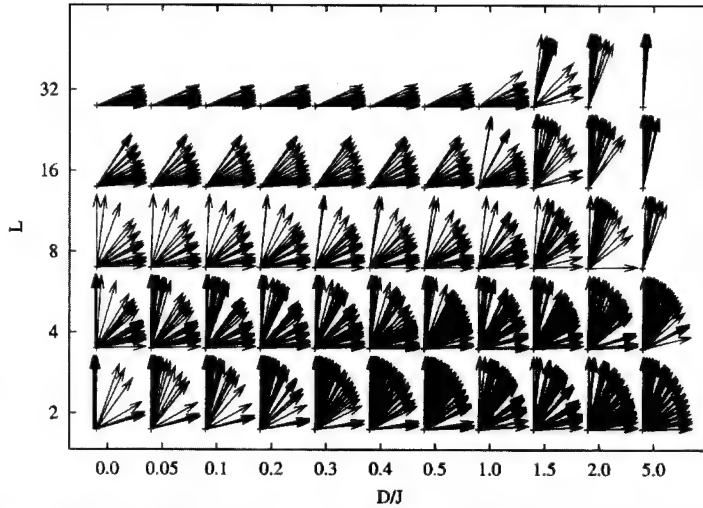


Figure 3: Average direction of FM spins for every random configuration. The AFM easy axis, (001), is taken to be parallel to the y-axis of the plot. In the case $D=0$ and $L=2$ (4), 80% (50%) of the configurations are collinear with the AFM easy axis.

energy minimum has the FM moments pointing at angle between 0 and 90 degrees with regard to the AFM easy axis (this choice of initial condition corresponds to the field cooling procedure). As expected, the coupling is always collinear for small cells and perpendicular when the cells are large. When the anisotropic exchange is non zero, the coupling direction strongly varies between different configurations of the smaller and mid size cell but is always perpendicular to the AFM easy axis when the cells are large.

As was done in the previous section, we consider the cell size in the model to correspond to domain sizes in the film and further recognize that different domains correspond to different random configurations of the interfacial exchange in the computational cell. To simplify the argument, let us assume that the field was applied along the (1-10) direction during the field cooling procedures, i.e. perpendicular to the AFM easy axis. The domain pattern in the AFM will arrange itself such that the coupling direction of most domains is parallel to the cooling field. When the direction of the applied field and the FM magnetization is subsequently rotated to a different direction, the AFM domain pattern will adjust by moving domain walls to minimize the energy. While it remains to be shown explicitly, the displacement of such domain walls in real samples, with defects at which these walls are pinned, is likely an irreversible process. According to the results plotted in Figure 3, the coupling direction of the larger domains will not be affected by the rearrangement of domain walls. Together with the energy differences plotted in Figure 2, this will lead to a unidirectional anisotropy that has similar order of magnitude as that found with the random field Ising model. Since the coupling direction of the smaller domains depends strongly on the random configuration, changing the domain pattern will lead to new configuration with adjusted coupling directions that follows the FM magnetization. This will give rise to a rotating component of the anisotropy which adjusts with direction of the applied field. In this model the dissipation would take place in the irreversible displacement of domain walls in the AFM and thus does not require the superparamagnetic rotation of all the moments in smaller grains.

ACKNOWLEDGMENTS

This research was sponsored by the Laboratory Technology Research Program of the Work supported by Department of Energy, Office of Science through BES-DMSE, and OASCR-MICS as well as the Laboratory Technology Research Program of OASCR-TRD under Contract No. DE-AC05-00OR22725 with UT-Battelle LLC.

REFERENCES

1. Meiklejohn, W.H. and C.P. Bean, *A new magnetic anisotropy*. Physical Review B, 1956. **102**: p. 1413.
2. Nogues, J. and L.K. Schuller, *Exchange bias*. Journal of Magnetism and Magnetic Materials, 1999. **192**(2): p. 203-232.
3. Berkowitz, A.E. and K. Takano, *Exchange anisotropy - a review*. Journal of Magnetism and Magnetic Materials, 1999. **200**(1-3): p. 552-570.
4. Stiles, M.D. and R.D. McMichael, *Coercivity in exchange-bias bilayers*. Physical Review B, 2001. **63**05(6): p. art. no.-064405.
5. Li, Z. and S. Zhang, *Coercive mechanisms in ferromagnetic-antiferromagnetic bilayers*. Physical Review B, 2000. **61**(22): p. R14897-R14900.

6. Leighton, C., et al., *Thickness-dependent coercive mechanisms in exchange-biased bilayers*. Physical Review B, 2002. **65**(6): p. art. no.-064403.
7. Fulcomer, E. and S.H. Charap, *Thermal Fluctuation Aftereffect Model for Some Systems with Ferromagnetic-Antiferromagnetic Coupling*. Journal of Applied Physics, 1972. **43**(10): p. 4190-&.
8. Stiles, M.D. and R.D. McMichael, *Model for exchange bias in polycrystalline ferromagnet-antiferromagnet bilayers*. Physical Review B, 1999. **59**(5): p. 3722-3733.
9. Wagner, V. and D. Hermann-Ronzaud, *Neutron Inelastic Scattering 1977*. IAEA, Vienna 1977, 1977. **Part II**: p. 135-143.
10. Here we will discuss uniaxial AFMs that consist of two ferromagnetic sublattices with anti-aligned moments and we assume nearest neighbor exchange between AFM and FM spins at the interface with exchange parameter J
11. Kiwi, M., *Exchange bias theory*. Journal of Magnetism and Magnetic Materials, 2001. **234**(3): p. 584-595.
12. Stamps, R.L., *Mechanisms for exchange bias*. Journal of Physics D-Applied Physics, 2000. **33**(23): p. R247-R268.
13. Malozemoff, A.P., *Random-Field Model of Exchange-Anisotropy at Rough Ferromagnetic-Antiferromagnetic Interfaces*. Physical Review B, 1987. **35**(7): p. 3679-3682.
14. Malozemoff, A.P., *Mechanisms of Exchange-Anisotropy*. Journal of Applied Physics, 1988. **63**(8): p. 3874-3879.
15. Nowak, U., et al., *Domain state model for exchange bias. I. Theory*. Physical Review B, 2002. **66**(1): p. art. no.-014430.
16. Koon, N.C., *Calculations of exchange bias in thin films with ferromagnetic/antiferromagnetic interfaces*. Physical Review Letters, 1997. **78**(25): p. 4865-4868.
17. Hinchey, L.L. and D.L. Mills, *Magnetic-Properties of Ferromagnet-Antiferromagnet Superlattice Structures with Mixed-Spin Antiferromagnetic Sheets*. Physical Review B, 1986. **34**(3): p. 1689-1699.
18. Schulthess, T.C. and W.H. Butler, *Consequences of spin-flop coupling in exchange biased films*. Physical Review Letters, 1998. **81**(20): p. 4516-4519.
19. Schulthess, T.C. and W.H. Butler, *Coupling mechanisms in exchange biased films (invited)*. Journal of Applied Physics, 1999. **85**(8): p. 5510-5515.
20. Dzyaloshinsky, I., *A thermodynamic theory of "weak" ferromagnetism of antiferromagnetics*. J. Phys. Chem. Solids, 1958. **4**: p. 241-255.
21. Moriya, T., *Anisotropic Superexchange Interaction and Weak Ferromagnetism*. Physical Review, 1958. **120**(1): p. 91-98.
22. Crepieux, A. and C. Lacroix, *Dzyaloshinsky-Moriya interactions induced by symmetry breaking at a surface*. Journal of Magnetism and Magnetic Materials, 1998. **182**(3): p. 341-349.
23. Katsnelson, M.I., V.V. Dobrovitski, and B.N. Harmon, *Many-spin model and the spin Hamiltonian of Mn-12 clusters*. Journal of Applied Physics, 1999. **85**(8): p. 4533-4535.

Interdiffusion, Crystallinity and Exchange Bias in $\text{Mn}_x\text{Pt}_{1-x}/\text{Co}$ Bilayers

Erie H. Morales, Yikuan Wang and D. Lederman

Department of Physics, West Virginia University, Morgantown WV 26506-6315

Abstract

The structure of the antiferromagnet (AF) in the Ta/ $\text{Mn}_x\text{Pt}_{1-x}$ /Co /Ta system must have the face-centered tetragonal CuAu structure in order to obtain a measurable exchange bias (H_E). The formation of this structure has an onset temperature of approximately 240 °C. Increasing the annealing temperature increases the amount of CuAu ordering, which increases H_E , and also increases the MnPt/Co interdiffusion, which decreases H_E . These two competing processes result in an optimum annealing temperature that maximizes H_E .

Introduction

The exchange bias anisotropy, discovered by W.H. Meiklejohn and C.P. Bean [1], is due to the coupling of an antiferromagnet (AF) and a ferromagnet (F). This unidirectional anisotropy effectively pins the F when the AF is below its Néel temperature (T_N). This effect has applications in magnetic sensors and magnetic random access memory [2].

In this study we address the formation of the crystalline structure for the AF and quantitatively show that the interdiffusion at the AF/F boundary decreases the coupling.

Experimental Details

The samples were grown in a vacuum chamber at a base pressure of 6×10^{-7} Torr using magnetron sputtering. Separate targets for each material were used and the $\text{Mn}_x\text{Pt}_{1-x}$ alloy was

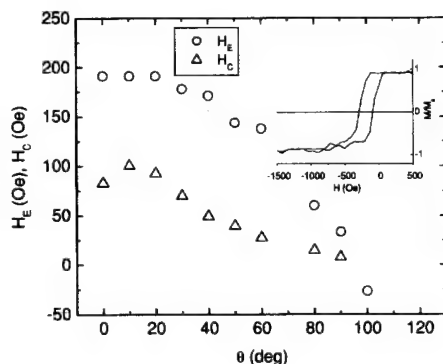


Figure 1 Exchange bias (H_E) and Coercivity (H_C) as functions of angle measured from the setting field direction. The sample Mn concentration is $x = 0.48$ and the annealing temperature $T_A = 318$ °C. Inset is the MH loop for $\theta = 0$.

co-sputtered. Si (111) substrates were degreased without removing the native oxide layer. Typical sample structures consisted of Ta(10nm)/Mn_xPt_{1-x}(25nm)/Co(8nm)/Ta(20nm). The Ta capping layer was used to prevent oxidation and degradation of the sample. X-ray rocking curves indicated that the as-grown samples were polycrystalline. We post-annealed the samples at different temperatures in a magnetic field in order to obtain an appreciable H_E . The annealing procedure consisted of ramping to the desired temperature in 20 minutes and then waiting one hour for stabilization. A 1200 Oe permanent magnet was then placed underneath the sample and left there during the annealing time. This was done in order to align the AF in the field direction so that after the temperature is lowered the F is pinned. Samples were characterized by x-ray diffraction and reflectivity using a rotating anode attached to an 18 kW power supply and Cu K α radiation ($\lambda \sim 0.1542$ nm).

H_E was determined from the shift of the magnetic hysteresis loops away from $H = 0$ using the magneto optical Kerr effect (MOKE). A typical MOKE result for different angles with respect to the direction of the applied field during annealing is shown in Figure 1. The loop is not symmetric, in agreement with the model proposed by D. Mauri et al. [3] where a domain wall is formed in the AF during domain reversal in the F.

The annealing procedure was performed only once on each sample. The interface interdiffusion was determined with a computer program [4] that recursively calculates the x-ray reflection coefficient of each layer from top to bottom adding a grading at the AF/F layer where the index of diffraction varies linearly from the AF value to the F value.

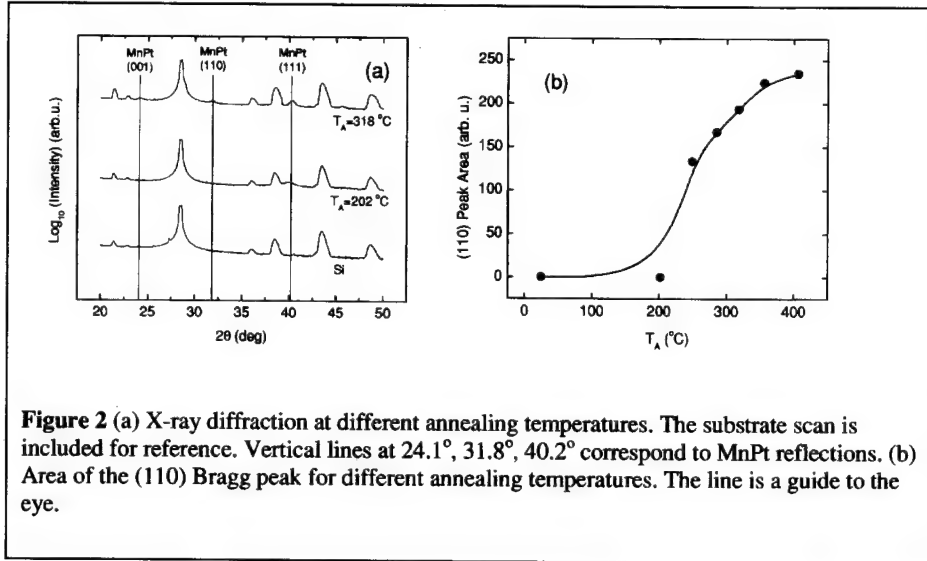


Figure 2 (a) X-ray diffraction at different annealing temperatures. The substrate scan is included for reference. Vertical lines at 24.1°, 31.8°, 40.2° correspond to MnPt reflections. (b) Area of the (110) Bragg peak for different annealing temperatures. The line is a guide to the eye.

Results and Discussion

Conventional wisdom holds that the annealing temperature (T_A) has to be greater than T_N in order to obtain H_E . In this case, however, this is not necessary, presumably due to the low magnetic anisotropy of the AF. Figure 2 (a) shows that the onset of the CuAu structure is not complete at $T_A = 202$ °C, while the $T_A = 318$ °C sample shows the MnPt (110) reflection. This reflection can only occur for the ordered CuAu structure. According to Krén et al. [6], the T_N for this concentration of $x = 0.48$ is 682 °C. In order to quantify the amount of CuAu structural ordering, the area of the (110) reflection was measured for each annealing temperature. The area grows monotonically throughout the entire temperature range and at $T_A = 406$ °C seems to be close to its maximum, as shown in Figure 2 (b). This is important because the exchange bias also should have increased in the same temperature range if it only had been proportional to the amount of CuAu ordering. The exchange bias, however, peaked at $T_A = 318$ °C, as shown in Figure 3. Hence, there must have been other factors that contributed to the decrease at higher annealing temperatures.

X-ray reflectivity results qualitatively show a loss of sharp interfaces as T_A is increased, as shown in Figure 4. In the as-grown sample there are high frequency peaks, corresponding to the total thickness of the sample, modulated by a low frequency signal, corresponding to the individual layer thicknesses. This low frequency modulations for the most part are absent for the sample annealed at $T_A = 407$ °C. This means that the interfaces become less well pronounced as the annealing temperature increases. This was verified by the fit to the spectra shown in Figure 4. The results for the interdiffusion roughness for the MnPt/Co interface ($\sigma_{\text{MnPt/Co}}$) are shown in Figure 5. The sample with the maximum H_E has an interdiffusion of $\sigma_{\text{MnPt/Co}} = 1.4$ nm. This amount of roughness might at first sight seem excessive, but it is consistent with the results of

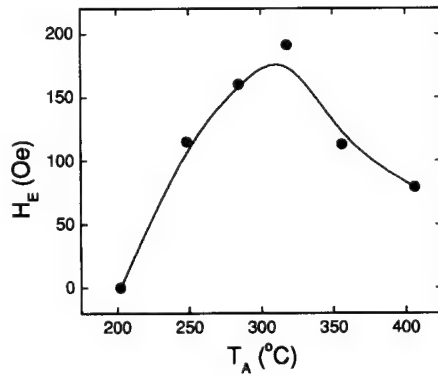


Figure 3 Exchange bias as a function of annealing temperature for nominally identical samples.

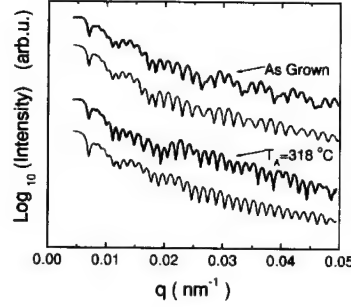


Figure 4: X-ray reflectivity for as-grown and $T_A = 318^\circ\text{C}$ samples with their corresponding fits below are shown.

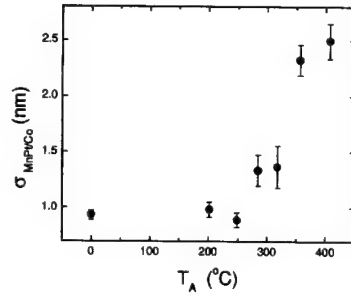


Figure 5: Roughness at the AF/F interface as a function of annealing temperature determined from x-ray reflectivity modeling.

Honda et al., who measured an appreciable H_E in MnPt/FeCo with up to 2 nm of Ag placed at the AF/F interface [7]. Furthermore, the fits showed that increasing the roughness parameters of all the other interfaces did not reproduce the measured spectra and did not increase systematically as the annealing temperature (T_A) was increased [8]. This indicates that most of the interdiffusion occurs at the MnPt/Co interface.

Conclusions

Our results indicate that there is a minimum temperature required to obtain the CuAu ordered structure. Below this temperature the crystalline ordering does not provide the correct antiferromagnetic structure and the measured H_E is zero. For greater annealing temperatures the amount of CuAu structural order increases and saturates above 400°C . However, the exchange bias peaks at 318°C because of increasing interdiffusion at the MnPt/Co interface, which presumably weakens the AF/F exchange coupling. These results indicate that the exchange bias could be increased further if the interdiffusion could be suppressed during the annealing procedure.

References

1. Meicklejohn and C. P. Bean, *Phys. Rev.* **102**, 1413 (1956).
2. B. Dieny, V. S. Spreriosu, S. Metin, S. S. P. Parkin, B. A. Gurney, P. Baumgart and D. R. Wilhoit, *J. Appl. Phys.* **69**, 4774 (1991).
3. D. Mauri, H.C. Siegmann, P.S. Bagus and E. Kay, *J. Appl. Phys.* **62** (7), 1987.
4. T. Charlton, J. McChesney, D. Lederman, F. Zhang, J.Z. Hilt and M.J. Pechan, *Phys. Rev. B* **59**, 11897 (1999).
5. B. Vidal and P. Vincent, *Apl. Opt.* **23**, 1794 (1984).
6. E. Krén, G. Kádár, L. Pál, J. Sólyom, P. Szabó and T. Tarnóczy, *Phys. Rev.* **171**, 574 (1968).
7. S. Honda, M. Nawate and T. Norikane, *J. Magn. Magn. Mater.* **220**, 85 (2000).
8. Erie H. Morales, Y. Wang and D Lederman, A. J. Kellock and M. J. Carey (unpublished).

Crystal-field Effect on Magnetic Moment and Exchange-Coupling for Fe/W(100) and Fe/W(110)

X. Qian^{1,2} and W. Hübner^{2,3}

1. Department of Physics, Colorado State University, Fort Collins, CO 80523, USA

2. Max-Planck-Institut für Mikrostrukturphysik, Weinberg 2, D-06120, Halle, Germany

3. Department of Physics, Kaiserslautern University, Box 3049, D-67653 Kaiserslautern, Germany

Abstract

The Full-potential Linearized Augmented Plane-wave (FP-LAPW) method was employed to investigate the magnetic properties of 1 monolayer (ML) Fe on W(100) and W(110) substrates. Magnetic moments of the Fe overlayer are found to be very different with $\sim 2.0 \mu_B$ for Fe on W(100) and $\sim 2.56 \mu_B$ for Fe on W(110). The exchange coupling between Fe film and W substrate are also found to be orientation-dependent. The electronic coupling in Fe/W(100) thin film is found to be more long-range, compared to the one in Fe/W(110). These differences could be explained by the differences of local atomic bonding and crystal-field splitting in these two orientations.

1. Introduction

Exchange coupling between atomic layers constitutes many interesting phenomena including Giant Magneto-resistance (GMR) and spin-waves in magnetic multilayers. It was found that both the strength and oscillation period of interlayer exchange coupling depend strongly on the thickness of the spacer layer and crystal orientation [1]. Two theories have been developed and employed to explain the interlayer exchange couplings [2,3]. One is based on the Ruderman-Kittel-Kasuya-Yosida (RKKY) spin-dependent scattering model [2]. The other is based on the quantum size effect, i.e. the modulation of density-of-states (DOS) due to quantum confinement [3]. Later Bruno [4] showed that these two theories are actually equivalent. Indeed, in electronic structure calculations, full multiple-scattering yields the density-of-states (DOS). These two theories are quite successful in explaining most of the experimental observations [4]. Despite the good agreement in GMR between theory and experiment, so far the short oscillation periods of the exchange coupling predicted by theory in the (110) oriented multilayers have not been observed in experiments [5]. Some attribute this discrepancy to the surface and interface roughness or disorder effect [6,7]. It was indeed possible to make the short oscillation period disappear when the effect of disorder was included in the calculations [6]. However, the underlying physical reason is still uncertain. Understanding exchange coupling on the short-range scale is necessary in order to understand the effects of interface atomic structure on GMR.

Besides interlayer exchange coupling, ferromagnetism in transition metals is still not completely understood [8-10]. So far the relative contribution of intra- and inter-atomic exchange interaction to magnetic moment and their effect on magnetic coupling is not entirely clear. Whether these two interactions are collaborative or competing largely depend on the system and its atomic structure under study. For a given metallic system, if inter-atomic interaction dominates, larger inter-atomic distances tend to favor ferromagnetism and an

increased magnetic moment due to a narrower d band. In the situation where intra-atomic interaction dominates, larger inter-atomic distance means smaller crystal-field splitting for the d orbitals. Therefore an enhanced magnetic moment is also expected. At a given inter-atomic spacing, the magnetic property of the system depends on many competing interactions including magnetic, electronic, elastic, and magneto-elastic interactions that eventually lead to the lowest energy state. The surface and interface effects are important when magnetism is dominated by inter-atomic exchange interaction because of its sensitivity to chemical bonding. However, interface will also affect intra-atomic interaction due to the change in crystal-field and therefore the width and splitting of the d -band. The temperature dependence of magnetism actually concerns largely the relative importance of inter-atomic and intra-atomic exchange interactions in magnetism [11]. The fact that Fe, Co and Ni elements in bulk or thin films possess magnetic moments less than Hund's second rule predicts for isolated atoms means that inter-atomic interaction is important in these elements.

Monolayer Fe films grown on W(100) and W(110) substrates are used as examples to illustrate the orientation dependence of the exchange coupling on a short-range scale, and to understand the effect of crystal-field on magnetic moment of the Fe overlayers.

II. The Systems

Ultrathin Fe films grown on W(100) and W(110) substrates are prototype magnetic systems for studying thin film magnetism due to their thermal stability, large lattice mismatch of 9.4%, and pseudomorphic growth. However, Fe films deposited on W(100) and W(110) substrates exhibit very different magnetic properties [12-16]. It was observed that there are magnetic 'dead-layers' in the sub-monolayer coverage of Fe on W(100) [16,17] above the experimental temperature of 115 K and 140 K respectively, while an enhancement of the surface magnetic moment was observed for the 1 ML Fe/W(110) system [13,18,19]. In both experiments [12] and theoretical calculations [18], it was found that Fe has an enhanced moment of about $2.56 \mu_B$ in 1 ML Fe/W(110) film compared to the moment of $2.2 \mu_B$ in bulk bcc Fe. Further, a Curie temperature of 282K was observed for the monolayer Fe on W(110) [12,13]. So far, this difference has not been extensively explored nor understood.

Since electronic structure directly reflects the atomic structure of the system, magnetism is very sensitive to the details of the atomic structure. 1 ML Fe/W(100) has a C_{4v} point-group symmetry, while 1 ML Fe/W(110) has a lower C_{2v} . Since symmetry is crucial in crystal-field splitting of the d orbitals, it is not unexpected that Fe/W(110) and Fe/W(100) films exhibit different magnetic properties. Indeed, according to crystal-field theory, the $3d$ orbitals will be split into different bands for different symmetry. As a result, the interaction between Fe and W will be greatly affected by the symmetry. The relative strength of the crystal-field depends on the nature of chemical bonding and geometric effects.

III. Results and Discussion

The WIEN97 code [20] based on the FP-LAPW method was used to carry out the calculations. Repeated slab geometries consisting of a total of 5 W substrate layers and 1 Fe layer on each surface were employed in all of the calculations. A total of 3000 k-points in the full Brillouin Zone was used for both Fe/W(110) and Fe/W(100) films to ensure complete convergence and a proper comparison. The Generalized Gradient Approximation (GGA) was

	$d(\text{Fe-W}_1)$ (Å)	$d(\text{W}_1\text{-W}_2)$ (Å)	$\mu_B(\text{Fe})$	$\mu_B(\text{W}_1)$	$\mu_B(\text{W}_2)$	$\mu_B(\text{W}_3)$
Fe/W(100)	1.25	1.61	2.09	-0.25	0.090	-0.076
Fe/W(110)	1.97	2.26	2.56	-0.085	-0.000053	-0.00027

Table I. Comparison of atomic interlayer distances and magnetic moments between 1 ML Fe/W(100) and Fe/W(110).

adopted. Additional computational details were described in our earlier publications [18,21].

The theoretical equilibrium bcc W lattice constant of 3.205 Å was used for the in-plane lattice parameter in 1 ML Fe/W(110) and 1 ML Fe/W(100) films. The vertical lattice spacings were completely relaxed. The magnetic moments were determined by taking the majority spin numbers minus the minority spin number. Table I exhibits the interlayer atomic distances

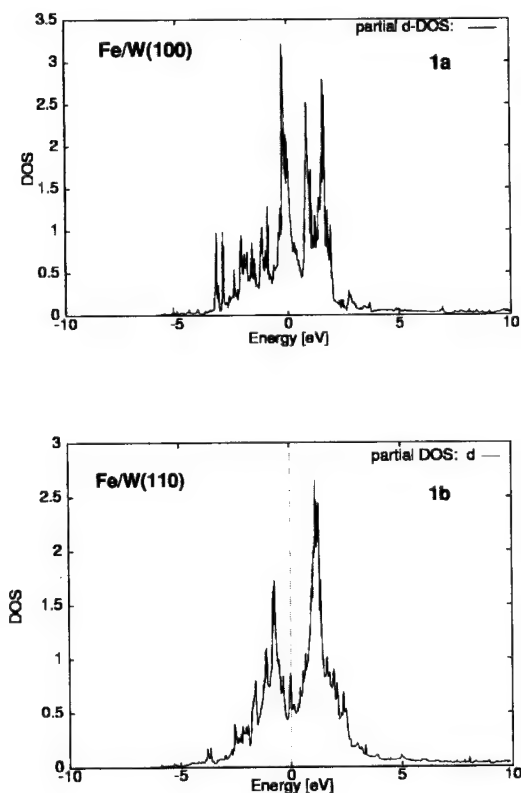


Figure 1. Fe minority-spin partial- d density-of-states (DOS) for 1 ML Fe/W(100) (Fig. 1a) and 1 ML Fe/W(110) (Fig. 1b)

and magnetic moments for the two systems.

As can be seen from Table I, 1 ML Fe grown on W(100) and on W(110) has very different interlayer distances and magnetic moments. In Fe/W(100) system, the Fe-W interlayer distance is much shorter compared to the one in Fe/W(110), a contraction of 36.5%. The W-W interlayer distance in Fe/W(100) is 28.8% smaller than that of Fe/W(110). It is true that the nearest-neighbor interatomic distances in both (100) and (110) oriented films are the same. However, four of the nearest-neighbor bonds lie in-plane in (110) oriented films, while all of the nearest-neighbor bonds are out-of-plane in (100) oriented films. It suggests that the interlayer interaction in Fe/W(100) is stronger compared to the one in the Fe/W(110) system because of the greater overlap between the interlayer valence orbitals in (100) oriented films than in (110) films.

Figures 1a and 1b show Fe 3d minority-spin density-of-states (DOS) for Fe/W(100) and Fe/W(110) respectively. It can be seen that the splittings of the 3d orbitals are different for the C_{4v} and C_{2v} symmetries as expected from crystal-field theory. There are 3 major peaks in the Fe 3d band grown on W(100) substrate, while only two major peaks can be observed for Fe/W(110) film. This means that crystal-field effect is important for the minority-spin DOS, which in turn largely determines the magnetic moment. Table II shows the contribution from Fe valence 4s, 4p and 3d orbitals to the total magnetic moment.

The Fe magnetic moments are found to be different in these two orientations with $2.09 \mu_B$ and $2.56 \mu_B$ for 1 ML Fe grown on W(100) and W(110) substrates respectively. The magnetic moment of Fe is enhanced by 16% in 1 ML Fe/W(110) compared to the bulk bcc Fe value of $2.2 \mu_B$ in agreement with previous experimental results [12,13]. However, the Fe magnetic moment is much reduced for the (100) orientation. As seen from this Table II, the major contribution to the difference of Fe magnetic moments in these two films is from $3d_{xz}$ and $3d_{xy}$ orbitals. Moreover, the interfacial W atom in (110) film acquires an induced moment of $0.085 \mu_B$, which is much smaller compared to $0.25 \mu_B$ for the interfacial W atoms in the (100) films. Recent experimental data [22] also demonstrate an induced interfacial W moment of $\sim 0.2 \mu_B$ for Fe/W(100) in good agreement with our current calculations. The inner W atoms have very small induced moments in the (110) film, while the induced moments for W persist for the inner layers in the (100) films. The second and third layer W atoms have moments of $\sim 0.09 \mu_B$ and $\sim 0.07 \mu_B$ respectively in the (100) oriented films. Interestingly, the W magnetic moments are ferromagnetically coupled to each other in W(110) substrate, in contrast to the anti-ferromagnetic coupling in W(100) substrate. This difference perhaps could be understood from the different interlayer distances in these two orientations. The (100) oriented film has a much shorter inter-layer distance compared to the (110) oriented film, thus ferromagnetic coupling is favored in the (110) films when inter-atomic exchange interaction plays an important role.

The difficulty in observing the short-oscillation period of magnetic coupling in (110) oriented films may be related to the rapid-decay of induced magnetic moments in W seen here in the Fe/W(110) system. The (100) oriented film, on the other hand, sustains a substantial value of induced magnetic moment even for the inner W layers seen from Table I. The underlying reason

spin (\uparrow - \downarrow)	μ_B	s	p	d_{tot}	d_z^2	$d_{x^2-y^2}$	d_{xy}	d_{xz}	d_{yz}
Fe/W(100)	2.09	0.033	0.004	2.059	0.628	0.521	0.189	0.391	0.331
Fe/W(110)	2.562	0.020	-0.005	2.547	0.585	0.608	0.411	0.665	0.279

Table II. Contributions to the total Fe magnetic moment from valence s , p and d orbitals

could be attributed to the shorter inter-layer distances in (100) films than those in (110) films. As a result, a larger overlap of the valence-orbitals in (100) films occurs.

The magnetic 'dead-layer' observed in the submonolayer Fe coverage on W(100) substrate [16,17] could be partially attributed to the reduced moments calculated here for Fe/W(100). However, there must be other mechanisms contributing to the complete suppression of magnetic signal. It is possible that the Curie temperature for the 1 ML Fe/W(100) system is much lower than the corresponding Curie temperature of 282K for the 1 ML Fe/W(110). It is known that Curie temperature is very sensitive to the film thickness, the coordination number, the capping and substrate layer thickness, and the interatomic distance [23-27]. Since exchange coupling J decays as $\sim 1/R^3$ [28], in which R is the interatomic distance, the Curie temperature will be dependent upon the crystallographic orientation of the thin film as demonstrated in [27]. If only nearest-neighbor coordination and distance are considered, then the Curie temperature for 1 ML Fe/W(100) will be around or below 100K, which is below the previous experimental temperature [16,17]. The lower magnetic moment for the monolayer Fe on W(100) substrate will reduce the Curie temperature even further compared to the corresponding W(110) substrate case [27]. All in all, our theoretical calculation does not find a magnetically dead monolayer Fe on W(100). However, it is possible that the Curie temperature of this system is far below the 1 ML Fe/W(110) case and below the experimental temperature conducted.

IV. Summary

It is shown that crystal-field effect is important for the magnetic moments and interlayer exchange coupling in ultrathin Fe/W(110) and Fe/W(100) magnetic films. The crystal-field energy splitting of the outer d orbitals and their relative positions are strongly symmetry dependent. As a result, the magnetic interactions including exchange coupling and magnetic moments are strongly affected by the crystal-field splitting and therefore by the symmetry of the thin films.

V. Acknowledgement

The authors would like to thank Prof. Kirschner for support and together with Dr. Sander for helpful discussions.

References

1. P. Grünberg, R. Schreiber, Y. Pang, M.B. Brodsky, and H. Sower, *Phys. Rev. Lett.* **57**, 2442 (1986); S.S.P. Parkin, N. More, and K.P. Roche, *Phys. Rev. Lett.* **64**, 2304 (1990).
2. Y. Yafet, *Phys. Rev. B* **36**, 3948 (1987); C. Chappert and J.P. Renard, *Europhys. Lett.* **15**, 553 (1991); P. Bruno and C. Chappert, *Phys. Rev. Lett.* **67**, 1602 (1991); **67**, 2592 (E) (1991); P. Bruno and C. Chappert, *Phys. Rev. B* **46**, 261 (1992); R. Coehoorn, *Phys. Rev. B* **44**, 9331 (1991).
3. D.E. Edwards, J. Mathon, R.B. Muniz, and M.S. Phan, *Phys. Rev. Lett.* **67**, 493 (1991); J. Mathon, M. Villeret, and D.M. Edwards, *J. Phys.: Condens. Matt.* **4**, 9873 (1992).
4. P. Bruno, *J. Magn. Magn. Mater.* **121**, 248 (1993); P. Bruno, *Phys. Rev. B* **52**, 411 (1995); M.D. Stiles, *Phys. Rev. B* **48**, 7238 (1993).

5. P. Bruno, "Magnetism: Molecules to Materials III Nanosized Magnetic Materials" edited by Joel S. Miller and Marc Drillon (WILEY-VCH, Weinheim, 2002), pp. 329 – 353.
6. L. Nordström, P. Lang, R. Zeller, and P.H. Dederichs, *Phys. Rev. B* **50**, 13058 (1994).
7. N. N. Lathiotakis, B.L. Györfy, and B. Újfalussy, *Phys. Rev. B* **61**, 6854 (2000).
8. J.E. Hirsch, *Phys. Rev. B* **56**, 11022 (1997).
9. T. Momoi and K. Kubo, *Phys. Rev. B* **58**, R567 (1998).
10. C.D. Batista, J. Bonča, and J.E. Gubernatis, *Phys. Rev. Lett.* **88**, 187203 (2002).
11. K. Maiti, M.C. Malagoli, A. Dallmeyer, and C. Carbone, *Phys. Rev. Lett.* **88**, 167205 (2002).
12. H.J. Elmers, G. Liu, and U. Gradmann, *Phys. Rev. Lett.* **63**, 566 (1989).
13. U. Gradmann, 'Magnetism in ultrathin transition metal films', in Handbook of Magnetic Materials, Vol. 7, Chapter 1, Edited by K.H.J. Buschow, (1993) 1-96.
14. D. Sander, R. Skomski, C. Schmidthal, A. Enders, and J. Kirschner, *Phys. Rev. Lett.* **77**, 2566 (1996).
15. J. Hauschild, U. Gradmann, and H. J. Elmers, *Appl. Phys. Lett.* **72**, 3211 (1998); J. Hauschild, H.J. Elmers, and U. Gradmann, *Phys. Rev. B* **57**, R677 (1998).
16. W. Wulfhek, W.F. Zavaliche, F. Poratti, H.P. Oepen, and J. Kirschner, *Europhysics Letters* **49**, 651 (2000).
17. G.A. Mulhollan, R.L. Fink, J.L. Erskine, and G.K. Walters, *Phys. Rev. B* **43**, 13645 (1991).
18. X. Qian and W. Hübner, *Phys. Rev. B* **60**, 16192 (1999).
19. I. Galanakis, M. Alouani, and H. Dreyssé, *Phys. Rev. B* **62**, 3923 (2000).
20. P. Blaha, K. Schwarz and J. Luitz, 'WIEN97, A full potential linearized augmented plane wave package for calculating crystal properties', (Karlheinz Schwarz, Tech. Univ. Wien, Vienna 1999), ISBN 3-950103104.
21. X. Qian, and W. Hübner, *Phys. Rev. B* **64**, 092402 (2001).
22. F. Wilhelm, P. Pouloupoulos, H. Wende, A. Scherz, and K. Baberschke, *Phys. Rev. Lett.* **87**, 207202 (2001).
23. W. Weber, D. Kerkmann, D. Pescia, D. A. Wesner, and G. Güntherodt, *Phys. Rev. Lett.* **65**, 2058 (1990).
24. C.M. Schneider, P. Bressler, P. Schuster, and J. Kirschner, *Phys. Rev. Lett.* **64**, 1059 (1990).
25. R. Vollmer, S. van Dijken, M. Schleberger, and J. Kirschner, *Phys. Rev. B* **61**, 1303 (2000).
26. M. Pajda, J. Kudrnovský, I. Turek, V. Drchal, and P. Bruno, *Phys. Rev. Lett.* **85**, 5424 (2000).
27. R. Zhang, and R. F. Willis, *Phys. Rev. Lett.* **86**, 2665 (2001).
28. M. Pajda, J. Kudrnovský, I. Turek, V. Drchal, and P. Bruno, *Phys. Rev. B* **64**, 174402 (2001).

Correlation between Magnetic Property and Cation Distribution in Z-type Hexagonal Barium-Ferrite ($\text{Ba}_3\text{Co}_{2-x}\text{Fe}_{24+x}\text{O}_{41}$) by Neutron Diffraction

Yukio Takada¹, Takeshi Tachibana^{1,2}, Takashi Nakagawa¹, Takao A. Yamamoto¹, Takeshi Shimada² and Shinji Kawano³

¹Graduate School of Engineering, Osaka University, Suita Osaka 565-0871 Japan.

²Sumitomo Special Metals Co., Ltd, Shimamoto Osaka 618-0013, Japan.

³Research Reactor Institute, Kyoto University, Kumatori Osaka 590-0490, Japan.

ABSTRACT

Z-type hexagonal ferrite samples in which cobalt is partially substituted with iron, $\text{Ba}_3\text{Co}_{2-x}\text{Fe}_{24+x}\text{O}_{41}$ ($x = 0, 0.2, 0.4, 0.6$), were prepared by the ceramic process under a sintering oxygen partial pressure, $P_{\text{O}_2} = 21.3$ or 101.3 kPa, at 1573 K. The influence of the substitution ratio and oxygen partial pressure on the complex permeability was investigated by examining the cobalt distribution over various cation sites in the Z-type structure with the neutron powder diffraction analysis performed at 294 K (neutron wave length was 1.006\AA). The neutron diffraction pattern was studied with the Rietveld method. A significant difference in the preferential occupation of cobalt on various kind of cation sites was observed between the samples obtained under $P_{\text{O}_2} = 21.3$ and 101.3 kPa. Almost all cobalt atoms are on the $12k$ octahedral site at the boundary between S- and R-blocks in the sample of $x = 0$, $P_{\text{O}_2} = 21.3$ kPa. On the other hand, in the sample of $x = 0$, $P_{\text{O}_2} = 101.3$ kPa, cobalt atoms are as well on other sites, the $12k$ octahedral site at the boundary between S- and T-blocks, the $4e$ tetrahedral site in S-block, the $2a$ octahedral site in T-block and the $2d$ five fold (trigonal bipyramid) site in T-block.

INTRODUCTION

In recent years, rapid progress of information society has been promoting downsizing of various electronic devices. In this trend, portable computer and mobile phone systems have been prevailing and becoming cordless, which needs improvements in the device integration technology and processing signals with much higher frequency (from MHz region to GHz). Electromagnetic noises radiated from these devices must be also in GHz region, so that obstruction and/or interference in normal operation are concerned [1]. Therefore, electromagnetic noise absorbent materials effective even in the GHz band have been required.

Z-type hexagonal barium ferrite $\text{Ba}_3\text{Co}_2\text{Fe}_{24}\text{O}_{41}$ is a promising candidate material because of its high permeability even at high-frequency region of GHz [2]. However, it is not easy to prepare the Z-type hexaferrite material as a single phase. Impurities of Y- ($\text{Ba}_2\text{Co}_2\text{Fe}_{12}\text{O}_{22}$) and W- ($\text{BaCo}_2\text{Fe}_{16}\text{O}_{27}$) phases easily occur and degrade resultant permeability because their intrinsic permeabilities are lower than that of the Z-type. We investigated synthesis conditions for obtaining single phase material of the Z-type hexaferrite varying temperature, oxygen partial pressure and substitution ratio of cobalt for iron. We found that a higher oxygen partial pressure and substitution of cobalt for iron are favorable for occurrence exclusively of the Z-phase and then for higher permeability [3]. We examined neutron diffraction (ND) patterns of the Z-phase samples by the Rietveld analysis in order to investigate sites occupied preferentially by iron or cobalt ions. We have already reported the results on iron-substituted

Z-type hexaferrite $\text{Ba}_3\text{Co}_{2-x}\text{Fe}_{24+x}\text{O}_{41}$ ($x = 0, 0.2, 0.4, 0.6$) sintered at $P_{\text{O}_2} = 101.3$ kPa [4]. In this paper, we report on results on the samples sintered at $P_{\text{O}_2} = 21.3$ kPa and compare them with the previous results in order to study correlation between the permeability and the site occupation preference.

EXPERIMENTAL

The samples with various compositions, $\text{Ba}_3\text{Co}_{2-x}\text{Fe}_{24+x}\text{O}_{41}$ ($x = 0, 0.2, 0.4, 0.6$) were prepared by the ceramic method as already reported [4]. Stoichiometric amounts of BaCO_3 , Co_3O_4 and Fe_2O_3 powders were mixed in a ball-mill with deionized water for 24 hours. They were dried and calcined at 1273K in air, crushed and shaped into pellets. They were then sintered at 1573 K for 16 hours under an oxygen partial pressure of 21.3 or 101.3 kPa. Their X-ray diffraction (XRD) patterns were measured in the range of diffraction angle $2\theta = 15 - 100^\circ$ at intervals of 0.02° . The neutron diffraction (ND) patterns at 294K were obtained by using the TAS spectrometer in a double axis mode at the beam line of KUR-TAS-B2 in Kyoto University Research Reactor. The sample powder was set in a vanadium cylindrical container with 20-mm diameter. The neutron flux at the sample position was about $10^5 \text{ cm}^{-2} \text{ s}^{-1}$. The diffraction angle 2θ was traced in the range of $7.5 - 42.5^\circ$. Its angle step $\Delta 2\theta$ was 0.1° and the measured time at each step was 90 s. These XRD and ND diffraction patterns at room temperature were examined with the Rietveld method analysis in order to optimize parameters regarding the crystal structures [5]. The XRD data was first analyzed for determining atomic coordinates and lattice parameters, and then the ND pattern was analyzed for determining the distribution of magnetic ions Fe and Co.

CRYSTAL STRUCTURE OF Z-TYPE HEXAGONAL FERRITE

The crystal structure of the Z-type hexagonal ferrite, $\text{Ba}_3\text{Co}_2\text{Fe}_{24}\text{O}_{41}$, is a complex one which consists of 44 atomic layers stacking up along the c -axis. In this structure, S, R and T blocks are ordered as RSTSR*S*T*S*, where the asterisk indicates rotation of each block by 180° around the c -axis. Figure 1 describes a part of atomic arrangement on (110) plane, in which iron and

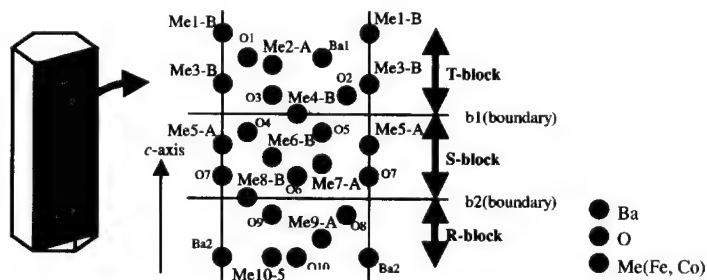


Figure 1. Partial schematic illustration of atomic sites in Z-type hexagonal ferrite as a view from [110] direction. Attached labels are mentioned in the text.

cobalt, represented as Me, are not distinguished. Me4 and Me8 sites are respectively on boundaries of T-S and S-R and labeled b1 and b2. Attached marks to the labels, -A, -B and -5, show that each Me ion are in tetrahedral, octahedral, and five fold (trigonal bipyramid) sites, respectively. The crystal structure is represented by a space group of $P6_3/mmc$, and, ideal atomic coordinates and lattice parameters were reported as $a = 5.88 \text{ \AA}$, $c = 52.31 \text{ \AA}$ by Vinnik [6]. Atomic coordinates of Ba, Me (Co and Fe) and O given by this space group are tabulated in Table 1. Ba ions are distributed over two sites labeled Ba1 and Ba2, and iron and cobalt ions over ten sites labeled Me1-Me10 [7].

RESULTS AND DISCUSSION

First, we performed XRD pattern refinement starting with the ideal atomic coordinates tabulated in Table 1. In this refinement, we have imposed several restrictions on performing refinements; (1) only Z-coordinates are allowed to change, while X- and Y-coordinates are kept constant. (2) two sites on a plane normal to c-axis share a Z-coordinate; Ba1-O1, O2-O3, O4-O5, O6-O7 and O8-O9. (3) atomic coordinates of Ba2, Me1, Me10 and O10 are kept constant in order to conserve the crystal symmetry. Me1-Me10 sites for iron or cobalt ions are assumed to

Table 1. Initial Atomic coordinates of Z-type hexagonal ferrite and Results of the Rietveld for X-ray and Neutron Diffraction of $P_{O_2} = 21.3 \text{ kPa}$.

Space group $P6_3/mmc$			Initial atomic coordinates of $Ba_3Co_2Fe_{24-x}O_{41}$			Refined structural parameters for $Ba_3Co_{2-x}Fe_{24+x}O_{41}$							
Sites Description			$a = 5.88 \text{ (\AA)}$ $c = 52.31 \text{ (\AA)}$			$x = 0$		$x = 0.2$		$x = 0.4$		$x = 0.6$	
Label	Wyckoff letter	Block	x	y	z	z		z		z		z	
Spin dir.						XRD	ND	XRD	ND	XRD	ND	XRD	ND
Me1-B ↑	2a	T	0	0	0	0	0	0	0	0	0	0	0
Me2-A ↓	4f	T	1/3	2/3	.0341	.0331(9)	.0299(1)	.0348(9)	.0339(3)	.0363(9)	.0296(5)	.0360(4)	.0364(9)
Me3-B ↓	4e	T	0	0	.0454	.0556(1)	.0605(3)	.0535(3)	.0579(9)	.0530(9)	.0543(9)	.0566(2)	.0566(9)
Me4-B ↑	12k	b ₁	1/2	0	.0909	.0908(2)	.0900(5)	.0912(3)	.0941(5)	.0913(5)	.0902(5)	.0910(5)	.0933(9)
Me5-A ↓	4e	S	0	0	.125	.1285(7)	.1291(5)	.1287(3)	.1252(1)	.1275(1)	.1199(4)	.1275(8)	.1240(5)
Me6-B ↑	4f	S	1/3	2/3	.1364	.1384(6)	.1467(7)	.1376(2)	.1394(3)	.1373(0)	.1517(9)	.1384(8)	.1396(5)
Me7-A ↓	4f	S	2/3	1/3	.1477	.1498(3)	.1533(9)	.1508(7)	.1488(2)	.1501(0)	.1479(0)	.1519(3)	.1505(9)
Me8-B ↑	12k	b ₂	1/6	1/3	.1818	.1867(8)	.1903(3)	.1861(7)	.1879(4)	.1873(4)	.1942(1)	.1868(8)	.1883(3)
Me9-B ↓	4f	R	2/3	1/3	.2273	.2201(8)	.2235(4)	.2236(9)	.2245(1)	.2212(1)	.2252(6)	.2236(1)	.2260(1)
Me10-S ↑	2d	R	1/3	2/3	.25	.25	.25	.25	.25	.25	.25	.25	.25
Ba2	2b	R	0	0	.25	.25	.25	.25	.25	.25	.25	.25	.25
Ba1	4f	T	2/3	1/3	.0227	.0274(7)	.0268(9)	.0277(9)	.0279(9)	.0277(2)	.0356(3)	.0271(2)	.0265(9)
O1	12k	T	1/6	1/3									
O2	12k	T	1/3	1/6	.0682	.0655(9)	.0435(0)	.0699(9)	.0685(3)	.0873(2)	.0926(1)	.06816(6)	.0688(0)
O3	4f	T	1/3	2/3									
O4	12k	S	1/6	1/3	.1136	.1059(4)	.1023(4)	.1091(1)	.1108(7)	.1207(5)	.1215(1)	.1111(3)	.1120(8)
O5	4f	S	2/3	1/3									
O6	12k	S	1/2	0	.1591	.1587(9)	.1586(4)	.1576(3)	.1640(8)	.1553(7)	.1587(3)	.1566(6)	.1641(3)
O7	4e	S	0	0									
O8	12k	R	1/3	1/6	.2045	.1989(1)	.2030(2)	.1986(6)	.2122(3)	.1907(7)	.1866(2)	.1999(1)	.2110(2)
O9	4f	R	1/3	2/3									
O10	6h	R	0	1/2	.25	.25	.25	.25	.25	.25	.25	.25	.25
S-parameter						3.93	3.61	2.62	2.97	4.17	3.58	3.42	2.8

Remark) Coordinates in italic are invariables.

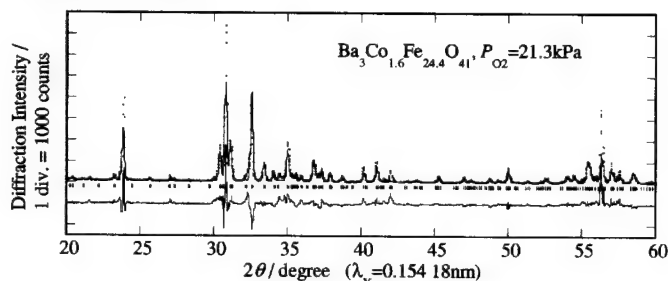


Figure 2. A typical result of present Rietveld refinement for XRD diffraction patterns of $P_{O_2} = 21.3$ kPa.

be filled only with iron, because X-ray scattering factors of iron and cobalt ions are almost same and they are indistinguishable. Thus optimized atomic coordinates and lattice parameters, shown in Table 1, were then submitted to ND pattern refinement. On the ND pattern refinement, another three restrictions were imposed in addition to those mentioned above; (4) the valences of iron and cobalt ions are Fe^{3+} and Co^{2+} , and the moment sizes are $5 \mu_B$ and $3 \mu_B$, respectively. (5) the valence of iron ion substituted for cobalt is Fe^{2+} with moment size of $4 \mu_B$. (6) these moments orientate up or down as shown in Table 1 [9]. Thus optimized atomic coordinates are as well tabulated in Table 1 for comparison with those obtained from XRD data.

Typical results of the present Rietveld analyses for XRD and ND are respectively shown in Figs. 2 and 3, in which experimental plots and refined patterns are together. Both are for the samples sintered at $P_{O_2} = 21.3$ kPa. It is noticed that deviation of the profile from the data around peaks due to (00 l) planes was of significance in the XRD refinements whilst not in the ND. This significant deviation is reasonably ascribed to preferential orientation of (00 l) planes normal to the XRD specimen plate [4, 8]. The sample of the ND was just a powder charged into a cylinder without any compression and therefore free from such orientation. The S -parameters associated with the present refinements are given at the bottom of the table.

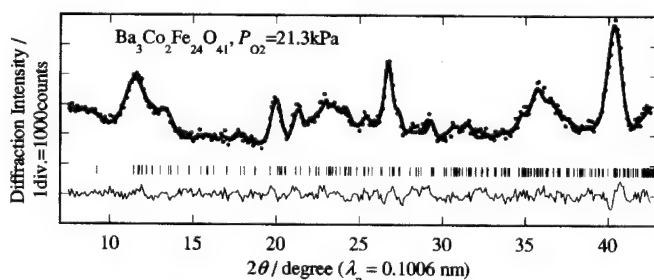


Figure 3. A typical result of present Rietveld refinement for ND diffraction patterns of $P_{O_2} = 21.3$ kPa.

Table 2. Iron and Cobalt site distribution determined by the Rietvelt refinements of the neutron diffraction data of $P_{O_2} = 21.3$ kPa.

Label, Spin direction	Site	Multiplicity Wyckoff letter	Block	g: Fractional Occupation Number							
				$x = 0$		$x = 0.2$		$x = 0.4$		$x = 0.6$	
				Fe	Co	Fe	Co	Fe	Co	Fe	Co
Me1-B ↑	2a	T		0.96	0.04	0.96	0.04	0.98	0.02	1	-
Me2-A ↓	4f	T		1	-	1	-	1	-	1	-
Me3-B ↓	4e	T		1	-	1	-	1	-	1	-
Me4-B ↑	12k	b1		1	-	1	-	1	-	1	-
Me5-A ↓	4e	S		0.98	0.02	0.99	0.01	0.98	0.02	1	-
Me6-B ↑	4f	S		1	-	1	-	1	-	1	-
Me7-A ↓	4f	S		1	-	1	-	1	-	1	-
Me8-B ↑	12k	b2		0.68	0.32	0.71	0.29	0.74	0.26	0.77	0.23
Me9-B ↓	4f	R		1	-	1	-	1	-	1	-
Me10-S ↑	2c	R		1	-	1	-	1	-	1	-
Magnetic moment angle ϕ with c-axis				83°		90°		90°		84°	

Previous our measurements on temperature dependence of the ND patters clearly indicated that the peaks in a range of $10 - 15^\circ$ are caused by the magnetic scattering from ordered magnetic ions [4]. The Rietveld refinement of the ND patterns can, therefore, throw light on the distribution of iron and cobalt ions over the ten sites, Me1-Me10, and orientation of the magnetic moment. Table 2 shows thus estimated occupation ratios of cobalt located in these sites and angle between the moment vector and the c-axis. Magnetic moment angles with c-axis listed at the bottom were found to be almost 90° . Cobalt ions were found to be located only in four sites out of the ten, Me1-B↑, Me5-A↓, Me8-B↑, and Me10-S↑, as has been found with samples sintered under $P_{O_2} = 101.3$ kPa [4]. Figure 4 shows the occupation numbers of cobalt for the four sites, which are obtained by multiplying the occupation ratio by each site number. The present results for $P_{O_2} = 21.3$ kPa are shown on the right-hand side, while the previous our results for $P_{O_2} = 101.3$ kPa on the left-hand. A clear difference is noticed between the right- and the left-hand: Cobalt ions are distributed over the four sites in the left-hand side while substantially only on a site, Me8↑, in the right-hand. When x increases, substituting Fe^{2+} ions for cobalt go dominantly into Me1-B↑(2a) in case of 101.3 kPa, while into Me8-B↑(12k) in case of $P_{O_2} = 21.3$ kPa.

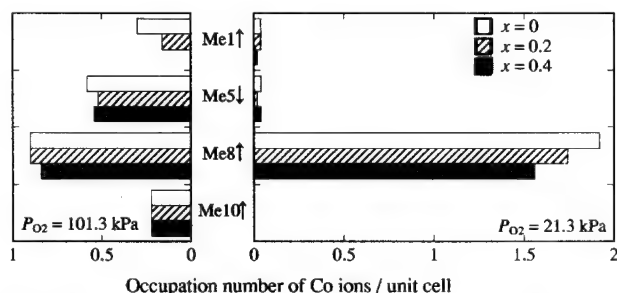


Figure 4. The occupation number of cobalt ions in $Ba_3Co_{2-x}Fe_{24+x}O_{41}$.

Now we examine correlation amongst thus estimated spin orientations of the sites, moment sizes of ions located there and resultant permeability. As shown in Table 1, there are 32 ions with up-spin and 20 with down-spin in the unit cell. The present our results indicates that, in the sample sintered under $P_{O_2} = 101.3$ kPa, the down-spin site, $Me5\downarrow$, is significantly occupied by cobalt with smaller magnetic moment, $3\mu_B$, than that of iron, which contributes to an increase in saturation magnetization and then permeability. However, any down spin site seemed not to be occupied by cobalt when $P_{O_2} = 21.3$ kPa. Recall here that the permeability of $P_{O_2} = 101.3$ kPa was larger than that of $P_{O_2} = 21.3$ kPa [3]. These facts are consistent with each other, which would support reliability of the present analyses and results regarding preferential site occupation by cobalt and iron ions.

CONCLUSION

We investigated correlation between permeability and magnetic cation distribution in $Ba_3Co_{2-x}Fe_{24+x}O_{41}$ ($x = 0, 0.2, 0.4, 0.6$) prepared by the ceramic method under oxygen partial pressure $P_{O_2} = 101.3$ and 21.3 kPa, and found; (1) Cobalt ions occupy almost a particular site ($12k$) out of 10 sites for $P_{O_2} = 21.3$ kPa, while 4 sites ($12k$, $4e$, $2a$ and $2d$) for $P_{O_2} = 101.3$ kPa. (2) The additional Fe^{2+} ions are mainly substituted for cobalt in $2a$ site for $P_{O_2} = 101.3$ kPa, while $12k$ site of $P_{O_2} = 21.3$ kPa.

REFERENCES

- [1] Martha Pardavi-Horvath, J. Magn. Magn. Mater. 215-216 (2000) 171.
- [2] J. Smit and H.P.J. Wijn: "Ferrites", Philips Technical Library, Eindhoven, The Netherlands, (1959) 268
- [3] T. Tachibana, K. Ohta, T. Shimada, T. Nakagawa, T. A. Yamamoto, M. Katsura: Proceedings of the 8th International Conference on Ferrites (ICF8), Kyoto and Tokyo, Japan, JSSPM (2000) 888
- [4] T. Tachibana, T. Nakagawa, Y. Takada, K. Izumi, T. A. Yamamoto, T. Shimada and S. Kawano, J. Magn. Magn. Mater. (in press).
- [5] F. Izumi and T. Ikeda, Mater. Sci. Forum, 321-324 (2000) 198
- [6] M.A. Vinnik: "PHASE RELATIONSHIPS IN THE BaO-CoO-Fe₂O₃ SYSTEM", Russian Journal of Inorganic Chemistry, Vol.10, No.9 (1965) 1164
- [7] R.B. Braun: "THE CRYSTAL STRUCTURE OF A NEW GROUP OF FERROMAGNETIC COMPOUNDS", Philips Res. Rep. 12 (1957) 491
- [8] R.A. Young: "THE RIETVELD METHOD", Oxford Univ. Press, Oxford (1993) Chap. 13.
- [9] J. Smit and H.P.J. Wijn: "Ferrites", Philips Technical Library, Eindhoven, The Netherlands, (1959) 188

NONSTOICHIOMETRY OF EPITAXIAL $\text{FeTiO}_{3+\delta}$ FILMS

Tatsuo Fujii*, Makoto Sadai, Masakazu Kayano, Makoto Nakanishi and Jun Takada
Department of Applied Chemistry, Okayama University, Okayama 700-8530, Japan
*Email: tfujii@cc.okayama-u.ac.jp

ABSTRACT

Epitaxial thin films of (001)-oriented $\text{FeTiO}_{3+\delta}$ were prepared on $\alpha\text{-Al}_2\text{O}_3(001)$ single crystalline substrates by helicon plasma sputtering technique. The $\text{FeTiO}_{3+\delta}$ films had large oxygen nonstoichiometry, which seriously depended on both substrate temperature and oxygen pressure during the sputtering deposition. The valence states of Fe ions in $\text{FeTiO}_{3+\delta}$ changed monotonically from Fe^{2+} to Fe^{3+} with decreasing the substrate temperature from 900 to 400°C or with increasing the oxygen pressure from 0.9 to 1.8×10^{-6} Pa. The change of Fe valence states from Fe^{2+} to Fe^{3+} induced the magnetic phase transition only for the films prepared at 900°C. The films containing Fe^{2+} were paramagnetic while those with Fe^{3+} were antiferromagnetic at room temperature. The oxygen nonstoichiometry of the $\text{FeTiO}_{3+\delta}$ films was probably produced by cation vacancies and disarrangement of Fe^{3+} and Ti^{4+} ions, which randomly occupied both interstitial and substitutional sites of the FeTiO_3 related structure.

INTRODUCTION

Solid solutions of $\alpha\text{-Fe}_2\text{O}_3\text{-FeTiO}_3$ (hematite-ilmenite) series are known to have interesting magnetic and electric properties [1,2]. Though the end members of this series are antiferromagnetic insulators, the intermediate compositions between them are half-metallic ferrimagnets. The compositions are nominally expressed as $\text{Fe}^{3+}_{2-2x}\text{Fe}^{2+}_x\text{Ti}^{4+}_x\text{O}_3$, where x is the mole fraction of ilmenite. The crystal structure of them has rhombohedral symmetry and is considered as a slightly distorted hcp O^{2-} framework with cations lying in two thirds of octahedral interstices in ordered way. We have recently succeeded in preparing well-crystallized epitaxial $\text{Fe}_{2-x}\text{Ti}_x\text{O}_3$ films by activated reactive evaporation [3,4]. The films of intermediate composites had large ferrimagnetic moments and their resistivity dropped to $10^{-1}\Omega\text{cm}$ at room temperature. However the Fe^{2+} content of the films was rather small as compared with stoichiometric $\text{Fe}_{2-x}\text{Ti}_x\text{O}_3$. The Ti-rich films we previously prepared seemed to have large oxygen nonstoichiometry about $\delta=0.3$ in $\text{Fe}_{2-x}\text{Ti}_x\text{O}_{3+\delta}$.

Prior to preparing the stoichiometric solid-solution films of $\text{Fe}_{2-x}\text{Ti}_x\text{O}_3$, we tried to confirm preparation conditions of stoichiometric FeTiO_3 films. According to a literature on bulk crystal growth of FeTiO_3 [5], very low oxygen pressure of about 10^{-12} Pa is required to prevent the oxidization of Fe^{2+} . In the present study helicon plasma sputtering (magnetron sputtering assisted by inductively coupled RF plasma) technique was applied to prepare stoichiometric FeTiO_3 . The helicon plasma sputtering system we used had very high vacuum and low contaminations. The base pressure was less than 10^{-7} Pa. The structural and magnetic properties of epitaxial $\text{FeTiO}_{3+\delta}$ films were reported as a function of the preparation conditions, *i.e.* stoichiometry of the films. The carefully controlled heating temperature and oxygen pressure should be essential to prepare stoichiometric films.

EXPERIMENT

$\text{FeTiO}_{3+\delta}$ films were prepared on $\alpha\text{-Al}_2\text{O}_3(001)$ single-crystalline substrates. Fig.1

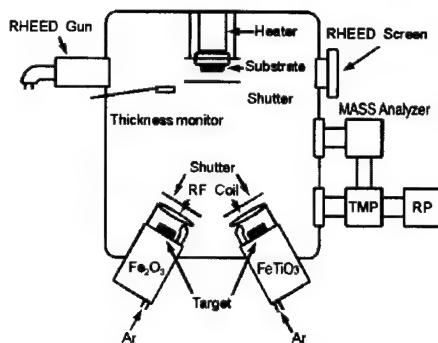


Figure 1. Schematic drawing of the helicon plasma sputtering system we used.

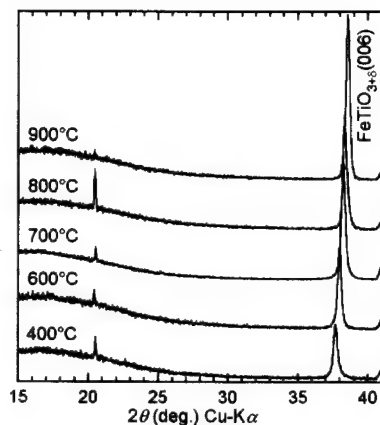


Figure 2. XRD patterns of $\text{FeTiO}_{3+\delta}$ films prepared on $\alpha\text{-Al}_2\text{O}_3(001)$ substrates at different substrate temperatures.

shows a schematic drawing of the helicon plasma sputtering system we used. Two targets for helicon cathodes were made of sintered $\alpha\text{-Fe}_2\text{O}_3$ and FeTiO_3 , respectively. In the present study only the FeTiO_3 target was operated. The base pressure of the system was 10^{-7} Pa, and the oxygen partial pressure during the sputtering deposition was measured *in situ* by a mass analyzer unit. Before the sputtering deposition an $\alpha\text{-Al}_2\text{O}_3(001)$ substrate was annealed in vacuum at about 900°C for 1 hour in order to obtain a clean and well-ordered surface. $\text{FeTiO}_{3+\delta}$ films with the thickness of 100 nm were deposited on the substrates at various substrate temperatures ranging from 400 to 900°C . The deposited films were characterized by conventional θ - 2θ x-ray diffraction (XRD) measurement, XRD pole figure measurement and conversion electron Mössbauer spectroscopy (CEMS). Chemical formula of prepared $\text{FeTiO}_{3+\delta}$ films analyzed by energy dispersive X-ray spectroscopy (EDS) was $\text{Fe}_{1.23}\text{Ti}_{0.77}\text{O}_{3+\delta}$.

RESULTS AND DISCUSSION

Substrate Temperature

Fig.2 shows XRD patterns of the sample films prepared at various substrate temperatures between 400 and 900°C . All sample films showed only one intense diffraction line just beside a strong $\alpha\text{-Al}_2\text{O}_3(006)$ line at $2\theta=41.68^\circ$. It is well-known that FeTiO_3 has the same hcp O^{2-} framework as $\alpha\text{-Al}_2\text{O}_3$, so the films could epitaxially formed on the substrates. Assuming the same lattice parameters as those of bulk FeTiO_3 crystals [6], the $\text{FeTiO}_3(006)$ diffraction line should appear at $2\theta=38.29^\circ$ which was very consistent with the observed 2θ values for the sample films shown in Fig.2. Therefore the observed lines were indexed as $\text{FeTiO}_{3+\delta}(006)$. However the 2θ values of $\text{FeTiO}_{3+\delta}(006)$ depended considerably on the substrate temperature when the films were prepared. With decreasing the substrate temperature the 2θ value decreased gradually than that of the bulk FeTiO_3 crystals. Moreover the line intensity was decreased in addition to the line broadening. The calculated grain size by using a Scherrer's equation was typically 325 \AA at

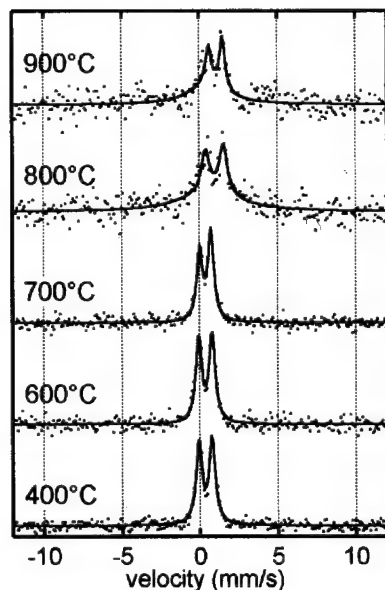


Table I. Fitted parameters for CEMS spectra shown in Fig. 3.

Substrate temperature (°C)	Isomer shifts (mm/s)	Quadrupole splitting (mm/s)
900	1.13	0.98
800	1.03	1.14
700	0.37	0.73
600	0.37	0.87
400	0.35	0.85

Figure 3. Room temperature CEMS spectra of $\text{FeTiO}_{3+\delta}$ films prepared at different substrate temperatures.

900°C and 260 Å at 400°C, respectively.

Room temperature CEMS spectra of sample films prepared at various substrate temperatures are shown in Fig.3. All sample films were paramagnetic. Assuming the analyzed chemical formula of $\text{Fe}_{1.23}\text{Ti}_{0.77}\text{O}_3$, the Néel temperature of stoichiometric films should be about -25°C [1], *i.e.* below the room temperature. The magnetic properties seemed to be consistent with those of bulk crystals. But the valence states of Fe ions evaluated from the Mössbauer isomer shifts showed considerable changes depending on the substrate temperature. The films prepared at higher substrate temperature consisted of Fe^{2+} ions, while those at lower substrate temperature consisted of Fe^{3+} ions. The isomer shifts of sample films gradually increased with increasing the substrate temperature. The quadrupole splitting also reflected the valence states of Fe ions. Fe^{2+} ions, which had a remnant orbital angular momentum in crystal fields, normally gave larger quadrupole splitting than Fe^{3+} ions.

Oxygen Pressure

The 2θ values of $\text{FeTiO}_{3+\delta}(006)$ seriously depended on the oxygen pressure during the sputtering deposition. Fig.4 shows the 2θ values for sample films prepared at the substrate temperature of 900°C as a function of the oxygen pressure. With increasing the oxygen pressure the 2θ value increased from literature values for stoichiometric $\text{Fe}^{2+}\text{TiO}_3$ [6] to $\alpha\text{-Fe}^{3+}_2\text{O}_3$ [7]. There were small possibilities that the $\text{FeTiO}_{3+\delta}$ films decomposed into two phases like $\alpha\text{-Fe}_2\text{O}_3$ and TiO_2 , because the diffraction lines of $\text{FeTiO}_{3+\delta}(006)$ maintained sharp profiles and no diffraction lines due to the secondary phases appeared when oxygen pressure was increased.

Room temperature CEMS spectra of sample films prepared at various oxygen pressures are shown in Fig.5. The spectrum with a paramagnetic doublet at lower oxygen pressure

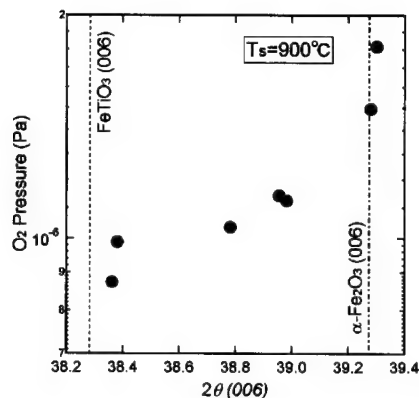


Figure 4. 2θ values for $\text{FeTiO}_{3+\delta}$ films prepared at 900°C as a function of the oxygen pressure during the sputtering deposition.

changed to magnetically split sextet patterns at higher oxygen pressure. The Néel temperature of sample films increased gradually above room temperature. Moreover the valence states of Fe ions evaluated from the Mössbauer isomer shifts changed from Fe^{2+} to Fe^{3+} with increasing the oxygen pressure. Fe^{3+} ($S=5/2$) ions had a larger spin magnetic moment than Fe^{2+} ($S=2$) ions. Therefore the formation of Fe^{3+} ions from Fe^{2+} ions raised the Néel temperature of the films.

The increased oxygen pressure and the decreased substrate temperature seemed to produce same effects on the iron valence states of the $\text{FeTiO}_{3+\delta}$ films. However the 2θ values of $\text{FeTiO}_{3+\delta}(006)$ gave the contrary results depending on the respective preparation conditions. The oxidized films owing to the increased oxygen pressure showed the increased the 2θ values, while the films prepared at the decreased substrate temperature had the decreased 2θ values. This contradictory was probably due to the inferior crystallinity of the $\text{FeTiO}_{3+\delta}$ films prepared at lower

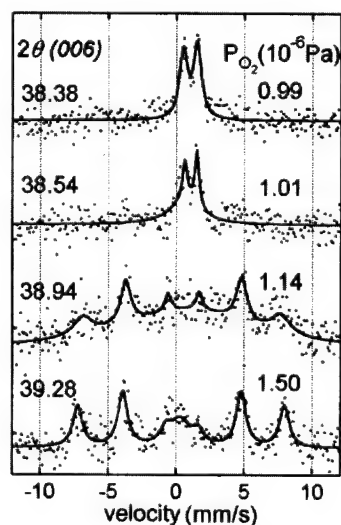


Table II. Fitted parameters for CEMS spectra shown in Fig. 5.

2θ value (deg.)	Isomer shifts (mm/s)	Quadrupole splitting (mm/s)	Hyperfine field (kOe)
38.38	1.02	1.01	-
38.54	0.82	0.88	-
38.94	0.50	-	449.9
39.28	0.40	-	470.5

Figure 5. Room temperature CEMS spectra of $\text{FeTiO}_{3+\delta}$ films prepared at different oxygen pressures.

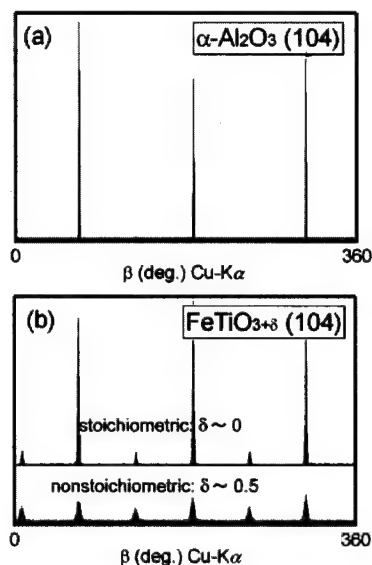


Figure 6. β -scan profiles for (104) pole figures of (a) an α - Al_2O_3 substrate and (b) stoichiometric and nonstoichiometric $\text{FeTiO}_{3+\delta}$ films.

substrate temperature. The films prepared at lower substrate temperature earned small crystallization energy and loosened the lattice structures. The inferior crystallinity of sample films maintained the paramagnetic properties though the films contained Fe^{3+} ions with larger spin magnetic moment.

Crystal Structure

It was very interesting to know the crystal structure of nonstoichiometric $\text{FeTiO}_{3+\delta}$. In oxidation studies of FeTiO_3 bulk crystals, nonstoichiometric $\text{FeTiO}_{3+\delta}$ easily decomposed into stable phases of Fe_2TiO_5 and TiO_2 , or $\text{Fe}_2\text{Ti}_3\text{O}_9$ and Fe_2O_3 [8]. As far as we know, the nonstoichiometric $\text{FeTiO}_{3+\delta}$ was not observed in a bulk form. An epitaxial relationship between the α - Al_2O_3 substrate and the $\text{FeTiO}_{3+\delta}$ film was obtained by XRD pole figures. Fig.6 shows the β -scan profiles of (104) diffraction lines for the α - Al_2O_3 substrate, the stoichiometric $\text{Fe}^{2+}\text{TiO}_3$ film, and the nonstoichiometric $\text{Fe}^{3+}\text{TiO}_{3+\delta}$ film. According to the crystal symmetries of corundum and ilmenite structures, the (104) poles should have three-fold symmetry and appeared in every 120° for β -scan. The β -scan profiles clearly suggested that the stoichiometric FeTiO_3 film had nearly the same in-plane symmetry as that for the corundum or ilmenite structure. However the (104) poles for the nonstoichiometric $\text{FeTiO}_{3+\delta}$ film had six-fold symmetry because the diffraction lines appeared in every 60° . The change of in-plane symmetry for nonstoichiometric $\text{FeTiO}_{3+\delta}$ suggested the redistribution of cation occupancies in octahedral interstices of hcp oxygen layers. Fe^{3+} and Ti^{4+} ions randomly occupied both interstitial and substitution sites in the ilmenite-related structure. And cation vacancies were introduced into the structure to maintain the charge neutrality. The disordered cation occupancies we proposed here were already reported in Sn-, Ti-, and Mg-substituted α - Fe_2O_3 [9].

ACKNOWLEDGEMENT

This work was partly supported by grant-in-aid from Ministry of Education, Science, Sports and Culture, Japan.

REFERENCES

1. Y. Ishikawa, J. Phys. Soc. Jpn. **17**, p.1835 (1962).
2. Y. Ishikawa, J. Phys. Soc. Jpn. **13**, p.37 (1958).
3. T.Fujii, K. Ayama, M. Nakanishi, and J. Takada, J. Magn. Soc. Jpn. **22**, S1, p.206 (1998).
4. T. Fujii, K. Ayama, M. Nakanishi, M. Sohma, K. Kawaguchi, and J. Takada, Mat. Res. Soc. Symp. Proc. **623**, p.191 (2000).
5. R. K. Pandey, S. Sunkara, and J. Muthusami, AIP Conf. Proc. **361**, p.193 (1996)
6. Powder diffraction files, JCPDS 29-733.
7. Powder diffraction files, JCPDS 33-664.
8. R.A. Briggs and A.Sacco Jr., Meal. Trans. **24A**, p.1257 (1993).
9. F.J. Berry, C. Greaves, Ö. Helgason, J. McManus, H.M. Palmer, and R.T. Williams, J. Solid State Chem. **151**, p.157 (2000).

Microstructure and Magnetic Property of L1₀ CoPt-20 at.% C Magnetic Thin Film

D.Y. Oh and J.K. Park

Department of Materials Science and Engineering

Korea Advanced Institute of Science and Technology

373-1 Kusong-dong, Yusong-gu, Daejeon, 305-701, Korea.

ABSTRACT

The CoPt-20at.%C thin films of 20nm thickness were sputter-deposited in the form of CoPt/C_n (n=1: carbon layer thickness=4nm; n=4: each carbon layer thickness=1nm) and were transformation-annealed at 650°C for various times. Carbon was found to dissolve into CoPt lattice and enlarge the c/a ratio of the ordered CoPt lattice. The amount of carbon dissolution increases with the decreasing carbon layer thickness at a given total carbon concentration.

The carbon dissolution larger than a critical amount can lead to a shift of the phase equilibrium of ordering and produce a stable fine two-phase mixture of ordered and disordered phases at the equi-atomic composition of Co:Pt. This results in a fine and uniform stagnant grain structure of about 20nm on annealing at 650°C. The carbon dissolution by increasing the c/a ratio of the ordered CoPt lattice reduces both the saturation magnetization and the magnetocrystalline anisotropy constant of the film and leads to a reduction of coercivity of CoPt films.

INTRODUCTION

The ordered L1₀ CoPt granular film is a potential candidate for ultra high density recording media because of its high magneto-crystalline anisotropy constant. This film is however known to be prone to the occurrence of excessive grain growth during transformation annealing and to high transition noise because of lack of magnetic granular isolation. To solve this problem, the composite film of L1₀ granular CoPt particles imbedded in the carbon matrix has been the subject of extensive studies[1,2]. The composite film was fabricated either by co-sputtering Co, Pt, and C[1] or by sputtering in the form of multilayers (CoPt/C)_n [2] followed by annealing.

We were interested in exploring the possibility of fabricating optimum monolithic, instead of composite, CoPt(C) granular film by incorporating a minor amount of carbon in the form of CoPt/C_n(n=1, 4). We investigated the effect of C mixing on the grain structure and magnetic properties of L1₀ CoPt granular film. Particular attention was paid to the mixing behavior of

carbon layer with CoPt layer by dividing the given carbon layer into several thin layers for mixing experiments.

EXPERIMENTS

Equiatomic CoPt film was RF-sputter deposited on the thermally oxidized Si substrate at room temperature under the Ar pressure 5 mtorr in a vacuum chamber with a base pressure less than 1×10^{-6} torr. The intercalated carbon layer was DC-sputter deposited using carbon target. The total film thickness of CoPt layer was fixed to 20 nm and that of carbon layer was fixed to 4 nm, which amounts to about 20 at.% C. To investigate the effect of thickness effect on the carbon mixing with CoPt lattice, alternate sputtering was carried out to fabricate a multilayer structure of CoPt/C_n (n=1, 4) by dividing the total carbon layer (n=1: thickness=4nm) into 4 thin carbon layers (n=4: thickness=1nm). The films were annealed at 650°C for various times in a vacuum furnace. The ordering transformation was studied using X-ray diffractometer and TEM DF technique. The grain structure was characterized using TEM and the in-plane grain size distribution was measured using an image analyzer. The number of counted grains was 200-500. The magnetic hysteresis loop was measured using VSM.

RESULTS AND DISCUSSION

The examination of in-plane grain structure CoPt thin film (n=0) showed that the grain grows rapidly during the initial period of annealing at 650°C and tends to be stagnant at a later stage. The addition of carbon of 20 at.% into CoPt film in the form of multilayer CoPt/C_n (n=1, 4) was observed to greatly retard the initial growth rate. Furthermore, the stagnant grain structure was found to be greatly dependent on the number of divided carbon layers, n at a given total carbon thickness, namely on the thickness of each carbon layer.

The grain size distribution (GSD) of 20nm CoPt thin films is plotted in terms of frequency vs. logarithm of the normalized grain size (Fig.1a). The as-deposited film exhibits a lognormal grain size distribution. With the progress of annealing, the grain population near the peak diminishes with a concurrent rise of grain population at the leading edge, i.e., the side of small grains. This eventually leads to a bimodal-like grain size distribution on annealing for 30 min. Further progress of annealing recovers a monomodal grain size distribution and the GSD approaches a lognormal distribution. This variation is qualitatively in correspondence with that of the transformation fraction of L1₀ ordered CoPt phase with annealing. The X-ray diffraction study (Fig.1b) indicated that the transformation rate is rapid at 30 min of annealing and the rate

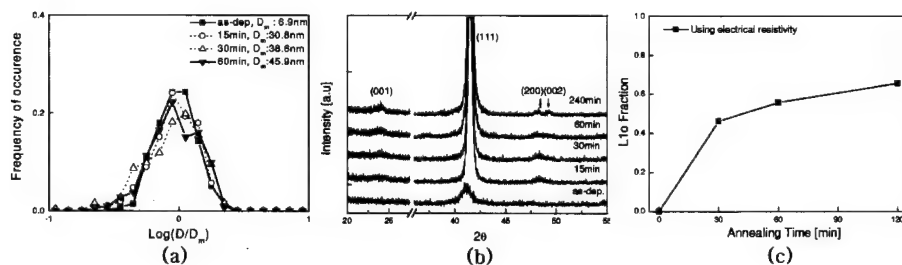


Figure 1. Plot of the frequency of occurrence vs. logarithm of the normalized grain size with respect to the average grain size D_m (a) ; XRD patterns of of 20nm CoPt ($n=0$) films as-deposited and annealed at 650°C for various times (b) ; Plot of L1o fraction vs. annealing times at 650°C in 40nm CoPt ($n=0$) films.

slows down after 60 min of annealing. This result was further confirmed in the measurement of transformed volume fraction of ordered phase for 40nm CoPt thin films using electrical resistivity technique (Fig.1c).

This result shows that the ordering transformation occurs by nucleation of ordered clusters and their growth. It appears that these clusters do not grow fast because of the presence of interface between ordered and disordered phases and that small particles were found at 30 min of annealing. The presence of small ordered particles was in fact observed in a TEM DF study in agreement with the previous work by Coffey et al. [3].

Figure 2 shows the GSD in 20nm CoPt/C_n ($n=1, 4$) thin films. The GSD rather resembles to a mono-modal than a bi-modal distribution, which is particularly true for thin film with $n=4$ (each carbon layer thickness=1nm): there appears to be some faint trace of bimodal distribution for film with $n=1$ (carbon layer thickness=4nm) for a long time annealing. The cumulative-frequency plot showed that the GSD's are all close to a lognormal distribution except at the region of small grains, i.e., the leading edge. The leading edge with a long time annealing always better fits to the lognormal distribution. It is to remark here that the GSD of the film with $n=4$ approaches a nearly perfect lognormal distribution on annealing for 240min, although the average grain size at this condition is only about the size of film thickness, 20nm. This is a premature stagnation of grain structure in view of the well established fact that the grain stagnation usually occurs at $D \sim 2.5 t$ [4].

We believe that this premature stagnation of grain structure arises from the formation of a stable two-phase mixture of ordered and disordered phases in CoPt/C₄ films, which is also

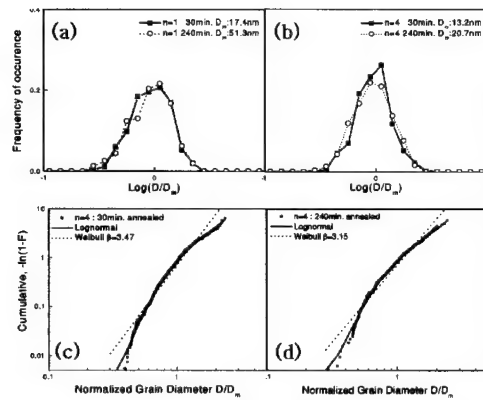


Figure 2. Plot of the frequency of occurrence vs. logarithm of the normalized grain size of the CoPt/C_n films with n=1 (a) and n=4 (b) and the cumulative-frequency plot of the CoPt/C₄ films for different annealing times (c, d).

responsible for the formation of very fine and uniform GSD's (Fig.2). The reason for the exceptional stability in the n=4 film is that the ordering transformation is extremely limited over a long period of annealing time in the film with n=4 (carbon one-layer thickness = 1nm) unlike from the film with n=1 (carbon one-layer thickness = 4nm) despite the fact that the total carbon thickness is the same in both films. The X-ray diffraction study (Fig.3a) clearly showed the difference: the ordering transformation is greatly suppressed in the film of CoPt/C₄ as compared with the film of CoPt/C₁ although the total carbon thickness is the same. In addition, the (111) peak is shown to significantly shift to a larger angle in the n=1 film as compared with the CoPt film, indicating that carbon dissolves into CoPt lattice. The result further shows that the (111) peak in the n=4 film experiences a peak separation due to ordering transformation, a small secondary ordered peak appearing at the high angle side of principal peak: this indicates that the transformation is incomplete in this film even after a sufficient annealing. Furthermore, the angular position of this secondary ordered peak is clearly at a larger angle than that of (111) peak in the film with n=1. This clearly indicates that the amount of dissolved carbon increases with increasing n, that is, with the decreasing carbon layer thickness. The (001) ordered peak, however, appears not to change with carbon addition, although its accurate position is somewhat obscure because of a low intensity.

From the information of the X-ray diffraction studies, we can conclude that the carbon dissolves into ordered L1₀ CoPt lattice and that the carbon solubility increases with decreasing

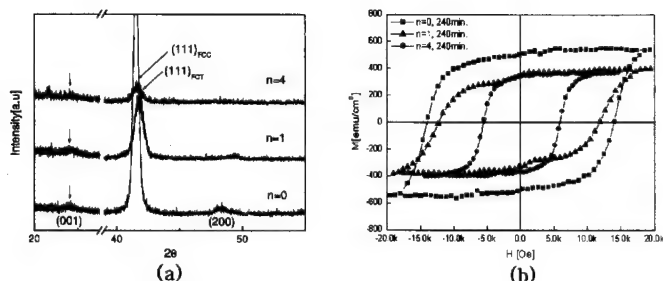


Figure 3. XRD patterns of CoPt/Cn ($n=0, 1, 4$) films annealed for 30 min at 650°C (a) and in-plane magnetic hysteresis loops of CoPt/Cn ($n=0, 1, 4$) films annealed for 240 min at 650°C (b).

individual carbon layer thickness at a given total carbon thickness. The dissolved carbon makes the c/a ratio bigger by reducing a and the c/a increases with the number of divided carbon layer, i.e., with the diminishing individual carbon layer thickness at a given total thickness. The approximate calculation of c/a ratio from the present X-ray data indicated that the c/a ratios are 0.945 for $n=0$, 0.957 for $n=1$ and 0.964 for $n=4$.

We believe that a large increase of c/a ratio in the $n=4$ film is primarily responsible for a great suppression of ordering transformation and for the formation of stable two-phase mixture of ordered and disordered phases. The origin of the formation of a stable two-phase mixture is believed not to be the kinetic one but rather to be thermodynamic one, in view of its great thermal stability. This result suggests that T_c shifts toward a higher temperature and Pt-rich composition so that the film with $n=4$ is found within the two-phase region at 650°C. It is to remark here that this does not happen in the film with $n=1$ although the overall carbon composition is the same. This suggests that a critical amount of carbon dissolution is necessary in order to significantly shift the equilibrium phase field of Co-Pt system.

The fact that carbon dissolves into L1₀ CoPt lattice and that the amount of carbon dissolution depends on the carbon layer thickness is also well manifested in the magnetic hysteresis loops of CoPt films. The measurement of hysteresis loops (Fig.3b) showed that the coercivity, among others, is reduced as a result of carbon incorporation into the ordered CoPt lattice and the amount of reduction strongly depends on the thickness of initial carbon layer. We believe that this is because the increase of c/a ratio of ordered phase with carbon incorporation reduces the degree of ordering of L1₀ CoPt lattice as well as its transformation fraction. Both factors contribute to a reduction of effective K_u of CoPt film and lead to a reduction of its

coercivity. The carbon dissolution into the ordered CoPt lattice also reduces the M_s of L1₀ CoPt phase. A similar M_s value is observed in the films with $n=1$ and $n=4$. This is because the film with $n=4$ consists of ordered and disordered phases, the latter phase exhibiting a larger M_s value. All of these results suggest that the CoPt-20at.%C film is one of promising candidates for solving the excessive grain growth and transition noise problems of the high density magnetic recording media based on CoPt alloys.

CONCLUSIONS

The CoPt-20at.%C thin films of 20nm thickness were sputter-deposited in the form of CoPt/C_n ($n=1$: carbon layer thickness=4nm; $n=4$: each carbon layer thickness=1nm) and were transformation-annealed at 650°C for various times. Carbon was found to dissolve into CoPt lattice and enlarge the c/a ratio of the ordered CoPt lattice. The amount of carbon dissolution increases with the decreasing carbon layer thickness at a given total carbon concentration.

The carbon dissolution larger than a critical amount can lead to a shift of the phase equilibrium of ordering and produce a stable fine two-phase mixture of ordered and disordered phases at the equi-atomic composition of Co:Pt. This results in a fine and uniform stagnant grain structure of about 20nm on annealing at 650°C. The carbon dissolution by increasing the c/a ratio of the ordered CoPt lattice reduces both the M_s and the effective K_u of the film and leads to a reduction of coercivity of CoPt films.

ACKNOWLEDGMENTS

The authors are grateful to the Ministry of Science and Technology, Korea for the financial support of this research through the Nanostructure Technology Project

REFERENCES

1. M. Yu, Y. Liu, and D. J. Sellmyer, *J. Appl. Phys.* **87**, 6959 (2000).
2. I. Panagiotopoulos, S. Stravroyiannis, D. Niarchos, J. A. Christodoulides, and G. C. Hadjipanayis, *J. Appl. Phys.* **87**, 4385 (2000).
3. R. A. Ristau, K. Barmak, L. H. Lewis, K. R. Coffey, and J. K. Howard, *J. Appl. Phys.* **86**, 4527 (1999).
4. J. E. Palmer, C. V. Thompson, and H. I. Smith, *J. Appl. Phys.* **63**, 2492 (1987).

Role of Spin Momentum Current in Magnetic Non-Local Damping of Ultrathin Film Structures

G. Woltersdorf, R. Urban, and B. Heinrich

Simon Fraser University, 8888 University Dr., Burnaby, BC, V5A 1S6, Canada

Non-local damping was investigated by Ferromagnetic Resonance (FMR) using ultrathin magnetic single and double layer structures prepared by Molecular Beam Epitaxy (MBE). The double layer structures show magnetic damping which is caused by spin transport across a normal metal spacer (N). In double layer structures a thin Fe layer, F1, was separated from a thick Fe layer, F2, by a Au(001) spacer. The interface magnetic anisotropies separated the FMR fields of F1 and F2 by a big margin allowing one to investigate FMR in F1 while F2 had a negligible angle of precession, and vice versa. The Fe films in magnetic double layers acquire non-local interface Gilbert damping. It will be shown that the precessing magnetic moments act as spin pumps and spin sinks. This concept was tested by investigating the FMR linewidth around an accidental crossover of the resonance fields for the layers F1 and F2. There is another possible mechanism for non-local damping which is based on a "breathing Fermi surface" of the spacer. The temperature dependence of the non-local damping indicates that this mechanism is weak in Au spacers. Surprisingly the Au spacer acts as an additional impedance for the spin pump mechanism. Finally, it will be shown that electron-electron correlations in a Pd spacer can lead to a significant enhancement of the non-local damping.

I. INTRODUCTION

The small lateral dimensions of spintronics devices and high density memory bits require the use of magnetic metallic ultrathin film structures where the magnetic moments across the film thickness are locked together by the intra layer exchange coupling. Since spintronics and high density magnetic recording employ fast magnetization reversal processes it is important to understand the spin dynamics and magnetic relaxation processes of multilayers in the nano-second time regime. The spin dynamics is described by the Landau Lifshitz Gilbert (L.L.G.) equation of motion

$$\frac{1}{\gamma} \frac{\partial \mathbf{M}}{\partial t} = -[\mathbf{M} \times \mathbf{H}_{eff}] + \frac{G}{\gamma^2 M_s^2} \left[\mathbf{M} \times \frac{\partial \mathbf{M}}{\partial t} \right], \quad (1)$$

where γ is the absolute value of the electron gyromagnetic ratio, M_s is the saturation magnetization and G is the Gilbert damping parameter. The effective field \mathbf{H}_{eff} is given by the derivatives of the Gibbs energy, U , with respect to the components (M_x, M_y, M_z) of the magnetization vector $\mathbf{M}(t)$ [1]. The second term in eq. 1 represents the well known Gilbert damping torque.

II. NON-LOCAL DAMPING: EXPERIMENT

The role of non-local damping was investigated in high quality crystalline Au/Fe/Au/Fe(001) structures grown on GaAs(001) substrates, see details in [2-5]. In-plane Ferromagnetic Resonance (FMR) experiments were carried out using 10, 24, 36 and 72 GHz systems [4, 6].

Single Fe ultrathin films with thicknesses of 8, 11, 16, 21, and 31 monolayers (ML) were grown directly on GaAs(001) and covered by a 20 ML thick Au(001) cap layer for protection in ambient conditions. FMR measurements were used to determine the in-plane four-fold and uniaxial magnetic anisotropies, K_1 and K_u , and the effective demagnetizing field perpendicular to the film surface, $4\pi M_{eff}$, as a function of the film thickness d [6]. The magnetic anisotropies were well described by the bulk and interface magnetic properties, respectively [2]. The thin Fe films which were studied in the single layer structures were grown again as a part of magnetic double layer structures. The thin Fe film (F1) was separated from the second thick Fe layer (F2) by a Au(001) spacer (N) of a variable thickness between 8 to 100 ML. The magnetic double layers were covered by a 20 ML Au(001) capping layer. The thickness of the Au spacer layer was always smaller than the electron mean free path (38 nm) [7], and hence allowed ballistic spin transport between the magnetic layers.

The interface magnetic anisotropies separated the FMR fields of F1 and F2 by a big margin (~ 1 kOe), see Fig.1 allowing one to carry out FMR measurements in F1 with F2 possessing a small angle of precession compared to that in F1, and vice versa. The thin Fe film in the single and double layer

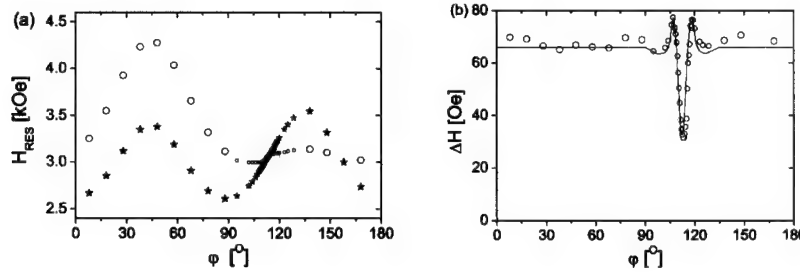


FIG. 1: (a) The FMR fields at 24 GHz in the layer F1(16Fe, shown by (o)) and layer F2(40Fe, (*)) in 20Au/40Fe/16Au/16Fe/GaAs(001) (integers represent the number of atomic layers) as a function of the angle φ between the applied field and the in-plane [100] crystallographic direction. A large in-plane uniaxial anisotropy field in F1 leads to an accidental crossover at $\varphi = 115$ and 150 Deg. Notice that the FMR fields get locked together by the spin pumping effect at the accidental crossover. Away from the crossover the resonance fields are separated by as much as ten FMR linewidths.

(b) The FMR linewidths corresponding to F1 in Fig.1(a). The measured and calculated FMR signals were analyzed using two Lorentzian lineshapes. The Lorentzian peaks were characterized by their amplitudes, resonance fields and linewidths. The solid lines were obtained from calculations using eqs 7. Note that the FMR linewidth for F1 first increases before it reaches its minimum value corresponding to that of a single layer structure.

structures had the same FMR field showing that the static interlayer exchange coupling in the double layer [2] through the Au spacer was negligible. The absence of static interlayer coupling is due to short atomic terraces [1].

The results are as follows: (a) The FMR linewidth in the thin films F1 always increased in the presence of F2, and vice versa; (b) The additional FMR linewidth, ΔH_{add} , followed an inverse dependence on the thin film thickness d_1 , see [2]; and (c) the additional FMR linewidth ΔH_{add} in both the parallel (H in-plane) and perpendicular (H perpendicular to the plane) FMR configuration was linearly dependent on the microwave frequency with no zero frequency offset [5]. The additional Gilbert damping for the 16 ML thick Fe film was found to be only weakly dependent on the crystallographic direction, with the average value $G_{\text{add}} = 1.2 \times 10^8 \text{ s}^{-1}$. This is comparable to the intrinsic Gilbert damping in the single Fe film, $G_{\text{int}} = 1.4 \times 10^8 \text{ s}^{-1}$.

III. THEORY OF NON-LOCAL DAMPING

Tserkovnyak et al. [8] showed that the interface damping can be generated by spin current from a ferromagnet (F) into the adjacent normal metal reservoirs (NM). The spin current is generated by a precessing magnetic moment. A precessing magnetization at the F/NM interface acts as a "peristaltic spin -pump". The direction of the spin current is perpendicular to the F/NM interface and points away from the interface towards NM. The spin momentum which is carried away by the spin current is

$$\mathbf{j}_{\text{spin}} = \frac{\hbar}{4\pi} A_s \mathbf{m} \times \frac{d\mathbf{m}}{dt}, \quad (2)$$

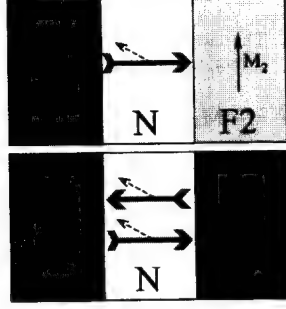


FIG. 2: A cartoon representing the dynamic coupling between two magnetic layers which are separated by a non-magnetic spacer N. (a) represents two magnetic layers with different FMR fields. F1 is at resonance, and F2 is nearly stationary. A large grey arrow in the normal spacer describes the direction of the spin current. The dashed lines represent the instantaneous direction of the spin momentum. For small angle of precession they are nearly parallel to the transverse rf magnetization component shown in short solid arrows. F1 acts as a spin pump, F2 acts as a spin sink. (b) represents a situation when F1 and F2 resonate at the same field. Both layers act as spin pumps and spin sinks. In this case the net spin momentum transfer across each interface is zero. No additional damping is present.

where \mathbf{m} is the a unit vector in direction of \mathbf{M} . The spin current can cause magnetic damping. A_r is the interface scattering parameter, and for F films thicker than spin coherence length, $\pi/(k_F^{\uparrow} - k_F^{\downarrow})$, given by

$$A_r = \frac{1}{2} \sum_{m,n} |r_{mn}^{\uparrow} - r_{mn}^{\downarrow}|^2, \quad (3)$$

where $r_{mn}^{\uparrow,\downarrow}$ are the electron reflection matrix elements at the NM/F interface for the spin up and down electrons. $k_F^{\uparrow,\downarrow}$ are the Fermi k vectors for majority and minority electrons, respectively. The sum in A_r is close to the number of the transverse channels in NM [9]. The sum is given by

$$\frac{A_r}{S} = \frac{k_F^2}{4\pi} = 0.85n^{2/3}, \quad (4)$$

where S is the area of the interface, k_F is the Fermi wavevector and n is the density of electrons per spin in NM [9]. Brataas et al. [9, 10] showed that A_r can be evaluated from the interface mixing conductance $G_{\uparrow\downarrow}$ [11]. $A_r = \frac{\hbar}{e^2} G_{\uparrow\downarrow} = S g_{\uparrow\downarrow}$, where $g_{\uparrow\downarrow}$ represents "dimensionless interface mixing conductivity".

The generated spin current propagates through the normal metal spacer N, and is deposited at the N/F2 interface. It was shown [10, 12] that the transverse component of the spin current in N is entirely absorbed at the N/F2 interface, see Fig.2a. For small precessional angles the spin current is almost entirely transverse. This means that the N/F2 interface acts as an ideal spin sink, and provides an effective spin brake for the precessing magnetic moment in F1 [4, 5, 13]. The spin momentum \mathbf{j}_{spin} which is carried away by the spin current has the form of Gilbert damping. The resulting Gilbert damping is given by the conservation of the total spin momentum

$$\mathbf{j}_{spin} - \frac{1}{\gamma} \frac{\partial \mathbf{M}_{tot}}{\partial t} = 0, \quad (5)$$

where \mathbf{M}_{tot} is the total magnetic moment in F1. After simple algebraical steps one obtains an expression for the dimensionless spin pump contribution to the damping, α_{sp} ,

$$\alpha_{sp} = \frac{G_{sp}}{\gamma M_s} = g\mu_B \frac{g_{\uparrow\downarrow}}{4\pi M_s d_1}, \quad (6)$$

where d_1 is the thickness of F1, g_{11} is the dimensionless mixing conductivity, and G_{sp} is the spin pump Gilbert parameter. g is the electron g -factor. The inverse dependence of α_{sp} on the film thickness clearly testifies to its interfacial origin. The layers F1 and F2 act as mutual spin pumps and spin sinks. For small precessional angles the eq. of motion for F1 can be written as [4]

$$\frac{1}{\gamma} \frac{\partial \mathbf{M}_1}{\partial t} = -[\mathbf{M}_1 \times \mathbf{H}_{eff,1}] + \frac{G_1}{\gamma^2 M_s^2} \left[\mathbf{M}_1 \times \frac{\partial \mathbf{M}_1}{\partial t} \right] + \frac{\hbar}{4\pi d_1} g_{11,1} \mathbf{m}_1 \times \frac{\partial \mathbf{m}_1}{\partial t} - \frac{\hbar}{4\pi d_1} g_{11,2} \mathbf{m}_2 \times \frac{\partial \mathbf{m}_2}{\partial t}, \quad (7)$$

where \mathbf{M}_1 is the magnetization vector of F1, $\mathbf{m}_{1,2}$ are the unit vectors along $\mathbf{M}_{1,2}$, and d_1 is the thicknesses of F1. The exchange of spin currents is a symmetric concept and the eq. of motion for the layer F2 is obtained by interchanging the indices 1 \leftrightarrow 2. The third and fourth terms in eq. 7 represent the spin pump and spin sink of F1. The fourth term is generated by the spin pump from F2. For clarity it is worthwhile to point out that the signs (+) and (-) in the third and fourth terms in eq. 7 represent the spin current directions (F1 \rightarrow F2) and (F2 \rightarrow F1), respectively.

The spin pump model is a rather exotic theory to those who are working in magnetism. One would expect that there is a direct connection to a more common concept which is applicable to magnetic multilayers. The obvious choice is interlayer exchange coupling. In the past interlayer exchange interaction was treated only in the static limit [14]. Recently it was shown that its dynamic part can create magnetic damping [4, 13, 15]. One can show that the spin pumping theory is equivalent to the dynamic response of the interlayer exchange coupling. Since the dynamic coupling is derived from the rf susceptibility one can account for electron-electron correlation effects in the normal metal spacer [13]. It has been shown [15] that the Gilbert damping is enhanced by the square of the Stoner factor $S_E = [1 - UN(E_F)]^{-1}$,

$$G_{s-d}^{enh} = G_{s-d} S_E^2, \quad (8)$$

where U is the screened interatomic Coulomb interaction and $N(E_F)$ the electron density of states, per atom, at the Fermi level in NM.

It is worthwhile to realize that the $s-d$ exchange relaxation mechanism also applies to bulk ferromagnets, and was evaluated by Heinrich et al. [16, 17]. The Gilbert damping in this case is given by

$$G_{s-d}^{bulk} = \frac{\chi_P}{\tau_{sf}}, \quad (9)$$

where χ_P is the Pauli susceptibility and τ_{sf} is the spin flip relaxation time of itinerant electrons in the ferromagnet. It should be noted that $1/\tau_{sf}$ in metals is proportional to the square of the spin orbit interaction [16, 17]. Using χ_P from Kriesman and Callen [18] and τ_{sf} from the spin diffusion length in Current Perpendicular to Plane (CPP) GMR measurements one obtains for the bulk Gilbert damping $G = 5 \times 10^6 \text{s}^{-1}$ and $1 \times 10^8 \text{s}^{-1}$ for Co and permalloy (Py), respectively, see the details in [17]. This contribution is small in Co but it explains the intrinsic damping in Py. Fe is expected to behave like Co.

One expects that there has to be an additional mechanism which depends explicitly on τ_{sf} . Its origin can be understood in the following way. The mechanism of the interlayer exchange coupling lies in the itinerant nature of the electron carriers [13]. The energy of electrons depends on the instantaneous orientation of the magnetic moments, and consequently the occupation number $n_{k,\sigma}$ of electronic states having energy $\varepsilon_{k,\sigma}$ changes during precession of the magnetization, and this results a "breathing Fermi surface", this concept was also used in bulk materials [19, 20]. However, this redistribution cannot be achieved instantaneously. The time lag between the instantaneous exchange field and the induced moment in the spacer is described by the transverse spin relaxation time, τ_{sf} , which is proportional to the momentum relaxation time entering conductivity [21]. In the limit of slow precessional motion the effective damping field can be evaluated [4, 13],

$$\mathbf{H}_{damp}^{int} = \tau_{sf} \sum_{k,\sigma} \delta(\varepsilon_{k,\sigma}[\mathbf{M}_1] - \varepsilon_F) \left(\frac{\partial \varepsilon_{k,\sigma}[\mathbf{M}_1]}{\partial \mathbf{M}_1} \right)^2 \frac{1}{d} \frac{\partial \mathbf{M}_1}{\partial t}, \quad (10)$$

where the sum is carried out per unit area. In this case the damping field is proportional to the spin relaxation time τ_{sf} . This mechanism is explicitly dependent on the conductivity and it represents a different contribution to the non-local damping compared to the spin pumping mechanism which is independent on τ_{sf} .

IV. DISCUSSION OF THE RESULTS

The spin pumping and breathing Fermi surface theories predict Gilbert damping, which results in a strictly linear dependence of ΔH_{add} on the microwave frequency. This is indeed experimentally observed over a wide range of microwave frequencies [3, 4].

The validity of the spin-pumping theory can be tested by comparing calculations using eqs 7 with the experimental results. Fig.2 shows two extreme situations. In Fig. 2(a) the FMR fields in F1 and F2 are separated by a big margin. In Fig.2(b) the FMR fields are same. In (a) one expects the full contribution from the non-local damping. ΔH_{add} for F1 and F2 should scale with their respective $1/d$ terms. In (b) the situation is symmetric; the net spin momentum current through both interfaces is zero, and the additional damping is absent. This behavior is well demonstrated in Fig.1b. The good agreement between theory and experiment clearly shows the validity of the spin pumping and spin sink concept which is described by eqs 7. Even in the absence of static interlayer exchange coupling the magnetic layers are coupled by the dynamic part of the interlayer exchange. The spin sink effect at the N/F interface starts to be inefficient only when the thickness of the normal metal spacer N becomes comparable to the spin diffusion length [22]. Since the resistivity ratio in our structures is a factor of two, see Fig.4 the spin diffusion length in Au is at least of the order of 100 nm. The static interlayer exchange coupling vanishes in our samples due to interface roughness on a length scale of a mere 10 ML (2 nm). One should point out that when the N metal spacer thickness starts to be comparable to the spin diffusion length then the N spacer absorbs a part of the spin current [23, 24].

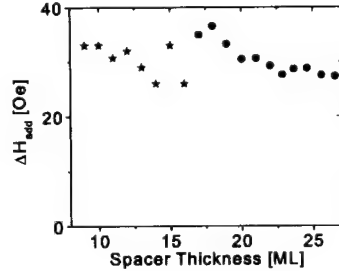


FIG. 3: The additional FMR linewidth, ΔH_{add} , as function of the Au spacer thickness in 20Au/8-27Au/16Fe/GaAs(001). The samples with the Au spacer thickness between 8 to 16ML were grown separately. The samples with the spacer thickness between 17 and 27ML were grown using a wedged Au(001) layer. One can see some degree of variation in ΔH_{add} with a period of ~ 3 ML. These oscillations are marginal.

The quantitative comparison with predictions of the spin pumping theory is very favorable. First principles electron band calculations [11] resulted in $g_{\uparrow\downarrow} \approx 1.11 \times 10^{15} \text{cm}^{-2}$ for a clean Cu/Co(111) interface. By scaling this value to Au using eq.4 one obtains $G_{sp} = 1.37 \times 10^8 \text{s}^{-1}$ which is only 14% higher than the value measured at room temperature. This is surprising agreement considering the fact that calculations of the intrinsic damping in bulk metals have been carried out over the last three decades, and yet they have not been able to produce a comparable agreement with experiments [17].

The breathing Fermi surface contribution to the Gilbert damping is proportional to the electron relaxation time τ_{sf} of the N metal spacer, see eq.10. Since this contribution is using the concept of interlayer exchange coupling one can expect some degree of oscillatory behavior with a changing spacer thickness.

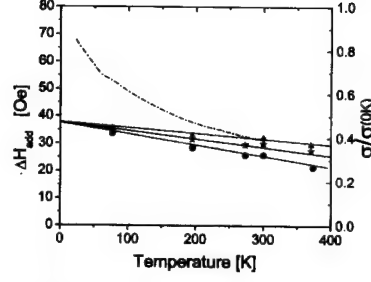


FIG. 4: The temperature dependence of the additional FMR linewidth, ΔH_{add} , for 3 different samples: (▲) 20Au/40Fe/14Au/16Fe/GaAs(001), (★) 20Au/40Fe/40Au/16Fe/GaAs(001), and (●) 20Au/40Fe/100Au/16Fe/GaAs(001). The temperature dependence of the sheet conductivity, σ , for the (●)-sample is shown in the dashed line. Note that the temperature dependence of ΔH_{add} is linear and weak for all samples. One can fit the temperature dependence by eq. 11.

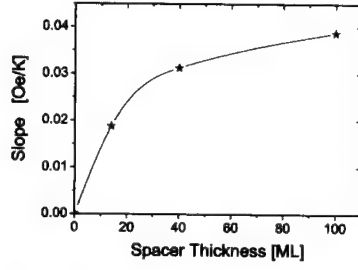


FIG. 5: The slope, $(\partial\Delta H_{add}/\partial T)$, of the additional FMR linewidth, as function of the spacer thickness. The slope was obtained for the samples shown in Fig.4. The solid line is a spline fit to guide the reader's eye.

The measurements shown in Fig. 3 indicate that this behavior is only weakly present. A better test of the breathing Fermi surface contribution can be carried out by measuring the temperature dependence of the non-local damping. One expects proportionality with the sheet conductance ($\tau_{sf} \sim \tau_{orb} \sim \sigma$) of the N spacer. The temperature dependence of the sheet conductance and the additional FMR linewidth is shown in Fig. 4. The temperature dependence of ΔH_{add} is linear and obviously does not scale with the conductivity. This clearly indicates that the strength of the breathing Fermi surface contribution is unimportant in the Fe/Au/Fe(001) samples. Note, that the slope of ΔH_{add} as a function of temperature increases with an increasing spacer thickness. One can fit the temperature dependence by the linear function

$$\Delta H_{add} = \text{Slope} \cdot T + \Delta H_{add}(T = 0 \text{ K}). \quad (11)$$

Note, that $\Delta H_{add}(T = 0 \text{ K})$ is equal for all measured Au spacers. Fig. 5 shows the fitted slope as function of the spacer thickness. One can see that the slope saturates for higher spacer thicknesses. This implies that a part of the Au spacers at finite temperatures decreases effectiveness of the spin pump mechanism and acts as an additional resistance in series with the interface mixing resistance $1/g_{T1}$. This decreases the spin current reaching the N/F2 interface. The additional resistance in Au decreases with decreasing temperature and becomes zero for $T = 0 \text{ K}$. Since the spin diffusion length in Au is much bigger than the Au spacer thickness no additional resistance in Au is expected. The linear temperature dependence of $\Delta H_{add}(T)$ can be indicative that the Au resistance follows the temperature dependence of inverse

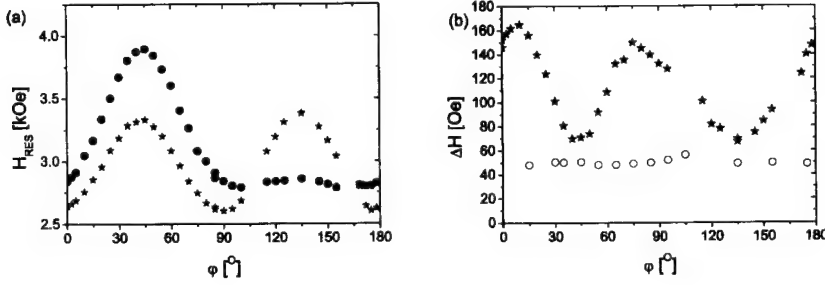


FIG. 6: (a) The FMR fields of the two Fe layers in the GaAs/16Fe/9Pd/40Au/40Fe/20Au(001) sample. (●) and (★) correspond to 16Fe and 40Fe, respectively. The measurements were carried out at 24GHz. (b) shows the FMR linewidth for 16Fe in single [GaAs/16Fe/9Pd/20Au(001)] (○), and double layer [GaAs/16Fe/9Pd/40Au/40Fe/20Au(001)] (●) sample. We did not analyze the FMR data around the accidental crossover of resonance fields at 110 and 165 degrees, respectively. Around these points the two FMR peaks resulted in a broad and asymmetric spectrum not allowing one to carry out a reliable analysis.

susceptibility ($1/\chi \sim T$) of "loose spins" [1, 25]. The impurity Fe atoms (loose spins) can be interdiffused up to certain depth (see saturation of this effect with increasing Au spacer thickness in Fig. 3) around the F1/N interface by surfactant Arsenic during the deposition of Au on F1 [7]. Using this picture one can argue that the temperature dependence of $\Delta H_{\text{add}}(T)$ in Fig. 3 could be a consequence of "loose spins" which contribute to the impedance of the spin pumping mechanism. It is worthwhile to note that the measured value of $G_{\text{sp}} = 1.4 \times 10^8 \text{ s}^{-1}$ at $T = 0 \text{ K}$ is very close to that estimated from the spin pumping theory, $G_{\text{sp}} = 1.37 \times 10^8 \text{ s}^{-1}$.

The dynamic exchange coupling theory [13], includes the Stoner enhancement factor, see eq.8. Our recent results using 20Au/4Pd/[Fe/Pd]₅/14Fe/GaAs(001) single and 20Au/40Fe/40Au/4Pd/[Fe/Pd]₅/14Fe/GaAs(001) double layer samples, see [13], show a strong evidence for the Stoner enhancement factor. This structure incorporates a magnetic [Fe/Pd]₅ superlattice with 5 repetitions of a [1Fe/1Pd] unit cell. The N metal spacer is 4Pd40Au(001). The additional FMR linewidth along the cubic crystallographic axes was enhanced by as much as a factor of four, see [4, 13] and is significantly bigger than that expected from the simple spin pumping mechanism. It turns out that one can get the same enhancement in non-local damping using a simple GaAs/16Fe/9Pd/40Au/40Fe/20Au(001) double layer structure, see Fig. 6 where the [Fe/Pd]₅ superlattice is replaced by 5 atomic layers of Pd. In this case the single layer structure is GaAs/16Fe/9Pd/20Au(001) and shows no enhanced damping, see Fig. 6. The metallic Pd is known to exhibit a strong Stoner enhancement in the dc susceptibility [26]. The Fermi surface of Pd is not spherical and can lead to a significant angular dependence of the Stoner enhancement factor which satisfies the (001) symmetry of our samples, see Fig. 6. These results clearly show that electron correlation effects in normal metal spacers have to be considered.

V. CONCLUSIONS

We have shown that non-local damping by the transfer of spin momentum can be realized in magnetic multilayer films. This effect is significant in ultrathin films. Theoretical models were presented for the non-local damping. It has been demonstrated that the non-local interface Gilbert damping in magnetic multilayers is well described by the concept of spin pumps and spin sinks. It has been shown that this effect is directly related to the dynamics of the interlayer exchange coupling. By proper engineering of multilayer structures one can create magnetic damping which significantly surpasses that in the bulk materials.

The Authors thank Y. Tserkovnyak, A. Brataas, G.E.W. Bauer, J. F. Cochran, D. Riemann, E. Rozenberg, and K. Myrtle for their assistance and valuable discussions during the course of this work. Financial support from the Natural Sciences and Engineering Research Council of Canada (NSERC) and Canadian Institute for Advanced Research (CIAR) is gratefully acknowledged. G.W. thanks the German Academic Exchange Service (DAAD) for generous financial support.

- [1] B. Heinrich and J. F. Cochran, *Adv. Phys.* **42**, 523 (1993).
- [2] R. Urban, G. Woltersdorf, and B. Heinrich, *Phys. Rev. Lett.* **87**, 217204 (2001).
- [3] B. Heinrich, R. Urban, and G. Woltersdorf, *IEEE Trans. Mag.* **38**, 2496 (2002).
- [4] B. Heinrich, G. Woltersdorf, R. Urban, and E. Simanek, Conference on Mag. Mag. Mat., Tampa, Florida, 2002, *J. Appl. Phys.* (submitted).
- [5] B. Heinrich, R. Urban, and G. Woltersdorf, *J. Appl. Phys.* **91**, 7523 (2002).
- [6] B. Heinrich and J. A. C. Bland, *Ultrathin Magnetic Structures II*. (Springer-Verlag, 1994), section Radio Frequency Techniques.
- [7] A. Enders, T. Monchesky, K. Myrtle, R. Urban, B. Heinrich, J. Kirschner, X.-G. Zhang, and W. Butler, *J. Appl. Phys.* **89**, 7110 (2001).
- [8] Y. Tserkovnyak, A. Brataas, and G. Bauer, *Phys. Rev. Lett.* **88**, 117601 (2002).
- [9] A. Brataas, Y. Tserkovnyak, G. Bauer, and B. Halperin, *Phys. Rev. B* **66**, id060404 (2002).
- [10] A. Brataas, Y. Nazarov, and G. Bauer, *Erp. Phys. J. B* **22**, 99 (2001).
- [11] K. Xia, P. Kelly, G. Bauer, A. Brataas, and I. Turek, *Phys. Rev. B* **65**, 220401 (R) (2002).
- [12] M. Stiles and A. Zangwill, *J. Appl. Phys.* **91**, 6812 (2002).
- [13] B. Heinrich, G. Woltersdorf, R. Urban, and E. Simanek, Moscow International Symposium on Magnetism, Moscow 2002, *J. Mag. Mag. Mat.* (in press).
- [14] J. Slonczewski, *J. Mag. Mag. Mater.* **126**, 374 (1993).
- [15] E. Simanek and B. Heinrich, *arXiv:cond-mat/0207471* (2002).
- [16] B. Heinrich, D. Praitová, and V. Kamberský, *Phys. Stat. Sol.* **23**, 501 (1967).
- [17] B. Heinrich and J. A. C. Bland, *Ultrathin Magnetic Structures III* (Springer Verlag, 2003), chap. B. Heinrich on Spin Relaxations in Magnetic Metallic Layers and Multilayers.
- [18] C. Kriesman and H. Callen, *Phys. Rev.* **94**, 837 (1954).
- [19] V. Korenman and R. Prange, *Phys. Rev. B* **6**, 2769 (1972).
- [20] V. Kamberský, *Can. J. Phys.* **48**, 2906 (1970).
- [21] R. J. Elliot, *Phys. Rev.* **96**, 266 (1954).
- [22] R. Silsbee, A. Janossy, and P. Monod, *Phys. Rev. B* **19**, 4382 (1979).
- [23] S. Mizukami, Y. Ando, and T. Miyazaki, *J. Mag. Mag. Mat.* **226**, 1640 (2001).
- [24] R. Urban, G. Woltersdorf, and B. Heinrich, *J. Appl. Phys.* (submitted).
- [25] J. Slonczewski, *J. Appl. Phys.* **73**, 5957 (1993).
- [26] M. Brodsky and A. Freeman, *Phys. Rev. Lett.* **45**, 133 (1980).

Study of the Low Field Microwave Response in Yttrium Aluminates Dilutely Doped with Manganese

Rakhim R. Rakhimov, David E. Jones, and George B. Loutts.

Center for Materials Research, Norfolk State University, Norfolk, VA 23504, U.S.A

ABSTRACT

Microwave response near zero magnetic field was observed in YAlO_3 and CaYAlO_4 crystals dilutely doped with Mn in concentration ranging from 0.05 to 2 atomic %. The response is due to non-resonant microwave absorption, which co-exists with normal electron paramagnetic resonance (EPR) absorption due to different paramagnetic valence states of manganese. Mn^{2+} and Mn^{4+} charge states were identified in Mn-doped YAlO_3 , and Mn^{2+} , Mn^{4+} and Mn^{5+} in Mn-doped CaYAlO_4 . The low field response has the opposite phase with respect to the paramagnetic absorption. This shows that Mn-doped YAlO_3 and CaYAlO_4 exhibit magnetically induced microwave absorption, which has a minimum at zero magnetic field and increases with the applied magnetic field. This effect is similar to microwave magneto-resistance effects observed in manganite perovskites, where spin-dependent electron tunneling occurs between ferromagnetically coupled manganese ions in different valence states. We show, however, that in the present case of diluted paramagnetic systems, magneto-induced microwave losses are due to intramolecular spin-dependent tunneling, where central paramagnetic ion does not change its charge state and spin-dependent charge migration occurs in the first coordination sphere of paramagnetic ion. Evidences are presented that this ion is Mn^{2+} exhibiting the highest electron spin $S = 5/2$.

INTRODUCTION

Recent discoveries of manganese based single molecular magnets, exhibiting magnetization tunneling, inspire the search for manganese doped insulating materials, where similar spin-dependent tunneling may occur within paramagnetic dopant ion and be accompanied by charge displacement current. Since the displacement current is one of the sources of microwave losses in materials, the search for spin-dependent tunneling in insulating materials can be realized through the investigation of their microwave dielectric properties.

Study of microwave dielectric properties of rare-earth aluminates is of interest for their potential applications as dielectric resonators and substrates for high temperature superconductors (HTSC) [1]. In particular, yttrium orthoaluminate YAlO_3 was suggested as a substrate material for microstrip antennas utilizing HTSC thin films [1]. Study of the mechanism of the charge carrier mobility is important in understanding of unique dielectric properties of insulators like rare-earth aluminates. YAlO_3 doped with manganese has been shown to be a potential material for holographic and data storage [2]. The high holographic recording efficiency in Mn-doped YAlO_3 may imply non-centrosymmetric charge distribution. Then microwave properties associated with charge displacement current can be expected in the crystal.

Microwave losses associated with spin-dependent tunneling can be measured by means of microwave response with the applied magnetic field, as it was demonstrated, for example, in manganites [3, 4]. Changes in electron transport characteristics of materials in external magnetic

fields are of great fundamental and practical interests. Externally applied magnetic field may dramatically change properties of the materials from insulators to conductors, for example in manganite perovskites [5-7]. The large magneto-resistance effect in manganite perovskites is presently explained by the enhanced electron hopping migration occurring via double-exchange mechanism in mixed valence Mn^{3+} -O- Mn^{4+} structures and additional magnetic coupling energy that provides ferromagnetism [5]. Thus, magneto-resistance effects are usually considered in materials containing highly concentrated transition metals, as a result of coupling between metal ions in different valence states. Accordingly, microwave magneto-resistance effects have been studied so far in materials containing transition metals as major components.

The purpose of this study is to show that microwave magneto-resistance effects may occur in an insulator dilutely doped with a transition metal. Since there is no possibility for ferromagnetic coupling between largely separated dopant ions, the spin-dependent transport may take place only within a coordination sphere of the paramagnetic dopant ion. In this paper we present the observation of microwave losses induced by low magnetic field in Mn-doped $YAlO_3$ and $CaYAlO_4$.

EXPERIMENTAL DETAILS

Mn-doped $YAlO_3$ and $CaYAlO_4$ crystals were grown by the Czochralski technique in an iridium crucible under nitrogen ambient atmosphere with up to 0.5% of oxygen. 99.999% purity chemicals were used. Manganese in $Mn:YAlO_3$ was introduced in the melt at 0.05 and 0.5 atomic % (with respect to Al) in the form of MnO_2 . The crystals were pulled along the c direction of the orthorhombic unit cell. The pull rate was maintained at 1.5 mm/h and the rotation rate at 15 rpm. In order to alter manganese valence state, three $Mn:YAlO_3$ crystals were co-doped with cerium in the concentration of 0.05, 0.1 and 0.5% and one crystal was co-doped with cerium and calcium (both dopant concentrations of 0.5%). Cerium and calcium were added in the melt as CeO_2 and $CaCO_3$, respectively. Manganese in $Mn:CaYAlO_4$ was introduced in the melt at 0.1, 0.5 and 2.0% in the form of MnO_2 .

Electron paramagnetic resonance (EPR) spectra and microwave losses (non-resonant microwave absorption) of the crystals were recorded by Bruker EMX spectrometer operating at ~9.6 GHz. EPR spectra were recorded at 77 K in liquid nitrogen and in the temperature range 90-300 K using Bruker BVT 3000 liquid nitrogen temperature control system

DISCUSSION

Low field microwave response and EPR of Mn-doped $YAlO_3$

Single crystal and powder sample EPR spectra of $Mn:YAlO_3$ were studied in Ref. [8]. Two paramagnetic charge states of manganese, Mn^{2+} (total electron spin $S = 5/2$) and Mn^{4+} ($S = 3/2$) were identified. Comparison of the ionic radii of dopants and host cations, as well as optical spectroscopic studies [2, 9, 10] show that Mn^{2+} and Mn^{4+} are located in yttrium and aluminum sites, respectively. In this part of the paper we discuss the observation of a new sharp line centered at zero magnetic field in addition to previously observed EPR signal. We have observed this line by sweeping magnetic field through the zero value (zero field crossing) and using considerably higher values of microwave irradiation power (figure 1). As it can be seen from figure 1, the sharp zero field signal has the opposite phase relative to paramagnetic

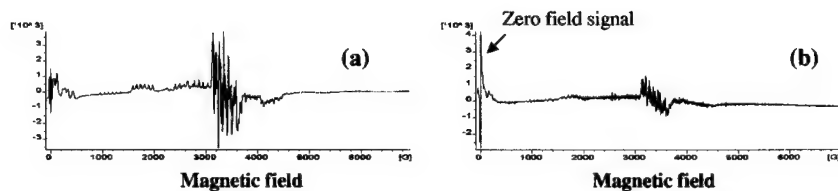


Figure 1. Polycrystalline EPR spectra of 0.5%Mn:YAlO₃ recorded at 77 K and different values of microwave power: (a) $P = 2$ mW, (b) $P = 200$ mW.

absorption due to Mn^{2+} and Mn^{4+} . It means that the low field microwave absorption is a minimum at zero field and rapidly increases with the applied magnetic field. This feature of the low field response is similar to the non-resonant microwave absorption commonly observed in HTSC materials, where this absorption may co-exist with normal paramagnetic absorption due to paramagnetic ions.

The following experimental observations further distinguish the zero field microwave response from the resonant paramagnetic absorption. Figure 2 shows the dependence of the signal line amplitudes of the different parts of the overall EPR spectrum upon microwave power and temperature. At 295 K (figure 2, a) with the microwave power P ranging from 0 to 200 mW the zero field signal does not saturate in contrast to the rest of the overall EPR signal, which is a superposition of paramagnetic absorption due to Mn^{2+} and Mn^{4+} . The saturation curve for Mn^{2+} goes through a maximum and then the Mn^{2+} signal decreases at higher microwave power, which is a characteristic of the homogeneously broadened line [11]. The saturation curve for Mn^{4+} shows that its paramagnetic absorption is characterized by inhomogeneously broadened line [11], which can be explained by a slight distribution of spin Hamiltonian parameters for Mn^{4+} . At 77 K the saturation curve for Mn^{4+} signal retains its form of a plateau as it does at 295 K. In the case of Mn^{2+} , the paramagnetic signal rapidly reaches its maximum with increasing the microwave power, and is significantly suppressed down to 20% of the maximal value (figure 2, b). Such significant drop of the Mn^{2+} paramagnetic signal also causes the decrease in the intensity of the zero field response. This implies that the low field microwave absorption is correlated with spin polarization of Mn^{2+} .

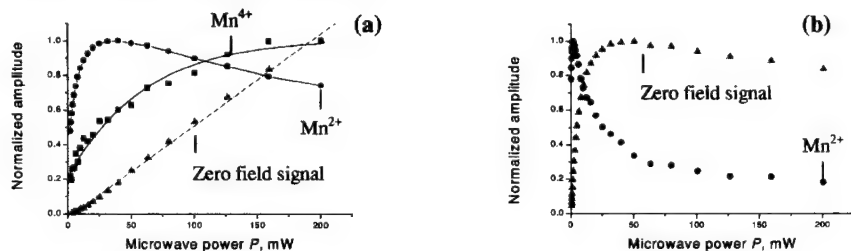


Figure 2. The effect of microwave power P on the EPR and zero field signal amplitudes in 0.5%Mn:YAlO₃ at 295 K (a) and 77 K (b).

It was shown in Ref. [8] that co-doping of the YAlO_3 crystal with Ce decreases the amount of Mn^{4+} due to its reduction to Mn^{3+} and results in the disappearance of the Mn^{4+} EPR spectrum. In this crystal we further found that both Mn^{2+} EPR signal and low field response are not affected by the presence of Ce. Co-doping of the YAlO_3 crystal with Ca simultaneously increases the EPR signal due to Mn^{2+} ion and the low field microwave response.

Therefore the above data show that the low field microwave response is related to the Mn^{2+} ion, although the response cannot be described as a paramagnetic signal.

Low field microwave response and EPR of Mn-doped CaYAlO_4

In the crystal structure of CaYAlO_4 [12], aluminum ions are octahedrally coordinated by oxygen atoms. Calcium and yttrium ions are statistically distributed in lattice positions surrounded by nine oxygen atoms. EPR spectra of Mn-doped CaYAlO_4 crystals are shown in figure. 3. The reversed phase microwave response centered at zero magnetic field is observed in addition to the normal EPR spectrum with five spectral components (marked with vertical arrows in figure 3, b) of the fine structure due to Mn^{2+} ($S = 5/2$) and some weaker components of the fine structure due to Mn^{4+} ($S = 3/2$). The latter is distinguishable only by the low field part of the three-component fine structure in the EPR spectrum of Mn^{4+} . This feature of the EPR spectrum of Mn^{4+} in CaYAlO_4 is similar to that observed for the Mn^{4+} ion in YAlO_3 [8] and implies that Mn^{4+} occupies octahedral aluminum site. In the case of CaYAlO_4 , the EPR spectra show that manganese is predominantly present in the form of Mn^{2+} and, apparently, occupies the Ca^{2+} site with no need for the charge compensation. The orientation dependence of the position of fine structure components of the Mn^{2+} ion, obtained by the two-axis rotation of the crystal in the external magnetic field, is consistent with the tetragonal lattice symmetry of the CaYAlO_4 crystal [12]. The central component of the fine structure is related to the spin $-1/2 \leftrightarrow +1/2$ transition and less sensitive to the crystal orientation. It has a distinct six line hyperfine structure due to interaction of the unpaired electron with the ^{55}Mn nucleus (nuclear spin $I = 5/2$). The other components of the Mn^{2+} fine structure exhibit sufficient broadening due to the distribution of zero field splitting parameters, which is the result of the distribution of the crystal field in the disordered Ca^{2+} site in CaYAlO_4 .

Compared to $\text{Mn}:\text{YAlO}_3$ crystals, the low field microwave response in $\text{Mn}:\text{CaYAlO}_4$ is detectable at higher temperatures and lower values of microwave power. Since at the same doping level of manganese in both crystals the amount of Mn^{2+} ions in $\text{Mn}:\text{CaYAlO}_4$ is much greater than in $\text{Mn}:\text{YAlO}_3$, we can conclude that the low field microwave response is due to Mn^{2+} . Moreover, the shape of the low field microwave response is identical in both crystals, although the zero field splitting parameters for Mn^{2+} are different by an order of magnitude.

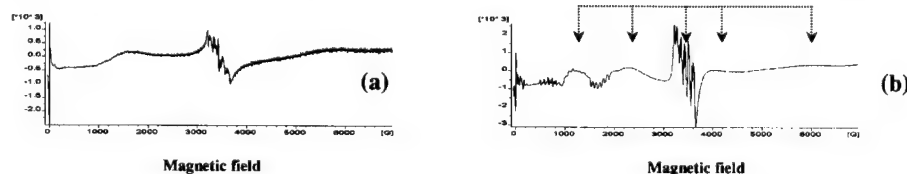


Figure 3. EPR spectra of 0.5% $\text{Mn}:\text{CaYAlO}_4$ recorded at 77 K and $P = 200$ mW for polycrystalline sample (a), and single crystal (b). The single crystal was oriented such that c and a crystal axes were respectively perpendicular and parallel to the external static magnetic field.

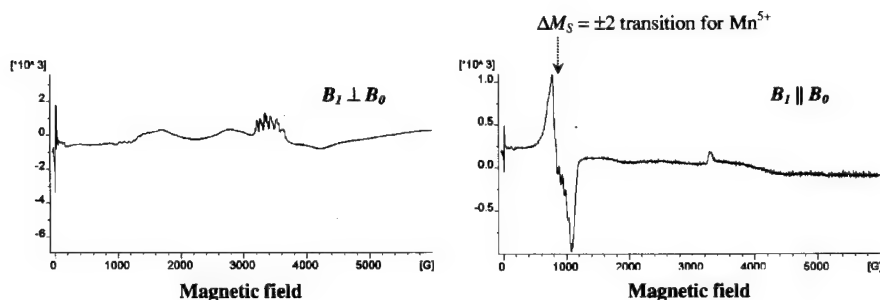


Figure 4. Single crystal EPR spectra of 0.5%Mn:CaYAlO₄ recorded at 90 K, $P = 200$ mW with normal ($B_1 \perp B_0$) and parallel ($B_1 \parallel B_0$) polarization of microwave field. Crystal orientation was as follows: $c \perp B_0$, $a \wedge B_0 = 40^\circ$.

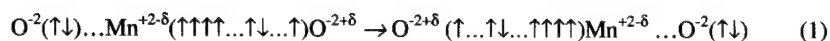
In figure 4, we compare single crystal EPR spectra of Mn-doped CaYAlO₄ that were recorded using normal polarization ($B_1 \perp B_0$) of the magnetic component of microwave B_1 with respect to static external magnetic field B_0 , and parallel polarization ($B_1 \parallel B_0$). Normal polarization detects allowed $\Delta M_S = \pm 1$ spin transitions. These transitions are not usually seen for manganese charge states with integer electron spin, e.g. Mn³⁺ ($S = 2$) and Mn⁵⁺ ($S = 1$), while in some cases these ions can be identified by parallel polarization that detects “forbidden” $\Delta M_S = \pm 2$ transitions. We observed this transition (figure 4) in Mn-doped CaYAlO₄ single crystal. The crystal orientation dependence analysis of this transition shows that it is due to Mn⁵⁺.

Experimental details and results on EPR of Mn⁵⁺ in CaYAlO₄ will be reported elsewhere. However, at this stage of our discussion we refer to figure 4 and note that the low field microwave response (zero field signal) is not sensitive to mutual orientations of microwave and static magnetic fields as much as resonant paramagnetic absorption. This finding confirms the non-resonant nature of the low field microwave absorption.

Model of spin-dependent charge migration in the vicinity of Mn²⁺ as a source of magnetically induced microwave losses

The presence of non-resonant absorption in YAlO₃ and CaYAlO₄ with the concentration of Mn as low as 0.1% does not allow assumptions about ferromagnetic or exchange coupling between manganese ions with different charge states, that were used for explanation of magnetoresistance in manganite perovskites [5-7]. Therefore, the observed effect cannot be related to changes in d.c. conductivity of the yttrium aluminates, but should be considered as the enhancement of microwave dielectric losses associated with charge displacement current.

Based on local non-centrosymmetric environment of Mn ions in YAlO₃ [2], we assume that coordination sphere of Mn²⁺ ion is characterized by a non-zero electric dipole moment due to partially covalent bond, Mn^{2+δ}-O^{-2+δ}, between manganese and one of the oxygen atoms in its coordination sphere. If the external magnetic field is applied, it will reduce fluctuation of unpaired electron spins and align them in one direction, so that electron can tunnel from one oxygen atom to another without the change of the total spin of the system,



In this case the dielectric loss will increase due to the additional tunneling migration of the charge $+\delta$. This additional transfer mechanism exists via p - d exchange type integral between Mn and O atoms described by Anderson and Hasegawa [13]. Further studies on the low field microwave absorption in diluted paramagnetic systems will be performed in near future to develop a quantitative model of spin-dependent tunneling (1).

CONCLUSIONS

We have observed magneto-induced non-resonant microwave absorption caused by dilutely dissolved paramagnetic manganese ions in insulating YAlO_3 and CaYAlO_4 crystals. This phenomenon is described in terms of spin-dependent dielectric loss or microwave magneto-resistance that derives from the tunneling charge migration between oxygen atoms via the Mn^{2+} ion exhibiting the highest effective electron spin $S = 5/2$. The spin-dependent tunneling described in the present work results in a distinct, detectable response in the low magnetic field region, which makes Mn-doped insulating yttrium aluminates potential materials for spin electronics.

ACKNOWLEDGEMENTS

This research was supported jointly by the Virginia's Center for Innovative Technologies (CIT) and Defense Advanced Research Projects Agency (DARPA) under CIT award No. ELC-02-006. The support from the National Science Foundation (NSF CREST project, cooperative agreement No. HRD-9805059) is also acknowledged.

REFERENCES

1. S.-Y. Cho, I.-T. Kim, and K. S. Hong, *J. Mater. Res.* **14**, 114 (1999).
2. G. B. Loutts, M. Warren, L. Taylor, R. R. Rakhimov, H. R. Ries, G. Miller, M. A. Noginov, M. Curley, N. Noginova, N. Kukhtarev, H. J. Caulfield, and P. Venkateswarlu, *Phys. Rev. B*, **57**, 3706 (1998).
3. S. E. Lofland, S. M. Bhagat, S. D. Tyagi, Y. M. Mukovskii, S. G. Karabashev, and A. M. Balbashov, *J. Appl. Phys.* **80**, 3592 (1996).
4. V. V. Srinivasu, S. E. Lofland, and S. M. Bhagat, *J. Appl. Phys.* **83**, 2866 (1998).
5. R. von Helmholt, J. Wecker, B. Holzapfel, L. Schultz, and K. Samwer, *Phys. Rev. Lett.* **71**, 2331 (1993).
6. K. Chahara, T. Ohno, M. Kasai, and Y. Kozono, *Appl. Phys. Lett.* **63**, 1990 (1993).
7. H. Y. Hwang, S.-W. Cheong, N. P. Ong, and B. Batlogg, *Phys. Rev. Lett.* **77**, 2041 (1996).
8. R. R. Rakhimov, A. L. Wilkerson, G. B. Loutts, M. A. Noginov, N. Noginova, W. Lindsay, and H. R. Ries, *Solid State Commun.*, **108**, 549 (1998).
9. M. A. Noginov, and G.B. Loutts, *J. Opt. Soc. Am. B*, **16**, 3 (1999).
10. M. A. Noginov, G.B. Loutts, and M. Warren, *J. Opt. Soc. Am. B*, **16**, 475 (1999).
11. Weil, J. A.; Bolton, J. R.; Wertz, J. E. *Electron Paramagnetic Resonance: Elementary Theory and Practical Applications*, John Wiley & Sons: New York, 1994.
12. C. F. Woensdregt, H. W. M. Janssen, A. Gloubokov, and A. Pajaczowska, *J. Cryst. Growth*, **171**, 392 (1997).
13. P. W. Anderson, and H. Hasegawa, *Phys. Rev.* **100**, 675 (1955).

Domain Wall Magnetoresistance and Complex magnetic Response in Antiferromagnetically Coupled Fe/Cr MultilayersF.G.Aliev¹, R.Villar¹, R.Schad² and J.L.Martinez³

(1) Dpto. de Física de la Materia Condensada, C-III, Universidad Autónoma de Madrid, 28049, Madrid, Spain

(2) CMIT, University of Alabama, Tuscaloosa, USA

(3) Instituto de Ciencia de Materiales Madrid, CSIC, Cantoblanco, 28049, Madrid, Spain

Abstract

For antiferromagnetically coupled Fe/Cr(100) multilayers the low field contribution to the resistivity, which is caused by the domain walls (DWs), is strongly enhanced at low temperatures. The low temperature resistivity increases approximately according to a power law with the exponent 0.7-1. This behaviour can be explained by the suppression of anti-localization effects by the nonuniform gauge fields caused by the domain walls. Analyses of complex low frequency magnetic susceptibility shows an enhancement of the magnetic losses at low magnetic fields, which may be related to the AC field induced DWs movement. At low temperatures ($T < 100\text{K}$) DWs become pinned. For frequencies ($10^2 < f < 10^3$) Hz at temperatures below 10K, this hysteretic low field peak in the magnetic losses transforms to a non-hysteretic dip for $|H| < 20$ Oe, indicating a possible qualitative change in the dynamics of the DWs. The frequency dependence of the dissipation at 2K, may be reasonably well fitted by the expression that describes the losses of a damped oscillator with a single relaxation time of about 10^{-4} sec.

Introduction

Influence of the domain walls and, in general, non-uniform magnetic fields (in the following-DWs) on the electron transport and low frequency- low field magnetic dynamics are related physical properties of magnetoelectronic devices. Their knowledge is essential both for fundamental physics [1] and possible applications. Although the number of DWs was controlled and directly observed in Fe [3] and in Co films [4] at room temperature, where DW formation is relatively well understood, no clear picture has emerged allowing to explain the results. The anisotropic magnetoresistance (AMR) dominates the low field magnetoresistance and complicates the extraction of the true DW contribution to the resistivity [5]. In order to minimize the AMR contribution, thin films with reduced magnetization and special DW configuration have been studied [6]. Apart from the ballistic contribution to the DW magnetoresistance [7], quantum interference also affects the electron transport through DWs [8,9].

Antiferromagnetically (AF) coupled magnetic multilayers (MMLs) are systems with reduced magnetization and consequently a strongly suppressed AMR. At high temperatures, weak pinning of the DWs in the MMLs may reduce DW magnetoresistance. For fixed magnetic field the DW magnetoresistance may then emerge only at sufficiently low temperatures where DWs become strongly pinned and their configuration is not affected by thermal fluctuations or by the applied electric current. In this situation, a combined study of static and dynamic properties, complemented by electron transport investigation, may give important new

information about properties of MMLs, practically unexplored up to now in the magnetic field region where formation and propagation of DWs is expected. In this paper we report on a detailed study of the DC magnetization, ac magnetic susceptibility and low field-low temperature magnetoresistance of antiferromagnetically coupled $[\text{Fe}/\text{Cr}(100)]_{10}$ multilayers at different frequencies below 10^4Hz , magnetic fields below 300 Oe and at temperatures down to 2K. Experimental details about sample grows and measurement techniques may be found in [10,11].

Magnetic losses in Fe/Cr multilayers

The main part in Figure 1 expands the low field dependence of the imaginary (in semi- logarithmic scale) contribution of the magnetic susceptibility in $[\text{Fe}(30\text{\AA})/\text{Cr}(13\text{\AA})]_{10}$ MML measured at 300, 20 and 5K. Detailed comparison of the real and imaginary response may be found in [10]. At high temperatures ($T > 100\text{K}$), independently of the applied ac drive field ($\text{acdf} = 2-8\text{ Oe}$), both real (χ') and imaginary (χ'') contributions to magnetic susceptibility show hysteretic dependence on the magnetic field with the maxima of the losses at $H < 30\text{ Oe}$. The observed maxima can be naturally explained by the formation of small-scale magnetic

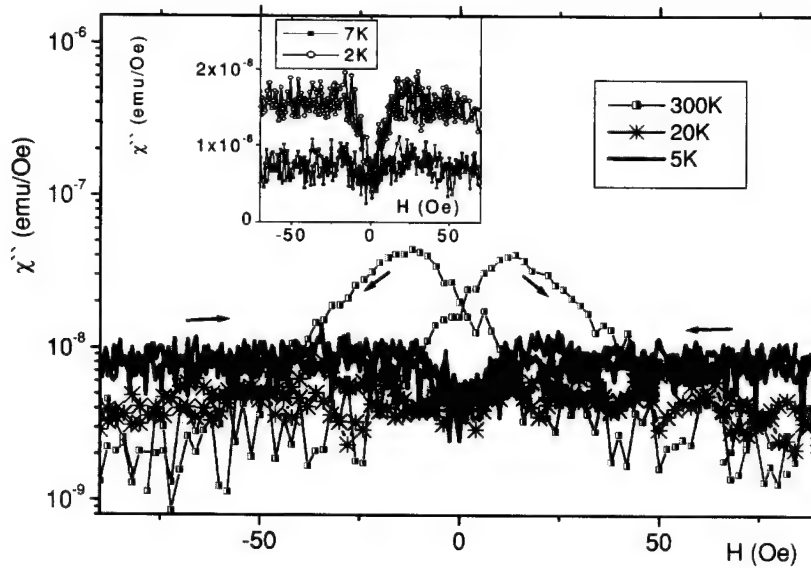


Figure 1. Imaginary contributions to the magnetic susceptibility of a $[\text{Fe}(30\text{\AA})/\text{Cr}(13\text{\AA})]_{10}$ multilayer measured at 987 Hz with $\text{acdf}=4\text{ Oe}$ and at 3 different temperatures. The insert shows the out of phase contributions to the magnetic susceptibility of $[\text{Fe}(30\text{\AA})/\text{Cr}(13\text{\AA})]_{10}$ multilayer measured at 987 Hz with $\text{acdf}=4\text{ Oe}$ and at temperatures 2 and 7K. Orientation of the magnetic field is along (110).

structures repeatedly observed in MML. Presence of the domain structure for the same sample was demonstrated by using magnetic force microscopy [11,12].

More interesting is the dependence of the losses on temperature variations. We refer here to the hysteretic maximum in losses in low magnetic fields. Lowering the temperature from 300K to about 10K, the losses show weak maximum at about 250K and then strongly decrease below about 100K (see Figure 1). Below 10K we do not observe any hysteretic maximum. Interestingly, at lower temperatures the losses begin to increase (see inset). The losses at fixed field and 5K are higher than at corresponding losses 300K (beyond the maxima observed at the latter temperature). At 2K they are even higher. The character of the dependence of the losses on the magnetic field changes as well. One more remarkable feature is an appearance at lower temperatures ($T < 7K$) of a minimum in the magnetic losses at $H=0$ (see inset to Figure 1). The frequency dependence of χ'' proves to be very surprising. We studied the frequency dependence of χ'' at $T=2K$ and $T=10K$. At higher temperatures the out-of-phase susceptibility is too small to investigate its frequency dependence. The main surprise is that it exhibits a well pronounced frequency dependence at $T=2K$ ($H=50Oe$) and this dependence may be reasonably fitted by the single relaxation time formula $\chi'' = \chi_0 \omega \tau / [1 + (\omega \tau)^2]$ with $\tau \approx 2.5 \cdot 10^{-4}$ s (see Fig.2).

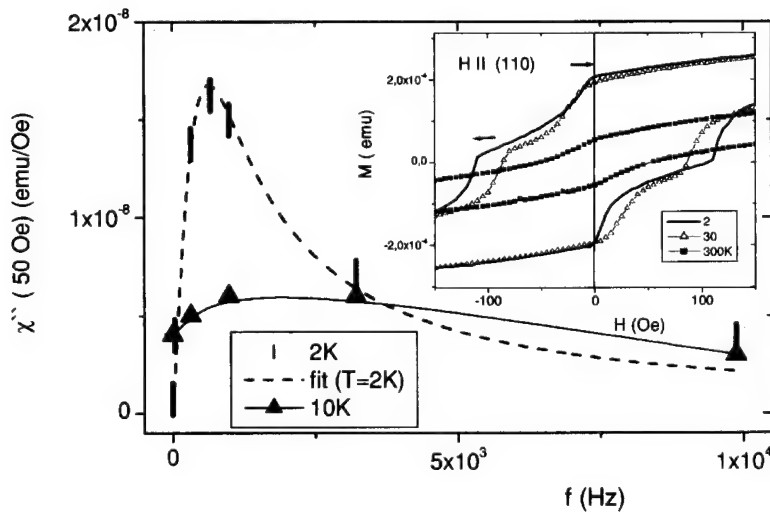


Fig.2 Frequency dependence of the dissipation at small nonzero magnetic field ($H=50$ Oe) at temperatures $T=2K$ and 10 K. The dashed line represents the fit described in the main text. Inset: magnetization vs. magnetic field for magnetic field along (110). Arrows show direction of the displacement of 2 kinks when temperatures are lowered.

One normally expects the response of domain structures to be characterized by a broad distribution of the relaxation times with χ'' almost independent of frequency. This seems to be the case for higher temperatures: the frequency dependence of χ'' at $T=10\text{K}$ is nearly nonexistent with a much broader maximum shifted to higher frequencies. Note that in the frequency range studied the real part of the susceptibility is, within a margin of 20 percent, independent of f when the frequency is varied between 3Hz and 9876 Hz. Dependence of χ'' on the magnetic field may be explained by the model of a single relaxation time [10].

In order to investigate the relationship between the observed effects and the degree of antiferromagnetic coupling, we measured χ' and χ'' for the samples with different GMR between 16% and 220% [10]. We found that low temperature dependences χ'' are now somewhat different. While the Fe/Cr sample with a record magnetoresistance (220 %) among MMLs shows a behaviour similar to that presented in Figures 1-2 for samples with GMR above 60%, the low frequency magnetic response of weakly coupled Fe layers in non epitaxial $[\text{Fe/Cr}]_{10}$ MML with enhanced interface roughness and small magnetoresistance is large for both the real and imaginary parts and shows strong hysteresis in χ'' down to 2K, but not the specific features we found in epitaxial antiferromagnetically coupled MMLs with GMR above 60 %.

The static magnetic properties of $[\text{Fe/Cr}(100)]_{10}$ multilayers are also unusual (see inset to Fig. 2). For the magnetic field directed along easy axis (100), the DC magnetization shows hysteresis which is typical for system with magnetization change due to thermally induced formation and propagation of domain walls, i.e. coercive field which increases as temperature decreases (not shown here). However, when the magnetic field is directed along the hard axis, we clearly observe the presence of two coercive fields (inset to Fig. 2). The first one at small fields (below 25 Oe) decreases when temperature is lowered. That is opposite to what is expected for thermally activated DW depinning). The second coercive field (of about 100 Oe) behaves in a usual way. The low field kink, which sharpens and moves to the zero magnetic field at lower temperatures, may be related to zero field "dip" in magnetic losses observed below 10K.

What could be the reason behind such unusual behavior of the losses at low temperatures? Part of the temperature evolution of the dependences $\chi''(H)$ might be due to the evolution of the domain structure which remains basically unknown for low temperatures. However, the changes are too drastic to be accounted for by a variation of the domain structure alone. It is, of course, rather surprising, that the one relaxation time model describes the main important features of the out of phase response in a multidomain system. What is the meaning of these nearly identical relaxators? It is tempting to relate the decrease in the relaxation time to tunnelling processes which provoke a "chain" or a "shock wave" of other processes thus leading to a rapid relaxation [13]. But, of course, one has first to understand why the distribution of the relaxation times becomes so narrow at low temperatures.

Low temperature magnetoresistance

Let us turn to low field-low temperature electron transport in Fe/Cr(001) multilayers at low temperatures. While our MFM measurements reveal a similar domain structure at room [12] and helium temperatures [11], the corresponding magnetoresistance curves, as shown in Fig. 3, are very different. The strongly low field magnetoresistance is observed in temperature range corresponding to enhanced

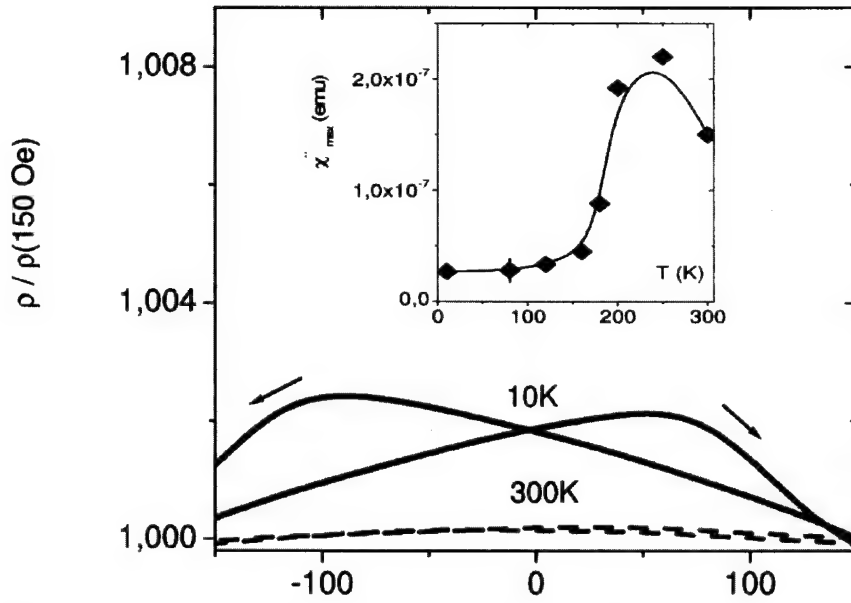


Fig. 3 Low field magnetoresistance and dependence of low field maxima in losses on temperature (inset).

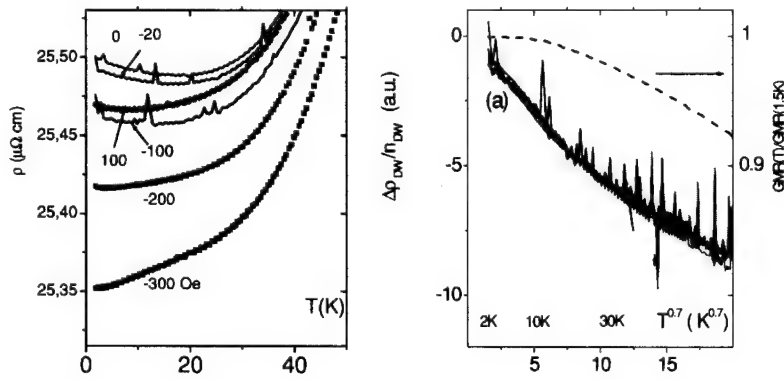


Fig.4 (a) Temperature dependences of the resistivity of $[\text{Fe/Cr}]_{10}$ multilayer at different small applied magnetic fields along the hard axis. (b) Scaling of the DW contribution to resistivity normalized by the effective DW concentration plotted as a function of $T^{0.7}$. Dotted line presents temperature scaling of the normalized GMR.

DWs pinning (see inset to Fig. 3 which shows dependence of low field maximum in losses on temperature).

Figure 4a shows the temperature dependence of the electrical resistivity ρ for an $[\text{Fe}(12 \text{ \AA})/\text{Cr}(12 \text{ \AA})]_{10}$ MML for different magnetic fields ($H < 300$ Oe). The magnetic field is applied in the plane of the film and is parallel to the current as well as to the longer side of the rectangular ($5 \times 25 \text{ \mu m}^2$) sample which is directed along the (110) axis. We determine the magnetoresistivity of the DWs by subtracting the temperature dependences of the resistivity measured in the presence and in the absence of DWs, respectively. In order to separate the magnetoresistivity induced by the GMR effect from the magnetoresistivity induced by the DWs, we define $\rho_{\text{DW}} = \rho(T, H) - \rho(T, H_s)$ with $|H_s| < 300$ Oe, where H_s is estimated field above which appear the changes in the angle between magnetic moments of the layers. We find that, in contrast to the GMR, the DW magnetoresistivity is strongly temperature dependent with no signal of saturation at low temperatures. Assuming that the magnetic field mainly changes the effective DW concentration n_{DW} , we expect $\Delta \rho_{\text{DW}}$ to scale according to $\Delta \rho_{\text{DW}} = \rho_{\text{DW}}(0) - \rho_{\text{DW}}(T) \propto n_{\text{DW}} \rho_{\text{DW}}^0(T)$ with $\rho_{\text{DW}}^0(T)$ a function describing the temperature dependent electron interaction with DWs. Our data analysis reveals that the DW resistivity is roughly given by $\Delta \rho_{\text{DW}} \propto n_{\text{DW}} T^{0.7}$ (Fig.4b) as long as $H_s < 300$ Oe. We have also demonstrated that neither the AMR, which depends on the relative orientation of the magnetization and the current I , nor the ordinary magnetoresistivity (caused by the Lorentz force), which depends on the relative orientation of I and the magnetic induction B , contribute to $\Delta \rho_{\text{DW}}(T)$ [11].

We have studied the low temperature scaling in DW magnetoresistivity for

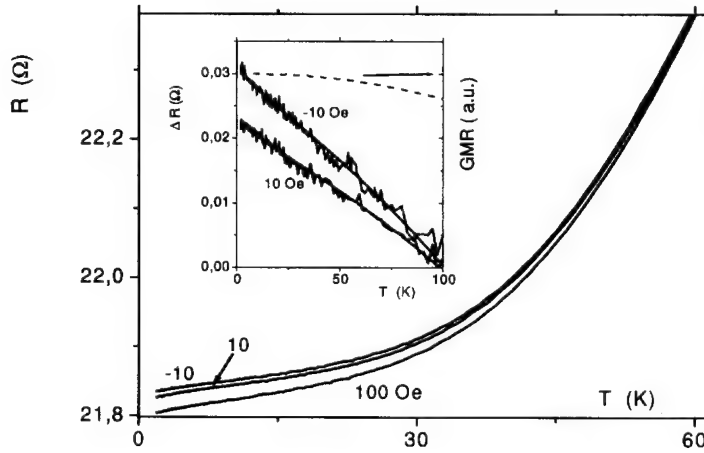


Fig.5 Temperature dependence of the resistance of $[\text{Fe}/\text{Cr}(100)]_{10}$ in three small applied fields which does not show any saturation to the lowest temperature. Inset shows the corresponding magnetoresistance. Solid lines correspond to fits within theory which takes into account suppression of weak anti-localization effect by DWs [11]. Dashed line estimates GMR.

three other AF coupled Fe/Cr samples with an Fe layer thickness of 9, 22 and 30 Å, respectively, and found that $\Delta\rho_{DW}$ follows approximately $\Delta\rho_{DW} \propto T^\alpha$ scaling behaviour with exponent α gradually increasing from 0.7 to about 1 with Fe thickness. This may reflect a change of the exponent (p) in the temperature dependence of the phase breaking time $\tau \propto T^{p/2}$ which should occur between "dirty" ($p=3/2$) and "clean" ($p=2$) limits [14]. Fig. 5 shows low temperature low field resistance and magnetoresistance in $[\text{Fe/Cr}(100)]_{10}$ multilayer when magnetoresistance varies almost linearly with temperature down to 1.9K.

In order to explain the strong variation of the DW magnetoresistivity at low temperatures, one can not use the ballistic approach and has to go beyond the classical theories [7]. A possibility is to link the observed phenomena either to standard, disorder related, weak localization effects or to scattering by isolated spins. Our experimental results are in conflict with both scenarios. Both [8] and [9] predict a destruction of weak electron localization by the domain walls, although the details of the destruction mechanism are different. Direct application of these models results in a sign of the DW magnetoresistivity, which is opposite to the sign of the experimentally observed magnetoresistance. However, the sign of the localization correction may be reversed due to strong spin-orbit (SO) scattering (anti-localization) [15]. Our measurements are consistent with an anti-localization effect in the absence of DWs ($H > 300$ Oe), which is suppressed in the presence of DWs ($H=0$). The fit of experimental data to this model shows that the effective DW width L_{DW} becomes about 2.5 times larger when the magnetic field is increased from 0 to 200 Oe [11].

Conclusions

In conclusion, we have shown that the out of phase low frequency magnetic response in antiferromagnetically coupled Fe/Cr multilayers is strongly dependent on temperature, magnetic field and, at very low temperatures, on frequency. At $T=2$ K and $H=50$ Oe the frequency dependence of the losses can be satisfactorily described within a single relaxation time scheme. At temperatures below 7K and for the ac drive frequencies $f \sim 10^2$ - 10^3 Hz we observed a dip in the magnetic field dependence of losses for fields $H < 10$ -15 Oe. The dependence of χ'' on the magnetic field as well as unusual dependence of one of coercive fields (small one) can be interpreted as the field dependence of the relaxation time which increases by an order of magnitude as the field changes from $H=50$ Oe to zero. The strong magnetic field dependence of the relaxation time at low temperatures might imply an involvement of quantum tunnelling phenomena. At low temperatures, when domain walls are strongly pinned, we observed strongly enhanced magnetoresistance. Temperature scaling of the magnetoresistance indicates possible suppression of quantum transport (weak antilocalization) by the domain walls at low temperatures.

Acknowledgements

We thank A.Chubukov, V.Dugaev, A.P.Levanuyk, C. van Haesendonck and F.Guinea for fruitful discussions. The research was supported in parts by Spanish MCyT under project BFM2000-0016 and by Comunidad de Madrid (07N/0049/2001).

References

- [1] L.Berger, J. Appl. Phys. **49**, 2156 (1978).
- [2] S.Gider, et al., Science **281**, 797 (1998).
- [3] U.Rüdiger, et al., Phys. Rev. Lett. **80**, 5639
- [4] J.F.Gregg, et al., Phys. Rev. Lett. **77**, 1580 (1996).
- [5] U.Rüdiger, et al., Phys. Rev. B **59**, 11914 (1999).
- [6] M.Viret, et al., Phys. Rev. Lett. **85**, 3962 (2000).
- [7] J.B.A.N.van Hoff, et al., Phys. Rev. B **59**, 138 (1999).
- [8] G.Tatara, H.Fukuyama, Phys.Rev.Lett. **78** 3773 (1997).
- [9] Y.Lyanda-Geller, et al., Phys.Rev.Lett. **81** 3215 (1998).
- [10] F.G.Aliev, et al., Phys. Rev. Lett., **88**, 187201 (2002).
- [11] F.G.Aliev, et al., to be published.
- [12] F.G.Aliev, R.Schad, A.Volodin, C.van Haesendonck, Y.Bruynseraede, R.Villar, J.M.@M.M., **226-230**, 745 (2001).
- [13] P.C.E.Stamp, E.M.Chudnovskii and B.Barbara, Int.J.Mod.Phys. **6**, 1355 (1992).
- [14] P.Lee, T.V.Ramakrishnan, Rev.Mod.Phys.**57** 287 (1985).
- [15] W.Knap et al., Phys. Rev. B **53**, 3912 (1996).

Annealing of $\text{Co}_x\text{Cu}_{1-x}$ / Cu Multilayers

Jörg Ebert, Mohammad Ghafari, Branko Stahl, and Horst Hahn

Darmstadt University of Technology, Institute of Material Science, Thin Films Division
Petersenstraße 23, 64287 Darmstadt, Germany

ABSTRACT

In the multilayer system cobalt / copper at the second antiferromagnetic coupling maximum (2. AFM) with a copper thickness of $d_{\text{Cu}} = 2,2$ nm it is possible to reduce magnetoresistive hysteresis by the use of either very thin Co-layers or by alloyed magnetic layers $\text{Co}_{1-x}\text{Cu}_x$. It was possible to achieve values for the giant magnetoresistance effect of $\text{GMR} \approx 20\%$ for as prepared samples. A heat treatment was applied to study the degeneration of the system. For annealing at moderate temperatures ($T_{\text{anneal}} \leq 250^\circ\text{C}$) an increase up to $\text{GMR} \approx 25\%$ was observed. Annealing at slightly higher temperatures lead to an rapid decrease in the GMR effect. To study the structural changes the method of x-ray reflectivity was utilized showing changes in interface roughness as well as in bilayer thickness.

INTRODUCTION

Since the discovery of the Giant Magnetoresistance effect (GMR)¹ there has been great effort to utilize it for industrial applications. The first branch that used GMR based devices was the computer industry. The assemblies are called Spin-Valves and are used in read heads of hard disc drives. In principle these devices consist of two ferromagnetic films with different coercivities separated by a nonmagnetic material. The thickness of the nonmagnetic layer must be high enough so that there is no magnetic interaction between the ferromagnetic layers.

Another basic principle is the use antiferromagnetically coupled multilayers based on Co and Cu. To reduce undesirable hysteresis Co is often alloyed with Fe². Some alternative approaches are discussed in literature like reducing the thickness of the magnetic layer³ or alloying the magnetic layer with the material of the spacer layer⁴.

Besides the reduction of the hysteresis the main duty is to guaranty the capability of the functional layers to withstand the high temperatures of complete production process of a magnetic sensor ($T_{\text{standard}} \approx 300^\circ\text{C}$)². The equilibrium phase diagram⁵ of Co and Cu shows that the two elements are not miscible promising a relative stable layer configuration with no intermixing. Nevertheless the preparation in UHV by sputtering with high energies may lead to implantation of the atoms of one species into the layer of the other element. As the dimensions of the single layers are in the nanoscale and the GMR is known to be an interfacial effect the control of the interface structure and the knowledge of its changes due to thermal annealing is of great importance for the successful application of GMR devices. There are different approaches to obtain the desired flat interfaces. One is the use of so called buffer layers made of Fe, $\text{Ni}_{80}\text{Fe}_{20}$, or Ta⁶. The other is the utilization of surfactants like Pb or Ag⁷, which float on the surface during the preparation process and inhibit island like growth leading to ferromagnetic pinholes⁸. To enhance the thermal stability it is suggested to alloy the spacer layer with a partially miscible element. This should lead to the formation of an alloy at the grain boundary region of the crystallites of the spacer layer, which should avoid the grain growth connected to thermal annealing. A method combining surfactant mediated growth and formation of stabilizing alloys is the use of targets

consisting of Cu, Ag, and Au⁹. Ag is not miscible with the other components and has a high surface tension, so it floats on the surface through the whole deposition process. Au is partially miscible with Cu and forms the desired interface alloy inhibiting the grain growth.

This study is focused on the annealing behavior of the basic Co / Cu system with alloyed magnetic layer $\text{Co}_{1-x}\text{Cu}_x$ and varying thickness d_{Co} . The magnetoresistive properties are measured by the standard four-point probe, the structural development is investigated by x-ray reflectivity techniques.

EXPERIMENTAL DETAILS

Preparation

The $\text{Co}_{1-x}\text{Cu}_x$ / Cu multilayers were prepared by the use of a commercial magnetron sputtering facility having three positions for sputter cathodes. The variation of the Cu content in the magnetic layer was possible due to a triple configuration on one of the cathode-places. One of these triple positions was equipped with a target of pure Cu another with pure Co. The Cu spacer layer was prepared by an independently working cathode with another pure Cu target. The film thickness was controlled by the sputtering power and the residence time underneath each cathode. The substrate was a Si wafer with 850 nm of thermally oxidized SiO_2 . In preliminary experiment the copper thickness d_{Cu} was varied to obtain the desired thickness for the 2nd AFM. It was found to be $d_{\text{Cu}} = 2,2$ nm. For defined growth conditions with flat interfaces a $\text{Ni}_{80}\text{Fe}_{20}$ buffer layer with $d_{\text{buf}} = 4$ nm was first deposited on the substrate. The base pressure was better than $5 \cdot 10^{-7}$ mbar. The sputtering gas was Ar of a pressure of $4 \cdot 10^{-3}$ mbar. The substrate temperature was 20 °C.

Two sets of samples have been prepared:

- i) alloyed magnetic layer, $d_{\text{CoCu}} = 1,5$ nm, $0 \leq x_{\text{Cu}} \leq 0,48$
- ii) pure magnetic layer, $0,5$ nm $\leq d_{\text{Co}} \leq 1,5$ nm

The thickness of the spacer layer was $d_{\text{Cu}} = 2,2$ nm for all samples corresponding to the 2nd AFM. The number of bilayers was $N = 24$.

Annealing

The annealing was preformed in a vacuum furnace with a pressure of $p \leq 1 \cdot 10^{-7}$ mbar with a annealing time of $t_{\text{anneal}} = 1$ h in the temperature range of $150^\circ\text{C} \leq T_{\text{anneal}} \leq 500^\circ\text{C}$ in subsequent annealing steps. The heating- and cooling rates were 10 K/min.

Characterization

The measurement of the GMR curves was done by a standard four-point probe at room temperature as well on the as prepared samples as on the samples after each annealing step. The sensing current was flowing in the film plane (CIP geometry) and was parallel to the external magnetic field created by an electromagnet and measured by a Hall probe. For a complete recording of all significant values the field was first set to a maximum value of + 300 mT and was lowered stepwise to the same negative value of - 300 mT. From there the same stepwise measurement was carried out to the starting point. So it was possible to determine the magnetic hysteresis exactly.

X-ray reflectivity measurements were applied for the characterization of the film thickness, interface roughness and periodicity of the multilayered system. The apparatus (Siemens D5000) was equipped with a Cu tube and a secondary monochromator. The incident angle was varied

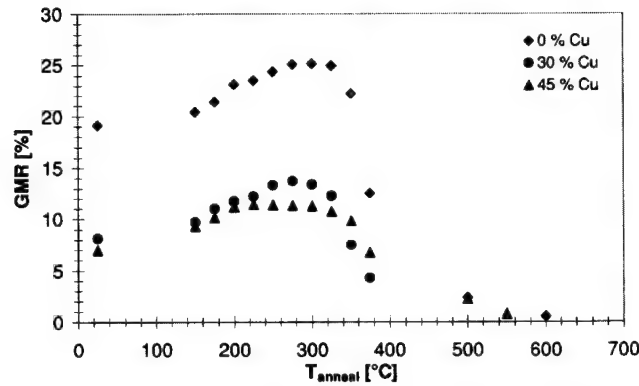


Figure 1. The GMR effect as a function of annealing temperature T_{anneal} for the system with $d_{\text{CoCu}} = 1,5\text{nm}$ and $d_{\text{Cu}} = 2,2\text{ nm}$

from $0,2^\circ \leq \theta \leq 3^\circ$. A part of the X-rays is reflected at the sample surface, another part at inner surfaces. Interference between these reflected parts cause a characteristic oscillation of the intensity depending on the incident angle θ (Kiessig-fringes). The measured reflectograms can be approximated by simulated ones. The parameters of the simulations are the electron density, the thickness of the single layers and the interface roughness.

The superimposed bilayer periodicity causes additional interferences (Bragg-peaks). The position θ_{Bragg} allows the calculation of the bilayer thickness.

DISCUSSION

Alloying of the magnetic layers yielded to a lower GMR effect compared unalloyed system (see Figure 1). Remarkable is the big improvement of 4 % to 5 % for all systems due to the soft annealing. The maximum GMR effect was observed for $T_{\text{anneal}} \approx 250^\circ\text{C} - 275^\circ\text{C}$. Annealing at higher temperatures ($T_{\text{anneal}} \geq 300^\circ\text{C}$) caused a rapid decrease in GMR. This limiting temperature was almost the same for all Cu concentrations.

The dependence of the hysteresis on the annealing temperature and the Cu concentration is shown in Figure 2. Alloying of the magnetic layer with 30 % of Cu leads to a reduction of the hysteresis from 6 mT to 1 mT, which is within the specifications. Annealing at temperatures that give rise to the increase of the GMR cause no significant change in the hysteresis. If the threshold of the rapid decrease is exceeded the hysteresis is increasing. This increase is more distinct for the unalloyed samples than for the alloyed one.

The results for the unalloyed system with varying d_{Co} are presented in Figure 3 and Figure 4. The decrease in GMR due to reduction of the thickness of the magnetic material is clearly visible. Even for the thinnest layer with $d_{\text{Co}} = 0,56\text{ nm}$ the GMR is still $\approx 10\%$ whereas alloying lead to further reduction ($\text{GMR}_{\text{min}} \approx 7\%$ for $x_{\text{Cu}} = 45\%$). The lowering of the hysteresis is not as significant as in the alloyed case.

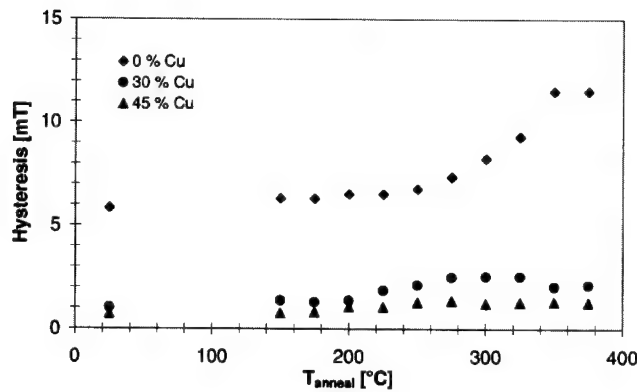


Figure 2. Dependence of the hysteresis on T_{anneal} for different Cu-concentrations in the magnetic layer of the thickness $d_{\text{CoCu}} = 1,5 \text{ nm}$ ($d_{\text{Cu}} = 2,2 \text{ nm}$)

The annealed unalloyed samples show a similar rapid degradation for higher annealing temperatures. The threshold temperature of this degeneration is depending on the thickness of the magnetic layer d_{Co} . The thinner the magnetic layer the lower is the limiting temperature. An improvement due to soft annealing is also found but is limited to $d_{\text{Co}} \geq 1,02 \text{ nm}$. The improve is more pronounced for the sample with the thickest magnetic layer. If $d_{\text{Co}} < 1,0 \text{ nm}$ there is no improve in GMR. The dependence of the hysteresis on the thickness of the magnetic layer is comparable to that of the GMR effect. For $d_{\text{Co}} \geq 1,02 \text{ nm}$ a drastic increase is observed if a threshold temperature of $T_{\text{anneal}} \approx 275^\circ\text{C}$.

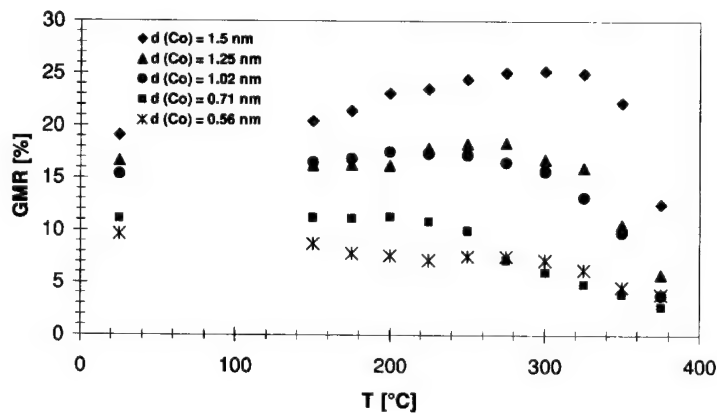


Figure 3. Dependence of the GMR effect on the annealing temperature T_{anneal} and the thickness of the magnetic layer d_{Co} ($d_{\text{Cu}} = 2,2 \text{ nm}$)

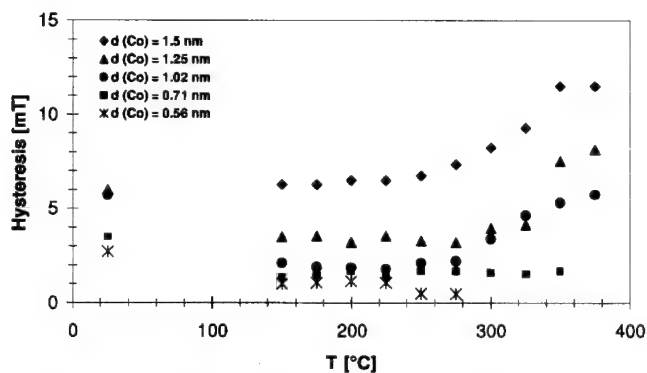


Figure 4. Dependence of the hysteresis on the annealing temperature T_{anneal} and the thickness of the magnetic layer d_{Co} ($d_{\text{Cu}} = 2,2 \text{ nm}$)

The hysteresis of samples with thinner magnetic layers is relatively stable.

Since the GMR effect is known to be an interface phenomenon the interface sensitive method of X-ray reflectivity measurements has been applied after selected stages of the heat treatment. A sequence of the obtained curves is shown in Figure 5 for the unalloyed systems with $d_{\text{Co}} = 1,5 \text{ nm}$. The reflectogram of the as prepared sample is compared to the just before the beginning of the rapid decrease and to a sample which showed no GMR at all after though heat treatment at $T_{\text{anneal}} = 600^\circ\text{C}$ for $t_{\text{anneal}} = 8 \text{ h}$. The X-ray reflectivity experiments reveal an increase in bilayer thickness due to the soft annealing (shift of the Bragg-peak to smaller angles). The increased intensity of the Bragg peak gives rise to the assumption that the interfaces between Co and Cu have been sharpened.

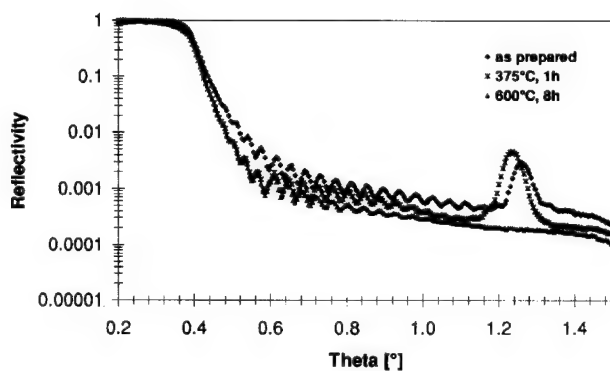


Figure 5. X-ray reflectivity curves for different stages of the heat treatment of unalloyed samples with $d_{\text{Co}} = 1,5 \text{ nm}$.

The geometrical roughness has increased as indicated by the steeper decay of the curve and the less pronounced Kiessig fringes. The roughly treated sample shows no Bragg-peak any more meaning the total destruction of the bilayer structure.

CONCLUSIONS

Based on these results and unpublished data^{10, 11} a model for the development of the microstructure and its influence on the GMR effect is developed. In as prepared samples the interfaces are characterized by an intermixing of Co and Cu due to the deposition process. This causes a non-optimal antiferromagnetic coupling and a comparable high basic resistance. The soft annealing initiates out-diffusion of the atomic species at the interfaces. This process lowers the basic resistance and improves the antiferromagnetic coupling and thus the GMR effect. This phenomenon occurs although the geometrical roughness of the interfaces increases. Annealing above a critical temperature results in the further increase of the interface roughness and the onset of discontinuities of the interfaces leading to a decrease of the magnetoresistance. It is possible to reduce the hysteresis by alloying Co with Cu or by the use of thin Co-layers. Especially for thinner magnetic layers a reduction of the critical temperature for the onset of the degeneration has been observed. The materials selection always has to be a compromise between high GMR, low hysteresis, and desired thermal stability.

REFERENCES

- ¹ M.N. Baibich, J.M. Fert, F. Nguyen Van Dau, F. Petroff, *Pys. Rev. Lett.* 61, 2472 (1988)
- ² D.Wang, J. Anderson, and J.M. Daughton, *IEEE Trans. Magn.* 33 (5), 3520 (1997)
- ³ D.J. Kubinski and H. Holloway, *J. Appl. Phys.* 79 (3), 1661 (1996)
- ⁴ D.J. Kubinski and H. Holloway, *J. Appl. Phys.* 82 (1), 322 (1997)
- ⁵ T.B. Massalski, H. Okamoto, P.R. Subramanian, and L. Kacprzak (Editors), *Binary Alloy Phase Diagrams*, 2nd edition, Volume 1, Metals Park, Ohio, American Society for Metals ASM International
- ⁶ S. Gangopadhyay, J.X. Shen, M.T.Kief, J. Barnard, and M.R. Parker, *IEEE Trans. Magn.* 31 (6), 3933 (1995)
- ⁷ M. Kamiko, R. Furukawa, K.-Y. Kim, M. Iwanami, and R. Yamamoto, *J. Magn. Magn. Mater.* 198 – 199, 716 (1999)
- ⁸ H. Kikuchi, J.-F. Bobo, and R.L. White, *IEEE Trans. Magn.* 33 (5), 3933 (1997)
- ⁹ J.M. Daughton, US Patent No. 5,617,071, April 1, 1997
- ¹⁰ D. Rafaja, J. Ebert, G. Miehe, N. Martz, M. Knapp, B. Stahl, M. Ghafari, H. Hahn, and H. Fuess, submitted to *J. Phys.*
- ¹¹ J. Ebert, B. Stahl, M. Ghafari, and H. Hahn, to be published

Magnetoresistance and Hall Effect Characterisation on Magnetic Thin Films Multilayers

Jenica Neamtu¹ and Marius Volmer

Transilvania University, 29 Eroilor, Brasov 2200, Romania

¹Research and Development Institute for Electrical Engineering, 313 Splaiul Unirii, Bucharest, Romania

ABSTRACT

We have performed both Hall effect, and magnetoresistance measurements on thin films of Permalloy (Py 10 nm) and Py(t_{Py})/Cu(t_{Cu})/Py(t_{Py}) multilayers deposited on thermally oxidized Si substrates, where t_{Py} =4 and 10 nm and t_{Cu} =4 and 8 nm. The measurements were made at room temperature in a setup that allows us to perform both Hall effect and magnetoresistance measurements. The Hall effect measurements were performed varying the angle, $\Delta\theta$, between the magnetic field direction and the normal to the film plane from 0 to 90 degrees. The measured voltages present hysteresis loops at low magnetic field even for $\Delta\theta=0^\circ$. From these measurements we can obtain some information regarding the magnetic properties of our samples.

INTRODUCTION

Multilayered structures consisting of ferromagnetic layers separated by a nonmagnetic, conducting or insulating, spacer are very attractive for development of magnetic sensors and data storage techniques. Such structures can exhibit anisotropic magnetoresistance (AMR) and giant magnetoresistance (GMR) effects and these two give the total magnetoresistance (MR) effect. The AMR effect leads to the 'pseudo-, or planar Hall effect' (PHE) [1] which has the following two characteristics: (i) The output voltage measures an electric field that is perpendicular to the applied current; and (ii) the magnetic field vector lies in the plane of the current and voltage electrodes. The field dependence of the Hall effect becomes more interesting when the applied magnetic field is out of the film plane. In this paper we show the good sensitivity of the PHE signal which can be, together with MR measurements, a useful technique for thin films characterization. To achieve this goal we present the dependence of the PHE as a function of the field at different out of planes angles and discuss the origin of the hysteresis. To complete this discussion we used a micromagnetic simulator [2] to calculate the hysteresis loop of the sample. The results are related with the samples microstructure.

EXPERIMENTAL DETAILS

Thermally evaporated Py thin films and Py/Cu/Py multilayers (MLs) were deposited on to oxidized Si substrates at room temperature. Here Py denotes permalloy ($\text{Ni}_{80}\text{Fe}_{20}$). Two types of samples were obtained by this method: Si/SiO₂/Py(10 nm) thin films and Si/SiO₂/Py(t_{Py})/Cu(4 nm)/Py(t_{Py}) magnetic multilayers with t_{Py} =4 and 10 nm. The local surface topography was studied using atomic force microscopy (AFM). The magnetization measurements have been performed at room temperature using a vibrating sample magnetometer (VSM). Resistance is measured in a four-point contact geometry with the contacts in line or forming a square of approximately 5 mm each side. This last setup, presented in figure 1, allows us to perform both magnetoresistance and Hall effect measurements.

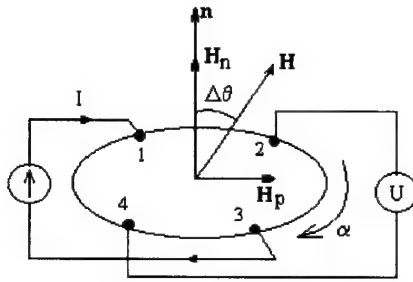


Figure 1. Schematic diagram of the connections used in the planar Hall effect experiments. Also shown are the definitions of some of the angles used in the discussion. Here, the angle between the current direction, I , and the in plane magnetic field, H_p , is $\alpha=45^\circ$.

H is the applied magnetic field which makes the angle $\Delta\theta$ with respect to the surface normal n . We denote with H_p , the in plane component of H and with H_n the component of H which is normal to the sample plane. To maximize the PHE values in these films, the in plane component of the magnetic field (H_p) has to be applied at an angle $\alpha=45^\circ$ to current direction, as shown in figure 1. In some cases the samples were rotated back ($\alpha=0^\circ$) in order to minimize the influence of the AMR effect on the Hall effect measurements. In this case the current, I , is parallel to H_p .

DISCUSSION

The AFM topography for a 4 nm permalloy thin film deposited on to oxidized Si substrate reveals a rough surface with a rms-roughness of 1.1 nm. The maximum height of the surface roughness was about 10.7 nm. This is a characteristic for evaporated thin Py layers [3,4]. During the first stage of Py deposition, isolated Py islands are formed on the surface. The percolation occurs at Py thickness of about 2 nm when the samples are deposited on to Si/SiO₂ substrates [4]. These facts suggest that the Py(4 nm)/Cu(4 nm)/Py(4 nm) sample presents distortions of the multilayer structure and intermixing between permalloy and Cu layers. The predominant conduction mechanism is diffusive scattering at interfaces, grain boundaries and defects that alter the MR and Hall effects. The MR ratio found is no grater than 0.08 %. When the Py thickness increases the film becomes uniform in microstructure. For a Py(10 nm)/Cu(4 nm)/Py(10 nm) ML, the average roughness is very low, 0.87 nm. The average grain size, D , is about 15 nm. The Hall resistivity is about four times grater than for the ML with $t_{Py}=4$ nm. For these reasons thermally evaporated MLs with very thin Py layers are not interesting for practical applications.

When the thickness of the magnetic film is grater than 5 nm the spin-dependent scattering of the electrons takes place predominantly in the bulk of the magnetic layers and the galvanomagnetic properties are close related with the magnetic properties [5]. We present, in figure 2, the $R_L(H)$ curve (longitudinal MR effect) and the corresponding hysteresis loop of a Py(10 nm) thin film. The magnetization loop was calculated from the MR measurements assuming a quadratic dependence between the MR effect and the thin film magnetization.

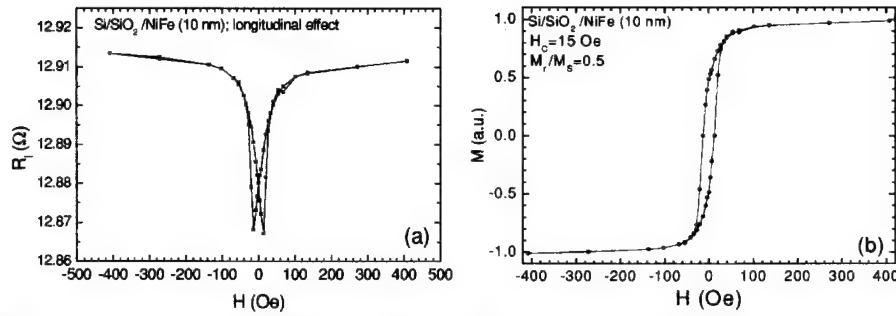


Figure 2. (a) Resistance as function of the applied magnetic field and (b) the corresponding hysteresis loop for an evaporated Py(10 nm) thin film when the applied magnetic field is parallel with the current direction

On the other hand we have simulated the magnetization curve using a collection of 12×12 single domains of Permalloy. Each single domain is an island 10 nm thick and 95 nm each side. The distance between the adjacent domains is 5 nm. This model was inspired from the film structure. The calculations were made using the micromagnetic simulator SimulMag [2]. The results of this simulation are in good agreement with other experimental data [4], for the remnant-to-saturation magnetization ratio $M_r/M_s \approx 0.71$, and with the MR measurements for the value of the coercive field, $H_c = 15$ Oe. Also we can see the domains structures in the demagnetizing state. The spin structure for the coercive field, H_c , and the magnetization curve, when the magnetic field is applied in the film plane, are shown in figure 3.

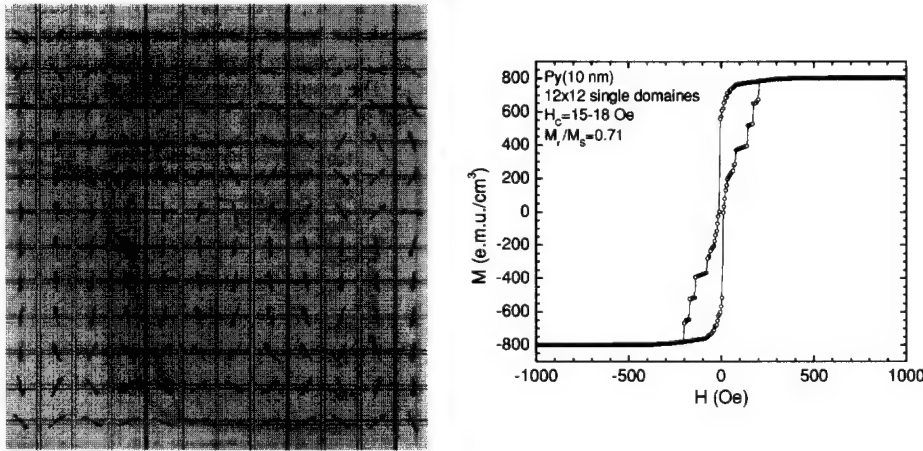


Figure 3. The results of the micromagnetic simulation for an evaporated Py(10 nm) thin film. The magnetic field is applied in the film plane.

The magnetization curves of the Py(10 nm)/Cu(4 nm)/Py(10 nm) multilayer deposited by high vacuum evaporation displayed typical characteristics of ferromagnetically coupled multilayers. The GMR effect is less than 0.05 %. The AMR effect ratio is about 0.5 %. This value is much smaller than the AMR ratio in bulk samples. There are some effects that may contribute to this difference. First, the ML studied may be structurally less well-defined leading to additional electron scattering at grain boundaries and other defects. Second, diffusive scattering at the outer boundaries of the film (dimensionality effect) may affect the AMR ratio. Third, the Cu interlayer may play a shunting effect. Again, using the MR data we obtained the magnetization curve shown in figure 4(a).

To simulate the magnetization curve we used two Py layers each consisting in a collection of 10x10 single domains of permalloy. Each single domain is 10 nm thick and 95 nm each side. The distance between the adjacent domains is 5 nm. Again, the model was inspired from the film structure. The distance between the two layers is the interlayer thickness, $t_{Cu}=4$ nm. Now we have to estimate the ferromagnetic interlayer coupling. It was shown [6] that the dependence of the coupling constant J on the Cu-layer thickness, for $t_{Cu}>1.5-2$ nm, is well described by the Néel model for magnetostatic interlayer coupling, based on the interaction between the dipole fields produced by rough interfaces:

$$J = \frac{\pi^2}{\sqrt{2}} \frac{h^2}{\lambda} \mu_0 M_s^2 \exp\left(\frac{-2\pi\sqrt{2}t_{Cu}}{\lambda}\right) \quad (1)$$

Here, λ and h are the lateral length scale and amplitude of the roughness, respectively, and M_s is the saturation magnetization ($M_s=800$ kA/m or 800 emu/cm³ in CGS). In this model the roughness is assumed to be two-dimensional and sinusoidal. Here, λ is determined by the grain size. From AFM measurements [3] we have $h=1.35$ nm and $\lambda=15$ nm. If we consider $t_{Cu}=4$ nm the interlayer coupling is $J=0.23$ mJ/m². For this value the coupling field is $H_0=2457$ A/m (31 Oe). This value is correct only if we consider the magnetic layers completely separated by the Cu spacer. Because of the Py bridges that exists trough the spacer the coupling may have local variations that exceed 31 Oe. Between the top and the bottom layers we introduced coupling fields that have random values from 30 to 60 Oe. The results of our calculations using the micromagnetic simulator SimulMag are presented in figure 4(b).

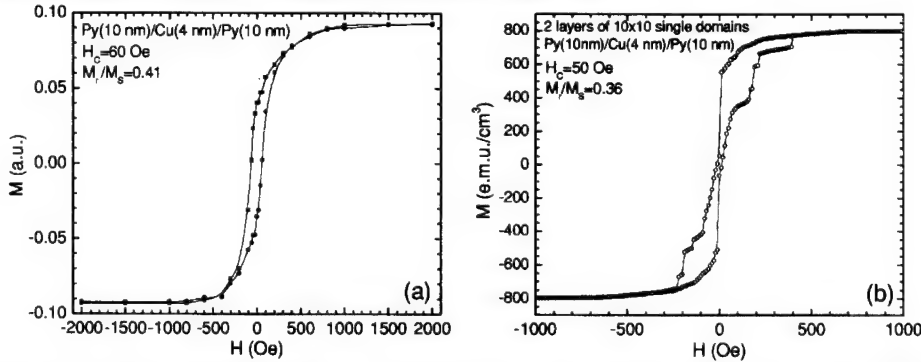


Figure 4. (a) The magnetization curve calculated for an evaporated Py(10 nm)/Cu(4 nm)/Py(10 nm) multilayer from the MR data. (b) The micromagnetic simulated magnetization curve.

We obtained a good agreement between the measured curve [3] and the calculated curves for the coercive field and the remnant-to-saturation magnetization ratio values. For our ML the ratio $M_r/M_s \approx 0.4$ is smaller than the value $M_r/M_s \approx 0.7$ obtained for a Py(10 nm) layer. This can be explained by the fact that in low (or zero) magnetic field the spins from the two magnetic layers start to rotate in a manner to minimize the total free energy.

Using a setup presented in figure 1, we performed Hall effect measurements both on Py and Py/Cu/Py ML. In what follows we present, in figure 5, the results obtained for thermally evaporated Py(10 nm) layer. In figure 5(a) are shown the field dependencies of the output voltage, U , for different angles $\Delta\theta$ between the applied field, H , and the perpendicular to the film plane n . Here $\alpha=45^\circ$ to maximize the AMR effect. We can see, in insert, the hysteretic behavior at low magnetic field for $\Delta\theta=0^\circ$. It is interesting to note that $U(H=0)$ takes the same values, in figure 5(a), for different orientations $\Delta\theta$ of the sample. This means that the remnant magnetization of the thin film takes the same values. This assumption can be illustrated by a simulation of the remnant magnetization state of the film starting from the saturated state for different values of $\Delta\theta$ varying from 0.5° to 90° . The result of our simulation is presented in figure 5(b). Using these observations we were able to extract the contribution of the AMR effect from the measured voltage and to obtain the field dependencies of the Hall voltages for different angles $\Delta\theta$. Such dependencies are shown for $\Delta\theta=0^\circ$, in figure 5(c) and for $\Delta\theta=5^\circ$, in figure 5(d).

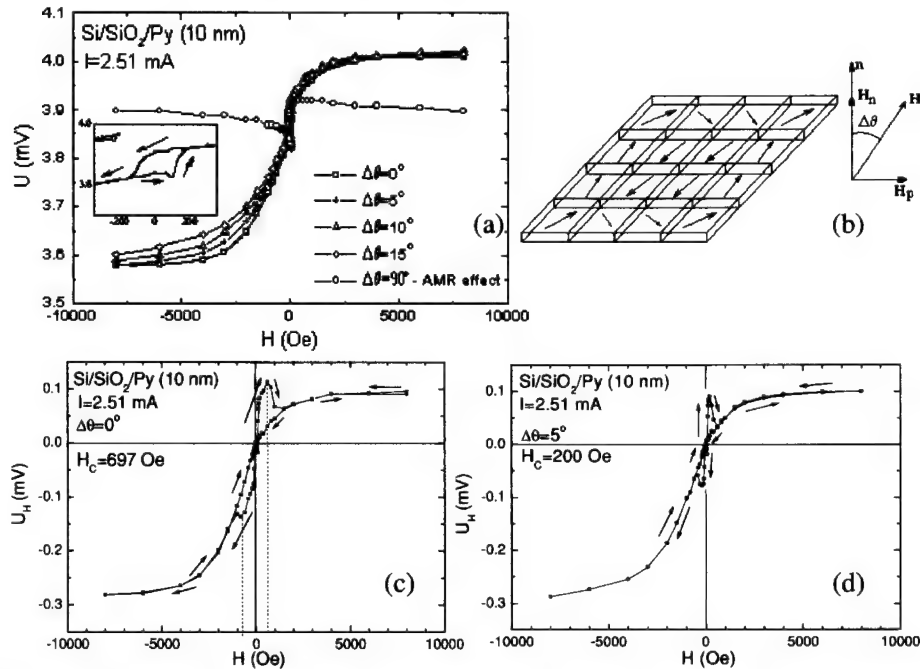


Figure 5. Field dependencies of the output voltage, U , and the Hall voltage, U_H , for different angles $\Delta\theta$ between the applied field, H , and the perpendicular to the film plane, n . The arrows are guides for the eyes.

The asymmetry between the positive and negative field regions is probably due to some other in-plane magnetoresistive effects like the asymmetry of the AMR effect as we can see from figure 5(a). The sharp "anomalies" of the Hall voltage, which appear in figure 5(c-d), can be connected with the reversal processes that take place in the film plane which produce a jump of the AMR ratio. With H_C we denote the critical values of the field for which the magnetization reversal takes place in the film plane. Now, we can make some assumptions regarding the reversal processes that take place in the film. For $\Delta\theta=0^\circ$ we see, in figure 5(c), a relatively large transition region. This suggests a reversal process mainly due to domain wall motion. As $\Delta\theta$ increases the width of the transition regions decreases as we can see from figure 5(d). For $\Delta\theta>10^\circ$ the magnetization reversal will take place mainly by coherent rotation. This is natural because of the relatively large values of the in plane component of H . For $\Delta\theta=10^\circ$ we obtained $H_C=108$ Oe and for $\Delta\theta=15^\circ$ we have $H_C=77.3$ Oe. The same discussion can be made for the Py(10nm)/Cu(4 nm)/Py(10 nm) ML. We found an increase of the H_C values relative to the Py film which is due to a positive coupling between the ferromagnetic layers. This is the case of the non-flatness layers [3,4,6]. The values of H_C (20 Oe for Py and 60 Oe for the Py/Cu/Py ML), when H lies in the film plane ($\Delta\theta=90^\circ$), are in very good agreement with the values measured using a VSM.

When $\alpha=0^\circ$ (in figure 1) the Hall effect measurements show the usual behavior because the influence of the AMR effect on the measured voltage is minimized. The saturation field obtained for our ML, when the magnetic field is applied normal to the film plane is $H_S\approx 6000$ Oe. This value is less than the value predicted from the shape anisotropy ($H_{S0}=4\pi M_S=10.5$ kOe) known for flat surfaces, but is consistent with the film surface topography [4]. This reduction of the perpendicular anisotropy can be explained by a large interface roughness which reduces the dipolar energy anisotropy and leads to a roughness effect [4] of about 5 nm for our MLs evaporated at RT on to oxidized Si substrates. These results are in good agreement with the AFM measurements and explain the absence of the AF coupling between the adjacent Py layers.

CONCLUSIONS

We used MR and Hall effect measurements to investigate the magnetic properties of the thin films and magnetic multilayers. Precise MR and Hall effect measurement can allow us to obtain some useful information about the magnetization curve and the reversal mechanism. The absence of the GMR effect in evaporated Py/Cu multilayers is caused by a rough interface. Using a micromagnetic simulator we were able to obtain the magnetization curves considering the film microstructure and material parameters.

REFERENCES

1. F.Y. Ogrin, S.L. Lee, Y.F. Ogrin, J. Magn. Magn. Mater. 219 (2000) 331
2. John O. Oti, SimulMag Version 1.0, *Micromagnetic Simulation Software*, User's Manual, Electromagnetic Technology Division, National Institute of Standards and Technology Boulder, Colorado 80303, December 1997
3. J. Neamtu, M. Volmer, A. Coraci, Thin Solid Films 343-344 (1999) 218
4. T. Lucinski, G. Reiss, N. Mattern, L. van Loyen, J. Magn. Magn. Mater. 189 (1998) 39
5. Y. Gondo, Y. Suezawa, Thin Solid Films 281-282 (1996) 496
6. J.C.S. Kools, Th. G.S.M. Rijks, A.E.M. De Veirman, R. Coehoorn, IEEE Trans. Magn., **31**, 3918 (1995)

Ab initio study of CPP transport in Fe/Cr/Fe trilayers: influence of transition metal impurities**Heike C. Herper¹, Peter Entel¹, Laszlo Szunyogh², and Peter Weinberger³**¹ Gerhard-Mercator University, Dept of Theoretical Physics,
Lotharstr. 1, D-47048 Duisburg, Germany² Budapest University, Dept of Theoretical Physics
Budafoki út 8, H-1521 Budapest, Hungary³ Center for Computational Materials Science, TU-Vienna,
Gumpendorferstr. 1a, A-1060 Vienna, Austria**ABSTRACT**

The transport properties of Fe(001)/Cr/Fe(001) trilayers are discussed with respect to the influence of transition metal impurities in form of layers. We are able to show that the periodicity of the giant magnetoresistance is directly influenced by the interlayer exchange coupling (IEC). Furthermore, it is observed that the behavior of the IEC strongly depends on whether an impurity overlayer of Mn or V is used. It turns out that the size of the GMR is only little effected by 3d-transition metal impurities, which is in agreement with the experimental findings. The electronic and magnetic properties of the trilayers have been investigated within the fully relativistic, spin-polarized SKKR method and the LDA. The transport properties of the Fe/Cr/Fe systems have been derived from the fully relativistic spin-polarized Kubo-Greenwood equation.

INTRODUCTION

The discovery of the giant magnetoresistance (GMR) in Fe/Cr multilayers by Baibich *et al.* [1] and the observation of the oscillating interlayer exchange coupling (IEC) two years earlier by Grünberg and coworkers [2] was the starting point of many intense studies of the electronic transport in these systems [3–6]. Recently, some effort has been devoted to examine the IEC in Fe/Cr/Fe trilayers with Mn impurities in the Cr spacer [7]. This is interesting, because it is assumed that the third transition metal transforms the spin density wave of Cr into a commensurate AF state, which in turn should change size and/or phase of the IEC. However, the experiments of Heinrich *et al.* have only been carried out for transition metal overlayers. Due to the strong tendency of Mn to segregate to the surface it was impossible to examine diluted CrMn alloys. Furthermore, it has turned out that the GMR of Fe/Cr multilayers is not much affected by a thin overlayer [8].

Here, we have investigated the GMR in current perpendicular to the plane (CPP) geometry and the IEC of Fe/Cr/T₁/Fe trilayers in terms of *ab initio* methods, whereby T₁ stands for a single monolayer of Mn or V. The influence of the overlayer has been studied for varying thickness of the Cr layer. This goes beyond the experimental studies, which were only carried out for a Mn overlayer (one and two ML) and a fixed number of Cr layers [7]. In contrast to experiment we have been able to examine the case of homogeneously distributed impurity atoms in the Cr spacer,

see Ref. [9]. However, here we present results for perfect Mn or V monolayers on top of the Cr spacer.

CALCULATIONAL DETAILS

We have used systems consisting of two semi-infinite Fe leads, which cover the actual spacer plus a particular number of lead layers acting as a buffer. The selfconsistently calculated part is then of the form

$$\text{Fe}_m/\text{Cr}_n/\text{T}_1/\text{Fe}_m, \quad 9 \leq m \leq 11, \quad 2 \leq n \leq 42, \quad \text{T} \in \{\text{Mn}, \text{V}\}.$$

The number of buffer layers varies, because of the special form of the two-dimensional structure constants [10]. All calculations have been performed on a bcc lattice with layer distance of 5.27 a.u. being the LDA value of bcc Fe. Relaxation effects have not been taken into account.

The electronic and magnetic properties of the above mentioned trilayers have been calculated within the fully relativistic spin-polarized version of the screened Korringa-Kohn-Rostoker (SKKR) method for layered systems developed by Szunyogh *et al.* [10, 11]. The calculations have been performed within the atomic sphere approximation (ASA) and the local density approximation (LDA). We have used two different magnetic configurations: parallel alignment of the magnetic moments of the two leads (FM) and antiparallel alignment (AF). In terms of total energies the interlayer exchange coupling can be defined by

$$\Delta E = E(\text{AF}) - E(\text{FM}). \quad (1)$$

In here, only the FM state has been calculated selfconsistently and the IEC has been investigated by using the magnetic force theorem [10]. The IEC is then given by the band energy difference of the two magnetic configurations

$$\Delta E_b = \int_{\epsilon_b}^{\epsilon_F} [n_p(\epsilon, \text{AF}) - n_p(\epsilon, \text{FM})] (\epsilon - \epsilon_F) d\epsilon, \quad (2)$$

where n_p is the layer-resolved density of states for a given magnetic configuration.

The electric transport properties have been obtained from the fully relativistic spin-polarized Kubo-Greenwood equation [13], which is sufficient to describe the influence of the interface structure. Within this method the CPP GMR the resistance of the multilayers have been calculated depending on the magnetic configuration, spacer type, and thickness. For a given sandwich with thickness of the spacer l can be written as

$$r(C, l, \delta) = \sum_{p,q}^l \rho_{pq}(C, l, \delta), \quad l = n + 2m + 1. \quad (3)$$

Here, ρ_{pq} is the resistivity at layer p caused by a current at layer q . The imaginary part of the complex Fermi energy δ is chosen to be 2 mRy, for details see Ref. [14]. It has been shown

elsewhere that the sheet resistance varies linearly with δ [14]. Therefore, the GMR for finite δ is rigidly shifted to lower values. Throughout this paper we have used the bounded definition of the GMR

$$R = \frac{r(\text{AF}) - r(\text{FM})}{r(\text{AF})}, \quad 0 \leq R \leq 1, \quad (4)$$

where we have assumed that the resistance for the AF configuration corresponds to the zero field resistance.

RESULTS

First we have investigated the Fe/Cr/Fe multilayers without impurity layers. The results are plotted in Fig. 1. It should be mentioned that the IEC of similar systems has already been investigated in previous papers [6, 15]. Here, we mainly focus on the GMR and its relation to the IEC. Only some general features of the IEC will be discussed, for details we refer to Ref. [9]. We have found the typical short two monolayer (ML) oscillation period, which is known from, e.g., electron microscopy and Brillouin light scattering experiments [7, 16]. The longer (12 ML) period could not be directly observed. This oscillation is related to the RKKY interaction of the layers and could only be obtained from a fit procedure with some RKKY type energy terms [15]. However, besides the short period we have observed phase slips every 15 layers, which are caused by the spin density wave of Cr. In contrast to other calculations the phase slips can directly observed, Fig. 1 and have not to be calculated from the oscillation periods [15].

The GMR slowly decreases with growing number of spacer layers from 28 % at four layers to $\approx 5\%$ at 42 ML of Cr (Fig. 1, top). The decrease is accompanied by a small oscillation of the GMR with the number of Cr layers. It can be suggested that these oscillations are related to the two ML period of the IEC. In order to verify this, we have plotted the oscillation depending on the number of Cr layers (Fig. 1, bottom). We have checked, whether the $\text{GMR}(n) < \text{GMR}(n+1)$ or vice versa. In the first case the value of the oscillation for the $(n+1)$ -layer system is set to one, whereas in the second case it is chosen to be zero. A similar procedure has been used for the IEC choosing zero for AF coupling and -1 for FM coupling, respectively. The results are displayed in Fig. 1 (bottom panel). This viewgraph clearly reflects the two ML period of the IEC and the phase slips can clearly be seen. Furthermore, it is obvious that the GMR shows the same short ML period as the IEC, whereby the maxima in the GMR are connected to AF coupling and the minima to FM coupling. The phase slips also occur in the GMR depending on the number of Cr layers, but they are slightly shifted and smeared out. Experimentally only the long periods have been observed in the GMR [4]. The short period can usually not be observed.

How the IEC and GMR change when an impurity overlayer is added to the system is shown in Fig. 2. The short period survives if the Cr spacer is covered with a single monolayer of Mn. In agreement with the experimental findings [7] no phase shift occurs due to the impurity layer, i.e., even numbers of Cr layers are still AF coupled. It should be mentioned that this is only true for systems with $n \leq 15$, because at this point the first phase slip occurs in the original Fe/Cr/Fe trilayer and the two systems are out of phase. This was not found by Heinrich *et al.*, because they focussed only on very thin Cr layers. In addition, no phase slips have been observed in the IEC of

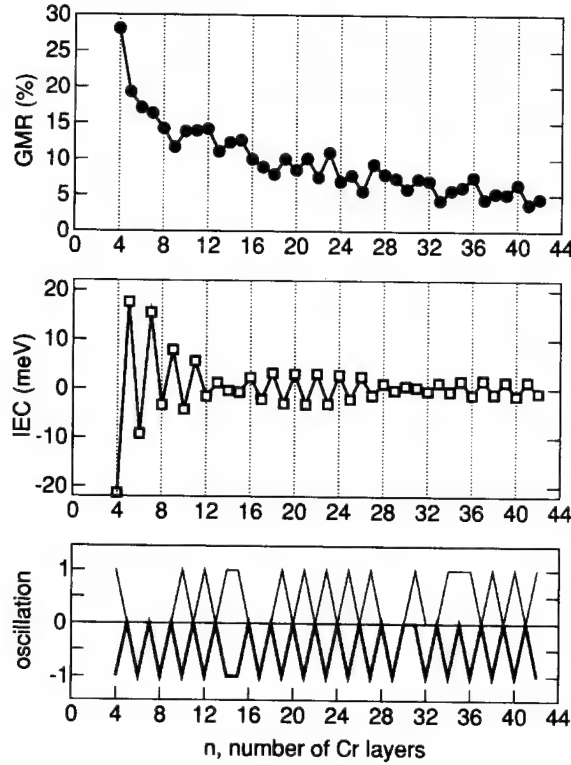


Figure 1. Top panel: The GMR of Fe/Cr/Fe trilayers depending on the thickness of the Cr Layer. Middle panel: The IEC for Fe/Cr/Fe as obtained from the band energy difference vs. the number of Cr layers. Bottom panel: Comparison of the oscillations of the GMR (thin lines) and the IEC (thick lines) of the above shown trilayers, for details see text.

Fe/Cr_n/Mn₁/Fe trilayers. This can be understood from the fact that the Mn monolayer transforms the Cr spin density wave in a commensurate AF state, for a detailed discussion see Ref. [9]. However, the IEC goes to zero at four and 18 ML, which may be still an indication of the spin density wave. In the regions far away from the phase slips of the original system the amplitude of the IEC does not change very much as compared to the Fe/Cr/Fe trilayer, see Figs. 1 and 2. Summarizing, the Mn overlayer leads only to small changes in the IEC. Similar observations have been made for the GMR (Fig. 2, bottom). The GMR of the two systems are comparable in size and phase, whereby the oscillations are more pronounced in the case of the Mn overlayer.

However, if a V overlayer is used instead of Mn the IEC and GMR behave different. In the case of V we have only examined systems with $6 \leq n \leq 12$ layers of Cr. Nevertheless, this results show already some trends. The GMR of the Fe/Cr_n/V₁/Fe systems is of the same size as the GMR of the

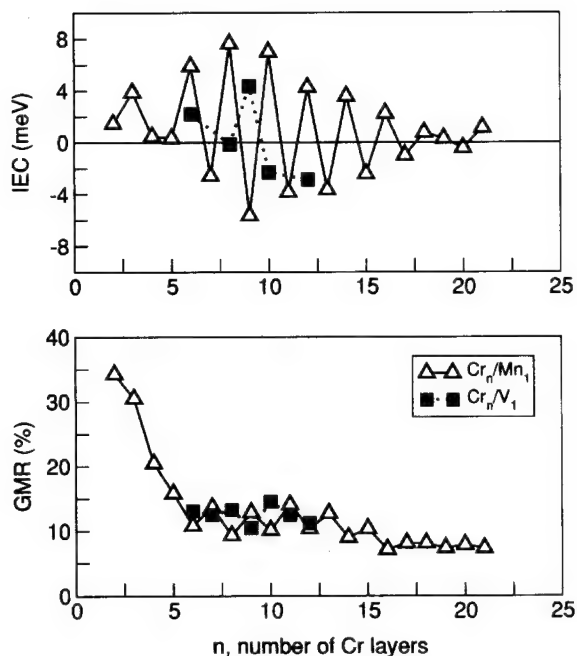


Figure 2. Top panel: The IEC of $\text{Fe}/\text{Cr}_n/\text{T}_1/\text{Fe}$ multilayers vs. the number of Cr layers n . Two different types of impurity overlayers have been used: Mn (open triangles) and V (filled squares). Bottom panel: The GMR vs. the number of Cr layers for the above described systems.

two types of systems discussed above (Fig 2), which has been expected from the experiments of Baumgart, who studied the GMR of $\text{Fe}(15 \text{ \AA})/(\text{Cr}(12 \text{ \AA})/\text{T}(t))_{20}$ multilayers [8]. In the case of a V overlayer a similar period of the GMR can be observed as for the two previously discussed systems (Fig. 2, bottom). In contrast to the Mn impurities an overlayer of V leads to a shift in the GMR; now local maxima occur at even numbers of Cr. This suggests that the IEC has changed, which can be confirmed by the results shown in Fig. 2 (top). Though, there are very few data points, it can be suggested that AF coupling is related to even numbers of Cr layers. In addition, the amplitudes of the IEC are smaller as compared to the IEC of the system with Mn impurities. For a more detailed analysis of the influence of V impurities on the GMR and the IEC of $\text{Fe}/\text{Cr}/\text{Fe}$ trilayers more data points have to be taken into account.

SUMMARY AND CONCLUSIONS

In this paper we have presented results for the GMR and IEC of $\text{Fe}/\text{Cr}/\text{Fe}$ trilayers in particular focusing on systems with a Mn or V overlayer on top of the Cr spacer. We have demonstrated that the periods of the GMR are directly related to the oscillations of the IEC. In agreement with the

experimental findings we have observed that a Mn overlayer does not change the phase of the GMR or IEC. It has been shown that the phase slips are vanishing due to the Mn impurities. Furthermore, we have been able to predict that a V overlayer would cause a phase shift and the IEC would be smaller than in the original Fe/Cr/Fe trilayer.

ACKNOWLEDGMENTS

This work has been partially funded by the RTN network "Computational Magnetoelectronics" (Contract No. RTN1-1999-00145) and by the Austrian science ministry (BM:bwk GZ45.504). The authors acknowledge financial support from the Hungarian National Science Foundation (Contract No. OTKA T030240 and T038162) and the German DFG through the SFB 491.

REFERENCES

1. M. N. Baibich, J. M. Broto, A. Fert, F. N. V. Dau, and F. Petroff, *Phys. Rev. Lett.* **61**, 2472 (1988).
2. P. Grünberg, R. Schreiber, Y. Pang, M. B. Brodsky, and H. Sowers, *Phys. Rev. Lett.* **57**, 2442 (1986).
3. J. J. Krebs, P. Lubitz, A. Chaiken, and G. A. Prinz, *Phys. Rev. Lett.* **63**, 1645 (1989).
4. S. S. P. Parkin, N. More, and K. P. Roche, *Phys. Rev. Lett.* **64**, 2304 (1990).
5. M. C. Cyrille et al., *Phys. Rev. B* **62**, 3361 (2000).
6. A. Vernes et al., *Phil. Mag. B* **82**, 85 (2002).
7. B. Heinrich, J. F. Cochran, T. Monchesky, and R. Urban, *Phys. Rev. B* **59**, 14520 (1999).
8. P. Baumgart et al., *J. Appl. Phys.* **69**, 4792 (1991).
9. H. C. Herper, P. Weinberger, L. Szunyogh, and P. Entel, to be published in *Phys. Rev. B*.
10. P. Weinberger and L. Szunyogh, *Comp. Mater. Sci.* **17**, 414 (2000).
11. L. Szunyogh, B. Újfalussy, and P. Weinberger, *Phys. Rev. B* **51**, 9552 (1995).
12. H. J. F. Jansen, *Phys. Rev. B* **59**, 4699 (1999).
13. P. Weinberger, P. M. Levy, J. Banhart, L. Szunyogh, and B. Újfalussy, *J. Phys: Cond. Matter* **8**, 7677 (1996).
14. H. C. Herper, P. Weinberger, A. Vernes, L. Szunyogh, and C. Sommers, *Phys. Rev. B* **64**, 184442 (2001).
15. S. Mirbt, A. M. N. Niklasson, and B. Johansson, *Phys. Rev. B* **54**, 6382 (1996).
16. J. Unguris, R. J. Celotta, and D. T. Pierce, *Phys. Rev. Lett.* **67**, 140 (1991).

Ab-initio theory of CPP transport

P. Weinberger

Center for Computational Materials Science
TU Wien, Getreidemarkt 6/134, A1060 Vienna, Austria

Abstract

The phenomenon of electric transport perpendicular to the planes of atoms is discussed in terms of an ab-initio approach based on the Kubo-Greenwood equation. Since level of description is fully relativistic “artifacts” due to spin resolution are avoided. Besides a formal discussion of the applied methods and an illustration of the numerical procedures, in particular the dependence of the magnetoresistance on the quality of interfaces, and issues concerning “tunneling” in metal/non-metal heterojunctions are discussed.

1 Introduction

Although current perpendicular to the planes of atoms (CPP) experiments seem to be easy to visualize in terms of a Landauer-type view of electric transport, its theoretical description poses quite a few questions. Is it sufficient to consider transmission and reflection matrices placed only at planes well-situated within the leads? What is the relationship between conductivity and resistivity? Which part of a heterojunction, spacer or interfaces actually causes a sufficiently large magnetoresistance ratio? If it is the spacer, how much matters its actual structure? If the magnetoresistance is mainly due to the interfaces, how about experimentally unavoidable interdiffusion? Are there any criteria in terms of the resistivity or resistance other than rules of thumb that would distinguish between “tunneling” and “weak” metallic conductance? Clearly enough on top of all these questions nags the doubt whether or not it is justified to consider “spin” as an observable, i.e., whether or not the concept of “spin currents” (spin-resolved currents) makes any sense.

In this contribution exclusively the Kubo-Greenwood equation [1, 2, 3, 4] is applied to CPP. Furthermore, in all applications and illustration shown a fully relativistic realization of this equation is used implying that right from the beginning “spin” will not be considered as an independent (“observable”) quantity. As recently two review articles appeared [5, 6] discussing various aspects of the “giant magnetoresistance” (GMR), including also CPP concepts, no attempt is made to present in here also other ab-initio type approaches. For a very detailed discussion of all theoretical implications of the present approach such

as collinearity and non-collinearity, magnetic configurations, inhomogeneous alloying, etc., the reader is referred to a forthcoming review article [11].

2 The relativistic Kubo-Greenwood equation for systems with two-dimensional translational symmetry

Within the (non-relativistic) Density Functional Theory (DFT) the Kohn-Sham-Dirac Hamiltonian is given by

$$\mathcal{H} = \boldsymbol{\alpha} \cdot \mathbf{p} + \square mc^2 + V^{eff}[n, \mathbf{m}] + \square \boldsymbol{\Sigma} \cdot \mathbf{B}^{eff}[n, \mathbf{m}] \quad , \quad (1)$$

$$\begin{aligned} \square_i &= \begin{pmatrix} 0 & \square_i \\ \square_i & 0 \end{pmatrix} \quad , \quad \square = \begin{pmatrix} I_2 & 0 \\ 0 & -I_2 \end{pmatrix} \quad , \\ \Sigma_i &= \begin{pmatrix} \square_i & 0 \\ 0 & \square_i \end{pmatrix} \quad , \quad I_2 = \begin{pmatrix} 1 & 0 \\ 0 & 1 \end{pmatrix} \quad , \end{aligned} \quad (2)$$

$$V(\mathbf{r}) \equiv V^{eff}[n, \mathbf{m}] = V^{ext} + V^{Hartree} + \frac{\delta E_{xc}[n, \mathbf{m}]}{\delta n} \quad , \quad (3)$$

$$\mathbf{B}(\mathbf{r}) \equiv \mathbf{B}^{eff}[n, \mathbf{m}] = \mathbf{B}^{ext} + \frac{e\hbar}{2mc} \frac{\delta E_{xc}[n, \mathbf{m}]}{\delta \mathbf{m}} \quad , \quad (4)$$

where n is the particle density, \mathbf{m} the magnetization density, $V^{eff}[n, \mathbf{m}]$ the effective potential, $\mathbf{B}^{eff}[n, \mathbf{m}]$ the effective (exchange) magnetic field, V^{ext} and \mathbf{B}^{ext} the corresponding external fields, and the \square_i are Dirac- and the \square_i Pauli (spin) matrices, see also refs. [7, 8].

If $G(z)$ denotes the resolvent of this Hamiltonian,

$$G(z) = (z - \mathcal{H})^{-1} \quad , \quad z = \square + i\delta \quad , \quad (5)$$

then within the Kubo-Greenwood equation [1, 2, 3, 4] the diagonal elements of the conductivity tensor are defined as

$$\square_{ii} = \frac{\hbar}{N_0} \text{tr}_{at} J \text{Im} G^+(\square_F) J_{ii} \text{Im} G^+(\square_F) \rangle \quad , \quad (6)$$

where $\text{Im} G^+(\square)$,

$$\text{Im} G^+(\square) = \frac{1}{2i} (G^+(\square) - G^-(\square)) \quad , \quad (7)$$

can be formulated in terms of the so-called side-limits of $G(z)$,

$$\lim_{|\delta| \rightarrow 0} G(z) = \begin{cases} G^+(\square) & ; \delta > 0 \\ G^-(\square) & ; \delta < 0 \end{cases} \quad . \quad (8)$$

Usually multiple scattering theory [8, 9] is applied in order to evaluate $G(z)$ in the configuration space representation (Green's function) and to perform the trace in eqn. (6). If the system under consideration can be characterized by two-dimensional translational symmetry (layered system; one and the same translational invariance has to apply in all atomic layers) then for a particular magnetic configuration C the diagonal elements of the conductivity tensor can be written [10, 11] as a double sum over atomic layers,

$$\square_{\square\square}(C; n) = \frac{1}{n} \sum_{p,q=1}^n \square_{\square\square}^{pq}(C; n) \quad , \quad (9)$$

where

$$\square_{\square\square}^{pq}(C; n) = \lim_{\delta \rightarrow 0} \square_{\square\square}^{pq}(C; n; \delta) \quad , \quad (10)$$

$$\square_{\square\square}^{pq}(C; n; \delta) = \frac{1}{4} \sum_{i,j=1}^2 (-1)^{i+j} \square_{\square\square}^{pq}(C; \square_i, \square_j; n) \quad , \quad (11)$$

and n denotes the total number of atomic layers taken into account.

3 Current-perpendicular to the planes of atoms (CPP)

Let z and z' denote continuous coordinate variables perpendicular to the planes of atoms in a two-dimensional translationally invariant system. In the steady state one can write the resistivity in the current-perpendicular to the planes of atoms geometry (CPP) as [12, 13]

$$\square_{CPP} = \frac{1}{L} \int \square(z, z') dz dz' \quad , \quad (12)$$

where $\square(z, z')$ is the inverse of $\square(z, z')$ as defined by

$$\int \square(z, z'') \square(z'', z') dz'' = \delta(z - z') \quad , \quad (13)$$

and L is the overall length of the structure for which the conductivity is calculated, see also ref. [14]. The sheet resistance r and resistance R are then defined by the following relations

$$r = AR = L \square_{CPP} = \int \square(z, z') dz dz' \quad , \quad (14)$$

where A is the unit area.

The conductivity tensor $\square(z, z')$ can now be mapped [15] ($f : \cdot$) onto the zz -components of the conductivity tensor for a layered system introduced earlier, $\square_{zz}^{ij}(n) \equiv \square_{ij}(n)$, $i, j = 1, n$, with i and j denoting planes of atoms,

$$f : \square(z, z') \rightarrow \square_{ij}(n) \quad , \quad (15)$$

such that the algebraic structure established by eqn. (13) is conserved,

$$\sum_{k=1}^n \square_{ik}(n) \square_{kj}(n) = \delta_{ij} \quad . \quad (16)$$

Clearly enough the sheet resistance r in eqn. (14) then serves as measure (g :) for the mapping f ,

$$g : r \rightarrow r(n) \quad , \quad r(n) = \sum_{i,j=1}^n \square_{ij}(n) \quad , \quad (17)$$

since according to the Cauchy convergence criterion the integral in eqn. (14) can be mapped onto a sum, i.e., onto $r(n)$, if and only if,

$$\left| r - \lim_{n \rightarrow \infty} r(n) \right| < \Delta \quad , \quad n \in \mathbb{N}^+ \quad , \quad (18)$$

or,

$$|r(n+m) - r(n)| < \Delta; \quad n, m \in \mathbb{N}^+ \quad , \quad (19)$$

where Δ is an infinitesimal small number.

Making use of complex Fermi energies, $\mathcal{E}_F = \bar{\mathcal{E}} \pm i\delta$, according to eqn. (8) the sheet resistance for a given magnetic configuration \mathcal{C} is defined by

$$r(\mathcal{C}; n) = \lim_{\delta \rightarrow 0} r(\mathcal{C}; n; \delta) \quad , \quad (20)$$

where

$$r(\mathcal{C}; n; \delta) = \sum_{i,j=1}^n \square_{ij}(\mathcal{C}; n; \delta) \quad , \quad (21)$$

and

$$\sum_{k=1}^n \square_{ik}(\mathcal{C}; n; \delta) \square_{kj}(\mathcal{C}; n; \delta) = \delta_{ij} \quad . \quad (22)$$

It should be noted that eqn. (20) simply refers to the side limiting procedure in eqn. (8).

4 CPP transport in heterojunctions

Suppose now for matters of simplicity that a typical heterojunction consists of n atomic layers of magnetic leads (L) and s atomic layers of a spacer X, i.e., suppose that a heterojunction is of the type $L_n X_s L_n$. The total number of atomic layers t amounts therefore to $t = 2n + s$ which in turn implies for a given number of spacer layers that the convergence criterion in eqn. (19) reads as follows

$$|r(\mathcal{C}; 2(n+m) + s) - r(\mathcal{C}; 2n + s)| < \Delta \quad , \quad m, n \in \mathbb{N}^+ \quad . \quad (23)$$

For each given spacer thickness s , the sheet resistance corresponding to a particular magnetic configuration C is therefore given by

$$r(C; s) = \lim_{m \rightarrow M} \lim_{\delta \rightarrow 0} r(C; 2(n+m) + s; \delta) \quad (24)$$

where M is a sufficiently large integer number. In practical terms eqn. (24) can be split up into two independent limiting procedures,

$$r(C; s; \delta) = \lim_{m \rightarrow M} r(C; 2(n+m) + s; \delta) \quad (25)$$

$$r(C; s) = \lim_{\delta \rightarrow 0} r(C; s; \delta) \quad (26)$$

4.1 Magnetoresistance ratio

The magnetoresistance ratio MR (GMR , "giant magnetoresistance") corresponds in the so-called "pessimistic view" to

$$MR = \frac{r(C'; s) - r(C; s)}{r(C'; s)} \quad (27)$$

and in the "optimistic view" to

$$MR = \frac{r(C'; s) - r(C; s)}{r(C; s)} \quad (28)$$

where in the case of collinear magnetic configurations C and C' usually are termed "parallel" and "antiparallel" configuration. The advantage of the definition in eqn. (27) is simply that thus the magnetoresistance ratio is bound by one. Unfortunately experimental data very often refer rather to the second kind of definition (because the value of the giant magnetoresistance ratio is larger?). It should be noted in this context, however, that eqn. (27) corresponds to the only useful definition of the angular dependence of the anisotropic magnetoresistance. In here exclusively the "pessimistic view" is used.

4.2 Physical significance of the imaginary part of the Fermi energy

Suppose that in the Kubo-Greenwood equation, see (6), the current operator can be approximated by a constant,

$$\square \sim tr \quad \text{Im } G^+(\square_F) \text{Im } G^+(\square_F) \sim n^2(\square_F) \quad (29)$$

which in turn implies that the sheet resistance can approximately be written as

$$\bar{r} = L \square^{-1} = L n^{-2}(\square_F) \quad (30)$$

Furthermore, suppose the density of states is calculated for complex Fermi energies, $\mathcal{E}_F = \bar{\mathcal{E}}_F + i\delta$,

$$\bar{r}(\delta) = L\bar{\mathcal{E}}_F^{-1} = Ln^{-2}(\bar{\mathcal{E}}_F + i\delta) \quad , \quad (31)$$

then from the properties of the density of states,

$$\frac{d[n(\bar{\mathcal{E}}_F + i\delta)]}{d\delta} = \begin{cases} > 0; & \text{"non-metallic"} \\ < 0; & \text{"metallic"} \end{cases} \quad , \quad (32)$$

follows immediately

$$\frac{d[\bar{r}(\delta)]}{d\delta} = \begin{cases} > 0; & \text{"metallic"} \\ < 0; & \text{"non-metallic"} \end{cases} \quad (33)$$

The functional form of the actually calculated sheet resistance with respect to the imaginary part of the Fermi energy, see eqns. (25) and (26), can therefore be used to qualitatively interpret the underlying type of conductance

$$\frac{d[r(\mathcal{C}; s; \delta)]}{d\delta} = \begin{cases} > 0; & \text{"metallic"} \\ < 0; & \text{"non-metallic"} \end{cases} \quad (34)$$

The last equation means *inter alia* that in the case of a negative slope of the sheet resistance with respect to δ "tunneling" might occur. The parameter δ obviously acts like a (small) constant selfenergy: in the regime of metallic conductance an increase of the selfenergy implies an increased resistivity (sheet resistance); in the non-metallic regime an increase of δ reduces the resistance, the system becomes more metallic.

Since very often the actual composition of a heterostructure is not known, i.e., no information about interdiffusion at the interfaces, macroscopic roughness, etc., are not available, in such a case it seems sufficient to consider the following magnetoresistance ratio,

$$MR(\delta) = \frac{r(\mathcal{C}'; s; \delta) - r(\mathcal{C}; s; \delta)}{r(\mathcal{C}'; s; \delta)} \quad , \quad (35)$$

where δ is sufficiently small, for a semi-quantative characterization.

5 CPP transport & IEC

Certain aspects of current-in-plane (CIP) and CPP electric transport have to be correlated with the so-called interlayer exchange coupling energy (IEC). The IEC classifies the type of coupling between the magnetic parts of a heterojunction, i.e., determines regimes of parallel and antiparallel coupling, or, can serve as (continuous) energy variable in an ab-initio description of the exchange bias in spin valve systems [16].

Up to now in most evaluations of the IEC the magnetic force theorem [17] was applied by considering the grand-potentials of the two magnetic configurations under investigation

$$\Delta E_b = E_b(\mathcal{C}) - E_b(\mathcal{C}_0) \quad , \quad (36)$$

evaluating, however, only one magnetic configuration (C_0 , one of them) selfconsistently. If c_i^p denotes the respective concentrations of the constituents A and B in layer p then in terms of the (inhomogeneous) CPA for layered systems [10], ΔE_b is given by

$$\Delta E_b = \sum_{p=1}^N \sum_{i=A,B} c_i^p \Delta E_{\square}^p, \quad \sum_{i=A,B} c_i^p = 1, \quad (37)$$

where the

$$\Delta E_{\square}^p = \int_{\square_b}^{\square_F} (n_{\square}^p(C, \square) - n_{\square}^p(C_0, \square)) (\square - \square_F) d\square, \quad (38)$$

refer to component- and layer-resolved contributions to the grand-potential at $T=0$. In eqn. (38) the $n_{\square}^p(C, \square)$ are component and layer projected DOS's corresponding to magnetic configuration C , \square_b denotes the bottom of the valence band and \square_F is the Fermi energy of the (nonmagnetic) substrate, see also ref. [8]. The energy integral in eqn. (38) is usually performed in the upper half of the complex plane using a contour starting at \square_b and ending at \square_F .

Note that because of the definition given in eqn. (36) this implies the following energetic order of magnetic configurations

$$\Delta E_b = \begin{cases} > 0; & \rightarrow C; \text{ preferred configuration} \\ < 0; & \rightarrow C_0; \text{ preferred configuration} \end{cases} \quad (39)$$

6 Numerical implementation

All examples and illustrations shown in here are based on applications of the fully relativistic versions of the Screened Korringa-Kohn-Rostoker (SKKR) method [8] and the Kubo-Greenwood equation [11]. Disorder such as interdiffusion at interfaces or alloying in the spacer part is described in terms of the (inhomogeneous) Coherent Potential Approximation (CPA) for layered systems [10].

7 Illustrations of the numerical procedures

In Fig. 1 the variation of the parallel (\mathcal{P}) and antiparallel (\mathcal{AP}) sheet resistance in bcc-Fe(100)/Fe_nGe_sFe_n/Fe(100) is shown for a particular value of δ and s versus the number of Fe lead layers. As can be seen for $n > 8$ the sheet resistances start to grow linearly with n . For $\delta \rightarrow 0$ the slope in this linear regime tends to zero [15], i.e., for a sufficient number of lead layers the sheet resistances become constant: the requirements in eqns. (25) and (26). The physical reason for the convergence properties with respect to the number of lead layers has to be correlated [15] with the oscillations of the (layer-resolved) Madelung potentials, which starting at the interface only slowly approach the Madelung potential in pure bcc-Fe(100).

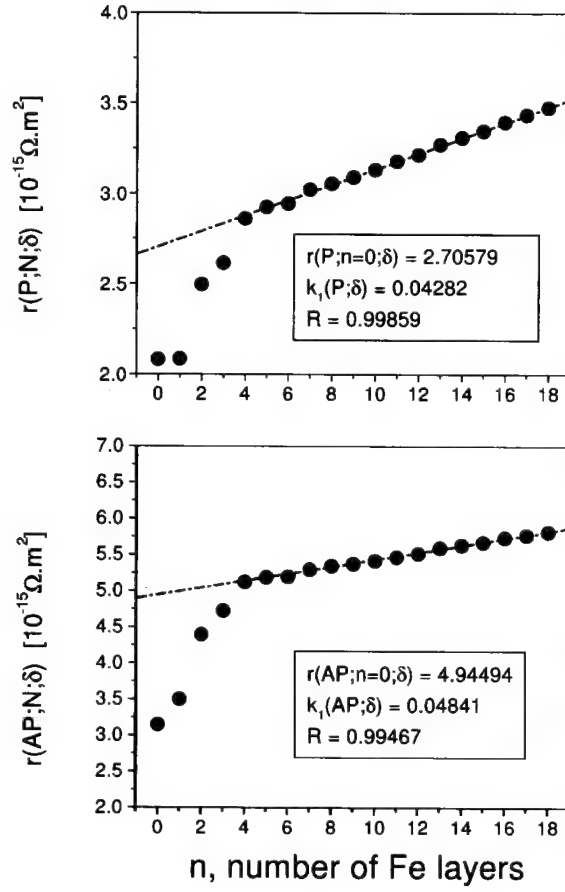


Figure 1: Variation of the sheet resistance $r(C; n; \delta)$ for bcc Fe(100)/Fe_nGe_sFe_n/Fe, $\delta = 2$ mry, $s = 9$, with respect to n . The upper panel refers to the parallel configuration, the lower to the antiferromagnetic configuration. Dashed lines indicate the extrapolation of the linear regime to $n = 0$. From ref. [15].

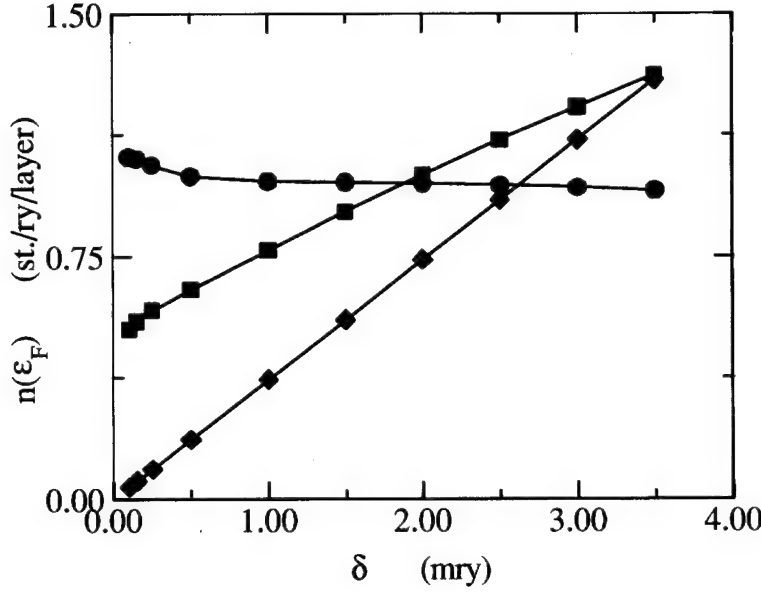


Figure 2: Density of states of the center vacuum layer at the complex Fermi energy $\epsilon_F + i\delta$ as a function of δ in bcc-Fe(100)/Fe₁₂Vac_sFe₁₂/Fe(100) for $s = 3$ (circles), $s = 6$ (squares; multiplied by 100), and $s = 9$ (diamonds; multiplied by 250). From ref. [18].

In Fig. 2 the density of states of bcc-Fe/Fe_nVac_sFe_n/Fe(100) at the Fermi level is displayed with respect to δ for 3, 6 and 9 layers of vacuum separating bcc-Fe(100) leads. This figure shows that only for $s > 9$ the density of states in the center layer vanishes completely. However, one can see also that for $s > 6$ the slope of $n(\epsilon_F + i\delta)$ with respect to δ is positive, while it is slightly negative for $s = 3$. Fig. 3 on the other hand proves that although the density of states for $s = 3$ has not vanished, the slopes of the sheet resistances with respect to δ are of different sign. In the antiparallel alignment a “tunneling” situation is characteristic, while in the parallel alignment – in accordance with the simple density of states picture – metallic conductance is predicted. Clearly enough in such a case the magnetoresistance ratio is rather very big.

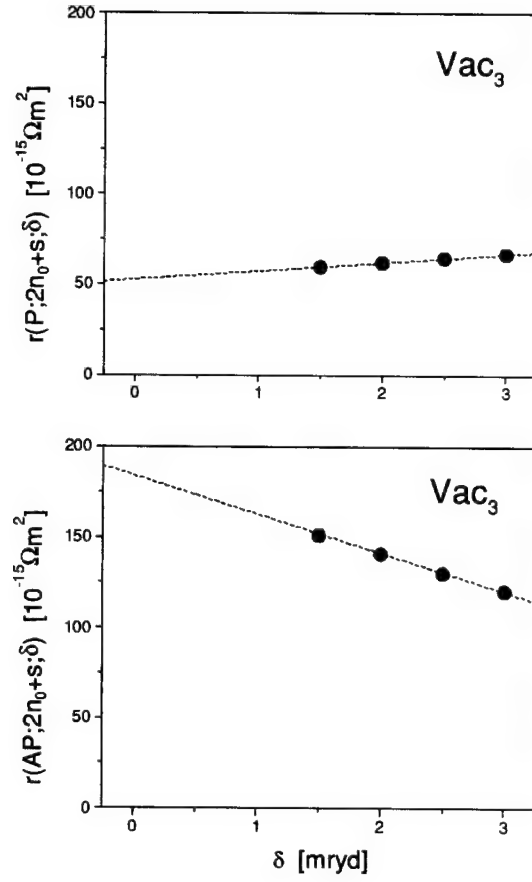


Figure 3: Analytical continuation of the sheet resistances $r(C; 2n + s; \delta)$ in bcc-Fe(100)/Fe₁₂Vac₃Fe₁₂/Fe(100), $n \geq 11$, $s = 3$, to the real energy axis. Top: parallel configuration, bottom: antiparallel configuration. Full circles refer to calculated values, dotted lines to the corresponding linear fit. From ref. [18].

8 Where does the GMR effect in heterojunctions come from?

For illustrative purposes the layer-resolved sheet resistances can be defined,

$$r_i(\mathcal{C}; t; \delta) = \sum_{j=1}^t \square_j(\mathcal{C}; t; \delta) \quad , \quad r_i(\mathcal{C}; t) = \lim_{\delta \rightarrow 0} r_i(\mathcal{C}; t; \delta) \quad , \quad (40)$$

where t is again the total number of atomic layers considered. It is important to note that only the sum over these layer-resolved sheet resistances,

$$r(\mathcal{C}; t; \delta) = \sum_{i=1}^t r_i(\mathcal{C}; t; \delta) \quad , \quad r(\mathcal{C}; t) = \lim_{\delta \rightarrow 0} r(\mathcal{C}; t; \delta) \quad , \quad (41)$$

is well-defined. By partitioning the difference of the sheet resistances

$$\Delta r(t) = r(\mathcal{AP}; t) - r(\mathcal{P}; t) \quad (42)$$

with respect to the magnetic configurations into contributions arising from different parts of the heterostructure, namely the left and right electrodes (leads), L_{left} and L_{right} , the interface regions between electrodes and spacer, I_{left} and I_{right} , and the remaining spacer part S ,

$$\begin{aligned} \Delta r(t; \delta) = & \Delta r_{L_{left}}(t; \delta) + \Delta r_{L_{right}}(t; \delta) \\ & + \Delta r_{I_{left}}(t; \delta) + \Delta r_{I_{right}}(t; \delta) + \Delta r_S(t; \delta) \quad , \end{aligned} \quad (43)$$

a very informative "picture" of where the magnetoresistance comes from can be given. Fig. 4 shows such a partitioning for the heterojunction $\text{bcc}(100)/\text{Fe}_n(\text{ZnSe})_s\text{Fe}_n/\text{Fe}(100)$. As can be seen in both kinds of termination the GMR effect is mostly determined by the Fe/ZnSe interfaces, indicating that the actual structure of the spacer is of little importance.

9 Interdiffusion at the interfaces

Very often interdiffusion at the interfaces occurs, usually causing the IEC and the magnetoresistance to decrease. An interesting case is $\text{bcc}(100)/\text{Fe}/\text{Si}/\text{Fe}(\text{bcc})$ since the regime of antiferromagnetic coupling is increased by interdiffusion, see Fig. 5. In this figure interface interdiffusion is restricted to a two-layer interdiffusion, meaning that the layers $\text{Fe}_c\text{Si}_{1-c}$ and $\text{Fe}_{1-c}\text{Si}_c$ form the interface, while all other layers remain "pure". For the magnetoresistance (see Fig. 6), however, interdiffusion in this system is disastrous as Fig. 7 shows. Independent of the spacer thickness a two-layer interdiffusion corresponding to an interdiffusion concentration of about 15 - 20% almost kills the effect. This is the very reason of why up-to-now in this system only a very

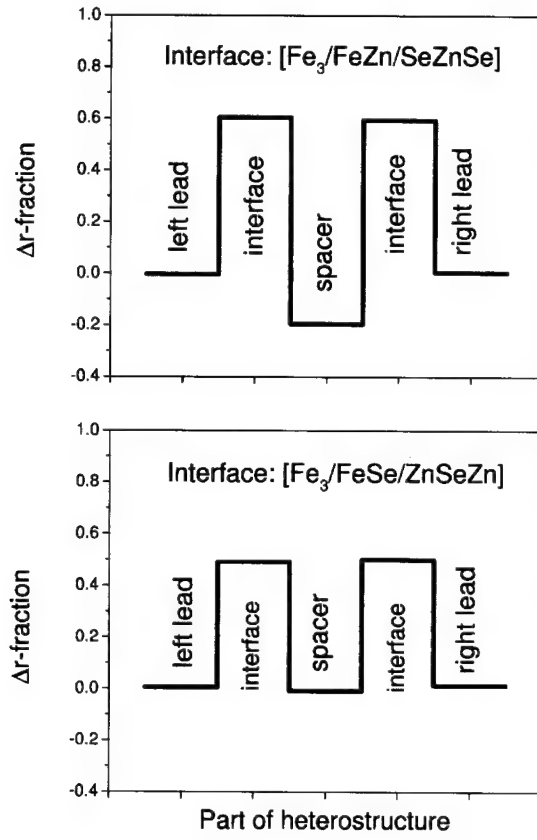


Figure 4: Normalized fractions of the difference in the sheet resistance between the antiferromagnetic and the ferromagnetic configuration in $\text{Fe}(100)/(\text{ZnSe})_{21}/\text{Fe}(100)$. The various regions of the heterostructure are given explicitly. From ref. [19].

small magnetoresistance ratio of less than 2% was found experimentally. Since however, the formation of ordered or disordered silicides at the interface is almost unavoidable, a Fe/Si/Fe heterojunction is probably a very bad candidate for a "TMR-device" (TMR: "tunneling magnetoresistance").

10 Tunneling or not-tunneling?

In the top part of Fig. 8 an interesting case is displayed, namely the layer-resolved Madelung potentials in the "academic" heterojunction bcc-Fe(100)/Fe₁₂Vac₁₂Fe₁₂/Fe(100) and modifications thereof in the interior part of the vacuum barrier. The lower part of this figure shows the corresponding changes in the parallel sheet resistance if the barrier is increased. As can be seen there is a very sharp increase of the sheet resistance as the value of the barrier increases. It should be noted that the open symbols in the top part of this figure correspond to the selfconsistent values, all other barrier heights are shifted by a constant with respect to the selfconsistent value. Fig. 9 presents the outcome of the opposite situation, namely reducing the value of the barrier. As can be seen (Fig. 9, top) the layer-resolved sheet resistances in the parallel configuration are reduced in the interior of the vacuum barrier as the barrier height is decreased. In the lower part of this figure the corresponding magnetoresistance ratios are depicted. As the barrier height is approaching the value of the Madelung potential in the semi-infinite leads (vertical line) a kink seems to develop separating the regime of metallic conducting from a regime of "tunneling". This figure suggests that any heterostructure with an average barrier for a (non-metallic) spacer of about less than 2 eV will show a reasonable magnetoresistance ratio. Whether this is due to "tunneling" or very bad metallic conductance has to be argued in terms of the functional form of the sheet resistances with respect to the imaginary part of complex Fermi energies, see Fig. 3. Arguments in terms of (decaying) states, etc., unfortunately have little in common with the product of two Green's function in the Kubo-Greenwood equation. Perhaps an experimentalist's resumé [21], namely "*tunneling is rare*", is the most witty answer to resolve the academic question of tunneling or not-tunneling.

11 Conclusion

It was shown that the present approach of evaluating CPP transport not only leads to a correct description of sheet resistances and magnetoresistance ratios for heterojunctions with in general interdiffused interfaces, but can be used also to discuss the role of interfaces. Furthermore, in terms of a physical interpretation of the imaginary part of the Fermi energy an essentially new aspect of the occurrence of tunneling can be given. In particular the lower part of Fig. 9 indicates that there is a kind of cusp that separates metallic from a "non-metallic" conductance, which seems to characterize also quite generally realistic heterojunctions between magnetic metals and semi- or non-conducting material.

Acknowledgement

The author is grateful for many discussions with V. Drchal, P. M. Levy, C. Sommers and L. Szunyogh. Investigations reported in this paper were financially supported in part by the Austrian Ministry of Science via special projects.

References

- [1] R. Kubo, "Statistical-mechanical theory of irreversible processes. I. General theory and simple application to magnetic and conduction problems", J. Phys. Soc. Japan **12**, 570 (1957).
- [2] R. Kubo and S. J. Miyake, "Quantum theory of galvanomagnetic effect at extremely strong magnetic fields", Solid State Phys. **17**, 269 (1965).
- [3] R. Kubo, M. Toda, and N. Hashitsume, *Statistical Physics II: Nonequilibrium Statistical Mechanics*, Springer Verlag, Berlin, 1985.
- [4] D. A. Greenwood, "The Boltzmann equation in the theory of electrical conduction in metals", Proc. Phys. Soc. **71**, 585 (1958).
- [5] E. Y. Tsybal and D. G. Pettifor, "Perspectives of Giant Magnetoresistance", Solid State Physics Vol. **56**, 113 - 237 (2001).
- [6] P. M. Levy and I. Mertig, "Theory of Giant Magnetoresistance", Advances in Condensed Matter, Vol. 3 Science (Ed. by D.D. Sarma, G. Kotliar and Y. Tokura), Taylor & Francis, London and New York (2002).
- [7] H. Eschrig, *Fundamentals of Density Functional Theory*, B. G. Teubner Verlagsgesellschaft, Stuttgart, Leipzig, 1996.
- [8] P. Weinberger and L. Szunyogh, "Perpendicular magnetism", Computational Materials Science **17**, 414 (2000).
- [9] P. Weinberger, *Electron Scattering Theory for Ordered and Disordered Matter*, Clarendon Press (Oxford University Press), 1990.
- [10] P. Weinberger, P.M. Levy, J. Banhart, L. Szunyogh and B. Úfalussy, "Band structure and electrical conductivity of disordered semi-infinite systems", J. Phys. Cond. Matt. **8**, 7677 (1996).
- [11] P. Weinberger, "Ab initio theories of electric transport in solid systems with reduced dimensions", Physics Reports, in press (2003).

- [12] P. M. Levy, Solid State Physics Vol. 47, eds. H. Ehrenreich and D. Turnbull (Academic Press, Cambridge, MA, 1994) pp. 367-462.
- [13] H. E. Camblong, P. M. Levy, and S. Zhang, "*Electron transport in magnetic inhomogeneous media*", Phys. Rev. B **51**, 16052 (1995).
- [14] B. Nikolić, "*Deconstructing Kubo formula usage: exact conductance of a mesoscopic system from weak to strong disorder limit*", Phys. Rev. B **64**, 165303 (2001).
- [15] P. Weinberger, L. Szunyogh, C. Blaas, and C. Sommers, "*Perpendicular transport in Fe/Ge heterojunctions*", Phys. Rev. B **64**, 184429 (2001).
- [16] P. Weinberger, "*Exchange bias due to configurational magnetic rearrangements*", Phys. Rev. B **65**, 014430 (2002).
- [17] H. J. F. Jansen, "*Magnetic anisotropy in density-functional theory*", Phys. Rev. B **59**, 4699 (1999).
- [18] P. Weinberger, V. Drchal, J. Kudrnovsky, I. Turek, H. Herper, L. Szunyogh and C. Sommers, "*Aspects of magneto-tunneling drawn from ab-initio type calculations*", Philos. Mag. B **82**, 1027 - 1045 (2002).
- [19] H. C. Herper, P. Weinberger, A. Vernes, L. Szunyogh, and C. Sommers, "*Electric transport in Fe/ZnSe/Fe heterostructures*", Phys. Rev. B **64**, 184442 (2001).
- [20] H. Herper, P. Weinberger, L. Szunyogh, and C. Sommers, "*Interlayer exchange coupling, magnetic anisotropy and perpendicular electric transport in Fe/Si/Fe trilayers*", Phys. Rev. B **66**, 064426 (2002).
- [21] J. J. Akerman, I. K. Schuller, J. M. Slaughter, and R. W. Dave, "*Tunneling criteria for magnetic-insulator magnetic structures*", J. Appl. Phys. Lett. **79**, 1, (2001).

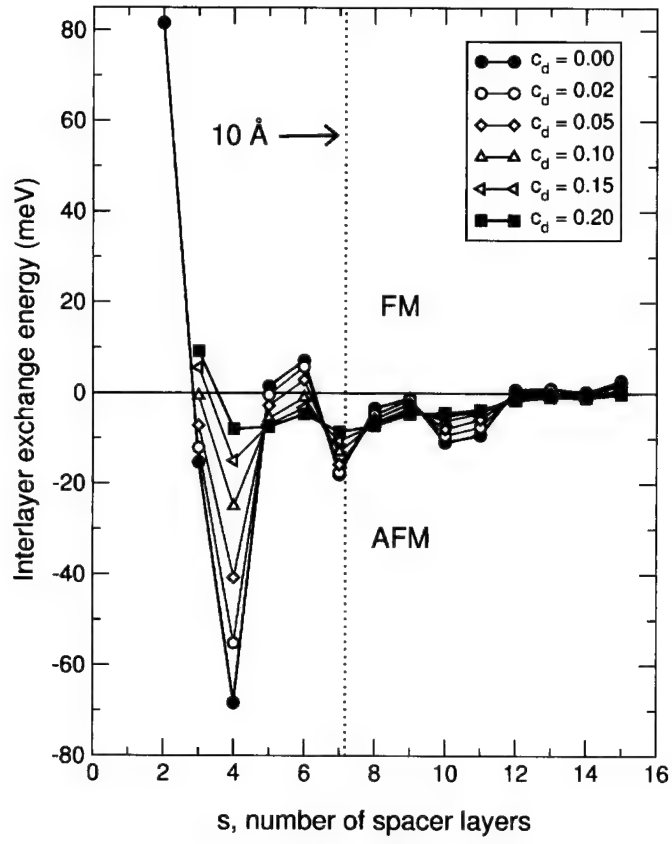


Figure 5: Changes of the IEC in bcc-Fe(100)/Si_s/Fe(100) with respect to the number of spacer layers for different interdiffusion concentrations c_d . From ref. [20].

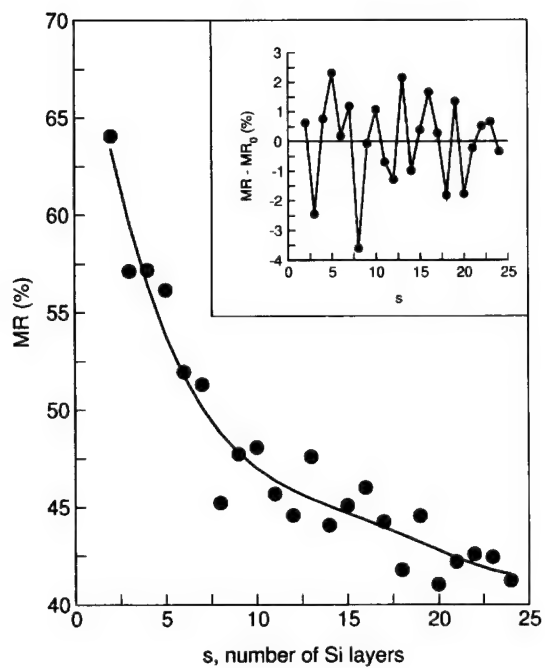


Figure 6: Magnetoresistance for Fe/Si_s/Fe trilayers versus the number of Si spacer layers s . The full line is a 4th order fit of the magnetoresistance to the data points. Inset: Difference between the calculated points and the fit depending on the number of Si layers. From ref. [20].

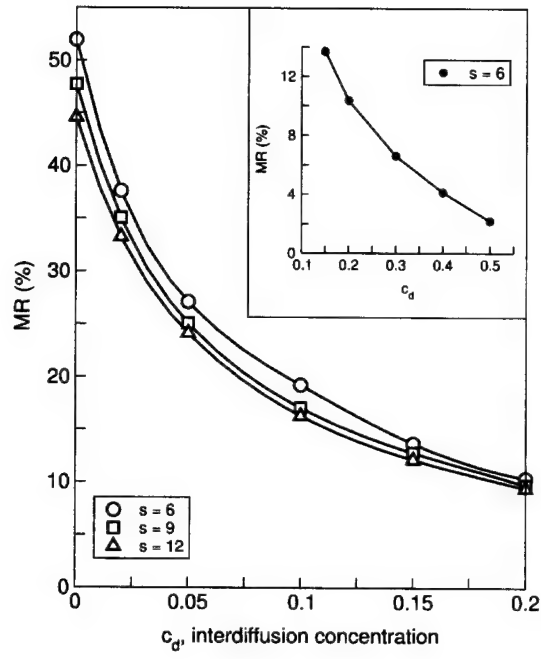


Figure 7: Dependence of the magnetoresistance on the interdiffusion concentration for Fe/Si_s/Fe systems. From ref. [20].

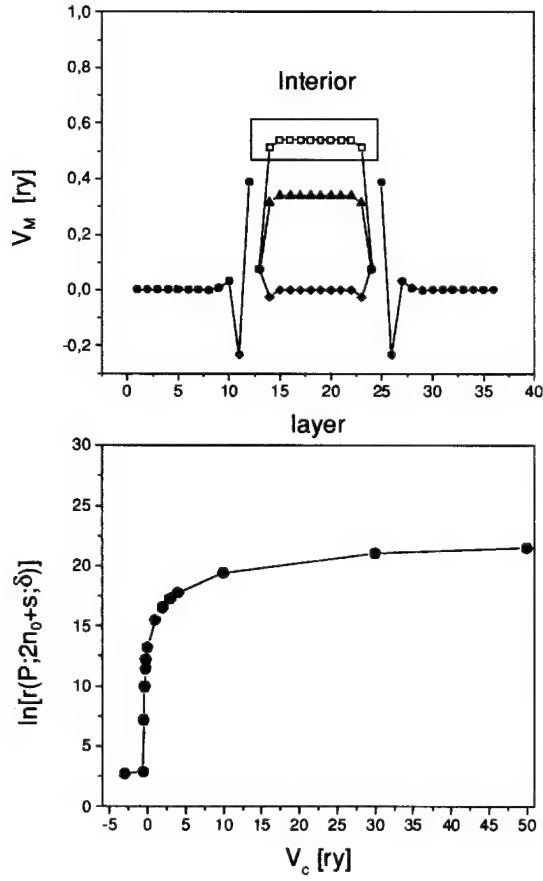


Figure 8: Top: Layer-resolved Madelung potentials and shifted potential barriers in the vacuum region of bcc-Fe(100)/Fe₁₂Vac₁₂Fe₁₂/Fe(100). Circles: Fe; squares, triangles and diamonds refer to the vacuum region with $V_C = 0$, -0.2 ry and $-V_M$, respectively. Bottom: $\ln[r(\mathcal{P}; 2n_0 + s; \delta)]$, $n \geq 11$, $\delta = 2$ mry, of bcc-Fe(100)/Fe₁₂Vac₁₂Fe₁₂/Fe(100) as a function of V_C . V_M denotes the selfconsistently determined barrier height in the center layer of the vacuum region. From ref. [18].

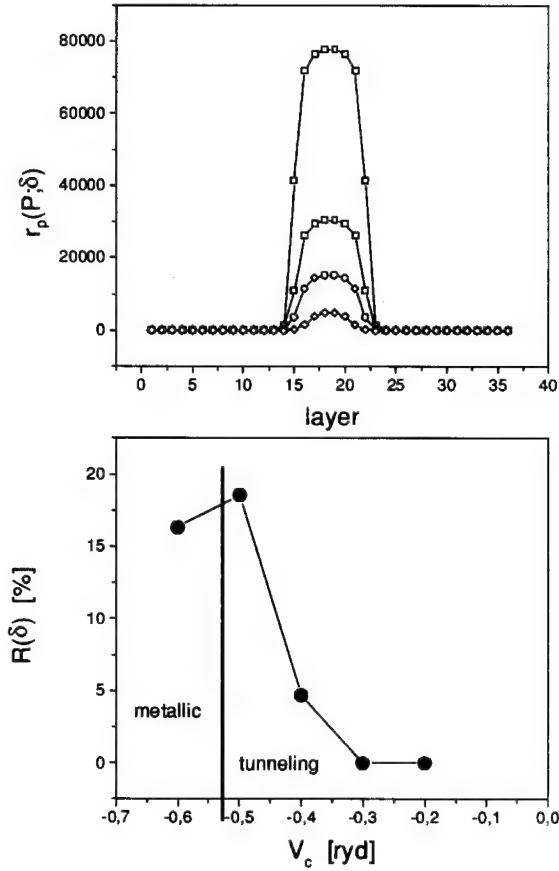


Figure 9: Top: Sheet resistance $r(P; 2n_0 + s; \delta)$ (top) and magnetoresistance $R(2n_0 + s; \delta)$ (bottom), $\delta = 2$ mry, in bcc-Fe(100)/Fe₁₂Vac₁₂Fe₁₂/Fe(100) as a function of the constant shift V_C . In the top part squares, triangles, circles and diamonds refer to $V_C = 0, -0.2, -0.3$ and -0.4 ryd, respectively, in the lower part the regimes of metallic and tunneling behavior of electric transport are separated by the condition $V_M = -V_C$ (vertical line). V_M denotes the selfconsistently determined barrier height in the center layer of the vacuum region. From ref. [18].

In-Plane Transport of Doped Manganite Trilayers

Lisa Berndt Alldredge

School of Applied & Engineering Physics, Cornell University, Ithaca, NY 14853

Y. Suzuki

Dept. of Materials Science & Engineering, Cornell University, Ithaca, NY 14853

[†] presently at Dept. of Materials Science & Eng., UC Berkeley, Berkeley, CA 94720

ABSTRACT

We have synthesized and characterized doped manganite trilayers composed of $\text{La}_{0.7}\text{Sr}_{0.3}\text{MnO}_3$ (LSMO) and $\text{La}_{0.7}\text{Ca}_{0.3}\text{MnO}_3$ (LCMO). Because of the isostructural nature of the Sr and Ca doped manganites, trilayers exhibit good epitaxy as observed in X-ray diffraction. Magnetization measurements reveal magnetization values consistent with bulk values. In-plane transport of these trilayers reveals anisotropic magnetoresistance and high field negative magnetoresistance attributed to the suppression of spin fluctuations at high fields.

INTRODUCTION

Colossal magnetoresistance (CMR) materials consist of a group of doped perovskite manganites of chemical composition $\text{A}_{1-x}\text{B}_x\text{MnO}_3$ (where A = trivalent rare earth and B = divalent alkaline earth). While the phase diagram of the doped manganites is rather complicated and includes ferromagnetic, antiferromagnetic, and paramagnetic phases, insulating and metallic phases and charge ordered phases, the subclass of materials that exhibit a transition from a ferromagnetic metallic phase to a paramagnetic insulating one are known as CMR materials. They exhibit large changes in resistance under an applied magnetic field and thus have been the subject of extensive research due to their possible application in computer read/write heads and storage devices. Magnetoresistance (MR) values as high as 80% in LCMO at ~200K and 35% in LSMO at ~330K have been observed under high magnetic fields (~5 Tesla).

Many groups have studied CMR and CMR-based devices in the hopes of obtaining large magnetoresistances at low fields and at room temperature. Some research groups have focused on fabricating CMR-based magnetic tunnel junctions to this end. Initial studies of CMR tunnel junctions have shown junction magnetoresistance (JMR) behavior on field scales as low as ~50 Oe [1,2]. Subsequent studies have shown JMR values as high as 100% at 13K [3,4]. However, JMR decreases rapidly with increasing temperature and vanishes by room temperature. In magnetic tunnel junctions, the interface quality, tunnel barrier quality, surface/interface roughness, ferromagnetic electrode quality,

magnetic domain walls as well as the intrinsic behavior of ferromagnetic surfaces/interfaces greatly affect the JMR. It has greatly complicated the interpretation of transport data and may contribute to the premature suppression of spin polarized tunneling to temperatures below the Curie temperature of the CMR electrodes. More recently, near room temperature operation of CMR-based tunnel junctions has also been observed by Obata et al. [5]. To minimize interface disorder, Goodenough's group incorporated a tunnel barrier of $(\text{La}_{0.85}\text{Sr}_{0.15})\text{MnO}_3$ between $\text{La}_{0.7}\text{Sr}_{0.3}\text{MnO}_3$ electrodes and obtained JMRs at temperatures as high as 295K [6].

Our approach has been to study magnetotransport in trilayers and tunnel devices composed of isostructural materials of $\text{La}_{1-x}\text{Sr}_x\text{MnO}_3$ and $\text{La}_{1-y}\text{Ca}_y\text{MnO}_3$ where good epitaxy can be obtained. In this paper, we present the synthesis and characterization of doped manganite trilayers of $\text{La}_{0.7}\text{Sr}_{0.3}\text{MnO}_3$ (LSMO) and $\text{La}_{0.7}\text{Ca}_{0.3}\text{MnO}_3$ (LCMO). The layers can grow coherently on one another by only changing one species ($\text{Sr} \rightarrow \text{Ca}$). Such structures have minimal lattice mismatch strain at the interfaces and therefore optimal interface quality.

EXPERIMENTAL SETUP

The epitaxial CMR thin film trilayers were deposited in a pulsed laser deposition (PLD) system with a KrF excimer laser (248nm) operating at 10 Hz with an energy density of $\sim 3 \text{ J/cm}^2$ for LSMO and LCMO. The films were deposited on (001) SrTiO_3 (STO) substrates. In this paper, we will describe the orientation of the manganites in terms of the pseudocubic lattice parameters $a'_{\text{bulk}} = b'_{\text{bulk}} = c'_{\text{bulk}} = 3.87\text{\AA}$. These lattice parameters are rotated 45 degrees from the rhombohedral, nearly cubic lattice parameters $a_{\text{bulk}} = b_{\text{bulk}} = c_{\text{bulk}} = 5.48\text{\AA}$. STO substrates place the overlying LSMO films under tensile strain. We grew trilayers with 350 to 1000Å thick LSMO electrodes and 20 to 100Å thick LCMO barrier layers.

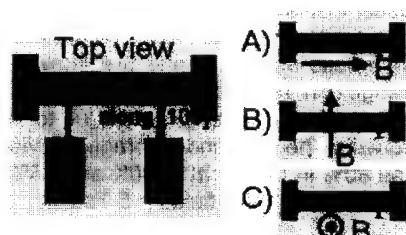


Figure 1. Schematic of resistivity bar for in-plane transport measurements (left). The magnetic field was applied in three different orientations (right): (A) in-plane and parallel to the current, (B) in-plane and perpendicular to the current, and (C) out of plane.

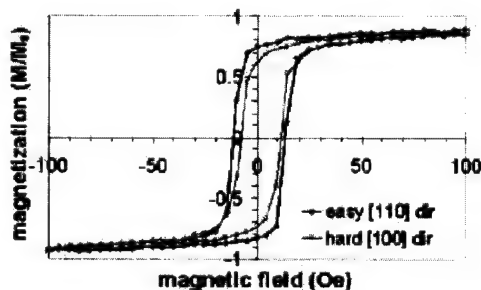


Figure 2. Vibrating sample magnetometer magnetization data for a LSMO trilayer film on a (001) STO substrate showing an easy [110] direction and a hard [100] direction.

X-ray diffraction of the trilayers was performed on a Scintag, Inc. theta-theta diffractometer to verify the epitaxy of the films. A vibrating sample magnetometer and a superconducting quantum interference device (SQUID) magnetometer were used to take magnetization measurements.

In-plane transport measurements were taken in a physical property measurement system. The trilayer films were patterned into resistivity bars using argon ion milling. The current was applied along the [100] direction, and the resistivity was measured with three possible orientations between the current and the magnetic field (Figure 1).

RESULTS AND DISCUSSION

X-ray diffraction 2θ measurements of the trilayer films only showed distinct peaks corresponding to the (001) orientation of LSMO films and the STO substrates, demonstrating the epitaxy of the trilayers.

Magnetization measurements taken with a SQUID magnetometer show that LSMO has a Curie temperature T_C of $\sim 350\text{K}$, while LCMO has a T_C of $\sim 250\text{K}$. The magnetic behavior of the trilayer films was similar to that of LSMO single layer films, with a decrease in magnetization and coercive field with increasing temperature. As shown in our previous work, in (001)-oriented LSMO films, the magnetocrystalline anisotropy gives rise to an in-plane easy direction along [110] and equivalent directions, and the hard directions are [100] and [010] [7]. As expected, the trilayer films show the same easy and hard directions (Figure 2). Moreover, the trilayer magnetization values are consistent with bulk values.

In-plane transport measurements were taken by first sweeping the magnetic field from high positive field to high negative field and then back to high positive field. All measurements show a negative, linear MR at high fields, which is attributed to

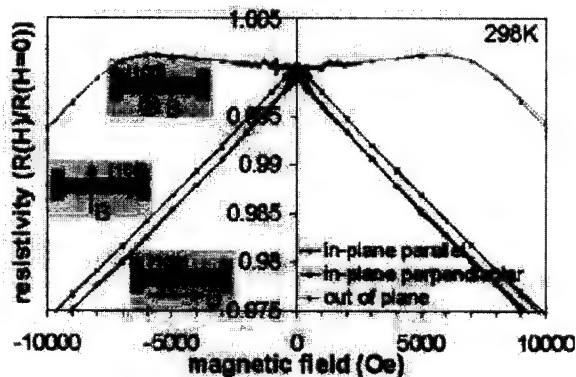


Figure 3. In-plane transport measurements at room temperature taken in the configurations A, B and C as marked.

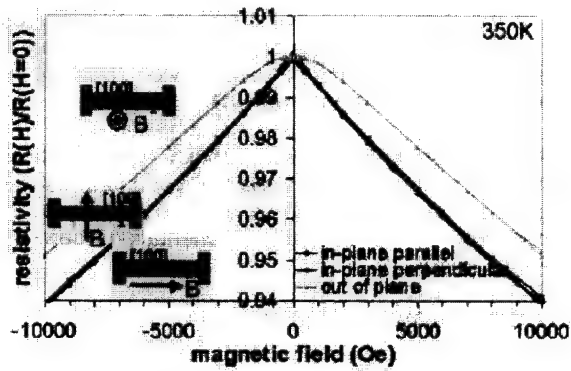


Figure 4. In-plane transport measurements at 350K taken in the configurations A, B and C as marked.

the suppression of spin fluctuations at high magnetic fields (CMR). The MR in the out-of-plane orientation (configuration C) is shifted due to demagnetization effects as seen in Figure 3. The curve exhibits demagnetization effects around 5kOe as well as irreversibility at ~ 1.5 kOe. The irreversibility corresponds to the domain wall motion that is observed in the magnetization loops.

In the in-plane perpendicular orientation of the current and field (configuration B), a positive MR is seen at low fields that crosses over to negative MR at higher

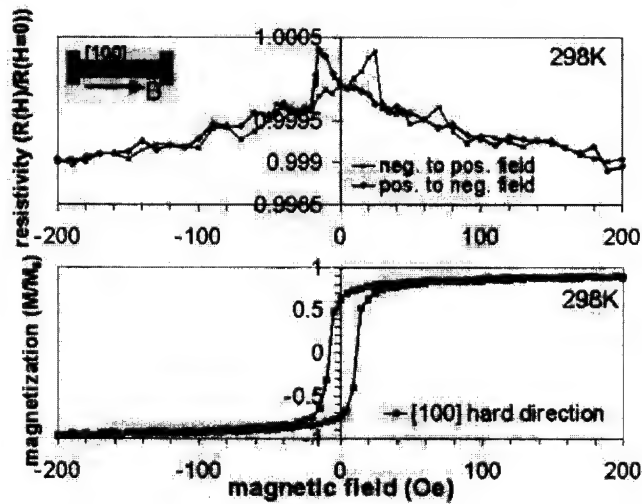


Figure 5. Low field in-plane transport measurements for the in-plane parallel field configuration (A) (top) and magnetization measurements (bottom) taken at room temperature.

fields. The field at which the crossover occurs does not correspond to the shape effect of the transport bar [8,9]. In fact, the field corresponds to the magnetic anisotropy field of the film. In the in-plane parallel orientation (configuration A), the MR exhibits a linear dependence with a superlinear deviation at low fields and an irreversibility corresponding to the coercive field. The MRs in the in-plane parallel and in-plane perpendicular orientations are shifted with respect to one another due to anisotropic magnetoresistance (AMR). AMR occurs when the resistance depends on the orientation between the magnetization and the current. In LSMO, the resistance is less when the magnetization is parallel to the current versus perpendicular to the current [10]. However, the AMR disappears for transport measurements taken just below the T_c of LSMO as the magnetization has decreased almost to zero (Figure 4).

In the in-plane parallel orientation (A), as soon as the magnetic field is decreased to below the anisotropy field, the magnetic moments rotate away from the applied field direction of [001] into the magnetically easy [110] directions. The magnetization is no longer pointing parallel to the current, and the MR increases, hence a superlinear deviation (Figure 5). However, for the in-plane perpendicular orientation (B), the magnetic moments start out pointing perpendicular to the current and then rotate to the easy diagonal directions. Since they are pointing more along the current in decreasing magnetic field, the MR drops, and hence we observe the sublinear deviation or a crossover from negative to positive MR (Figure 6). Moreover, we see that the hysteretic behavior of the low field MR in the in-plane configurations (see Figure 5,6) corresponds to the coercive fields of the magnetization loops and thus to domain wall motion.

Since LCMO is an insulator, we suspect that most of the current travels through the LSMO layers, and indeed our transport measurements of trilayers are similar to those of LSMO thin films [10,11].

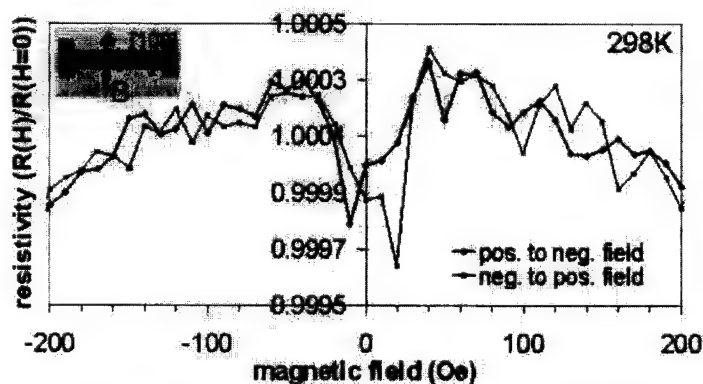


Figure 6. Low field in-plane transport for the in-plane perpendicular configuration (B) taken at room temperature.

CONCLUSIONS

We have synthesized and characterized doped manganite trilayers composed of LSMO and LCMO. Given the isostructural nature of the trilayer, with the substitution of the alkaline earth dopant, there is minimal disorder at the interfaces of the layers, and therefore, we are able to obtain trilayers with good epitaxy. In-plane transport measurements reveal the main MR effects to be CMR and anisotropic MR.

ACKNOWLEDGEMENTS

We acknowledge support from the National Science Foundation, in particular the MRSEC and Central Facilities at Cornell University.

REFERENCES

1. X. Li et al., J. Appl. Phys. **81** 5509 (1997).
2. J.Z. Sun et al., Appl. Phys. Lett. **73** 1008 (1998).
3. J.S. Noh et al., Appl. Phys. Lett. **79** 233 (2001).
4. Moon-Ho Jo et al., Appl. Phys. Lett. **77** 3803 (2000).
5. T. Obata et al., Appl. Phys. Lett. **74** 290 (1999).
6. H.Q. Yin et al., Appl. Phys. Lett. **77** 714 (2000).
7. L.M. Berndt et al., Appl. Phys. Lett. **77** 2903 (2000).
8. E.C. Stoner, Philos. Mag. **36** 803 (1945).
9. H.N. Bertram, Theory of Magnetic Recording (Cambridge University Press, New York, 1994), p. 172.
10. Y. Suzuki and H.Y. Hwang, J. Appl. Phys. **85** 4797 (1999).
11. Yan Wu et al., Appl. Phys. Lett. **75** 2295 (1999).

Complex magnetic response in magnetic tunnel junctions determined via magnetic and transport measurements

R.Guerrero¹, V.V.Pryadun¹, F.G.Aliev^{1*}, R.Villar¹, J.L.Martinez² and J.Moodera³

(1) *Dpto. de Física de la Materia Condensada, C-III,*

Universidad Autonoma de Madrid, 28049, Madrid, Spain

(2) *ICMM-CSIC, Cantoblanco, 28049, Madrid, Spain and*

(3) *Massachusetts Institute of Technology,*

Cambridge, Massachusetts, 02139, USA

We have studied the low frequency complex magnetization dynamics in $\text{Co}/\text{Al}_2\text{O}_3/\text{Ni}_{80}\text{Fe}_{20}$ magnetic tunnel junctions (MTJs) at temperatures between 4.2K and 300K. The measurements were carried out by using two different experimental techniques. The first method probes directly magnetic properties via DC magnetization and AC susceptibility, while the second one measures AC magnetization dynamics of the ferromagnetic electrodes near the cross area, which is related to the tunnelling resistance.

* - corresponding author: farkhad.aliev@uam.es

INTRODUCTION

Magnetic tunnel junctions (MTJ) with highly reliable magnetoresistance [1] are promising candidates for non-volatile memory, next generation of magnetic field sensors hard drive heads as well as important parts of more complicated magnetic nanostructures [2]. It was found recently that the magnetic domain walls (DWs) formed in the magnetic electrodes and correspondingly within cross area, may significantly affect operation of the MTJs, resulting in some cases even in long term degradation of the devices [3]. In addition, it is known that DWs strongly influence the noise of the magnetoresistive sensors [4, 5]. In their study of magnetic noise in magnetic multilayers Hardner et al. [4] proposed a simple method for evaluating dynamic magnetic properties of the systems with giant magnetoresistance (GMR) by studying the response in the electron transport of the structure subject to both DC and AC magnetic fields. Although DC transport and magnetic properties of MTJs

are reasonably well understood, little is known [6] about the AC magnetic and transport responses of MTJs. Knowledge of dynamic magnetic properties of MTJs could provide information about mechanisms of magnetization reversal, domain wall mobility, disorder and other characteristics of MTJs, important both for fundamental and applied research, and not accessible in the DC experiments. Indeed, a method proposed for investigation of the DW dynamics in magnetic nanowires by employing GMR effect as a detector [7], could not be directly applied to the standard MTJs because their geometry permits two-dimensional movement of the DWs. A recent demonstration of the applicability of the tunnel magnetoresistance (TMR) signal for analysis of the DWs structure in MTJs, completed by magnetic force microscopy [8] or magnetooptic analysis [9], reveals some interesting static, but not dynamic properties of the domain walls. This paper presents an investigation of the low frequency (below 100Hz) AC magnetization response of MTJs studied both via direct magnetic measurements and by using the TMR effect as spin detector.

SAMPLE PREPARATION AND EXPERIMENTAL SETUP

Details of sample preparation and characterization were described previously in [1]. In brief, a 1nm of Si is deposited on a glass substrate at 77K as a seed layer. Then cobalt (hard layer with thickness of 8nm) and aluminium (depending on the samples the thickness of Al was varied between 0.6nm and 1nm) layers were deposited at the same temperature. At the next stage, the samples were warmed to room temperature, and oxidation of the barrier was produced by glow discharge, followed by deposition of the permalloy layer (soft layer with thickness of 10nm), a magnetic field, of about 50Oe , was applied while the deposition of both magnetic electrodes, in order to fix the magnetic anisotropy of the layers. In the present study we used a sample with a cross area definition of $200 \times 200\mu\text{m}$, the room temperature (RT) resistance is about $1\text{ k}\Omega$, and the magnetoresistance is 12% (RT) and 18% (4.2K).

Direct DC magnetization (M) and AC magnetic properties (χ'_M and χ''_M) were studied by using a MPMS (Quantum Design) with the magnetic field directed along the easy axis of magnetization. Sample used in this experiments have the same dimensions as the one used in the transport measurements.

In order to measure the magnetic dynamic response via electron transport we developed a setup similar to ref. [4]. Our sample was introduced in an Oxford cryostat which allows

to vary the temperature from $300K$ to $4.2K$. The magnetic field was applied by using two solenoids placed outside the vacuum chamber. A DC current source controls the magnetic field H , directed along the easy axis of the sample. The AC source generates a small sinusoidal magnetic field with a frequency f and an amplitude δH parallel to the DC field. The sample has been biased by a DC current equal to $100\mu A$ in all the presented experiments. The AC signal generated in the sample as a response to the external AC magnetic field was detected by a lock-in amplifier and the DC response by a nanovoltmeter. In this way we obtain the in-phase ($X = \chi'_V(f) \cdot \delta H$) response which is proportional to the derivative $\frac{dV}{dH}$, and the imaginary response ($Y = \chi''_V(f) \cdot \delta H$) reflecting magnetic losses. In the following this method will be called as the indirect method.

RESULTS AND DISCUSSION

Figure 1 presents typical X and Y voltage responses obtained in the indirect method, at a drive frequency of $77Hz$, at a temperature $T = 77K$ and at two different excitations, when the DC field is varied. The curves were averaged over 6 measurements. The inset

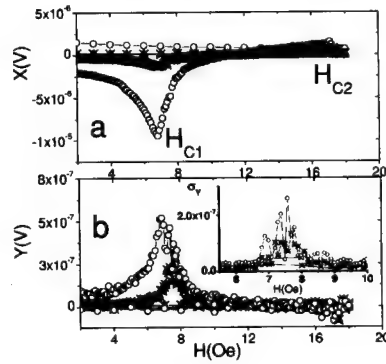


Figure 1: (a) Typical in-phase signal X and (b) out of phase signal Y as functions of the applied DC field for two different amplitude excitations $\delta H = 50mOe$ and $7mOe$, at $77K$ and $f = 77Hz$. Inset in (b) shows typical deviation (σ_Y) of the curve, the increase of this magnitude after the maximum indicates the change of the behavior of the losses in the permalloy layer from rotations to magnetization jumps.

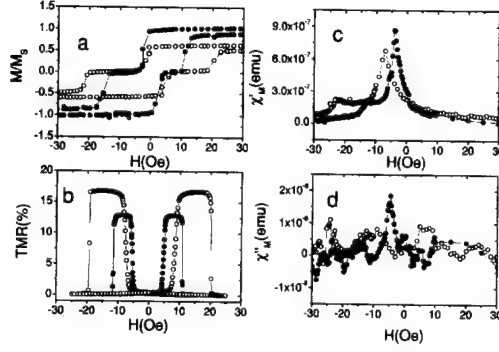


Figure 2: Tunnelling magnetoresistance of the MTJ used in the noise measurements and magnetic properties of a MTJ with the same composition as the one used for the indirect measurements. At 300K (closed points) and 4.2K (open points). Panel (a) shows the magnetization of the junction. Graph (b) presents tunnelling magnetoresistance defined as $TMR = [R_{AP} - R_P]/R_{AP}$. Panels (c) and (d) show AC susceptibility measurements at $f = 6Hz$ and $\delta h = 0.2Oe$. Part (c) is the real part and (d) is the imaginary part.

shows the corresponding dispersion for such averaging. The anomalies at the coercive fields $H_{C1} = 6 \pm 0.5G$ and $H_{C2} = 16 \pm 1G$ are related to orientation transitions in the cobalt and permalloy. We should also point out that typically the shape of the maximum in losses obtained via TMR is non-symmetric. Usually one observes a gradual increase in χ''_V when approaching H_{C1} (i.e. for $H < H_{C1}$) followed by an enhancement of the dispersion when $H \gtrsim H_{C1}$. This could be due to a gradual growth of the small domains for $H < H_{C1}$, followed by the process of converting them into larger ones, corresponding to a decrease in χ''_V and an enhanced Barkhausen noise.

Figure 2 shows the data obtained in the magnetic measurements at RT (closed points) and 4.2K (open points). Part a the DC magnetization, c and d are the real and the imaginary part of the AC susceptibility, respectively. Panel b is the magnetoresistance of the sample used in the transport measurement. Coercive fields in both samples are nearly the same.

Comparison of the data obtained in both methods points out some similarities and differences between magnetic susceptibility and the transport measurements. Independently of temperature, frequency or drive amplitude, for both signals we observe two anomalies

in their real parts, reflecting coercive fields H_{C1} and H_{C2} of permalloy and cobalt (Fig. 1a and 2c). The deep of the minimum in between the two transitions in the real part of the AC susceptibility depends on the degree of antiparallel alignment and, in addition, maybe affected by the edge effects coming from the electrodes.

The direct out-of phase measurements shows that the maximum in $\chi''_M(f)$, which corresponds to the losses during magnetization reversal in permalloy, disappears for temperatures below $77K$ (see Fig. 2d which compares data at $300K$ and $4.2K$). The situation is different for the indirect method where the maximum in $\chi''_V(f)$ near H_{C1} is clearly observed down to $4.2K$ (only data for $77K$ is shown here). The different behavior observed at low temperature is due to the sensitivity of the indirect method to the interface magnetization, because only few monolayers of permalloy, those near the barrier, contribute to the tunnel process. Therefore, one could argue that the DWs (or magnetic inhomogeneities) at the interface are free to move at low temperatures, when bulk domains became pinned. This results in the suppression of the maximum in the imaginary susceptibility at low temperature.

Finally we present the dependence of the complex response on the drive amplitude δh . Figure 3 shows the magnitude of the anomaly near the coercive field of permalloy layer as a function of the excitation amplitude. One can observe that, while the real part of

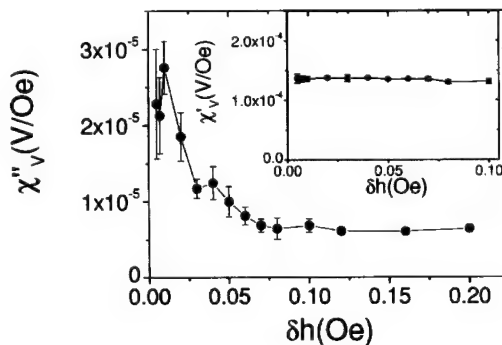


Figure 3: Dependence of the amplitude of the peak near the coercive field of permalloy at room temperature. Main part of the figure shows the amplitude of the peak in the imaginary part of the response. The inset shows the same quantity in the real part. Qualitatively similar behavior is observed at low temperatures.

the response changes linearly with δh ($\chi'_V \sim \text{constant}$), the imaginary response strongly deviates from linearity at low excitations. Magnetoelastic coupling cannot explain this data [10], because it depends on the DWs velocity, which seems to be too high comparing with the dimension of the sample divided by the excitation frequency. One could also think in terms of a transformation of the DW type when δh is increased. However, the thickness of our samples (10nm) is too small to provide such a transition. We believe that the observed nonlinearity in the out-of phase response (with a linear in-phase response) could be due to a strong dependence of the relaxation time on δh . Presence of structural and magnetic disorder at the oxide-ferromagnet interface in magnetic tunnel junctions could be a reason for the strong dependence of the relaxation time on the excitation. Further work is, however, needed to clarify this issue.

Authors are grateful to A.P.Levanuyk for critical reading of the manuscript and numerous discussion. The work was supported in parts by Spanish MCYT (BFM2000-0016) and by Comunidad de Madrid (07N/0050/2002).

-
- [1] J.S. Moodera, L.R. Kinder, T.M. Wong and R. Meservey, PRL, **74**, 3273 (1995).
 - [2] Stuart.S.P.Parkin, "Spin-Polarized Transport in Magnetic Tunnel Junctions and Magnetic Tunnel Transistors"- invited talk presented at Gordon Research Conference on magnetic nanostructures in Italy, 2002.
 - [3] S.Gider, et al., Science **281**, 797 (1998).
 - [4] H.T.Hardner, M.B.Weismann, M.B.Salamon, S.S.P.Parkin, Phys. Rev. **B48**, 16156 (1993).
 - [5] S. Ingvarson, G.Xiao, S.S.P. Parkin, W.J. Gallagher, G. Grinstein, R.H. Koch, PRL, **85**, 3289 (2000)
 - [6] P.Ripka, M.Tondra, J.Stokes, R.Beech, Sensors and Actuators, **76**, 225 (1999).
 - [7] T.Ono, H.Miyajima, K.Shigeto, K.Mibu, N.Hosoito, T.Shinjo, Science, **284**, 468 (1999).
 - [8] C.Tuisan, M.Hehn, T.Dimopolous, K.Ounadjela, J. Applied Physics, **89**, 6668 (2001).
 - [9] O.Lenoble, M.Hehn, D.Lacour, A.Schuhl, D.Hrabovsky, J.F.Bobo, B.Diouf, A.R.Fert, Phys. Rev. **B63**, 05240 (2001).
 - [10] V.G.Bar'yakhtar, B.A.Ivanov, M.V.Chetkin, Sov. Phys. Usp. **28**, 583 (1985).
 - [11] N. Papanicolaou, Phys. Rev. **B55**, 12290 (1997).

Bistable memory effect in chromium oxide junctions

A. Sokolov, C.-S. Yang, E. Ovtchenkov, L. Yuan, S.-H. Liou, B. Doudin

University of Nebraska Lincoln, Department of Physics and Astronomy, 115 Brace Laboratory, Lincoln NE 68588-0111

ABSTRACT

Magnetotransport properties of granular $\text{CrO}_2/\text{Cr}_2\text{O}_3$ films made of CrO_2 crystals covered by 1-2 nm native insulating Cr_2O_3 are presented. Electrical properties of a limited number of grains measured in series and parallel (10 to 15 grains) reveal intergrain tunneling characteristics. At lowest temperatures, a well pronounced zero bias anomaly indicates that impurities in the junctions block the electronic flow.

Hysteresis in the IV curves are observed at intermediate temperatures on zero-field cooled samples. Changing the polarity of a short excitation pulse (100ns) of amplitude smaller than 1 V triggers a change in the zero-bias resistance by 10-50%. These states are stable and well reproducible in the temperature interval ranging from 100K to 250K. Applying an external magnetic field cancels the IV hysteresis. The resistance of the devices in the $\text{k}\Omega$ range, the potential high-speed for writing and reading the resistance state, make these systems interesting candidates for magnetic non-volatile memories.

INTRODUCTION

The integration of magnetic materials in electronic components has become of increasing importance since the boost of research and development efforts initiated by the discovery of giant magnetoresistance effects. This new area of "spintronics" [1] opens the possibility to use magnetic configuration control as an extra degree of freedom for tuning the electric transport properties. The materials with high degree of spin polarization are the most desired for potential application in metal/insulator/metal devices [2], and magnetic multilayer geometries [3, 4].

Chromium dioxide (CrO_2) is among the best candidates for half-metallic ferromagnetic systems. Evidence of large spin polarization of conduction electrons has been observed using several methods [5-7]. Magnetoresistance (MR) measurements have been reported in polycrystalline films [8-10], epitaxial films [10-12] and powder compacts of CrO_2 [13]. Magnetoresistance values reaching 50% have been observed on $\text{CrO}_2/\text{Cr}_2\text{O}_3$ composites at low temperature [13]. The results were explained in terms of intergrain tunneling, and the large magnetoresistance (MR) values were attributed to the high degree of spin polarization existing in CrO_2 . In spite of relatively high T_c , of about 390K, the MR value decays rapidly with increasing temperature and disappointed few percent remains at ambient temperature. A possible explanation of such a behavior is given in terms of Coulomb blockade effects [14].

Another attractive feature of spin-electronic devices is the possibility of current induced magnetization reversal. Injection of spin-polarized electric current can modify the magnetic states of a small ferromagnet. This spin-transfer effect was theoretically predicted by Berger [15] and Slonczewski [16] and there are several experiments giving evidence of modification of the magnetization configurations in nano-magnetic materials induced by an electric current [17-22].

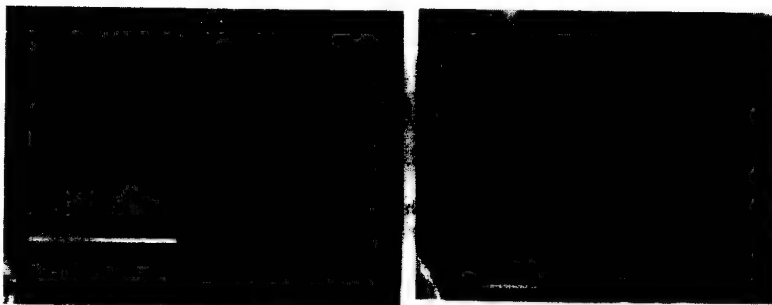


Fig.1 Optical micrograph (left) and SEM picture (right) of the chromium oxide thin films. Left picture show the geometry and typical size of mechanically scribed samples. Right picture shows a low-density film exhibiting typical sizes and shapes of the CrO_2 crystals.

In this paper we report the results of our study of compact powder CrO_2 in wide temperature interval of 1.5- 275K. Large bias current were applied in order to investigate the possibility of current-induced switching.

SAMPLE PREPARATION

Polycrystalline CrO_2 films were made by RF sputtering of a $\text{CrO}_3/\text{Cr}_2\text{O}_5$ target (obtained by sintering a pressed CrO_3 powder at 150°C) onto LaAlO_3 substrates and annealing in a high pressure cell. The sputtering was performed under of 10 mtorr argon and 2 mtorr oxygen pressure. Thickness of CrO_3 films ranged between $0.1\ \mu\text{m}$ and $1\ \mu\text{m}$. Treatment in about 100 atms of oxygen pressure at 390°C for 10 hours lead to stable CrO_2 phase, as confirmed by X-ray diffraction diagrams, with no detectable trace of Cr_2O_3 . The thinnest annealed films showed a grain density of about 10 crystals every $100\ \mu\text{m}^2$ area (Fig.1). The grains were generally elongated shapes, typically $5\ \mu\text{m}$ long and $0.5\ \mu\text{m}$ wide. Subsequent mechanical scribing allowed us to limit the sample to a limited number of crystals [14] (10-15) in series and in parallel (Fig. 1). Electrical contacts separated by typically 200 microns. Measurements were performed by DC and AC techniques in a 4-probe geometry.

RESULTS AND DISCUSSION

Photoemission experiments revealed that the CrO_2 crystals are covered by 1 - 2 nm of insulating Cr_2O_3 [23]. This thermodynamically more stable oxide phase plays the role of the native tunnel barrier between two adjacent crystallites. The temperature-dependent magnetoresistance properties for thick films (Fig. 2) are in qualitative agreement with previously reported results by others (for example [13]). The insert shows $R(H)$ curves, normalized to $R(H = 1\text{T})$. Increasing the applied field up to 9T shows continuous drop of resistance without visible saturation, which is consistent with scattering by magnetic impurities in the CrO_2 crystals [24]. Systematic studies of the IV curves and bias-dependent magnetoresistance properties, combined with photoemission studies [14], showed that the low-temperature magnetoresistance is

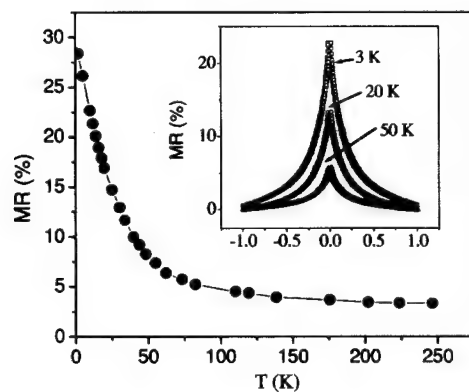


Fig.2 Temperature dependence of magnoresistance $(R(H)-R(H=1\text{ T})/R(H=1\text{ T}))$, normalized to R at $H=1\text{ T}$. Curves at several temperatures are depicted in the insert.

enhanced by Coulomb blockade effects though co-tunneling leakage current [25]. Inclusions in the barrier or near the $\text{CrO}_2/\text{Cr}_2\text{O}_3$ interface play the role of Coulomb island, of several meV blocking energy.

The related zero-bias anomaly at lowest temperature is commonly attributed to blockade of current by impurities in the barrier. Comparisons of the zero-bias anomaly width with

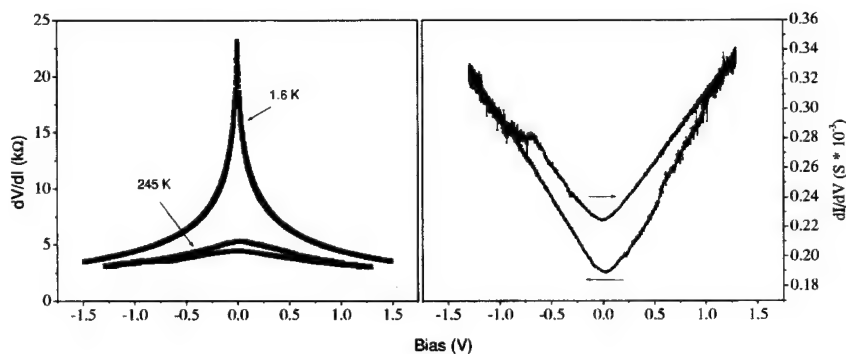


Fig. 3. Left: Differential resistance dV/dI versus applied DC bias at different temperatures. A zero bias anomaly is pronounced at low temperatures and hysteresis in the curve is found at higher temperatures. Right: Differential conductance dI/dV curve, measured at 245 K, shows indications of a threshold behavior for the hysteresis

observations by others [26], allows us to estimate that around 10 junctions are measured in series.

Sequential tunneling dominates the electronic transport in intergrain junctions at temperatures higher than several tens of K [14]. The resistance versus voltage (current) curves show non-reproducible characteristics. More precisely, hysteretic behavior in these curves is observed in temperatures ranging from 100 K to 250 K, being occasionally as low as 40 K and as high as 300 K. (Fig. 3, Fig.4). The effect disappears after applying a magnetic field typically larger than 1 kOe, and the resistance value stabilizes within the envelope of the hysteretic curve (Fig. 4). Heating effects when biasing the sample with large voltage (current) values are limited, because the normal IV curve observed after applying a magnetic field becomes hysteretic again after heating the sample to more than 400 K, and cooling under zero-field. These observations indicate that the hysteresis in the IV curves has a magnetic origin, related to the magnetic configuration at the junctions interfaces. The amplitude Δ of the bistability was investigated as a function of the maximum voltage, and a threshold-type behavior was found. We also tested the speed of the process, being able to keep the same Δ value when reducing the pulse duration down 100 ns (Fig. 5). Note that one state is less reproducible than the other when applying a voltage pulse. This observation at 245 K is related to the observation of a "fast" time decay of the high conductance state, showing a relaxation behavior of typical 10^4 s time scale at 275 K. Our experimental set-up essentially limits the pulse time, where amplifying electronics external to the cryostat are connected by significant cabling impedance, absorbing half of the charge corresponding to the 100 ns pulse.

Although the origin of this bi-stable memory effect is yet to be understood, the relevance of a model of current induced magnetization switching is discussed. The existence of threshold potential and the effect of a magnetic field could be ascribed to spin transfer on the

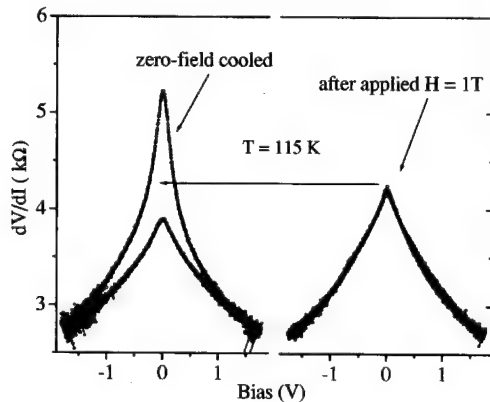


Fig. 4. Differential resistance as a function of current bias for 10-15 chromium junctions in series at 115 K. Left: the resistance value after a positive bias is significantly smaller than after a negative bias. Right: the effect disappears after applying a magnetic field.

magnetization direction of a small magnetic impurity, embedded in the barrier between two crystal with initial antiparallel alignment. We suppose a system made of two large magnets corresponding to the two neighbor CrO_2 crystals, and a nanomagnet embedded in the barrier, causing the observed Coulomb blockade at low temperatures. The nanomagnet orientation is being flipped parallel to the magnetization of the source of spin-polarized electrons. Reversing the current direction will change the magnetic orientation of the nanomagnet. IN such a device made of two tunnel junctions in series, with one junction in the parallel configuration (source) and the other one anti-parallel(drain). Reversing the current exchange thw two configurations. If one resistance is intrinsically very different form the other (for example if the nanomagnet is not equidistant from the two electrodes), the current-induced change of resistance Δ can reach the tunnel magnetoresistance value. An applied external field would realign the magnetizations at the interfaces and the asymmetry in the system vanishes. The existence of antiparallel magnetic alignment, which cannot be retrieved after applying an external magnetic field, is reminiscent of findings on magnetic multilayers used for CPP-MR investigations [27]. In other words, the antiparallel alignment of two neighbor crystals is maximized when the samples are in a virgin random magnetic state. An essential limitation for current-induced magnetization switching on tunnel junctions systems is the necessity to apply very large current densities. Investigations on Co nanomagnets showed critical current densities values larger than 10^7 A/cm^2 [18, 22] for area typically 10^3 - 10^4 nm^2 , in agreement with theoretical predictions. If we consider that a current of $1 \mu\text{A}$ is forced though an island of a few nm in diameter, current densities of 10^7 A/cm^2 can be reached. It corresponds to our observation, where several tens of μA were necessary to observe bistability. Such effects were only found on samples with thin Cr_2O_3 barriers, of a few $\text{k}\Omega$ estimate of single junction resistance, and therefore classified in the strong tunneling regime [14].

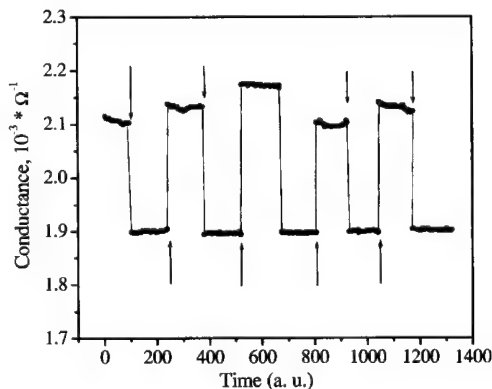


Fig. 5. Zero-bias conductance after applying a 100 ns pulse of 1 V amplitude at time values corresponding to the arrows. The temperature is 245 K. The high-conductance state, lacking reproducibility after applying a voltage pulse, shows strong relaxation effects at higher temperatures.

CONCLUSIONS

Chromium oxide junctions, showing Coulomb blockade effects at low temperatures, exhibit bistable resistance values at zero bias after applying a voltage of around 1 V, involving a current of a few tens of μA . The typical resistance values of several $\text{k}\Omega$ of our samples make them of interest for applications as non-volatile memory devices. A model of current-induced switching is used to explain the results, using a geometry involving a small particle trapped between two large magnets with antiparallel alignments. We show that current densities approaching those predicted and observed for metallic systems can be realized in strong tunneling regime involving very low area junctions.

REFERENCES

- [1] G.A. Prinz, *Science* **282**, 1660 (1998).
- [2] W. J. Gallagher et al., *J. Appl. Phys.* **81**, 3741 (1997).
- [3] K. Bussman, G. A. Prinz, S. F. Cheng and D. Wang, *Appl. Phys. Lett.* **75**, 2476 (1999).
- [4] N. Kikuchi et al., *J. Appl. Phys.* **90**, 6548 (2001).
- [5] Yu. S. Dedkov et al., *Appl. Phys. Lett.* **80**, 4181 (2002).
- [6] R. J. Soulen Jr. et al., *Science* **282**, 85 (1998).
- [7] Y. Ji et al., *Phys. Rev. Lett.* **86**, 5585 (2001).
- [8] A. Gupta, X. W. Li and Gang Xiao, *J. App. Phys.*, **87**, 6073, (2000).
- [9] S. M. Watts, et al., *Phys. Rev. B*, **61**, 9621, (2000).
- [10] Katsuhiko Suzuki and P.M. Tedrow, *Appl. Phys. Lett.*, **74**, 428 (1999).
- [11] S. J. Liu et al., *Appl. Phys. Lett.*, **80**, 4202, (2002).
- [12] P. A. Stampe, R. J. Kennedy, S. M. Watts and S. von Molnár, *J. Appl. Phys.*, **89**, 7696, (2001).
- [13] J. M. D. Coey, A. E. Berkowitz, L.I. Balcells, and F. F. Putris, *Phys. Rev. Lett.*, **80**, 3815 (1998).
- [14] A. Sokolov et al., *Europhys. Lett* **58**, 448 (2002).
- [15] L. Berger, *Phys. Rev. B* **54**, 9353-9358 (1996).
- [16] J. Slonczewski, *J. Magn. Magn. Mater.* **159**, L1 (1996).
- [17] E.B. Myers et al., *Science* **285**, 867 (1999).
- [18] F. J. Albert, J. A. Katine, R. A. Buhrman and D. C. Ralph, *Appl. Phys. Lett.* **77**, 3809 (2000).
- [19] J. Z. Sun, *J. Magn. Magn. Mater.* **202**, 157 (1999).
- [20] J.E. Wegrowe et al., *Europhys. Lett.* **45**, 626 (1999).
- [21] M Tsoi et al., *Phys. Rev. Lett.* **80**, 4281 (1998).
- [22] J. Grollier et al., *Appl. Phys. Lett.* **78**, 3663 -3665 (2001).
- [23] Ruihua Cheng et al., *Appl. Phys. Lett.* **79**, 3122 (2001).
- [24] L. Yuan et al., submitted to *J. Appl. Phys.*
- [25] S. Takahashi and S. Maekawa, *Phys. Rev. Lett.* **80**, 1758 (1998).
- [26] J. M. Rowell and L. Y. L. Shen, *Phys. Rev. Lett.* **17**, 15 (1966)
- [27] J. A. Borchers et al., *Phys. Rev. Lett* **82**, 2796 (1999).

Nanoscale analysis of a Co-SrTiO₃ interface in a Magnetic tunnel junction

J.-L. Maurice¹, F. Pailloux^{1*}, D. Imhoff², J.-P. Contour¹, A. Barthélémy¹, M. Bowen¹,
C. Colliex² and A. Fert¹.

¹Unité Mixte de Physique CNRS/Thales, 91404 Orsay, France

²Laboratoire de Physique des Solides, Université Paris-Sud, 91405 Orsay, France

ABSTRACT

We use High Resolution Electron Microscopy together with Electron Energy Loss Spectroscopy to analyze the crystallography and the chemical configuration of a Co/SrTiO₃ interface in a Co/SrTiO₃/La_{2/3}Sr_{1/3}MnO₃ magnetic tunnel junction.

PACS: 75.47.-m, 75.70.Cn, 68.37.Lp, 79.20.Uv

INTRODUCTION

Magnetic tunnel barriers present a conduction that depends on the respective spin polarizations of the two electrodes. Because it is a half metal, the La_{2/3}Sr_{1/3}MnO₃ (LSMO) compound is very interesting as a probing electrode for spin-dependent spectroscopy: voltage-dependent measurements at low bias should in principle reflect the spin-dependent density of states of the other electrode. Several systems have thus been studied by varying the material of the second electrode (Co, FeNi) and also the nature of the insulator [SrTiO₃ (STO) amorphous Al₂O₃, Ce_{1-x}La_xO_{(2-x)/2}], as the insulator also plays a role as a spin filter [1], [2]. These studies outline the key role played by the interfaces in such devices. Our analytical work on the STO/LSMO interface is published elsewhere [3], [4], [5]. Here, we present the analysis of the Co/STO interface in a Co/STO/LSMO junction. This kind of junction still gives rise to TMR effects at 330K, which is quite close the T_c of the LSMO thin films used as first electrode. The understanding of the behavior of these heterostructures requires the use of characterization methods that can probe one monolayer at the interface. Transmission electron microscopy (TEM) in cross section is particularly suitable in such a case. In this paper, we present an atomic scale characterization by high resolution TEM (HRTEM) and electron energy loss spectroscopy (EELS) in scanning TEM (STEM).

More precisely in a Co/STO/LSMO tunnel junction, the atomic configuration at the Co/STO interface determines the polarization of the tunneling electrons that are emitted or accepted by the cobalt electrode. De Teresa *et al.* [1] have observed *inverse* magnetoresistance in Co/STO/LSMO tunnel junctions, suggesting that the spin of conduction electrons at the Co/STO interface is antiparallel to the magnetization. They explained that tunneling electrons through an STO barrier are d-band electrons and that the d-band in cobalt or at a cobalt surface [6] happens

*Now at Laboratoire de Métallurgie Physique, Université de Poitiers, 86962, Futurscope, France

to be larger at the Fermi level for *minority* spins. Recently, Oleinik *et al.* have performed electronic structure calculations of the fcc Co(100)/STO interface, considering various atomic configurations [7]. These authors concluded that the most stable interface configuration between fcc Co (100) and SrTiO₃ is Co/TiO₂, with Co atoms lying on top of O anions. With this configuration, they found a magnetic moment of 0.25 μ_B on the interfacial Ti cations. As this magnetic moment was aligned antiparallel to the magnetization of the Co layer, they claimed that this might be at the origin of the inverse-TMR observed by de Teresa *et al.* Oleinik *et al.* also pointed out the lack of experimental structural data concerning such heterostructures. This is precisely what we bring here, on a junction prepared with the same equipment as that studied by De Teresa *et al.* [1].

GROWTH

We grow the oxide films by Pulsed Laser Deposition (PLD), a technique that allows the transfer of the cationic stoichiometry from the target to the substrate [8]. Using optimized growth parameters, thin LSMO films grown on (001) SrTiO₃ (STO) substrates exhibit physical properties more or less comparable to the bulk ones, depending on the deposited thickness [9]. In more detail, a frequency tripled Nd:YAG laser ($\lambda=355$ nm) has been focused on a sintered stoichiometric target of LSMO. During the deposition, the STO substrates have been heated to a temperature of 720°C and the oxygen pressure in the chamber has been set to 0.35 Torr. The STO 1.5-nm thin barrier was deposited in the conditions optima for LSMO (with the same oxygen pressure). At the end of the deposition, that pressure was raised to 300 Torr and maintained at this value during the cooling of the sample. The STO/LSMO interface is abrupt [4] and presents no significant chemical segregations [3].

Cobalt was deposited on top of STO by sputtering in another equipment. The transfer between the PLD and sputtering equipments has been performed under nitrogen, with a brief (< 1 min) exposition to ambient air.

EXPERIMENTAL METHODS

Cross-sectional samples for TEM have been thinned by mechanical polishing, using a tripod polisher to about 5 to 10 μm , then ion-milled using a Gatan-PIPS ion miller (Ar, 2.5keV, 6°) until electron transparent [10]. Transmission electron microscopy has been carried out using a Topcon EM002B electron microscope, operated at 200kV (0.19 nm spatial resolution). In order to interpret HRTEM images, we have compared the experimental pictures with simulated images calculated with the EMS software package using the multislice method [11]. We have determined the best imaging conditions by calculating thickness/defocus maps. Since Co is not oriented as to give a definite HRTEM contrast, we have optimized the STO/LSMO contrast. The best defocus values are between -30 nm and -40 nm for a sample thickness laying between 17.2 nm and 18.5 nm. Under these conditions, the bright dots observed in STO correspond to the projection of both atomic columns of strontium and TiO. The bright dots seen in the LSMO correspond to the projection of MnO atomic columns, whereas lanthanum/strontium columns are imaged weakly [3]. For the clarity of the interpretations, we refer to the pseudo-cubic unit cell of LSMO (instead of the R-3C rhombohedral one) for which the lattice parameter is $a_0 = 0.3873$ nm and the pseudo-cubic angle is $\alpha = 90.26^\circ$ [12]. This symmetry is preferred because of its similarity to the STO symmetry ($a_0 = 0.3905$ nm, $\alpha = 90^\circ$).

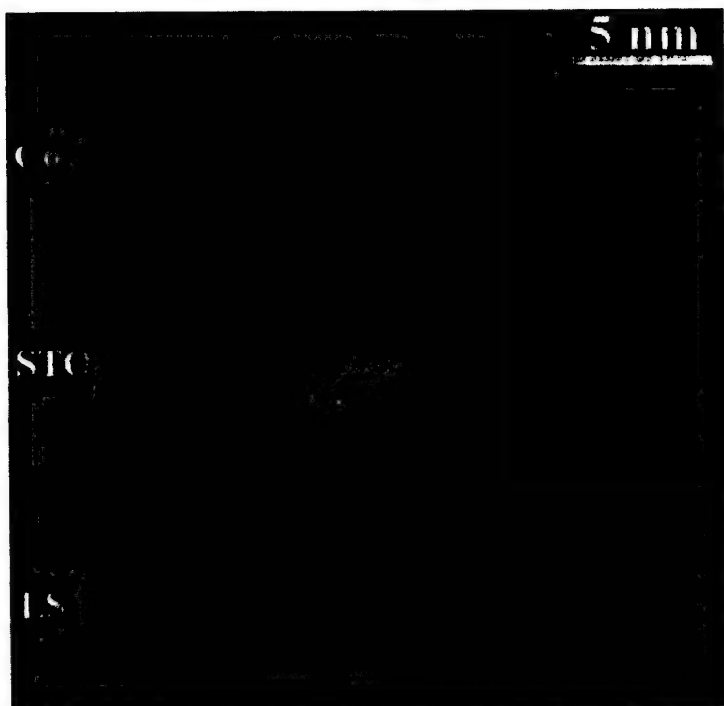


Figure 1. HRTEM picture of the Co/STO/LSMO tunnel junction. The white circles indicate the path and size of the probe used for the EELS spectrum lines.

EELS experiments have been performed in a VG HB 501 dedicated STEM, operated at 100 kV with a field emission gun and equipped with a Gatan-PEELS spectrometer coupled to a CCD detector by optical lenses. We have focused on the Energy-Loss Near Edge Structure (ELNES) of elements constituting the tunnel junction. Reference spectra for the studied edges (O-1s, Co-2p) have been recorded from the “bulk” part of the thin foil. Energy dispersions as low as 0.2eV have been used, leading to an energy resolution of about 0.6eV (measured on the zero-loss peak). The spectrum line method [13] has been employed to record several spectra across the interfaces. In this mode, the probe (0.7nm) is scanned across the interface along a line inclined of about 25° with respect to the interface (Fig. 1). The large amount of data recorded using this procedure have been processed using different mathematical tools including the Multivariate Statistical Analysis (MSA) technique and the Normalized Spatial Difference (NSD) [14], [15], the Non Negative Least Square (NNLS) fit to enhance particular features.

RESULTS AND DISCUSSION

In this section, we describe and discuss the atomic configuration at the Co/STO interface. Figure 2 is an overview of the whole Au/CoO/Co/STO/LSMO heterostructure deposited on a

(001) STO substrate. Electron diffraction patterns (not presented here) evidence that the Co layer is polycrystalline and textured. The digital diffractogram shown in inset of Fig. 2 corroborates that the growing planes of the cobalt layer are mainly the (0001) planes of the hexagonal (hcp) structure of bulk Co. The main feature in this micrograph is the presence of steps at the Co/STO interface. Further examination of these steps reveals that their height is of the order of the lattice constant of STO (at equilibrium: 0.3905nm) and is the same for each step. These steps are periodically distributed along the interface, leading to a misorientation between the interface and the crystallographic planes of about 2° , which is roughly the nominal substrate misorientation. As stacking-faults (Ruddlesden-Popper faults) are observed in neither the LSMO nor the STO layer, and considering the height of the steps, we can state that the termination of the STO barrier is of the same type along the observed area of the sample. It means that the Co atoms located at the interface roughly have the same environment whatever their location.

A thorough investigation of HRTEM contrast using image simulation allows us to discriminate the various cationic sites in both the LSMO and STO layers. The comparison between experimental and simulated through-focus series [3] leads to the conclusion that, in Fig. 1 and Fig. 2, the large bright dots in the LSMO layer correspond to the Mn site, whereas the small bright dots are the image of the $\text{La}_{2/3}\text{Sr}_{1/3}$ atomic columns. The situation is a little more complex in the case of STO: the bright dots for both cationic site (Sr and Ti) give roughly the same intensity in experimental pictures. As we have shown previously [3], the perovskite stacking sequence is kept across the LSMO/STO interface. It is thus possible to discriminate between the Sr and Ti site in the STO layer: Ti cations are located in the continuation of the Mn atomic rows. The next step in the investigation is the determination of the atomic plane of the STO layer on which the Co layer will be deposited. HRTEM images reveal that on the terraces between the steps described above, the last well-crystallized layer is mainly a TiO_2 layer (Fig. 1),

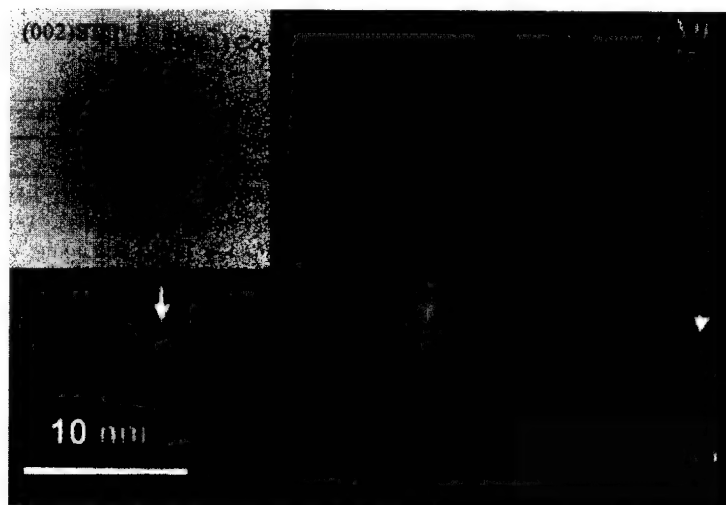


Figure 2. The whole stack of layers, from top to bottom: Au/CoO/Co/STO/LSMO (STO substrate not shown).

which is consistent with a recent work indicating that the last ordered layer at an STO {100} surface annealed under O_2 at high temperature is made of TiO_6 octahedra [16]. Between that layer and the first Co metallic layers, the transition plane exhibits in Fig. 2 weaker white dots at the places of the Sr columns of STO, and a contrast increase for the two first planes of Co. However, these details do not show in Fig. 1, which is taken at a different defocus.

Further information about this layer is obtained by EELS. Using signal processing routines such as MSA and NSD, we have observed that the O-1s edge is the combination of two signals at the STO/Co interface: the spectra acquired as the probe is located at the interface are a combination of those coming from STO and cobalt *monoxide* (CoO) (Fig. 3). Moreover, the non-negative least square (NNLS) fit of the whole spectrum line with the internal STO and CoO references confirms the presence of CoO-type bonding over a width of the order of a nanometer at the interface (Fig. 3b). The Co-2p edge also experiences a change of its shape at the Co/STO interface, which corroborates the previous analysis. This tends to indicate that the experimental Co/STO interface is not as simple as the one assumed in the calculation [7], as it includes an intermediate layer. Whether that layer acts as a supplement to the barrier or not, and whether it is paramagnetic or carries a magnetization opposite to that of cobalt (Néel temperature of bulk antiferromagnetic CoO is 292K [17]), remains to be demonstrated.

CONCLUSIONS

We have analyzed an interface that had been the object of magneto-transport measurements [1] and electronic structure calculations [7]. The latter was based on the assumption of fcc cobalt,

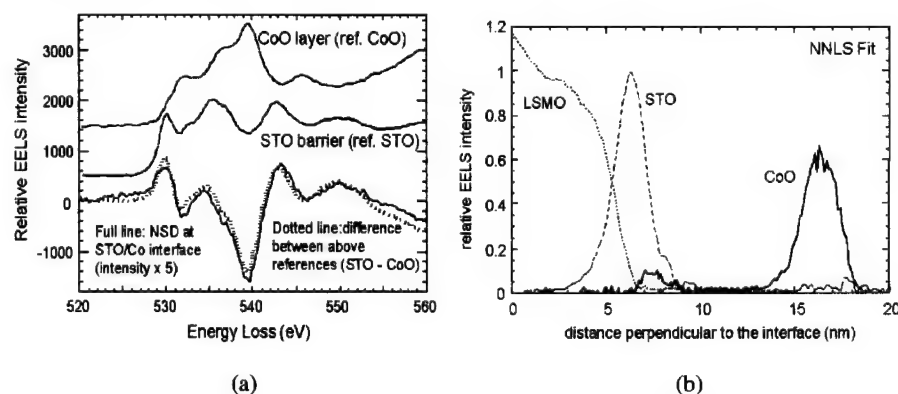


Figure 3. (a) EELS O-1s edges recorded in the CoO and STO layers (top) to serve as references for the analysis of the same edge at the Co/STO interface. Bottom: normalized spatial difference (NSD) spectrum at the interface (full line) compared with a weighted difference between CoO and STO references (dotted line). (b) Non-negative least square (NNLS) fit of the O-1s edge spectrum line, using the O-1s edges in the LSMO, STO and CoO layers as internal references, which unambiguously indicates the presence of CoO at the interface over a distance of the order of the nm.

(100) oriented. The first fact we bring is that the actual layer is hcp and polycrystalline, with a 0001 texture. The calculations [7] involving energy minimization are structure specific and cannot therefore apply to our particular experimental device. However, the interpretations of the inverse magnetoresistance in terms of cobalt density of state [1] can still hold as the d-band configuration at the Fermi level does not significantly depend on whether the cobalt is fcc or hcp or on its orientation. On the other hand, the layer of atomic thickness seen at the interface (be it CoO or other) probably influences the TMR but how this influence is important is difficult to assess.

ACKNOWLEDGEMENTS

We thank Prof. Revcolevschi (Université Paris-Sud) for providing the LSMO target, M. Bibès, F. Petroff (UMP CNRS/Thales), T. Sikora (LPS Université Paris-Sud) for fruitful discussions, and Mr Jacquet (UMP CNRS/Thales) for his help with PLD.

REFERENCES

- [1] J-M De Teresa, A. Barthélémy, A. Fert, J-P. Contour, R. Lyonnet, F. Montaigne, P. Seneor, A. Vaures, *Phys. Rev. Lett.* **82**, 4288 (1999); *Science* **286**, 507. (1999)
- [2] A. Fert *et al.*, *Materials. Science and. Engineering* **B84**, 1 (2001).
- [3] F. Pailloux, D. Imhoff, T. Sikora, A. Barthélémy, J.-L. Maurice, J.-P. Contour, C. Colliex, A. Fert, *Phys. Rev.* **B66**, 014417 (2002).
- [4] J.-L. Maurice, R. Lyonnet, J.P. Contour, *J. Magn. Magn. Mater.* **211**, 91 (2000).
- [5] L. Samet, D. Imhoff, J.-L. Maurice, J.-P. Contour, A. Gloter, T. Manoubi, A. Fert, C. Colliex, *to be published*
- [6] K. Wang, PhD thesis, New York University, 1999.
- [7] I.I. Oleinik, E.Y. Tsybal, D.G. Petiffor, *Phys. Rev. B* **65**, 020401(R) (2002).
- [8] J.P. Contour, C. Sant, D. Ravelosona, B. Ficher, L. Patlagan, *Jpn. J. Appl. Phys* **32**, 1134 (1993).
- [9] J.-L. Maurice, F. Pailloux, A. Barthélémy, A. Rocher, O. Durand, R. Lyonnet, J.-P. Contour, *Appl. Surf. Sci.* **188**, 176 (2002).
- [10] J. Benedict, R. Anderson, S. Klepeis, M. Chaker, *Mater. Res. Soc. Symp. Proc.* 199 (1990) 189.
- [11] P. Stadelman, *Ultramicroscopy* **21**, 131 (1987).
- [12] A. Hammouche, E. Siebert, A. Hammou, *Mat. Res. Bull.* **24**, 367 (1989).
- [13] C. Jeanguillaume and C. Colliex, *Ultramicroscopy* **28**, 252 (1989).
- [14] N. Bonnet, N. Brun and C. Colliex, *Ultramicroscopy* **77**, 97 (1999).
- [15] P. Trebbia and N. Bonnet, *Ultramicroscopy* **34**, 165 (1990).
- [16] N. Erdman, K. R. Poeppelmeier, M. Asta, O. Warschkow, D. E. Ellis and L. D. Marks, *Nature* **419**, 55 (2002).
- [17] See, e.g.: P.A. Cox, *Transition Metal Oxides* (Clarendon Press, Oxford, 1995).

Observation of the Verwey Transition in Fe_3O_4 Nanocrystals

Gil Markovich¹, Teipi Fried¹, Pankaj Poddar¹, Amos Sharoni², David Katz², Tommer Wizansky², and Oded Millo²

¹School of Chemistry, Tel Aviv University, Tel Aviv 69978, Israel

²Racah Institute of Physics and the Center for Nanoscience and Nanotechnology, The Hebrew University of Jerusalem, Jerusalem 91904, Israel

ABSTRACT

The electronic properties of arrays and isolated magnetite nanocrystals were studied using tunneling spectroscopy. Macroscopic tunnel junctions were used to study stacked arrays of the nanocrystals. The temperature dependent resistance measurements showed an abrupt increase of the resistance around 100 K, attributed to the Verwey metal-insulator transition, while the current-voltage characteristics exhibit a sharp transition from an insulator gap to a peak in the density of states near the Fermi energy. This conductance peak was sensitive to in-plane magnetic field showing large magnetoresistance. The tunneling spectra obtained on isolated particles using a Scanning Tunneling Microscope exhibit a gap-like structure below the transition temperature that gradually disappeared with increasing temperature, ending with a small peak structure around zero bias.

INTRODUCTION

The Verwey metal-insulator transition observed in magnetite (Fe_3O_4) has continuously attracted interest since its discovery more than 60 years ago [1]. Magnetite is a relatively good conductor at room temperature and on cooling below 120K its conductivity sharply drops by two orders of magnitude. It was described as a first-order metal-insulator transition accompanied by a structural phase transition where the cubic symmetry of the Fe_3O_4 crystal is broken by a small lattice distortion [2]. While the exact nature of the transition is still under controversy, it is understood that the driving force for this phenomenon is the strong electron-electron and electron-lattice interactions in the system.

Special attention has been focused on the roles played by long-range and short-range charge ordering in driving the Verwey transition. The former is believed to exist below the transition temperature, T_v , and the latter sustains well above it. The long-range order manifests itself by opening a gap in the electronic density of states (DOS) around the Fermi level (E_F). This gap was detected by photoemission [3,4], optical [5], and tunneling [6] spectroscopies. The effect of short-range ordering on the DOS is not as clear. However, recent photoemission experiments [3,4] suggest that a reduced gap in the DOS, associated with a short-range ordering, still exists well above the transition temperature.

In view of the importance of long-range charge ordering in determining the electronic properties below T_v , an intriguing question arises: Could the Verwey transition be observed in nanoscale magnetite crystals of diameter measuring several unit cells? Recently, Poddar et al. reported on the observation of a sharp Verwey transition in arrays of Fe_3O_4 (magnetite) nanoparticles of average size around 5.5 nm. This transition was manifested both in a resistance jump as well as in a change in the tunneling spectra measured on the arrays. However, it was not clear whether the observed transition pertained to the single nanocrystal (NC) or was a collective

array effect. In this paper we present scanning tunneling spectroscopy results on single nanoparticles, providing evidence that the transition occurs in isolated magnetite NCs. The tunneling spectra show a gap structure in the DOS below T_v , which gradually transforms into a peak around E_F .

EXPERIMENTAL DETAILS

The details of magnetite NCs array preparation are described elsewhere [7]. After synthesis, the NCs were coated with oleic acid, dispersed in non-polar organic solvents and separated by employing size selective precipitation to produce uniform samples of NCs in the 3-10 nm size range. Transmission electron microscopy (TEM) was used for size determination as well as to confirm the formation of NC monolayers. The monolayers were produced by depositing the hydrophobic magnetite nanocrystals from heptane solution at the air-water interface and compressing the film two-dimensionally to form a close-packed array. For the fabrication of the junctions, arrays of gold lines (width = 80 μm) and a thickness of 100 nm were deposited on a doped Si substrate with a 100 Å thick oxide layer. Consequently, five monolayers of Fe_3O_4 NCs were transferred from the air-water interface onto the patterned substrates using the Langmuir-Schaefer technique. A second array of gold lines perpendicular to the bottom electrodes was deposited by thermal evaporation through a shadow mask on top of the films while the substrate was maintained at 20 °C. The electrical contacts were formed by fixing Cu wires to pads on the gold electrodes using silver paste [8].

For the scanning tunneling microscopy (STM) measurements, the magnetite particles were spin-coated on gold films deposited on mica substrates and then dipped in oleic acid solution. The fatty acid molecules served as a protecting layer against NC oxidation. All this procedure was performed in an inert atmosphere. The low temperature tunneling spectra were obtained using the double barrier tunnel junction configuration, by positioning the STM tip above single NCs [9,10]. The tip was retracted as far as possible from the NC in order to form a highly asymmetric tunneling configuration and thus reduce single electron charging effects [10,11]. This was facilitated by the preparation procedure that ensured a relatively large capacitance and small resistance (large tunneling rate) for the substrate-NC tunnel junction. Nevertheless, many NCs did show charging effects that dominated the tunneling characteristics, thus masking the intrinsic NC density of states, and only about ten NCs could be used for studying the temperature dependence of the DOS around T_v .

RESULTS AND DISCUSSION

The temperature dependence of the two-terminal resistance of a macroscopic tunnel junction is shown in Figure 1a. The sharp resistance jump observed at 100 ± 5 K clearly manifests the first-order Verwey transition. The typical transition temperature measured for the arrays is smaller than T_v observed for high-quality bulk samples (~ 120 K). This may be due to either surface or finite size effects. This temperature is independent of the bias voltage used in the measurement but magnitude of the resistance jump decreases with increasing bias due to non-linearity. In Figure 1b we present dI/dV vs. V tunneling spectra measured above and below T_v , both with and without applying an in-plane magnetic field. Two significant effects can be observed in these data: 1. A pronounced change in the tunneling conductance curve takes place on cooling through T_v . The sharp peak around zero bias (E_F) seen right above T_v disappears abruptly, and a region of

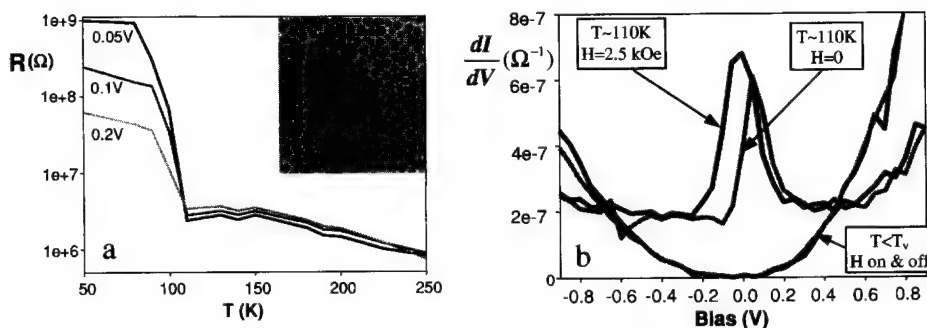


Figure 1. (a) Magnetite nanocrystal film resistance as function of temperature for three bias voltage values. Inset: TEM image of a magnetite NC monolayer with average particle size of 5.5 nm. (b) Differential conductance vs. bias voltage above and below the transition temperature, with (black lines) and without (gray lines) in-plane magnetic field of 2.5 kOe.

low conductance sets-in instead below T_v . 2. Upon application of an external magnetic field the conductance peak broadens and shifts to negative bias, resulting in a large negative magnetoresistance around zero bias. These effects were reversible and reproducible through several cooling-heating cycles [8].

The macroscopic tunnel junctions are perceived as consisting of parallel percolating current paths, where each path may include several inter-particle junctions. Hence, the details of the current-voltage curves are determined not only by the single-particle electronic structure but also by the RC constants of the various inter-particle tunneling junctions along the current paths. However, since the RC characteristics of the junctions are not sensitive to temperature, we believe that the abrupt change in the tunneling spectra is a manifestation of the MI transition in the single particle. In particular, it appears that in the metallic phase (above 100 K), the conductance peak near the Fermi level reflects the narrow conduction band of magnetite, as previously observed on bulk samples [12]. Below T_v the region of low conductance around zero bias results from opening a gap in the DOS around E_F of the NCs, but its width is determined by the inter-particle junction parameters. Tunneling spectroscopy measurements on single particles, as enabled by STM, may yield further information on the evolution of the gap in single NCs around T_v , as will be discussed below.

External magnetic field affects the electron transport in the arrays by aligning the magnetic moments of the individual superparamagnetic NCs along the conduction paths. As the magnetizations of the particles become aligned with the external field, their spin polarized conduction bands, located near E_F , align respectively, and the probability for electron tunneling through a chain of particles increases. This leads to a negative magnetoresistance behavior, as depicted in Fig. 1(b). The magnetic field influence on the tunneling spectra was found to decrease upon heating the samples to room temperature [8]. This effect is due to thermal agitation that disturbs the relative magnetization alignment between neighboring particles, consequently reducing the magnetoresistance. Increasing the temperature could also reduce the degree of spin polarization within individual particles, further contributing to the reduction in the magnetoresistance.

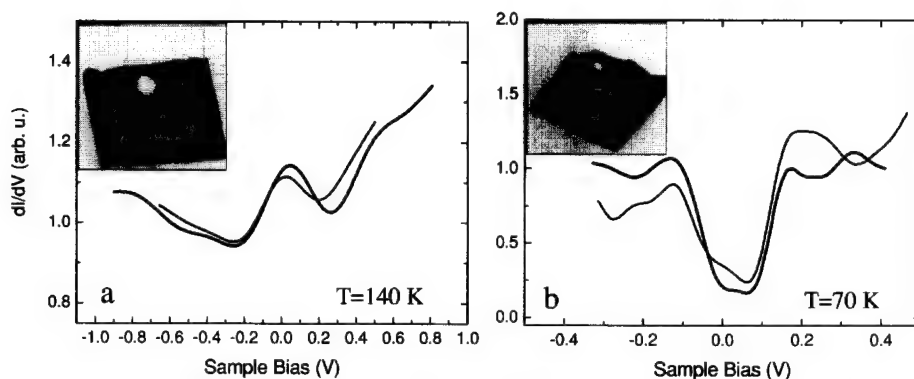


Figure 2. Tunneling spectra taken on isolated magnetite NCs above (a) and below (b) the Verwey transition temperature. The two curves in each frame were taken over the same NC with the same conditions, showing the variance in the data. The insets present STM images of the corresponding NCs (image sizes are: (a) 26x30 nm, (b) 52x40 nm).

Turning now to the STM results, we present in Fig. 2 tunneling spectra measured on single magnetite NCs, about 8 nm in diameter. The curves in Fig. 2(a) were measured at 140 K, well above T_v , whereas those in Fig. 2(b) were acquired at 70 K. Consistent with the macroscopic tunnel junction measurements, a peak in the DOS is observed above the Verwey transition while a gap develops below the transition. The reproducibility of the data can be appreciated from two typical curves plotted for each particle: the main features, namely, the peak and gap structures, are reproducible, but the background may fluctuate. Due to drift of the STM tip upon changing the temperature, we were not able to measure, in most cases, the same NC well above and well below T_v . The measured gap value in Fig. 2(b) is about 250 meV, which is significantly larger than previously measured on bulk samples using photoemission (~ 140 meV) [3,4] or STM (200 meV) [6]. This apparent gap broadening may be due to the effect of voltage division, inherent to the double barrier tunnel junction configuration [10,11]. We have observed a clear gap structure below T_v in about half of the measured nanoparticles that did not exhibit single electron charging effects, where the gap values varied between 250 to 350 meV. The peak width was typically 400 meV, somewhat larger than the value obtained using the macroscopic tunnel junction, ~ 300 meV (see Fig. 1).

Figure 3 depicts the evolution of the DOS around E_F with temperature. Here, the tunneling spectra were acquired on a small cluster of (single layer) NCs, nominally at the position marked by the white arrow. One can see that as the temperature is increased, the gap reduces, and the DOS at the Fermi energy gradually increases. The two spectra at 105 K may have been obtained (due to drift of the tip) at somewhat different positions, resulting in a different tunneling DOS. In these measurements it appears that a clear gap still exists even above 100 K (the transition temperature measured for the NC arrays) and the peak structure emerges only at a higher temperature, in contrast to the more abrupt change observed for the arrays, as discussed above. This may reflect the particle-to-particle fluctuations (e.g., in composition or surface condition), to which the STM is sensitive, as opposed to the macroscopic tunnel junction where the ensemble properties are measured. In this context we note that some of the NCs did not exhibit in our STM spectra any transition behavior whatsoever. Interestingly, the suppression of the gap

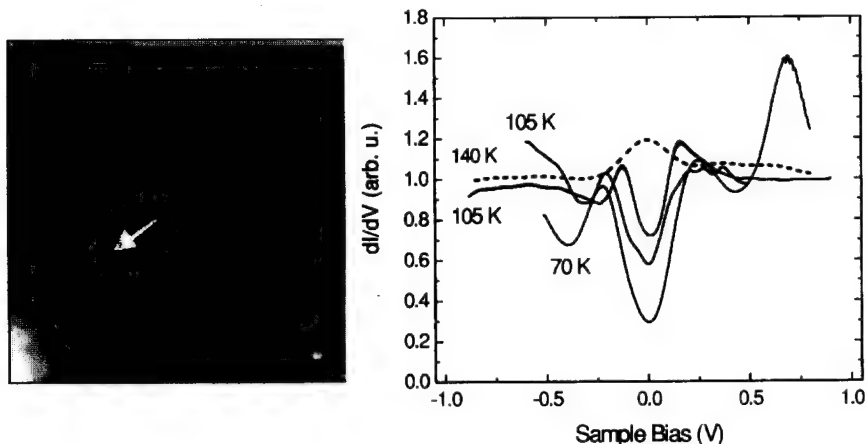


Figure 3. 20x20 nm² STM image showing a cluster of magnetite NCs (left) together with a series of tunneling spectra taken nominally at the position marked by the arrow at various temperatures, as indicated (right).

in the Fe₃O₄ NCs around T_v , as observed in both types of our tunneling experiments, is faster than that seen for bulk samples using photoemission and optical spectroscopies [3,4,5]. As the gap in the DOS above T_v was attributed to the short-range charge ordering, it is expected that this gap would exist also in the nanocrystals, and it is therefore puzzling why it was not detected in the tunneling spectra.

CONCLUSIONS

The combination of macroscopic tunnel junctions and scanning tunneling spectroscopy is demonstrated to be an effective tool for studying the electronic properties of Fe₃O₄ NC in the vicinity of the Verwey transition. In particular, the STM measurements clearly show that the sharp resistive transition observed for NC arrays is associated with, and probably governed by, an opening of a gap in the electronic DOS around E_F in single NCs. This result suggests that long-range order, that is believed to dominate the electronic properties at $T < T_v$, is significant even in nanometer size magnetite particles. More detailed size dependent experiments are still needed to resolve the finite size effects on the transition temperature and the electronic structure of the magnetite system. Understanding these issues as well as the magnetoresistance properties of the magnetite NC arrays may lead to its exploitation as a novel material for spin polarized nanodevices.

ACKNOWLEDGEMENTS

This work was supported in parts by the Israel Science Foundation, The Israel Ministry of Science and the DIP Foundation.

REFERENCES

1. E. J. W. Verwey, *Nature* **144**, 327 (1939).
2. M. Izumi, T. F. Koetzle, G. Shirane, S. Chikazumi, M. Matsui, and S. Todo, *Acta Crystallogr., Sect. B: Struct. Sci.* **38**, 2121 (1982).
3. J.H. Park, L.H. Tjeng, J.W. Allen, P. Metcalf, and C.T. Chen, *Phys. Rev. B* **55**, 12813 (1997).
4. A. Chainani, t. Yokaya, T. morimoto, T. Takahashi, and S. Todo, *Phys. Rev. B* **55**, 17796 (1995).
5. L.V. Gasparov, D.B. Tanner, D. B. Romero, H. Berger, G. Margariotondo, and L. Forro, *Phys. Rev. B* **62**, 7939 (2000).
6. J.Y.W. Wei, N.C. Yeh, R.P. Vasquez, and A. Gupta, *J. Appl. Phys.* **83**, 7366 (1998).
7. T. Fried, G. Shemer, and G. Markovich, *Adv. Mater.* **13**, 1158 (2001).
8. P. Poddar, T. Fried, and G. Markovich, *Phys. Rev. B* **65**, 172405 (2002).
9. A.E. Hanna and M. Tinkham, *Phys. Rev. B* **44**, 5919 (1991).
10. D. Katz, O. Millo, S. H. Kan, and U. Banin, *Appl. Phys. Lett.* **79**, 117 (2001).
11. E. P. A. M. Bakkers and D. Vanmaekelbergh, *Phys. Rev. B* **62**, R7743 (2000); E. P. A. M. Bakkers, et al., *Nano Lett.* **1**, 551 (2001).
12. A.Gupta and J.Z. Sun, *J. Magn. Magn. Mater.* **200**, 24 (1999).

Double Quantum Wire Magnetic Response

Anatoly Yu. Smirnov¹, Lev G. Mourokh² and Norman J.M. Horing²

¹D-WaveSystems Inc., 320-1985 W.Broadway

Vancouver, British Columbia, Canada V6J 4Y3

²Department of Physics and Engineering Physics

Stevens Institute of Technology, Hoboken, NJ 07030

ABSTRACT

The induced magnetic moment of a biased semiconductor tunnel-coupled parallel double quantum wire system is examined here. The wires are in a series arrangement with tunnel coupling to each other and to leads. Their parallel lengths and associated continuous spectrum are taken in the direction perpendicular to the lead-to-lead current. The equations of motion for the double-wire electron Green's function are formulated and analyzed using the transfer-tunneling Hamiltonian formalism. We determine the average magnetic moment of the double-wire system induced by a magnetic field applied perpendicular to the plane of the structure and we show that there are crossovers between diamagnetic and paramagnetic behavior, depending on the bias voltage, equilibrium chemical potential of the leads and temperature.

INTRODUCTION

There has recently been intensified interest in *extended* tunnel-coupled structures, in particular, parallel quantum wires [1-3], which have symmetric and antisymmetric states analogous to those of quantum dots [4,5]. Such double-quantum-wire systems have been fabricated by split-gate methods [6] or by cleaved edge overgrowth [7].

The double-wire system that we examine in regard to magnetic moment is illustrated in Fig. 1. It consists of two tunnel-coupled parallel quantum wires of finite length L with wire separation $2d$ placed between two metallic leads. There is electron confinement in two dimensions (y and z) in both wires, and the energy spectrum in the third direction (x) is taken to be continuous. Subject to the bias voltage, electrons tunnel sequentially from the left lead to the left wire, tunnel from the left wire to the right wire, and, finally, tunnel from the right wire to the right lead. We assume that tunneling from wire to wire is much faster than tunneling from the leads to wires, because the potential barriers between leads and wires are higher than the barrier between the wires themselves. We neglect the Coulomb interaction between electrons. A magnetic field is

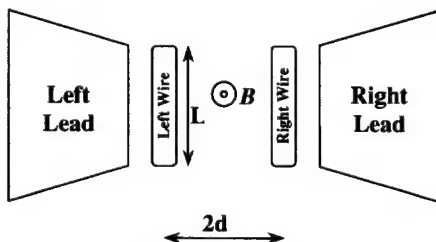


Figure 1. Schematic of the double-wire system.

taken to be applied perpendicular to the plane of this structure, facilitating the analysis of magnetic properties of the system. With the use of the nonequilibrium Green's functions, we analyze the magnetic moment of the double-wire system.

GREEN'S FUNCTION FORMULATION FOR DOUBLE-WIRE SYSTEM

The electron field operators in the left and right wires are described as

$$\hat{\Psi}_L(\mathbf{r}, t) = \psi_L(y) \psi_0(z) \hat{\psi}_L(x, t), \quad (1)$$

$$\hat{\Psi}_R(\mathbf{r}, t) = \psi_R(y) \psi_0(z) \hat{\psi}_R(x, t), \quad (2)$$

where $\psi_L(y) = \psi_0(y+d)$, $\psi_R(y) = \psi_0(y-d)$, ψ_0 is the ground state wave function for the y and z directions, and $\hat{\psi}_L(x, t)$, $\hat{\psi}_R(x, t)$ are the electron field annihilation operators for states of the x direction. The magnetic field, applied along the z -axis is taken in the gauge $\mathbf{A} = (-By, 0, 0)$. In this description, the second quantized double-wire Hamiltonian can be written in terms of an x -integral alone, using a δ -function confinement in the y direction to represent the narrow spatial extent of $|\psi_0(y)|^2$, as

$$\begin{aligned} \hat{H}_{DW} = \int dx & \left(\hat{\psi}_L^\dagger(x, t) \frac{(p_x - eBd/c)^2}{2m} \hat{\psi}_L(x, t) + \hat{\psi}_R^\dagger(x, t) \frac{(p_x + eBd/c)^2}{2m} \hat{\psi}_R(x, t) \right) \\ & - \Delta \int dx (\hat{\psi}_L^\dagger(x, t) \hat{\psi}_R(x, t) + \hat{\psi}_R^\dagger(x, t) \hat{\psi}_L(x, t)), \end{aligned} \quad (3)$$

where $-\Delta$ is the tunneling constant. The retarded, advanced and lesser Green's functions describing x -propagation of the electrons in the double-wire system are defined as

$$G_{\alpha\beta}^r(x, t; x', t') = -i \langle [\hat{\psi}_\alpha(x, t), \hat{\psi}_\beta^\dagger(x', t')]_+ \rangle \Theta(t - t'), \quad (4)$$

$$G_{\alpha\beta}^a(x, t; x', t') = i \langle [\hat{\psi}_\alpha^\dagger(x, t), \hat{\psi}_\beta(x', t')]_+ \rangle \Theta(t' - t), \quad (5)$$

and

$$G_{\alpha\beta}^<(x, t; x', t') = i \langle \hat{\psi}_\alpha^\dagger(x', t') \hat{\psi}_\beta(x, t) \rangle, \quad (6)$$

where $\alpha, \beta = L, R$, $[\dots]_+$ is an anticommutator, and $\Theta(t)$ is the Heaviside unit step function.

The coupling of the double-wire system to the leads is described by the Hamiltonian

$$\hat{H}_{L-DW} = \sum_\alpha \int dx (\hat{\psi}_\alpha^\dagger(x, t) C_\alpha(x, t) + C_\alpha^\dagger(x, t) \hat{\psi}_\alpha(x, t)), \quad (7)$$

where

$$C_\alpha(x, t) = \int dy dz \int d^3r' \psi_0^*(z) \psi_\alpha^*(y) V_\alpha(\mathbf{r} - \mathbf{r}') c_\alpha(\mathbf{r}', t) \quad (8)$$

with $\alpha = L, R$ for left, right and c_α^\dagger , c_α are the creation, annihilation operators of electrons in the α -lead and $V_\alpha(\mathbf{r} - \mathbf{r}')$ is the lead-wire coupling strength.

The leads are taken to be three-dimensional with Hamiltonian,

$$\hat{H}_{Ld} = \sum_\alpha \int d^3r c_\alpha^\dagger(\mathbf{r}, t) E_\alpha(\mathbf{p}) c_\alpha(\mathbf{r}, t), \quad (9)$$

having continuous spectrum in all three dimensions. The retarded and lesser Green's functions for the electrons in the leads (incorporating the lead-double-wire coupling strength) are given by

$$\text{Im } g_\alpha^r(E, p_x) = -\frac{1}{2} \Gamma_\alpha(E, p_x) \quad (10)$$

and

$$g_a^\zeta(E, p_x) = i f_a(E) \Gamma_a(E, p_x), \quad (11)$$

where $f_a(E)$ is the Fermi function,

$$f_a(E) = \frac{1}{\exp\left(\frac{E - \xi_a}{T}\right) + 1}, \quad (12)$$

$\xi_L = \xi + eU/2$, $\xi_R = \xi - eU/2$, ξ is the equilibrium chemical potential common to both leads, U is the applied bias voltage, and the lead-double-wire coupling constants $\Gamma_a(E, p_x)$ are defined as

$$\Gamma_a(E, p_x) = 2\pi \int \frac{dp_y}{2\pi\hbar} \frac{dp_z}{2\pi\hbar} |\psi_a(p_y)|^2 |\psi_0(p_z)|^2 |V_a(p)|^2 \delta(E - E_a(p)). \quad (13)$$

The energy origin is taken as the ground state energy of the wire confinement potential.

The average magnetic moment induced by the applied magnetic field may be written in terms of electron Green's functions of the double-wire structure as

$$\begin{aligned} \langle \mu_z \rangle = & -\frac{\partial \langle H \rangle}{\partial B} = -i \frac{e d L}{m c} \int \frac{dp_x}{2\pi\hbar} \int \frac{dE}{2\pi\hbar} (p_x (G_{LL}^\zeta(E, p_x) - G_{RR}^\zeta(E, p_x)) \\ & - \frac{e B d}{c} (G_{LL}^\zeta(E, p_x) + G_{RR}^\zeta(E, p_x))). \end{aligned} \quad (14)$$

MAGNETIC MOMENT OF THE QUANTUM DOUBLE WIRE SYSTEM

The equations of motion for the double-wire electron Green's functions (Eqs.(4-6)) imply that there are two subbands in the double-wire region associated with bonding and antibonding states. The bonding subband energy is given by

$$E_b(p_x) = \frac{p_x^2}{2m} + \frac{m \omega_c^2 d^2}{2} - \sqrt{\Delta^2 + \omega_c^2 p_x^2 d^2}, \quad (15)$$

and the energy in the antibonding subband is given by

$$E_a(p_x) = \frac{p_x^2}{2m} + \frac{m \omega_c^2 d^2}{2} + \sqrt{\Delta^2 + \omega_c^2 p_x^2 d^2}, \quad (16)$$

where $\omega_c = eB/mc$ is the cyclotron frequency. We use these solutions in the determination of the average magnetic moment of the double-wire system. In the wide-band limit [8] of a symmetric structure, in which the coupling constants are essentially the same for both leads and are energy-independent, the induced magnetic moment in the double-wire system is found to be

$$\langle \mu_z \rangle = -\frac{e d^2 L}{2c} \omega_c \int \frac{dp_x}{2\pi\hbar} \left[\left(1 + \frac{p_x^2}{m \Omega_p} \right) [f_L(E_a(p_x)) + f_R(E_a(p_x))] + \left(1 - \frac{p_x^2}{m \Omega_p} \right) [f_L(E_b(p_x)) + f_R(E_b(p_x))] \right]. \quad (17)$$

It is evident from Eq.(17) that the contribution of the antibonding subband to the magnetic moment (first term in the large square brackets) is always diamagnetic, while the contribution of the bonding subband (second term) is diamagnetic for the part of the subband involving small momenta ($p_x^2 < m \Omega_p$) and it is paramagnetic otherwise. This conclusion may also be obtained

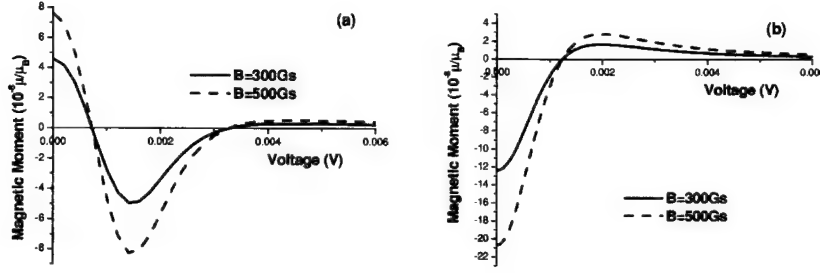


Figure 2. Bias dependence of the magnetic moment for two magnetic field strength, $B=300$ Gs (solid line) and $B=500$ Gs (dashed line) and for two equilibrium chemical potential of the leads, (a) $\xi=525\mu\text{eV}$ and (b) $\xi=-100\mu\text{eV}$; μ_B is the Bohr magneton.

by taking derivatives of the subband energies (Eqs.(15,16)) with respect to the applied magnetic field. This derivative is always positive for the antibonding state, but it involves both positive and negative terms for the bonding state.

Figure 2(a,b) illustrates the bias dependence of the average magnetic moment for two magnetic field strengths, for two equilibrium chemical potentials of the leads, $\xi=525\mu\text{eV}$ and $\xi=-100\mu\text{eV}$, and for the following parameters associated with a GaAs structure in our calculations: $\Delta = 75\mu\text{eV}$; $\hbar\Gamma = 7.5\mu\text{eV}$; $T = 3\text{K}$; $2d = 60\text{nm}$; $L = 10\mu\text{m}$ and $m = 0.067m_0$, where m_0 is the free electron mass. The magnetic moment is normalized to the Bohr magneton, $\mu_B = \hbar e/2m_0c = 9.27 \cdot 10^{-21} \text{ erg/Gs}$. One can see that the response of the system with equilibrium chemical potential of the leads $\xi=525\mu\text{eV}$, is paramagnetic in equilibrium, and it becomes diamagnetic with increasing bias, returning to paramagnetic at high bias. For the system with equilibrium chemical potential of the leads $\xi=-100\mu\text{eV}$, the equilibrium response is diamagnetic and there is only one crossover to paramagnetic behavior with increasing bias. It should be noted that, although the absolute values of the induced magnetic moment are different for different applied magnetic field strengths, the critical voltages for crossover between diamagnetic and paramagnetic response remain the same.

To achieve a better understanding of the magnetic response of the double-wire system and its bias dependence, we examined the dependence of the induced magnetic moment on the equilibrium chemical potential of the leads without bias, with the result shown in Figure 3(a); and with an applied bias, $U = 5 \cdot 10^{-4} \text{ V}$, as shown in Figure 3(b) for temperature $T = 1\text{K}$. The distribution functions of both leads are the same at zero bias and so are their contributions to the magnetic moment (Eq.(17)). Only the bottom of the bonding subband is populated for low values of ξ and T and the magnetic response is diamagnetic. The subband population increases with increasing ξ and, initially, the diamagnetic response increases when there are only electrons with low p_x -values. As electrons with larger p_x -values start to contribute, they compensate the contribution of the low- p_x electrons (the first inverted peak (negative) in Figure 3(a)) and the response even becomes paramagnetic when large- p_x electrons dominate. The antibonding subband is reached as ξ further increases, and its diamagnetic contribution leads to the second (positive) peak in Figure 3(a). The imposition of a finite bias differentiates the contributions of

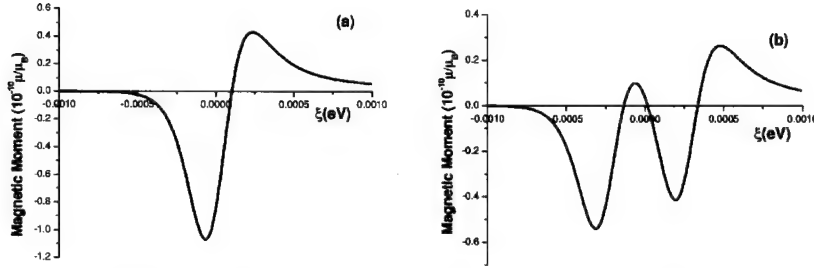


Figure 3. Induced magnetic moment as a function of equilibrium chemical potential of the leads for (a) zero bias, (b) $U = 5 \cdot 10^{-4}$ V.

the left and right leads, shifting the functional dependence of Figure 3(a) in opposite directions by $\pm U/2$, respectively. Taken together, they yield the induced magnetic moment as a function of the equilibrium chemical potential of the leads, shown in Figure 3(b). Increasing the bias shift between the left and right leads (with their equilibrium chemical potential fixed) results in the induced magnetic moment shown as a function of bias voltage in Figure 2. In regard to its specific shape, the bias dependence of the induced magnetic moment and, in particular, its sign at zero bias and critical voltages, are determined by the common equilibrium chemical potential of the leads. It is evident from Figure 3(a) that the equilibrium magnetic response is paramagnetic for $\xi = 525 \mu\text{eV}$ (see Figure 2(a)), whereas it is diamagnetic for $\xi = -100 \mu\text{eV}$ (see Figure 2(b)).

Higher temperatures smooth the distribution function of the leads and the peaks become less pronounced. The temperature dependencies of the induced magnetic moment are presented in Figure 4 for magnetic field strength 300Gs, for two values of equilibrium chemical potential of the leads and for two applied bias voltages. One can see that the induced magnetic moment decreases with increasing temperature and in this situation the effect of applied voltage also tends to vanish.

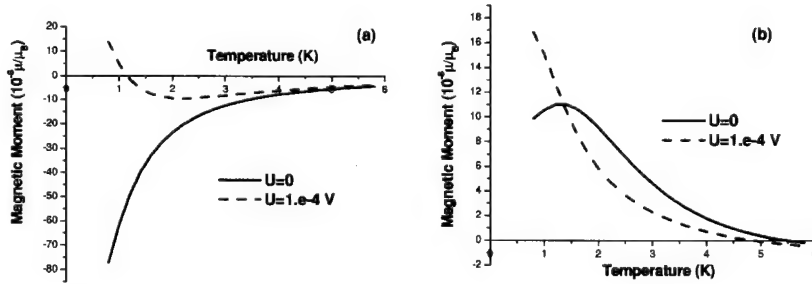


Figure 4. Temperature dependence of the induced magnetic moment for zero bias (solid lines) and $U = 5 \cdot 10^{-4}$ V (dashed lines) and for two equilibrium chemical potential of the leads, (a) $\xi = -100 \mu\text{eV}$ and (b) $\xi = 525 \mu\text{eV}$.

CONCLUSIONS

Our analysis of a biased tunnel-coupled double-quantum-wire system (connected to leads in a series arrangement, with a magnetic field normal to the plane of the wires) has led to the determination of the induced magnetic moment as a function of bias voltage, equilibrium chemical potential of the leads, and temperature. In this, we demonstrated that, at low temperatures, there are crossovers between diamagnetic and paramagnetic behavior with increasing bias voltage. These properties of the double-wire structure introduce a mechanism for the lead-to-lead bias control of the induced magnetic moment of this system.

ACKNOWLEDGEMENT

L.G.M. and N.J.M.H. gratefully acknowledge support from the Department of Defense, DAAD 19-01-1-0592.

REFERENCES

1. A. Berton, P. Bordone, R. Brunetti, C. Jacoboni, and S. Reggiani, *Phys. Rev. Lett.* **84**, 5912 (2000).
2. M. Governale, M. Macucci, and B. Pellegrini, *Phys. Rev. B* **62**, 4557 (2000).
3. D. Boese, M. Governale, A. Rosch, and U. Zülicke, *Phys. Rev. B* **64**, 085315 (2001).
4. L.P. Kouwenhoven, C.M. Marcus, P.L. McEuen, S. Tarusha, R.M. Westervelt, and N.S. Wingreen, in *Mesoscopic Electron Transport*, edited by L. Sohn, L.P. Kouwenhoven, and G. Schön (Kluwer Series E345, Dordrecht, 1997).
5. D. Loss and D.P. Divincenzo, *Phys. Rev. A* **57**, 120 (1998).
6. K.J. Thomas, J.T. Nicholls, M.Y. Simmons, W.R. Tribe, A.G. Davies, and M. Pepper, *Phys. Rev. B* **59**, 12252 (1999).
7. O. M. Auslaender, A. Yakoby, R. de Riccio, K. W. Baldwin, L. N. Pfeifer, and K. W. West, *Science* **295**, 825 (2002).
8. A.-P. Jauho, N.S. Wingreen, and Y. Meir, *Phys. Rev. B* **50**, 5528 (1994).

Ferromagnetic Single-Electron Transistor with RC Gate

Jun-ichi Shirakashi¹ and Yasushi Takemura²

¹Akita Prefectural University, 84-4 Ebinokuchi, Tsuchiya, Honjo, Akita 015-0055, JAPAN.

²Yokohama National University, 79-5 Tokiwadai, Hodogaya, Yokohama, Kanagawa 240-8501, JAPAN.

ABSTRACT

Ferromagnetic single-electron transistors coupled to the controlling gate potential by the gate resistance and gate capacitance in series are studied quantitatively. In this type of the device, several metastable charge states are possible within the Coulomb blockade range. The enhancement and hysteresis of tunnel magnetoresistance on drain and gate voltages are predicted. Inelastic macroscopic quantum tunneling of charge and existence of several charge states play an important role for the unique behavior of the tunnel magnetoresistance. This implies that RC-coupled ferromagnetic single-electron transistors have a new functionality as novel magnetoresistive nanostructure devices.

INTRODUCTION

Recent progress of nanotechnology to magnetic materials and magnetoresistive devices has attracted much attention. In ferromagnetic single-electron transistors (FMSETs), the interplay of the single-electron charging and spin-dependent tunneling effects is currently an attractive topic. In particular, the study of tunnel magnetoresistance (TMR) in FMSETs is a rapidly growing field. The proposal of single-electron transistors with capacitively and resistively coupled gates (C- and R-SETs) were first reported by Likharev in 1987 [1]. Since the structure of C-SET is easily realized experimentally, this has been studied in a great detail. In addition, capacitively coupled FMSETs (C-FMSETs) have also been investigated theoretically [2, 3] and experimentally [4-6]. In R-SETs, the gate resistance should be much larger than the quantum resistance to prevent quantum fluctuations of the island charge. Therefore, in contrast to C-SET, the R-SET is quite difficult to realize experimentally and has received practically no attention so far. However, theoretical and experimental studies on the R-SETs were presented recently [7, 8]. Moreover, electrical characteristics and TMR on resistively coupled FMSETs (R-FMSETs) have also been reported quantitatively in 2002 [9], but the R-FMSETs have not been studied experimentally.

In this paper, we propose another type of the FMSET, which is coupled to the controlling gate potential V_g by the gate resistance R_g and the gate capacitance C_g in series (RC-FMSETs). Since the current through the R_g may change the effective charge of the central electrode ("island") of the double junction system during the time interval between the tunneling events,

several metastable charge states are possible within the Coulomb blockade regime. Therefore, the potential of the island electrode and the drain current may exhibit hysteresis as a function of the gate potential. Considering the macroscopic quantum tunneling of charge (q-MQT) [10, 11], we study here transport properties of the electron in the RC-FMSET quantitatively.

MODEL

RC-coupled ferromagnetic single-electron transistor with double tunnel junction is shown in Fig. 1. The gate electrode consists of an RC circuit and connects an island electrode with the controlling gate potential. Source, drain and island electrodes are ferromagnetic metals. We assume that the magnetization in the electrodes usually shows the antiferromagnetic alignment in zero magnetic field (antiparallel configuration) and takes the ferromagnetic alignment with applying the magnetic field (parallel configuration). The polarization of source, drain and island electrodes can be taken into account by the difference between the tunnel resistances R_p (parallel) and R_{ap} (antiparallel) in each ferromagnetic tunnel junction. In other words, the tunnel resistance of each ferromagnetic tunnel junction is determined by the spin-dependent tunneling, which is R_p for the ferromagnetic alignment and R_{ap} for the antiferromagnetic alignment, and is treated as the junction resistance.

As mentioned above, the RC-FMSET has an $R_g C_g$ coupling circuit between the island and the gate potential. Hence, the relaxation time of the coupling circuit affects the effective background charge of the double junction system due to the variation of the charge at the coupling capacitance C_g . As a result, the charge state of the spin accumulation in the island may be influenced and released by a finite current going through the coupling circuit. In addition, the spin-flip relaxation time, which is crucial for the observation of the spin accumulation, strongly depends on the material quality of the island [12-15]. Therefore, we assume that the spin in the island is equilibrated [2, 3, 16, 17].

We consider the ferromagnetic tunnel junction system with the TMR = 20 % under the

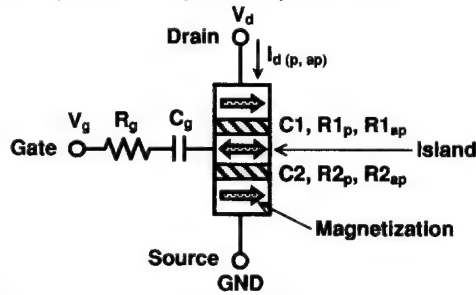


Figure 1. Schematic of an RC-coupled ferromagnetic single-electron transistor.

sequential tunneling regime, which corresponds to the spin polarization $P = 0.3$. So, if the tunnel resistances under the ferromagnetic alignment are assumed to $R_{1p} = 100 \text{ k}\Omega$ and $R_{2p} = 5 \times R_{1p} = 500 \text{ k}\Omega$, the tunnel resistances under the antiparallel configuration are given by $R_{1ap} = 1.2 \times R_{1p} = 120 \text{ k}\Omega$ and $R_{2ap} = 1.2 \times R_{2p} = 600 \text{ k}\Omega$. Capacitance of each ferromagnetic tunnel junction is also assumed to $C_1 = C_2 = 1 \text{ aF}$. The gate resistance R_g should be greater than the quantum resistance $R_Q = h/e^2$ and is set to $10 \text{ M}\Omega$ ($R_g \gg R_{1(p,ap)}, R_{2(p,ap)}$). The gate capacitance C_g is also given by $C_g/(C_1+C_2) = 3$. These parameters lead that the energy scale of the quantum fluctuations of the $R_g C_g$ coupling circuit $\hbar/(R_g C_t)$ (where $C_t = C_g(C_1 + C_2)/(C_1 + C_2 + C_g)$) is less than $e^2/(C_1 + C_2)$. This implies that for the typical current $I_{d(p,ap)} \sim e/((R_{1(p,ap)} + R_{2(p,ap)})(C_1 + C_2))$ the relaxation time of the $R_g C_g$ coupling circuit is greater than the typical time interval of the tunneling events $e/I_{d(p,ap)}$. The dynamics of the RC-FMSET can be calculated within the framework of the semiclassical model [18]. In the calculation, Monte Carlo procedure is used, and the rate of 2nd order inelastic q-MQT (co-tunneling) is also considered in addition to the rate of usual single-electron tunneling.

RESULTS AND DISCUSSION

Figure 2 shows drain currents for parallel and antiparallel configurations and TMR as a function of the drain voltage on the RC-FMSET. In this result, the temperature and the gate voltage are set at $T = 1 \text{ K}$ and $V_g = 0 \text{ V}$, respectively. Due to the large difference between $R_{1(a,ap)}$ and $R_{2(a,ap)}$, one can see the Coulomb staircases. Furthermore, the drain currents clearly show the hysteresis as a function of the drain voltage. Although the TMR shows 20 % when the Coulomb blockade is released as expected, the TMR is increased up to 44 % under the Coulomb blockade regime. This is due to the difference in the rate of the single-electron tunneling and the inelastic q-MQT. Moreover, hysteresis of the TMR is also observed, which is due to the hysteresis on the Coulomb blockade. This is a unique feature of the RC-FMSET in contrast to the usual C- and R-

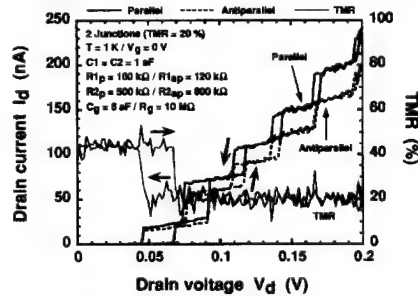


Figure 2. Drain currents and TMR ratio as a function of drain voltage on an RC-coupled ferromagnetic single-electron transistor.

FMSETs. From the semiclassical model on the RC-FMSET, the charge injection from the $R_g C_g$ coupling circuit to the island electrode is determined by the potential $V_{RC} = V_g - V_d C_1 / (C_1 + C_2)$. Therefore, for the charge state with definite number n of excess electrons in the island electrode, charge Q_n on the equilibrium in the $R_g C_g$ coupling circuit is expressed as $Q_n = (ne + Q_0 + C_g V_{RC}) / (C_1 + C_2) / (C_1 + C_2 + C_g)$, where Q_0 is the background charge of the island electrode. Since the condition of the blockade for the definite charge state n is given by $|Q_n| < e/2$, the charge Q_n shows the several metastable charge states satisfying the condition $|Q_n| < e/2$. The charge Q_n of the RC-FMSET implies that the addition of the electron to the island electrode causes the increase of the effective charge Q_n only by $e(C_1 + C_2) / (C_1 + C_2 + C_g)$, leading that several stable states are possible within the blockade. This is the origin of the hysteresis on the drain currents and the TMR. In this system, the stability threshold voltage for a certain charge state n is given by $V_{th}(n) = \min\{(e/2 - Q_n)C_1, (e/2 + Q_n)C_2\}$ ($V_{th}(n) > 0$) and can be varied by changing the gate potential. The maximum value becomes to $V_{th, \max} = e / (C_1 + C_2)$ from the condition $(e/2 - Q_n)C_1 = (e/2 + Q_n)C_2$. Its minimum value corresponds to the condition $V_{th}(n) = V_{th}(n+1)$ which gives $V_{th, \min} = e C_g / ((C_1 + C_2)(C_1 + C_2 + C_g))$. Hence, in RC-FMSET one can't suppress the threshold voltage to zero by varying the gate potential.

Figure 3 (a) shows the modulation characteristics of the drain current in a parallel configuration with different gate voltages. The gate voltages are varied from 0 mV (bottom) to 30 mV (top). Each curve is shifted vertically by 50 nA for clarity. One can see the periodic modulation of Coulomb blockade region by the variation of the gate voltage. Furthermore, hysteresis window of the drain current is also modified by the variation of the gate voltage. The relation between the TMR and the drain voltage at each gate voltage is illustrated in Fig. 3 (b). The TMR is clearly enhanced and defined to 44 % inside the Coulomb blockade. The modulation of the hysteresis window is clearly observed by varying the gate voltage.

Drain currents for parallel and antiparallel configurations and TMR as a function of the gate voltage are shown in Fig. 4. The temperature and the drain voltage are set at $T = 1$ K and $V_d = 50$ mV, respectively. The charge state of the device moves to the neighboring stable state when the

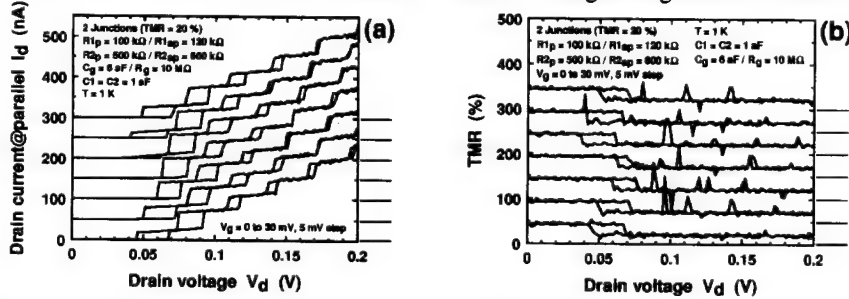


Figure 3. (a) Drain current and (b) TMR ratio as a function of drain voltage on an RC-coupled ferromagnetic single-electron transistor.

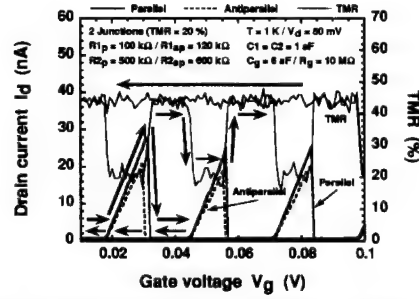


Figure 4. Drain currents and TMR ratio as a function of gate voltage on an RC-coupled ferromagnetic single-electron transistor.

gate voltage is increased. Thus the drain currents for a fixed drain voltage show a periodic function of the gate voltage with the period of e/C_g , which is similar to that of the C-FMSET. Then, as the gate voltage is decreased, the drain currents hardly show current flow, which is due to that the device is in the Coulomb blockade state. The behavior of the drain currents depending on the sweep direction of the gate voltage causes the hysteresis of the TMR as illustrated in Fig. 4. The TMR is increased up to 44 % within the Coulomb blockade range and is modulated between 20 % and 44 % depending on the behavior of the drain currents.

Figure 5 (a) shows the drain currents for parallel and antiparallel configurations at $T = 1$ K and $V_d = 50, 70$ and 90 mV as a function of the gate voltage. The curves are shifted vertically by 30 nA for clarity. As expected, the drain currents at the fixed gate voltage increase with increasing the drain voltage. Since the maximum threshold voltage of the Coulomb blockade becomes to $V_{th, max} = e/(C1 + C2) = 80$ mV in this device, the hysteresis of the drain currents becomes clear when the drain voltage is greater than the $V_{th, max}$. The potential of the island electrode V_{island} is defined as $V_{island} = (Q_n + V_d C1)/(C1 + C2)$, therefore the V_{island} exhibits hysteresis due to the several charge states by the variation of the gate voltage, resulting in the hysteresis of the drain current on the gate voltage. The relation between the TMR and the gate

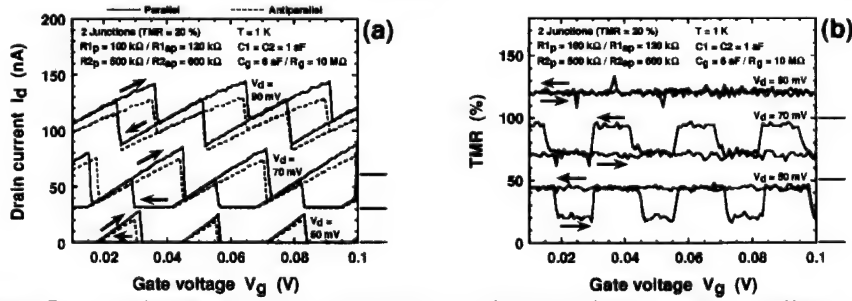


Figure 5. (a) Drain current and (b) TMR ratio as a function of gate voltage in different drain voltages.

voltage is shown in Fig. 5 (b). The curves are shifted vertically by 50 % for clarity. The TMR is 20 % at $V_d = 90$ mV, in which the bias condition is away from the blockade. In contrast, the TMR is successfully modulated within the blockade conditions ($V_d = 50$ and 70 mV), depending on the behavior of the drain currents. It should be noted that by using RC-FMSET, the enhancement and hysteresis of the TMR could be controlled by the drain and gate voltages.

CONCLUSIONS

In conclusion, we have proposed and studied ferromagnetic single-electron transistors controlled with RC gate. The inelastic q-MQT process under the Coulomb blockade regime leads to a considerable enhancement of TMR. Several metastable charge states within the Coulomb blockade range cause a clear hysteresis of TMR. These features have a specific dependence on the gate and drain voltages. This result implies a new functionality of the RC-FMSET.

REFERENCES

1. K. K. Likharev, *IEEE Trans. Magn.* **MAG-23**, 1142 (1987).
2. S. Takahashi and S. Maekawa, *Phys. Rev. Lett.* **80**, 1758 (1998).
3. J. Shirakashi and Y. Takemura, *J. Appl. Phys.* **89**, 7365 (2001).
4. K. Ono, H. Shimada, and Y. Ootuka, *J. Phys. Soc. Jpn.* **66**, 1261 (1997).
5. H. Shimada, K. Ono, and Y. Ootuka, *J. Phys. Soc. Jpn.* **67**, 1359 (1998).
6. K. Ono, H. Shimada, and Y. Ootuka, *J. Phys. Soc. Jpn.* **67**, 2852 (1998).
7. A. N. Korotkov, *Appl. Phys. Lett.* **72**, 3226 (1998).
8. Yu. A. Pashkin, Y. Nakamura, and J. S. Tsai, *Appl. Phys. Lett.* **74**, 132 (1999).
9. J. Shirakashi and Y. Takemura, *J. Appl. Phys.* **91**, 7442 (2002).
10. D. V. Averin and Yu. V. Nazarov, *Phys. Rev. Lett.* **65**, 2446 (1990).
11. D. V. Averin and Yu. V. Nazarov, in *Single Charge Tunneling, Coulomb Blockade Phenomena in Nanostructures*, edited by H. Grabert and M. H. Devoret (Plenum, New York, 1992), p. 217.
12. M. Johnson and R. H. Silsbee, *Phys. Rev. Lett.* **55**, 1790 (1985).
13. M. Johnson, *Phys. Rev. Lett.* **70**, 2142 (1993).
14. M. Johnson and R. H. Silsbee, *Phys. Rev. B* **37**, 5326 (1988).
15. P. M. Tedrow and R. Meservey, *Phys. Rep.* **238**, 174 (1994).
16. J. Barnaś and A. Fert, *Phys. Rev. Lett.* **80**, 1058 (1998).
17. K. Majumdar and S. Hershfield, *Phys. Rev. B* **57**, 11521 (1998).
18. D. V. Averin and K. K. Likharev, in *Mesoscopic Phenomena in Solids*, edited by B. L. Altshuler, P. A. Lee and R. A. Webb (North-Holland, Amsterdam, 1991), p. 173.

Metal/Self-Assembled Monolayer/Metal Junctions for Magnetoelectronic Applications.Y.A Ovchenkov, Chunjuan Zhang¹, J. Redepenning¹, B. Doudin*Department of Physics and Astronomy, University of Nebraska-Lincoln, Lincoln, NE 68588-0111*¹*Department of Chemistry, University of Nebraska-Lincoln, Lincoln, NE 68588-0304***ABSTRACT**

Metal/organic self-assembled monolayer/metal junctions were investigated for junction areas 10^{-2} to $10^2 \mu\text{m}^2$. Several types and thickness of monolayers are investigated, and magnetic electrodes were made. Electroless deposition was used to make the top metal without disrupting the organic film. This deposition is activated with Pd clusters obtained by evaporation or by chemical reduction of a Pd-based catalyst. This method allows us to obtain a high yield of junctions that are not electrically shorted and are mechanically and electrically stable over a wide temperature range. Low-temperatures investigations reveal strong non-linearity in the IV curves and an increase of resistance with decreasing temperature. Zero bias anomalies observed at low temperatures are attributed to a Coulomb blockade associated with the Pd clusters.

INTRODUCTION

Metal-Insulator-Metal (MIM) tunnel junctions are of great interest for applications as magnetic sensors and memory devices. If both metals are ferromagnetic, the tunnel resistance of the system depends on the relative magnetic orientations of the two magnetic layers [1]. The magnitude of this effect (typically reaching 40%) depends on the properties of the insulator. The main desirable properties are the possibility to make very thin barriers (smaller than 1 nm), with atomically sharp interfaces. To date, the vast majority of tunnel magnetic junctions have been constructed using Al_2O_3 barriers. We intend to examine the possibility to use organic films as an alternative to Al_2O_3 in MIM structures.

It is well-documented that a variety organic thiols can be used to construct self assembled monolayers (SAM) on metallic surfaces [2]. However, significant synthetic difficulties are encountered when trying to deposit a top metallic electrode without disrupting the organic substructure. Evaporated and sputtered metal layers are often not stable on organic thiol monolayers [3]. High diffusibility of thiols [4], as well as low structural stability of evaporated/sputtered films, usually destroys the MIM structure.

We have successfully used electroless deposition (ELD) to plate ferromagnetic metal films on top of self-assembled organic tunnel barriers. Such metal films can show better structural stability than their evaporated or sputtered counterparts [5]. Mechanical and thermal damage to the organic layers is avoided. We can also tailor the distal end of alkanethiols with functional groups capable of activating ELD growth. This method is known as selective ELD [6].

We report here the preparation and characterization of two types of MIM junctions (Figure.1). The first, which was pattern using lithographic techniques, has a planar cross geometry with junction areas ranging from 10 to 100 μm^2 . The second type of junction was prepared by electrodeposition in a template to produce columnar MIM structures with 30 to 400 nm diameters. These geometries enable us to investigate junctions with areas spanning several orders of magnitude. The junctions with smallest cross-sectional area are particularly attractive for minimizing the probability of pinholes.

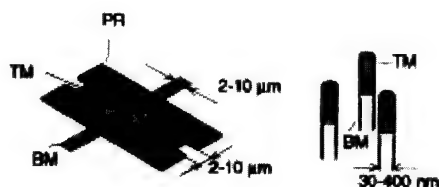


Figure 1. Schematics of the samples geometries for the planner junction (left) and nanowires (right). Thiol layer was deposited on bottom metal electrode (BM) from solution. Top metal electrode (TP) was obtained by electroless deposition. Photoresist mask (PR) was used in planar junction to limit the area.

SAMPLE PREPARATION

Planar MIM junction

Optical lithography was used to pattern lines down to a 2 μm width on silicon wafers coated with SiO(300nm)/Ti(10nm)/Au(100nm). Ni and Co top layers were then obtained by thermal deposition. An opening of a few μm was patterned using a second layer of photoresist. Depositions of alkanethiols were made in a Braun Labmaster 130 inert atmosphere box. The coating solutions were comprised of ca. 0.1 M alkanethiol (ethanethiol, pentanethiol, hexanethiol or dodecanethiol) dissolved in ethyl alcohol. All alkanethiols (Aldrich) were used as purchased. Ni and Co bottom metal layers were electrochemically cleaned to remove native oxides prior to SAM deposition. Some of the samples where subsequently heat-treated at 60-100 C for 1-24 hours. Top layers of Cu and Ni were made by ELD method. The ELD plating process was catalyzed by a Pd seed layer of 3 - 5 Å thickness. The seed layer was obtained by slow evaporation in a vacuum chamber. Cu films were made using a bath composition found in the literature [7]. Ni films were made using an electroless hypophosphate bath [5].

Nanowires in nonporous membranes.

We used polycarbonate nanoporous membranes (Watman corp.) with a thickness of 10 μm and nominal cylindrical pore diameters of 30, 100 and 400 nm. One side of the membrane was sputtered with gold, which served as working electrode. Growth of cylindrical wires of diameters slightly larger than the nominal pore diameter value was reported in the literature for a variety of materials [8]. Bottom Ni half-wires were plated from a classic Watt's bath by adjusting the deposition time to grow the wire approximately half way through the membrane. The membranes were then dried and transferred to an inert atmosphere box where they were electrochemically cleaned. A SAM was prepared from 2-mercaptoethylamine or 4-aminothiophenol. Both molecules have $-\text{NH}_2$ tail groups that are used to generate the Pd catalyst. (Synthetic details for the Pd catalyst can be found in [9]). Samples were exposed for 1 hour to the Pd catalyst solution, which was made by dissolving 10 mg Na_2PdCl_4 and 1.75 g of NaCl in 50 ml of H_2O , and then adjusting the solution to $\text{pH}=1$ with 37% HCl. Ni top electrodes were obtained by ELD deposition using the method described above for planar junctions. The deposition process was terminated when metal islands were visually detected on the membrane surface.

RESULTS AND DISCUSSION

Samples were investigated in a temperature range of 1.5 K – 300 K and under applied magnetic fields up to 10 T. Four point connections were made to perform AC and DC electrical measurements. Weak adhesion between the SAM and the top electrode was generally found on planar samples, indicating a lack of chemical bonding to the top electrode. The resistance values of the junctions varied over several orders of magnitude without any direct correlation with junction area or molecular length. We found a lower probability of electrical shorts for heat-treated SAMs, which indicates that this process leads to a highly ordered and more densely packed tunnel barriers. This conclusion is consistent with that found in a recent report concerning electrochemical characterization of SAMs [10].

Junctions with resistances ranging from tens of kOhm to several MOhm were investigated. Most samples showed good temperature stability, and were capable of sustaining several temperature sweeps between room temperature and a few Kelvin. We observed a slow variation of the resistance as a function of temperature between 300 K and 20 – 50 K. A much larger increase was observed upon lowering the temperature below 20 K. Such behavior is related to a large bias dependence of the differential resistance, spanning several orders of magnitude (Figure 2). These observations can be attributed to a Coulomb blockade caused by the Pd particles incorporated in the organic layers. If a particle is separated by a total capacitance C from the electrodes, the charging energy necessary to add one electron on the particle (i.e., $e^2/2C$) hinders the electron flow if the charging energy is significantly larger than the thermal energy [11]. From the temperature dependence of the resistance, a charging energy of several meV can be deduced, corresponding to the bias values at which the resistance of the sample diminishes significantly.

Some samples demonstrated complicated dependence of the resistance on bias. Asymmetrical shoulders and hysteresis on these shoulders (Fig. 3a) were observed. Since the width of $R(\text{Bias})$ curve is proportional to $1/C$, where C is capacitance of particle, the appearance of shoulders can be explained by a significant parallel current channel through smaller particles. In this case hysteresis may reflect metastability of particle positions. Switching instabilities

(Figure 3b) and long term relaxation after applying a magnetic field (not shown) were observed for these samples as well. Again, instabilities were attributed to mechanical variability of Pd clusters trapped inside the organic film. The nanowire junctions showed properties similar to those of larger areas, which confirms the assertion that the electrons flow through a limited area.

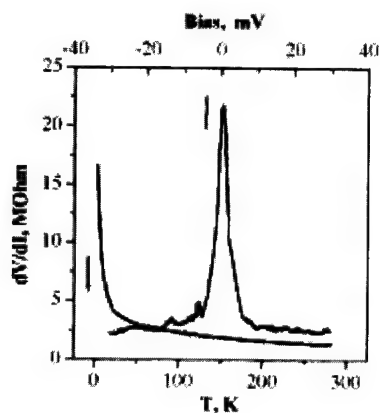


Figure 2. Zero bias differential resistance as a function of temperature (bottom scale) and as a function of voltage bias at 1.6 K (upper scale) for Ni-ethanethiol-Ni planar junction.

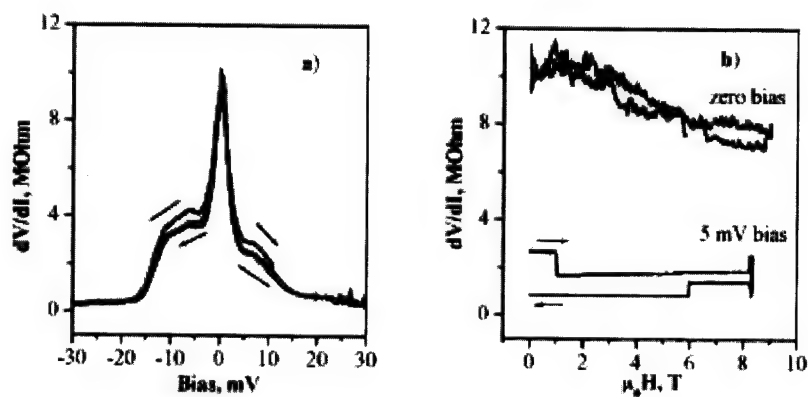


Figure 3. (a):Differential resistance of Au-dodecanethiol-Ni tunnel junction at 1.6 K as a function of applied bias. The hysteresis in the IV curves disappears after several voltage weeps, stabilizing the lower curve. (b)Magnetic field dependence for two voltage bias.

CONCLUSION

A variety of MIM structures were investigated, with area values varied from $10^{-2} \mu\text{m}^2$ to more than $10^2 \mu\text{m}^2$. We observe a systematic blocking of the current at small bias, which we interpret in terms of a Coulomb blockade associated with Pd clusters. Synthetic routes that do not rely on a Pd seed layer need to be found to avoid blockade effects. Alternatively, the use of lighter elements for seed clusters, or the use of magnetic seeds, will provide interesting systems for which the effect of Coulomb blockade on spin-dependent transport properties in tunnel junctions may be studied. Theoretical predictions [12,13], as well as preliminary experiments [14], indicate that magnetoresistance can be enhanced in the Coulomb blockade regime.

The partial support of this work by ONR is gratefully acknowledged.

REFERENCES

- [1] J.S.Moodera, J.Nassar, and G.Mathon, *Ann. Rev. Mater. Sci.* **29** 381-432 (1999)
- [2] Frank Schreiber, *Prog. In Surf. Sci.* **65** (2000) 151; Abraham Ulman, *Chem. Rev.* **96** 1533 (1996)
- [3] Michael J. Tarlov, *Langmuir* **8** 80 (1992),
- [4] P.E. Sheehan, L.J. Whitman *Phys. Rev. Lett.* **88** 156104 (2002)
- [5] M. Schlesinger in *Modern Electroplating* 4th edition, edited by M. Schlesinger, M. Paunovic, (John Wiley&Sons inc, New York, 2000) p. 667
- [6] A. Ulman, Self assembled monolayers of thiols, in *Thin Films*, vol. 24, Academic Press, San Diego, 1998
- [7] W. Goldie, *Plating*, **51** 1069 (1964)
- [8] C. R. Martin, *Nanomaterials* **266**, 1961 (1994).
- [9] H. Kind, A.M. Bittner, O. Cavalleri, K. Kern, T. Greber, *J. Phys. Chem. B* **102** 7582 (1998)
- [10] H. Hagenstorm, M.A. Schneeweiss and D.M. Kolb *Langmuir* **15** 7802 (1999)
- [11] H. Grabert and M. H. Devoret, *Single charge tunneling*, NATO ASI Series (Plenum, New-York), (1991).
- [12] S. Takahashi and S. Maekawa *Phys. Rev. Lett.* **80** 1758 (1998)
- [13] J. Barnas and A. Fert, *Phys. Rev. Lett.* **80** 1058 (1998)
- [14] K. Ono, H. Shimada, Y. Ootuka *J. Phys. Soc. Jpn.* **66** 1261 (1997)

Recent Developments in Magnetic Recording Heads

Atsushi Tanaka and Mitsumasa Oshiki
Storage System Laboratories, Fujitsu Laboratories Ltd.,
Atsugi, 243-0197, Japan

ABSTRACT

Recently developed and future magnetic head technologies are reviewed. Scaling of dimensions brought about significant increases in recording densities in the last decade. On the recording head aspect, as the read head is narrowed, large improvements in sensitivity are required. Therefore, spin-valve read heads have been improved by introducing synthetic ferromagnetic pinned layers, a spin filter back layer and a specular scattering layer. The current perpendicular to plane (CPP) structure is now being adopted instead of the current in plane (CIP) structure which is the present magnetic head structure. Under heads with a CPP structure, tunneling magnetoresistance (TMR) devices and multilayer GMR are candidates. In CPP mode, we can make better use of "spintronics" or spin-dependent conduction phenomena because device character depends more directly on the spin-dependent electronic states of the materials. Future technologies of read head are also discussed.

INTRODUCTION

Information and communication systems increasingly handle huge amounts of data, placing heavy demands on hard disk storage capacity and performance. Figure 1 shows the development of areal recording densities for mobile disk drive products with magnetoresistive (MR) heads and giant magnetoresistive (GMR) spin-valve heads. High annual growth rates of 80% or more have been achieved in areal recording density during this period. Areal recording density is approaching 70 Gbit/in² this year. Figure 1 also shows demonstrations made over several years at international magnetic conferences, including Intermag, MMM, and TMRC. These densities were achieved by combining advanced head technology with low-noise disk media [1-5]. The progress in developing spin-valve materials and high-sensitivity spin-valve read heads could enable us to achieve a continued increase in areal recording density in hard disk drives. In this paper recent developed GMR read head technologies are reviewed and promising future technologies of current-perpendicular-to-plane (CPP) are also mentioned.

GMR READ HEAD

Figure 2 summarizes the evolution of the spin-valve structure we have developed. The spin-valve films are classified as follows:

- a) Bottom type spin-valve
- b) Bottom type synthetic ferrimagnetic spin-valve with back layer
- c) Bottom type double specular spin-valve

The bottom type spin-valve film (Figure 2 (a)) has a simple structure consisting of four layers: a free layer, a Cu spacer layer, a pinned layer, and an antiferromagnet pinning layer. The resistance versus field R-H curve of the bottom type spin-valve in the early development stage is shown in Fig. 3(a). The film structure is Sub./Ta(5 nm)/NiFe(5)/PdPtMn(25)/CoFe(3.5)/Cu(3.5)/CoFe(5.5)/NiFe(2.5). The MR ratio is ~ 6.0% [4]. For the bottom type synthetic ferromagnetic spin-valve, two magnetic layers antiferromagnetically couple to each other

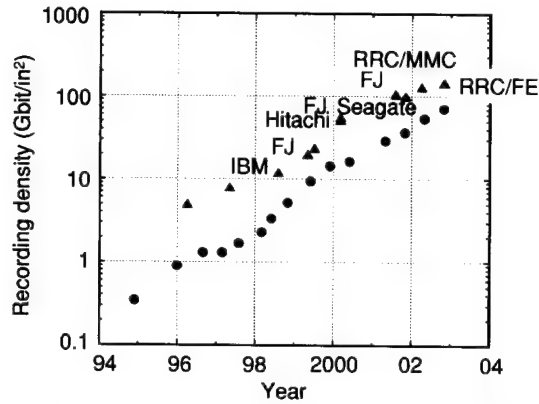


Figure 1. Trend of the recording density of hard disk drive (HDD). Circles indicate the evolution of mobile HDD products. Triangles indicate recording densities of demonstration reported at the major conferences.

through a very thin Ruthenium layer. This is an artificial antiferromagnetic state; this structure is called synthetic antiferromagnet (SAF) [6]. In this structure, the static magnetic field experienced by the free layer arising from the pinned layer is reduced and useful in keeping the proper magnetic bias point, especially when the sensor stripe height is reduced down to half a micron. Moreover, the magnetic moments stabilize each other, such that the effective exchange bias field from the antiferromagnet is enhanced and the pinning layer can be made thinner than in a conventional spin-valve.

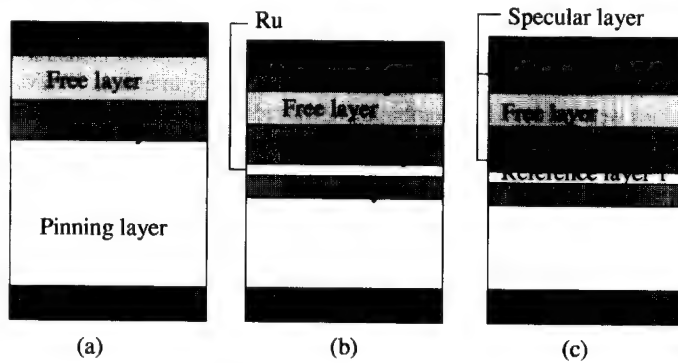


Fig. 2 Evolution of spin valve films. (a)bottom type spin valve, (b) synthetic ferrimagnetic spin valve with Cu back layer, (c) synthetic ferrimagnetic spin valve with double specular layers.

Fig. 2(c) shows a synthetic ferromagnetic double specular spin valve with an MR ratio of 15% MR as shown in Fig. 3(b). The film structure is Buffer (7 nm)/PdPtMn(10)/CoFeB(1.6)/Ru(0.75)/CoFeB(1.25)/Oxide/CoFeB(1.5)/Cu(2.3)/CoFeB(2)/Fe₂O₃(2)/Al₂O₃(32). The pinning layer is 10 nm thick and the magnetic state was stable with a very small hysteresis. This thin pinning layer was enabled by the synthetic ferrimagnetic structure and the film growth condition (background pressure $< 2 \times 10^{-7}$ Pa) [7]. The MR ratio of the double specular spin-valve is two times larger than that of a simple bottom type spin-valve. A larger signal output can therefore be expected.

CPP READ HEAD

Ultra-high density recording over 100 Gbit/in² requires a much higher sensitivity and a narrower read-core-width read head. To satisfy these requirements, the CPP heads have been extensively investigated and developed as CPP heads have several advantages compared to current in plane (CIP) heads, which are currently being used for recent hard disk drives (HDDs). Table I shows a comparison between CIP and CPP structure heads. If we assume the current density is limited at a constant value, the output voltage of the CIP heads is proportional to the core width and higher sensitivity sensor materials are required as the core width becomes narrower. On the other hand, expected output voltage is constant for a CPP head.

If the power consumption of the sense current is limited to avoid a temperature rise, the output voltage of the CPP head is roughly inversely proportional to the square root of the sensor area. For the CPP head structure, only the sensor film is in the read gap and is suitable for higher linear density recording. Higher heat conduction, which is important for stable head operation, can be expected for the CPP structure than for the CIP structure. The CPP structure therefore shows several advantages as the sensor size is reduced. However, the device resistance increases as the sensor area decreases and this resistance increase is the main problem in ultra high density CPP head.

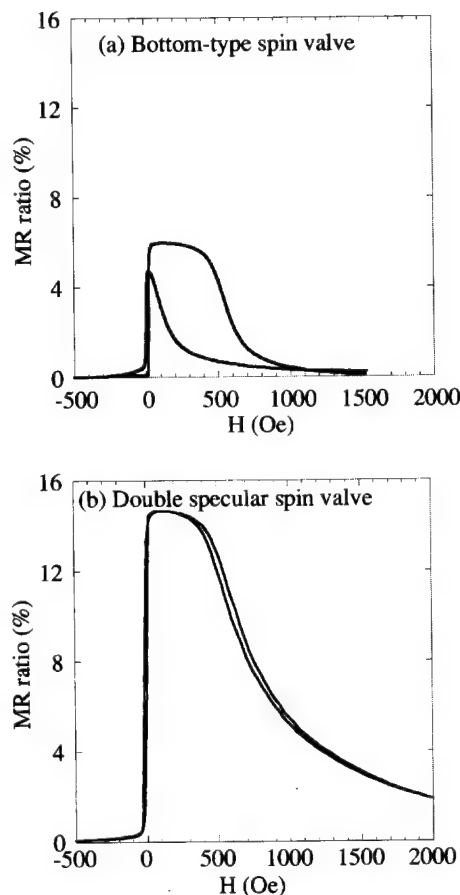


Fig. 3 R-H curves of the conventional bottom type spin valve (a), and double-specular spin valve (b).

Figure 4 shows the target properties for a $0.01 \mu\text{m}^2$ CPP element for 150 Gbit/in² read head application [8]. The area is estimated by considering the power consumption, electron migration of the element, and data transfer rate. A tunneling magnetoresistance (TMR) head is one of the candidates for realizing high sensitivity. However, TMR heads have large resistances, which lead to ESD (electrostatic discharge) problems, limit the operating frequency, and make the Johnson and Shot noise high. It is very difficult to make low-resistance barrier-layers and significant progresses in fabrication technology are needed. Another candidate for ultra-high densities is a CPP head using GMR films.

Several researchers have studied GMR properties in the CPP mode, and they have demonstrated magnetoresistance changes at room temperature twice as large as those in the CIP mode in calculation [9] and experiment [10]. CPP heads using GMR multilayers have also been investigated [11]. Although multilayer CPP heads are expected to obtain large output signals, they show problems such as hysteresis generation and difficult magnetic domain control of the read element. This is aggravated by the requirement for thinner read gaps. In contrast, a CPP element using a spin-valve (SV) film can be rid of such problems of GMR multilayers. We have studied the GMR properties of SV film in CPP mode and tried to improve their magnetoresistance change.

The MR ratio of conventional spin valve films in CPP mode is about 0.5 % as shown in Fig. 4. The MR ratio must be increased to 8%, if the product of sensor resistance and its area, RA , is to be kept constant. But this is difficult to realize by increasing ΔRA only, the product of sensor resistance change and its area. However, at the largest allowed RA , an MR ratio of only 3% is needed. This is an easier path to reach the target area as RA is also increased. However, for the corresponding sensor size at a 150Gbit/in² design, calculations show that the amplitude of the output voltage is still insufficient as shown in Fig. 4. In this study, we tried to improve the magnetoresistive properties of CPP-SV heads for 150 Gbit/in² recording.

Table I. CIP vs. CPP heads

	CIP head	CPP head
Output signal		
current density limit	Proportional to core width	Constant
power consumption limit	Constant	Inversely proportional to square root of sensor area
Read gap	Sensor and two gap layer thicknesses	Sensor thickness
Heat radiation	Mainly through terminals at both ends of the sensor	Direct heat connection to top and bottom terminals
Device resistance	Constant	Increase as sensor area decreases

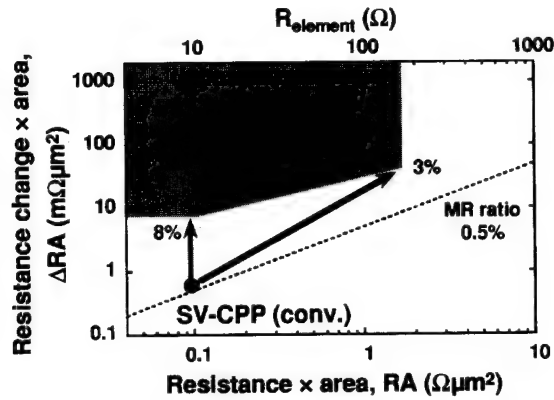


Fig. 4 Target region of 150Gbit/in² read head is shown as a function of RA and ΔRA . The required ΔRA is determined with the condition that the output signal >1 mV. The head efficiency is assumed to be 13.5%. Limitations due to data transfer, power consumption, and migration are also considered [8].

GMR PROPERTIES IN CPP MODE OF SPIN-VALVE FILMS

CPP properties were measured using a four-terminal technique. The spin-valves were sputter-deposited in an ultrahigh vacuum chamber and patterned by a photolithography and ion-milling processes. The element size was varied from 0.1 μm^2 to 1.0 μm^2 . Details of the fabrication process are published elsewhere [12]. The film structure of the single spin-valve was buffer/PdPtMn (13 nm) / CoFeB(1.5, 3)/Cu(4)/ CoFeB(1.5, 3)/ capping layer, and the dual spin valve films was buffer/PdPtMn(15)/ CoFeB(1.5, 3)/ Cu(4)/ CoFeB(3,6)/ Cu(4)/ CoFeB(1.5, 3)/ PdPtMn(15)/ capping layer. Both resistance (R) and resistance change (ΔR) are inversely proportional to the GMR size (A) of the CPP elements. As an example, for the single spin-valve with thinner magnetic layers, the RA was 81 $\text{m}\Omega\mu\text{m}^2$ and the ΔRA was 0.35 $\text{m}\Omega\mu\text{m}^2$; the MR ratio of the element was 0.43%. The RA and ΔRA are plotted

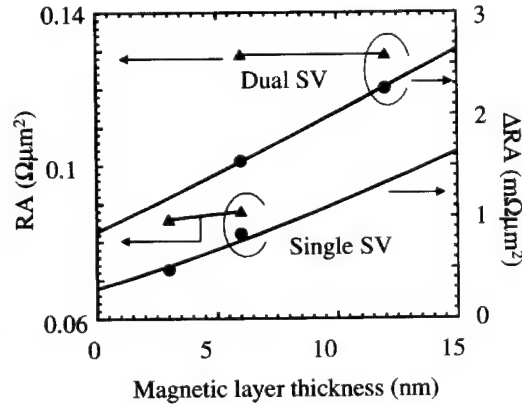


Fig. 5 The RA and ΔRA of single and dual spin valve films in CPP mode. The RA is almost constant for magnetic layer thickness. The behavior of the ΔRA was well described by the two-current series-resistor model [13].

for single and dual spin-valves in Fig. 5. The magnetic layer thickness is the total thickness of the free and reference layers. ΔRA increases as the magnetic layer thickness is increased. The dual spin valve shows a larger ΔRA than a single spin-valve due to the increase of magnetic/nonmagnetic interfaces. These can be explained by increments in the spin-dependent bulk and interface scattering, respectively. Each layer thickness is smaller than the spin diffusion length and the behavior of ΔRA is well described by the two-current series-resistors model [13].

GMR-PROPERTIES IN CPP MODE OF SPIN-VALVE FILMS WITH OXIDE LAYER

Even for dual-type SV films, ΔRA remains in the order of several $m\Omega\mu m^2$. Therefore, it is difficult to obtain sufficient output voltage using conventional spin-valve read heads. We tried to enhance ΔRA by inserting nano-oxide layers (NOL). The nano-oxide layer has highly conductive and resistive regions due to inhomogeneous oxidation. The effective element area is smaller than the physical size and leads to a "confined current path". If the confined path is in the vicinity of the free/Cu spacer/reference layers, then we can expect larger ΔRA while the RA does not increase so much.

The stacking structure of the film was Buffer/PdPtMn/CoFeB/Ru/CoFeB/Cu/CoFeB/Cu/CoFeB(t nm)-NOL/capping layer. The CoFeB under the capping layer was oxidized just after the deposition by oxygen gas at a controlled pressure. Fig. 6 shows RA , ΔRA , and MR ratio as a function of the thickness of the oxidized CoFeB. RA as well as ΔRA increase when $t < 0.9$ nm and the MR ratio is kept less than 1%. ΔRA increases more rapidly when the CoFeB is thicker than 1 nm and the MR ratio is enhanced to 1.5%. This MR ratio increment is thought to be due to the confined current path structure of CoFeB on the Cu back layer. The enhancement of MR is much clearer if the nano-oxide layer of the CoFeB is located between the reference and free layers [14]. In this structure, a ratio of more than 5% was observed in the range of $0.6 \Omega\mu m^2 < RA < 1.5 \Omega\mu m^2$. This GMR property is inside the target region for 150 Gbit/in² recording.

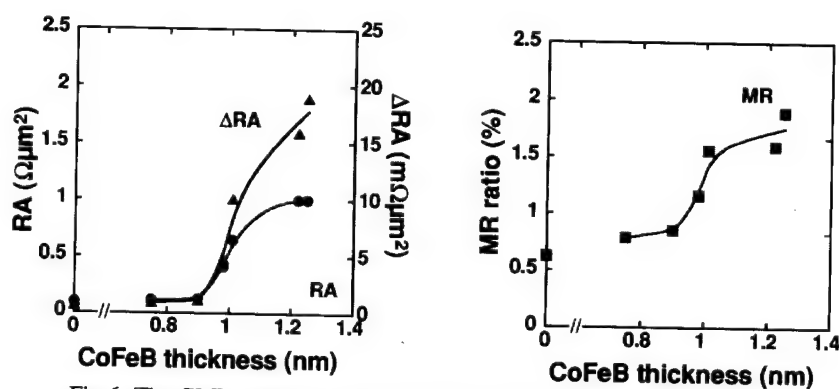


Fig 6. The GMR properties in the spin valve film with nano-oxide layer in CPP mode. MR enhancement was observed $t > 1$ nm, where t is the thickness of the oxidized CoFeB under the capping layer.

PROSPECTS OF SPINTRONICS HEAD

Spin-valve heads are already a kind of "spintronic" devices because they utilize spin-dependent electron conduction. However, CPP structure devices such as TMR and CPP-GMR are closer to being "full-pledged" spintronic device. In CPP mode, the conduction electrons pass through all the multilayers, and conduction and valence band levels show abrupt changes according to the band structure of each material. Therefore, we can make better use of the spin-dependent conduction in CPP structure devices than CIP ones.

Here, one of our recent breakthroughs which may be applicable for head devices are mentioned [15]. Though highly spin-polarized materials such as half metals enable significant enhancements of the magnetoresistance ratio [16], it is difficult to fabricate practical GMR devices using such novel materials.

We have tried to enhance the magnetoresistance by inserting a nonmagnetic thin Cu layer into the free layer, which is hereafter called a laminated free structure [15]. When a Cu layer is inserted in the free layer, the number of magnetic/nonmagnetic interfaces increases from three to five (see Fig. 7). The modification makes the difference between spin up and down resistance increase due to the additional interfaces, i.e., the inserted interfaces act as spin filters in the layer. The effect can be interpreted phenomenologically in the framework of the two-current series-resistor model [17, 15]. Figure 8 shows the enhancement of ΔRA due to the laminated free structure. It elucidates the role of the interfaces in the spin valves in the CPP mode, and the physics of CPP GMR.

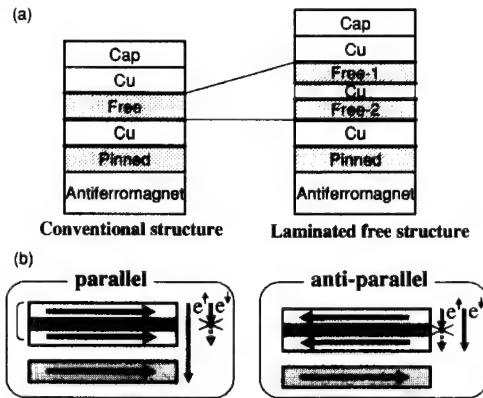


Fig. 7 (a) Schematic structure of the conventional (left) and laminated free-layer (right) spin-valves. Thick lines indicate magnetic/nonmagnetic interfaces. (b) Configuration of the magnetic moment of the laminated free layer. The Cu spacer between the free layers is less than 1 nm and the laminated free layer rotates in phase. The figure schematically shows the filtering effect of the laminated free layer.

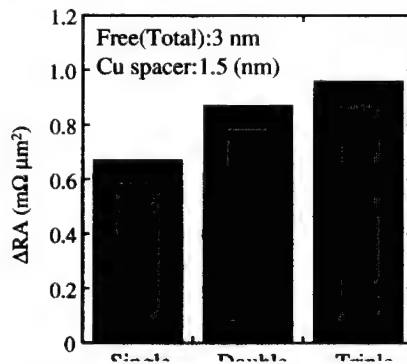


Fig. 8 The ΔRA of laminated free spin-valves. Double refers to two free layers with one Cu spacer; ΔRA increases by 30% compared to a conventional spin-valve. Triple refers to three free layers and two Cu spacer layers.

CONCLUSIONS

Spin valve read heads have been improved year by year, taking advantage of advancements in our knowledge of physics, as in the introduction of the synthetic ferrimagnetic structure and use of specular electron scattering at the interface of metal/oxide layers. The MR ratio of spin-valves has been improved beyond 15% and is now approaching 20%. However, with present materials and known techniques, the MR ratio can hardly be increased. Continuous growth of the recording density requires a new type of device instead of the current-in-plane (CIP) head. The current-perpendicular-to-the-plane (CPP) structure heads are more suitable for high density recording than CIP heads and both CPP-GMR and TMR are promising candidates for future read head over 150 Gbit/in². Single spin-valve heads with a nano-oxide layer exhibited an MR ratio of 5% and its GMR properties are sufficient for 150 Gbit/in² recording. We may simply be entering the vast world of "spintronics" through TMR and CPP-GMR. The layered structure and artificial junction technology consisting of magnetic and nonmagnetic metals, semiconductors, and insulator will provide us very high sensitive devices which may just work for future terabit recording.

REFERENCES

1. H. Kanai, K. Yamada, K. Aoshima, Y. Ohtsuka, J. Kane, M. Kanamine, J. Toda, and Y. Mizoshita: *IEEE Trans. Magn.*, **32**, 3368 (1996).
2. A. Tanaka, Y. Shimizu, H. Kishi, K. Nagasaka, and M. Oshiki, *IEEE Trans. Magn.*, **33**, 3592 (1997).
3. H. Kanai, J. Kane, K. Yamada, K. Aoshima, M. Kanamine, J. Toda, and Y. Mizoshita: *IEEE Trans. Magn.*, **33**, 2872 (1997).
4. A. Tanaka, Y. Shimizu, H. Kishi, K. Nagasaka, H. Kanai, and M. Oshiki, *IEEE Trans. Magn.*, **35**, 700 (1999).
5. E. N. Abarra, M. Suzuki, and I. Okamoto, AA-01, IEEE International Magnetism Conference, Toronto, Canada, April 2000.
6. J. L. Leal and M. H. Kryder, *J. Appl. Phys.*, **83**, 3720 (1998).
7. Y. Shimizu, A. Tanaka, M. Oshiki, and Y. Kataoka, *IEEE Trans. Magn.*, **35**, 2622 (1999).
8. K. Nagasaka, Y. Seyama, R. Kondo, H. Oshima, Y. Shimizu, A. Tanaka, *FUJITSU Sci. Tech. J.* **37** 192 (2001).
9. S. Zhang, and P. M. Levy, *J. Appl. Phys.*, vol. **69**, 4786 (1991).
10. W. P. Pratt Jr., S. F. Lee, J. M. Slaughter, R. Loloee, P. A. Schroeder, and J. Bass, *Phys. Rev. Lett.*, **66**, 3060 (1991).
11. R. Rottmayer, and J.-G. Zhu, *IEEE Trans. Magn.*, **31**, 2597 (1995).
12. K. Nagasaka, Y. Seyama, L. Varga, Y. Shimizu, and A. Tanaka, *J. Appl. Phys.* **89**, 6943 (2001).
13. H. Oshima, K. Nagasaka, Y. Seyama, Y. Shimizu, S. Eguchi, and A. Tanaka, *J. Appl. Phys.* **91**, 8105 (2002).
14. K. Nagasaka, Y. Seyama, H. Oshima, R. Kondo, Y. Shimizu and A. Tanaka, to be published.
15. H. Oshima, K. Nagasaka, Y. Seyama, Y. Shimizu, and A. Tanaka, *Phys. Rev. B*, **66** 140404 (2002).
16. Y. Ji, G.J. Strijkers, F.Y. Yang, C.L. Chien, J.M. Byers, A. Anguelouch, G. Xiao, and A. Gupta, *Phys. Rev. Lett.* **86**, 5585 (2001).
17. T. Valet and A. Fert, *Phys. Rev. B* **48**, 7099 (1993).

Micromagnetic Simulation of Thermal Effects in Magnetic Nanostructures

Rok Dittrich, Thomas Schrefl, Vassilios Tsiantos, Hermann Forster, Dieter Suess, Werner Scholz, and Josef Fidler
Solid State Physics, Vienna University of Technology,
Wiedner Hauptstr. 8-10/138, A-1040 Vienna, Austria

ABSTRACT

A path finding method and a stochastic time integration scheme for the simulation of thermally activated magnetization processes are introduced. The minimum energy path and the saddle points for the thermally induced transitions between the ground states of NiFe magnetic nano-elements are calculated.

INTRODUCTION

With decreasing size of magnetic nanostructures thermal effects become increasingly important. Prominent examples are magnetization noise in magnetic sensor elements [1-3] and the thermal stability of magnetic MRAM (Magnetic Random Access Memory) cells [4] or magnetic storage media [5]. Magnetic sensors require a high sensitivity so that small magnetic fields can be detected. On the other hand thermal fluctuations which will lead to thermal noise should be suppressed. The free layer of a multilayer sensor element is soft magnetic and may have a size well below one micrometer. Thermally induced magnetization processes may cause local or global magnetization rotations which cause the magnetization noise. With decreasing lateral extension of the elements thermal fluctuations become more pronounced. Magnetic storage elements require a low and well defined switching field which in practice is limited by the current through the write line in an array of MRAM cells. On the other hand the shape or the induced anisotropy should guarantee a life time of a stored bit of about 10 years. Again the energy barrier for thermally induced magnetization reversal decreases with increasing size of the storage elements. The corresponding time scales differ by several orders of magnitude: Thermal noise arises on a time scale of a few nanoseconds; thermally induced switching of the magnetization over energy barriers extends over seconds to years. Random thermal fluctuations of the magnetization are the underlying physical process which causes both thermal noise and spontaneous switching. The stochastic fluctuations arise from the interplay between the lattice vibrations and the magnetization.

A micromagnetic system will be close to a local minimum of the total magnetic Gibbs' free energy. Thermal fluctuations of the magnetization cause the magnetization to wander around this minimum. Occasionally the system will reach a region next to a saddle point. The system may cross the energy barrier and move into the basin of attraction of a different energy minimum. This process can be described by the Neel-Brown theory [6,7]. The relaxation time,

$\tau = f_0^{-1} \exp(E_b / k_B T)$, is the inverse of probability per unit time for crossing the barrier E_b . The attempt frequency, f_0 , depends on material parameters, like anisotropy, particle shape, and damping [8]. Its value, which ranges from $f_0 = 10^9$ Hz to $f_0 = 10^{12}$ Hz, sets the time scale for thermally assisted magnetization reversal, $\tau_0 = f_0^{-1} \approx 1$ ns.

The theoretical treatment of thermally induced magnetization processes starts from the stochastic Landau-Lifshitz Gilbert equation and the corresponding Fokker-Planck equation [7].

The energy barrier can be calculated for coherent rotation in single domain particles and the formation of reversed domains in thin ferromagnetic wires. The attempt frequency can be estimated by solving the Fokker-Planck equation numerically or analytically [7-10]. Alternatively, the stochastic Landau-Lifshitz Gilbert equation can be solved numerically for short time scales and small systems [11-14]. Recently, numerical solutions of the stochastic Landau-Lifshitz Gilbert equation were reported for extended micromagnetic systems [3,14]. Zhu [3] analyzed the magnetization noise in submicron sized sensor elements based on the numerical solution of the stochastic Landau-Lifshitz Gilbert equation. The time integration of the stochastic Landau-Lifshitz equation is restricted to small time scales and thus is a proper tool to analyze magnetization noise. The calculation of long term thermal effects needs a detailed characterization of the energy landscape along the most probable path which is taken by the system to cross the energy barrier. Berkov [15] calculated the transition path of interacting single domain particles by minimizing the action along the path. He showed that a direct minimization of the action may also give paths through local maxima which have to be excluded. Ren [16] proposed an elastic band method to calculate a minimum energy path in micromagnetic systems. Starting from an initial guess for the path which connects two local minima of the system, a highly probable path is found by moving the points along the path according to an algorithm which resembles tensioning an elastic band across a mountain. Variants of elastic band methods are commonly used to calculate transition rates in physical chemistry [17]. Dittrich and co-workers [19] originally applied the elastic band method to calculate energy barriers and saddle points in complex micromagnetic systems like discrete perpendicular recording media.

In this work we apply both stochastic time integration and path finding techniques in the framework of the finite element method, in order to simulate thermal effects in magnetic nanostructures. Thus it is possible to take into account complex geometries and realistic element shapes. Both methods are complementary. The stochastic time integration is restricted to simulation times of about 10 ns. As a consequence the calculation of barrier crossing by stochastic time integration is limited to small energy barriers. The transition rate for large barriers can be estimated from the barrier height which can be calculated from the minimum energy path. In addition to the energy barrier, the elastic band method provides a global view of the energy landscape such as local minima and saddle points along the path. The magnetization processes as computed from the stochastic time integration method and the minimum energy path are compared for transitions between different ground states in magnetic nano-elements.

MICROMAGNETIC AND NUMERICAL BACKGROUND

The micromagnetic description of the system starts from the total magnetic Gibbs' free energy [19]

$$E = \int \left(A \left[\sum_i \left(\nabla u_i \right)^2 \right] + K_1 [1 - (\mathbf{u} \cdot \mathbf{a})] - \frac{J_s}{2} (\mathbf{u} \cdot \mathbf{H}_s) - J_s (\mathbf{u} \cdot \mathbf{H}_{\text{ext}}) \right) dV. \quad (1)$$

E is the sum of the exchange energy, the anisotropy energy, the stray field energy, and the Zeeman energy; \mathbf{u} denotes the unit vector parallel to the magnetization, A is the exchange constant, K_1 is the uniaxial magnetocrystalline anisotropy constant, and J_s is the spontaneous magnetic polarization. The integral (1) is over the total volume of the magnetic particles. In a stationary state the magnetic system occupies a local minimum of (1). Owing to thermal

activation the system may overcome an energy barrier and spontaneously move towards a different local minimum of the energy.

We use the finite element method to evaluate E for complex magnetic systems. The direction cosines of the magnetization, u_k , are interpolated by piecewise linear functions on a tetrahedral finite element mesh. In order to calculate the magnetic stray field, \mathbf{H}_s , we use a hybrid finite element / boundary element method [20]. The simulation of the time evolution of the magnetization requires to calculate the effective field, \mathbf{H}_{eff} , defined by the negative variational derivative of E . The effective field on the nodes of the finite element mesh may be approximated using a box scheme

$$\mathbf{H}_{\text{eff}}^l = -\frac{1}{\mu_0} \frac{\partial E}{\partial \mathbf{m}^l}, \quad (2)$$

where \mathbf{m}^l is the magnetic moment associated with node l of the finite element mesh. The stochastic Landau-Lifshitz equation is a system of $3N$ Langevin equations with multiplicative noise

$$\frac{\partial u_i^l}{\partial t} = A_i^l(t) + \sum_k B_{ik}^l(t) H_{\text{th},k}^l(t) \quad (3)$$

$$A_i^l = \left[-\frac{|\gamma|}{1+\alpha^2} (\mathbf{u}^l \times \mathbf{H}_{\text{eff}}^l)_i - \frac{|\gamma|\alpha}{1+\alpha^2} (\mathbf{u}^l \times (\mathbf{u}^l \times \mathbf{H}_{\text{eff}}^l))_i \right] \quad (4)$$

$$B_{ik}^l = -|\gamma| \sum_j \varepsilon_{ijk} u_j^l - \frac{|\gamma|\alpha}{1+\alpha^2} (u_i^l u_k^l - \delta_{ik}) \quad (5)$$

where the indices i, j, k run over the three space directions, and the index $l = 1, \dots, N$ runs over the number of nodes. The drift term, A_i^l , is the right hand side of the deterministic Landau-Lifshitz-Gilbert equation. α is the Gilbert damping constant and γ is the gyromagnetic ratio. \mathbf{H}_{th}^l is the random thermal field. The thermal field is assumed to be a Gaussian random process with the following statistical properties:

$$\langle H_{\text{th},i}^l(t) \rangle = 0 \text{ and } \langle H_{\text{th},i}^l(t), H_{\text{th},j}^k(t') \rangle = 2D \delta_{ij} \delta_{lk} \delta(t-t') \quad (6)$$

The average of the thermal field, taken over different realizations, vanishes in each direction i in space. The thermal field is uncorrelated in time and space. The strength of the thermal fluctuations follows from the fluctuation-dissipation theorem [11]:

$$D = \frac{\alpha k_B T}{|\gamma| \mu_0 |\mathbf{m}^l|}. \quad (7)$$

Numerically the equations (3) to (5) are solved using a semi-implicit time integration method [21]. The time is divided into a lattice of discrete points t_n . The Langevin equation is

solved in the time interval t_n to t_{n+1} with the initial condition $u_i^l = u_i^l(t_n)$. The right hand side of (3) is evaluated at the midpoint $\bar{t}_n = (t_n + t_{n+1})/2 = t_n + \Delta t/2$. The update of the direction cosines is given by

$$\Delta u_i^l = A_i^l(\dots, \bar{u}_i^{l-1}, \bar{u}_i^l, \bar{u}_i^{l+1}, \dots) \Delta t + \sum_k B_{ik}^l(\dots, \bar{u}_i^{l-1}, \bar{u}_i^l, \bar{u}_i^{l+1}, \dots) \Delta H_{th,k}^l \quad (8)$$

with the noise integral

$$\Delta H_{th,k}^l = \int_{t_n}^{t_{n+1}} H_{th,k}^l(t) dt. \quad (9)$$

The magnetization directions at the midpoint of the time interval is

$$\bar{u}_i^l = (u_i^l(t_n) + u_i^l(t_{n+1}))/2 = u_i^l(t_n) + \Delta u/2, \quad (10)$$

assuming linearization of u_i^l within the time interval. The midpoint value, \bar{u}_i^l , is given implicitly by the equations (8) and (10) which is solved by functional iteration. Numerical tests show that about five iterations are sufficient to gain the required accuracy of 10^{-5} . From the midpoint value the magnetization at the time t_{n+1} is calculated from (10) and then normalized:

$$\tilde{u}_i^l(t_{n+1}) = 2\bar{u}_i^l - u_i^l(t_n), \quad \mathbf{u}^l = \tilde{\mathbf{u}}/|\tilde{\mathbf{u}}|. \quad (11)$$

A common feature of path finding methods is the discrete representation of the path connecting the initial state of the system with its final state. In micromagnetics we represent the magnetic states of a system by the set of magnetic moments $\mathbf{M} = \{\dots, \mathbf{m}^{l-1}, \mathbf{m}^l, \mathbf{m}^{l+1}, \dots\}$. The index $l = 1, \dots, N$ runs over all nodes of the finite element mesh. For the configuration space we use polar coordinates of dimension $2N$. First we construct a sequence of magnetic states in such a way as to form a discrete representation of a path from the initial magnetization state, $\mathbf{M}^{(i)}$, to the final magnetization state, $\mathbf{M}^{(f)}$. An optimization algorithm is then applied until at any point along the path the gradient of the energy is only pointing along the path. This path is called minimum energy path which means that the energy is stationary for any degree of freedom perpendicular to the path. The minimum energy path typically represents the path with the greatest statistical weight. From this path statistical quantities as for example transition rates for the thermally induced magnetization reversal can be estimated.

Henkelman and Jónsson proposed the nudged elastic band method to calculate minimum energy paths [17]. We represent a path by a sequence of images. An initial path is assumed which connects the initial magnetization state $\mathbf{M}^{(i)} = \mathbf{M}^{(1)}$ with the final magnetization state $\mathbf{M}^{(f)} = \mathbf{M}^{(m)}$. The index k runs from 1 to m . The path is optimal, if for any image $\mathbf{M}^{(k)}$ the gradient of the energy is only pointing along the path or in other words the component of the energy gradient normal to the path, \mathbf{D} , is zero. If \mathbf{t} denotes the unit tangent vector along the path, a minimum energy path has the following property

$$\mathbf{D}^{(k)} = \nabla E(\mathbf{M}^{(k)}) - [\nabla E(\mathbf{M}^{(k)}) \cdot \mathbf{t}] \mathbf{t} = 0, \text{ for } k = 1, \dots, m \quad (12)$$

The optimal path can be found using an iterative scheme. In each iteration step the images move towards lower energy in a direction perpendicular to the path. So the image $\mathbf{M}^{(k)}$ is moved into the direction, $-\mathbf{D}^{(k)}$. This iterative scheme is numerically very ineffective. Thus instead we solve a system of ordinary differential equations

$$\frac{\partial \mathbf{M}^{(k)}}{\partial t} = -\mathbf{D}^{(k)} \quad \text{for } k = 2, \dots, (m-1) \quad (13)$$

using an implicit, variable order, variable time step time integration method [22]. Here the time t is introduced for numerical convenience and has no physical meaning. In order to keep an equal distance between successive images a spring force may be introduced [17].

RESULTS

Small rectangular NiFe elements show two distinct ground: The S-state and the C-state. Thermal fluctuations may induce a transition between the different states. The C-state has a slightly lower energy than the S-state. Figure 1 shows the magnetic states during the thermally induced switching from the S-state to the C-state. The magnetization distributions are calculated from the numerical solution of the stochastic Landau-Lifshitz Gilbert equation at a temperature of $T = 350\text{K}$. The sequence of magnetization configurations in figure 1 covers a time of 5 ns.

The transition between the ground states were also calculated using the path finding method. The initial path was constructed connecting the two possible S-states. Along the initial path the different images are obtained by linear interpolation. Then a minimum energy path is found solving equation (13). Figure 2 shows the energy along the final path. In addition the magnetization states along the path are shown. The path finding algorithm identifies the C-state as a global energy minimum. The C-state is separated from the S states by saddle points. The comparison of the magnetization states presented in figure 1 and in figure 2 clearly shows that the magnetic states along the minimum energy path correspond to the magnetic states which are visited during the stochastic motion of the magnetization according to the Langevin equation.

ACKNOWLEDGEMENT

This work was supported by the Austrian Science Fund (Y-132 PHY).

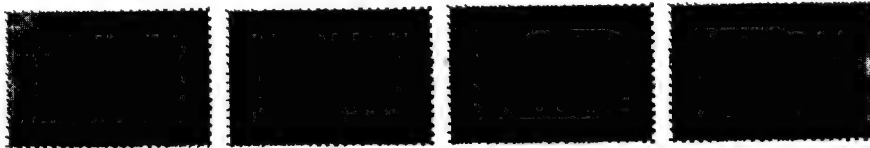


Figure 1. Magnetization states visited during the solution of the stochastic Landau-Lifshitz Gilbert equation. The NiFe element has an extension of $150 \times 100 \times 5 \text{ nm}^3$. An induced anisotropy of $K_1 = 500 \text{ J/m}^3$ was assumed parallel to the long axis. The grey scale maps the magnetization component parallel to the short axis of the element.

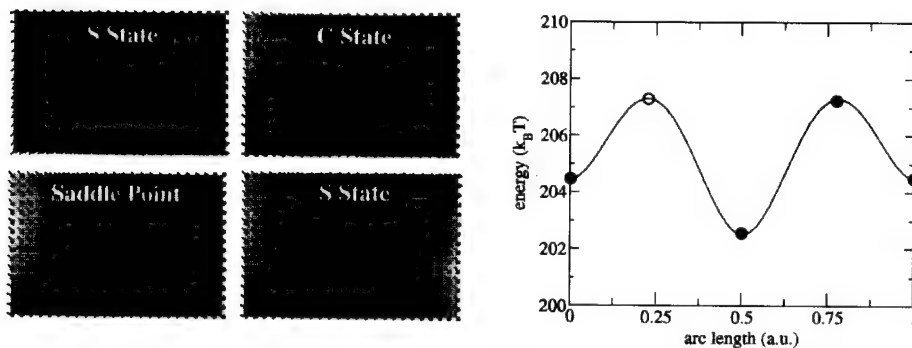


Figure 2. Magnetization configurations and energy along the minimum energy path. The temperature is $T = 350\text{K}$. The saddle point with the open symbols is not shown on the left hand side.

REFERENCES

1. N. Smith and P. Arnett, *Appl. Phys. Lett.* **78**, 1448 (2001).
2. H. N. Bertram, V. L. Safonov, Z. Jin, *IEEE Trans. Magn.* **38**, 2514 (2002).
3. J.-G. Zhu, *J. Appl. Phys.* **91**, 7273 (2002).
4. N. D. Rizzo, M. DeHerrera, J. Janesky, B. Engel, J. Slaughter and S. Tehrani, *Appl. Phys. Lett.* **80**, 2335 (2002).
5. D. Weller and A. Moser, *IEEE Trans. Magn.* **35**, 4423 (1999).
6. L. Néel, *Ann. Geophys.* **5**, 99 (1949).
7. W. F. Brown, Jr., *Phys. Rev.* **130**, 1677 (1963).
8. H.-B. Braun, *J. Appl. Phys.* **76**, 6310 (1994).
9. H. Fukushima, Y. Uesaka, Y. Nakatani and N. Hayashi, *J. Magn. Magn. Mater.* **242-245**, 1002 (2002).
10. W. T. Coffey, D. S. F. Crothers, J. L. Dorman, Yu. P. Kalmykov, E. C. Kennedy and W. Wernsdorfer, *Phys. Rev. Lett.* **80**, 5655 (1998).
11. J. L. Garcia-Palacios and F. J. Lazaro, *Phys. Rev. B* **58**, 14937 (1998).
12. K. Zhang, D. R. Fredkin, *J. Appl. Phys.* **85**, 5308 (1999).
13. W. Scholz, T. Schrefl and J. Fidler, *J. Magn. Magn. Mater.* **233**, 296 (2001).
14. W. Scholz, T. Schrefl and J. Fidler, *IEEE Trans. Magn.* **36**, 3189 (2000).
15. D. V. Berkov, *J. Magn. Magn. Mater.* **186**, 199 (1998).
16. Weinan E, W. Ren and E. Vanden-Eijnden, *Phys. Rev. B* **66**, 52301 (2002).
17. G. Henkelman, H. Jónsson, *J. Chem. Phys.* **113**, 9978 (2000).
18. R. Dittrich, T. Schrefl, D. Suess, W. Scholz, H. Forster and J. Fidler, *J. Magn. Magn. Mater.* **250**, 12 (2002).
19. W. F. Brown, Jr., *Micromagnetism*, (Interscience, New York, 1963).
20. D. R. Fredkin, T. R. Koehler, *IEEE Trans. Magn.* **26**, 415 (1990).
21. P. D. Drummond and I. K. Mortimer, *J. Comput. Phys.* **93**, 144 (1991).
22. S. D. Cohen and A. C. Hindmarsh, *Computers in Physics* **10**, 138 (1996).

Precessional strategies for the ultrafast switching of soft and hard magnetic nanostructures

T. Devolder, M. Belmeguenai, H.W. Schumacher, C. Chappert, Y. Suzuki*.

Institut d'Electronique Fondamentale, UMR CNRS 8622,

Université Paris-Sud, 91405 Orsay, FRANCE.

*National Institute of Advanced Industrial Science and Technology,
Electronics Institute, Tsukuba, JAPAN.

ABSTRACT

We discuss the precessional, quasi-ballistic switching of magnetization in magnetic nanostructures. In soft spin-valve cells, fast and energy-cost effective magnetization switching can be triggered by a transverse field pulse of moderate amplitude, below the in plane anisotropy field, because of an amplification effect brought by the demagnetizing field at the early stage of the reversal. The same effect is no more possible in hard nanomagnets with perpendicular easy magnetization axis. We propose a new type of nanostructured magnetic device, designed to overcome this limitation. The speed is obtained through the use of a very high effective magnetic field, obtained by incorporating a significant exchange field which stores the energy in the form of a constrained domain wall surrounding a region of high magnetic anisotropy. This stored energy is partially available to accelerate the magnetization reversal in a precessional scenario. We illustrate the concept by studying numerically a model system. The key parameter for the reversal is the ratio of the domain wall width to the structure lateral dimension. Possible routes for device preparation are discussed. Promising application to magnetic storage are anticipated.

INTRODUCTION

Obtaining reproducible magnetization switching within the sub-nanosecond regime and the sub-micron range is currently one of the most challenging tasks in nanomagnetism. On the information storage front, it is of particular industrial interest to propose a writing strategy, which is fast, error-free in a large array of cells, energy cost-effective, and easily down-sizable. Both theoretical models [1] and time-resolved magneto-optic [2] or electrical [3] experiments can now account in details for the sub-nanosecond behavior of soft magnetic thin films and nanoelements. The magnetization dynamics is described by the Landau-Lifshitz equation [4] :

$$\frac{d\vec{M}}{dt} = \gamma_0 \vec{H}_{\text{eff}} \times \vec{M} - \frac{\alpha}{\|\vec{M}\|} \left[\frac{d\vec{M}}{dt} \times \vec{M} \right] \quad (1)$$

where we use $\gamma_0 = -\gamma \mu_0$ instead of the classical gyromagnetic ratio γ . \vec{H}_{eff} is the instantaneous effective field: $\vec{H}_{\text{eff}} = \vec{H} + \vec{H}_K + \vec{H}_{\text{exch}} + \vec{H}_D$. Here, \vec{H} is the applied field, and \vec{H}_K is the magnetocrystalline anisotropy field and depends on the relative orientation between the crystalline axes and the magnetization. The exchange field \vec{H}_{exch} represents the energy stored in the magnetization torsion. The demagnetizing field $\vec{H}_D = -N\vec{M}$, where N is the demagnetizing tensor, depends mainly on the relative orientation between magnetization and the principal axes of the magnetic element shape. We shall restrict below to the case of flat nearly elliptical platelets, elongated along x , where we have the relation $N_x \leq N_y \ll N_z \approx 1$.

The time evolution scales with the Uniform Precession (UP) frequency $f_{\text{UP}} = (\gamma_0/2\pi) H_{\text{eff}}$, where $-\gamma/2\pi = 28 \text{ GHz/T}$. The relaxation towards equilibrium is described phenomenologically

by the damping constant α , with $1/\alpha\gamma_0 H_{\text{eff}}$, typically about 0.2-2 ns, characterizing the energy relaxation time. In the following, we affect the symbol "0" to zero applied field quantities.

The conventional strategy to reverse magnetization is to apply an external field \mathbf{H} antiparallel to the equilibrium magnetization. This strategy remains efficient in quasi-static reversal, when thermal activation helps to overcome the energy barriers [5]. In the ultrafast limit, a step of external field applied roughly antiparallel to \mathbf{M} makes it undergo multiple precessions about the local effective field before reaching full reversal ([2,3]). The resulting reversal times are thus much longer than the precession period.

The non-conventional ultrafast magnetization reversal strategies can be classified in two categories : (i) for magnetically soft material where the equilibrium effective field is almost zero or (ii) for magnetically hard material, where the equilibrium effective field can be huge. We shall in the following discuss two model configurations:

(i) In soft in plane magnetized elements, the effective field \mathbf{H}_{eff} is nearly zero when magnetization \mathbf{M} is at rest along its equilibrium axis. To achieve fast reversal, the external field \mathbf{H} creates a significant additional perpendicular demagnetizing field that drives the motion of the magnetization through the torque $\mathbf{H}_D \times \mathbf{M}$. The most striking application of this strategy is the so-called precessional switching [6-9] of soft elements, for which a magnetic field pulse is applied along the short axis of a soft platelet. The reversal lasts only typically few times $1/\gamma_0 \sqrt{2H \cdot M_s}$, and can be as small as 150 ps (section I).

(ii) In hard perpendicularly magnetized elements, the effective field incorporates the anisotropy field and can thus be huge at equilibrium, when $\mathbf{H}_{\text{eff}}^0$ and \mathbf{M}^0 are collinear. In consequence, to achieve reversal the applied field must first create a significant angle between the effective field $\mathbf{H}_{\text{eff}}^0$ and a displaced magnetization. To achieve cost-effective reversal, we propose that the external field is immediately relayed by a strong "helping" field with a *different symmetry* from the anisotropy field. The required helping field magnitude is typically $(H_K - M_s)/2$, and may be of exchange origin. Switching speeds below 150 ps may then be obtained. We propose a practical device, where the exchange field can be stored in the form of a domain wall surrounding a small, high magnetic anisotropy region (Section II). To access the real technological potential of the concept, we numerically study a model sample, that could for instance be realized by using local light ion irradiation techniques [10]. First attempts to fabricate such a device are reported.

I. PRECESSIONAL REVERSAL IN SOFT MAGNETIC MATERIALS

In this section we deal with soft magnetic materials. In related devices, $\mu_0 \mathbf{H}_K$ and the in plane shape anisotropy $(N_y - N_x)M_s$ are of the same order of magnitude and can be included in a total anisotropy field $\mu_0 \mathbf{H}_A$ of order typically a few mT. We will also assume a coherent reversal (\mathbf{M} stays uniform), and so \mathbf{H}_{exch} will be neglected.

I.A. Precessional reversal strategy in soft systems

For an efficient magnetization reversal scheme, the initial torque $\mathbf{H}_{\text{eff}} \times \mathbf{M}$ should be near maximum, and so the external field should be applied at an angle $\pi/2$ with respect to the magnetization.

The resulting magnetization reversal precessional scenario [11,12] in a soft rectangular platelet is depicted in Figure 1. The field pulse \mathbf{H} is applied along the short (hard) axis of the platelet (step 1). This initial torque pushes the magnetization out of the film plane at a rate $\gamma_0 M_s H$. The resulting demagnetizing field grows during a given settling time τ_1 (step 2 of Fig.1).

After this delay τ_1 , the demagnetizing torque gets greater than the Zeemann torque and magnetization precesses then mainly around the demagnetizing field, perpendicular to the platelet (step 3 of Figure 1). This induces a 180 degrees reversal of the magnetization of duration τ_2 . If the magnetic field is switched off at the particular time $\tau_1 + \tau_2$, magnetization falls into the nearest energy minimum, which has a reversed magnetization.

I.B. Experimental results on soft, micron-sized spin valve cells

This precessional strategy has been tested by H. W. Schumacher et al. [7,9] on stadium shaped $5\mu\text{m} \times 2.3\mu\text{m}$ spin-valve cells. The soft layer is CoFe 20 Å / NiFe 30 Å. The total in plane anisotropy field of that element is $H_A \sim 7.5$ mT. The transverse field pulse is generated by a current pulse injected into a buried high bandwidth coplanar line, while magnetization reversal is followed by magneto-resistance using a 40 GHz bandwidth electrical set-up [13].

A representative time-resolved measurement of the magnetization switching process in that soft cell is displayed on Figure 2. The 165 ps transverse pulsed field reaches 8 mT with rise time 45 ps (Fig.2B). Fig.2A is a macrospin simulation assuming a sample with diagonal demagnetizing tensor. Fig.2C is the experimental magneto-resistive response of the spin-valve. The 20%-80% reversal takes places in a time interval of 130 ps. As shown in [7], such precessional scenario can be obtained at applied fields below the Stoner-Wohlfarth scenario.

I.C. Discussion

We first estimate the time needed for the full switching of a soft cell, when using a precessional strategy. We then comment on the requirements on the magnitude of the applied field by comparison to the Stoner-Wohlfarth mechanism. A comprehensive discussion of the requirements on the field pulse duration can be found in ref. [7]. Also, we will assume here $H \gg H_A$: a more detailed treatment of the influence of H_A is beyond the scope of this paper.

1. Analytical estimate of the switching time

We assume $H \ll M_s$ and $\alpha \ll 1$ (energy conservation). We note ϕ the angle between \mathbf{M} and the platelet plane (xy). \mathbf{H} creates an initial torque which pushes \mathbf{M} out of the film plane as :

$$dM_z = \gamma_0 \mathbf{H} \cdot \mathbf{M}_x(t) dt \quad (2)$$

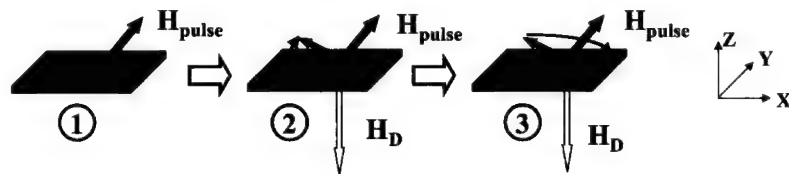


Figure 1 : Sketch of the precessional switching scenario on a soft platelet. At step 1, a hard axis field pulse is applied onto the platelet of initial magnetization (black arrow) along the easy axis. At step 2, magnetization is lifted out of the film plane, thus creating a strong out-of-plane negative demagnetizing field. Magnetization precesses about this demagnetizing field and proceeds to a 180° reversal (step 3).

This results in a demagnetizing field growing approximately as $-\gamma_0 H M_S t$. Eq. 1 projected on the (y) axis leads to a quadratic dependence of M_y at small t . The initial evolution of M_x is found by projecting Eq. 1 on the (x) axis and keeping the terms of lowest order in time dependence. M_x evolves quadratically with time as :

$$M_x(t) - M_x^0 \approx \frac{1}{2} \gamma_0^2 M_S H^2 t^2. \quad (3)$$

During this regime, the projection of $\mathbf{M}(t)$ on the easy axis will not change much. This appears to experimentalists as a delay τ_1 before reversal effectively starts.

After this delay τ_1 , the demagnetizing torque exceeds the Zeemann torque and magnetization precesses then mainly around the demagnetizing field. This induces the 180 degrees reversal lasting τ_2 .

To estimate τ_2 , we focus on the particular instant when \mathbf{M} is above the hard axis, i.e. between step 2 and 3 of Figure 1. We have $M_x=0$, $M_y = M_S \cos \phi$ and $M_z = M_S \sin \phi$. At that time, the initial Zeemann energy $\mu_0 \mathbf{H} \cdot \mathbf{M}(t=0)=0$ has decreased to $-\mu_0 H M_S \cos \phi$, and has almost entirely flown into the demagnetizing energy. We thus can write :

$$\mu_0 H M_S \cos \phi = \frac{1}{2} \mu_0 M_S^2 \sin^2 \phi. \quad (4)$$

Since $H \ll M_S$, the angle ϕ is weak, and $\sin \phi \approx \sqrt{2H/M_S}$. Around this instant the precession frequency is approximately $(\gamma_0 H_D / 2\pi)$, and the characteristic switching time τ_2 can be evaluated from this frequency:

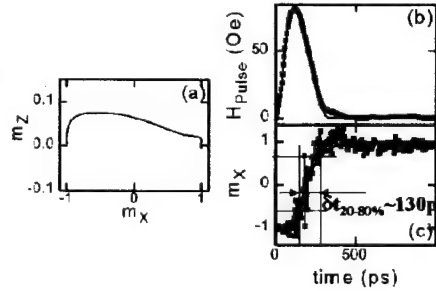
$$\tau_2 = \left(\frac{\pi}{\gamma_0 \sqrt{2H M_S}} \right) \quad (5)$$

The initial delay τ_1 is about the time it takes for \mathbf{H}_D to settle its magnitude and start switching the magnetization. In the linear approximation of Eq. 2, this time is passed when M_z reaches its maximum $\sqrt{2H M_S}$, and so we can evaluate τ_1 as:

$$\tau_1 \approx \left(\frac{2}{\gamma_0 \sqrt{2H M_S}} \right) \quad (6)$$

It follows immediately that the characteristic total reversal time will scales with: $1/\gamma_0 \sqrt{H M_S}$.

Figure 2 (courtesy of H.W. Schumacher, C. Chappert, R.C. Sousa, P.P. Freitas and J. Miltat, [9]). (A): Macrospin calculation of the precessional switching trajectory in the XZ plane. The field pulse is stopped after a 180° precession about H. (B): Experimental field pulse of 8 mT and 165ps duration. (C): Normalized experimental Magneto-resistive response of the spin-valve (gray dots) and simulation (full line) of the easy axis component of the magnetization.



The previous approach focused on the initial stages of the magnetization reversal. It is worth completing this approach by studying magnetization fluctuations long after the onset of the external field, which we now assume to be a Heavyside step function. In our hypothesis that $H > H_A$, the final magnetization lies along the in-plane hard axis. As a result, \mathbf{H} is transverse to \mathbf{M} at $t=0$ and longitudinal at $t \rightarrow \infty$.

Classical Ferromagnetic Resonance (FMR) theory [14] indicates that the long term uniform precession (UP) mode is about the applied field, with a frequency $\omega_{UP} = \gamma_0 \sqrt{(H - H_A)(H + (N_z - N_y)M_s)} \approx \gamma_0 \sqrt{H.M_s}$, and that this UP mode can be efficiently pumped at $t = 0^+$ because the initial field is transverse.

Hence the long-term characteristic FMR frequency and our estimated switching frequency both scale with $\gamma_0 \sqrt{H.M_s}$, which further confirms our evaluation.

2. Minimal cost in applied field

Stoner-Wohlfarth switching theory [15] assumes coherent rotation and zero temperature, and derives switching fields H_S from the sole criteria of energy local minimum. This gives the well know asteroid curve when plotting the orientation dependence of H_S in the plane of the samples.

Although the precessional switching is also a coherent behavior, it would be wrong to assume the same orientation dependence for the switching fields. The reason is that, while in Stoner-Wohlfarth analysis the field is swept *slowly*, such that the energy dissipation is *always* fast enough to stabilize magnetization in the nearest energy minimum, in the precessional strategy, the field is swept very rapidly and magnetization is *never* in an energy local minimum after $t=0$.

In the geometry described in this paper, with H greater than the anisotropy field H_A , there exists *only one* equilibrium magnetization orientation, along \mathbf{H} . As a result, the magnetization trajectory is almost symmetric around \mathbf{H} (in the case $\alpha \ll 1$), and the applied field pulse length must be fitted to odd multiples of the switching time to achieve reversal [7, 16]. Ballistic, non-ringing trajectories require to stop the applied field exactly when $M_x(t)=0$ [7, 9, 17].

The situation is more complex when H is smaller than the anisotropy field H_A , because there exists *two* degenerate stable magnetization orientations. The final state will thus depends on the history and can not be derived from sole energy considerations. Field pulse rise time and length must be precisely controlled, and switching can be obtained at fields lower than Stoner-Wohlfarth switching fields [12, 16]. For instance, G. Albuquerque et al. [17] have extended this analysis and shown that, in the limit of vanishing α and infinitely small rise-time, a transverse field of $H=H_A/2$, i.e. half of the Stoner-Wohlfarth switching field, is enough to trigger magnetization switching. The work of H.W. Schumacher et al. ([7, 9]) is to our knowledge the first experimental demonstration of such precessional, sub Stoner-Wohlfarth switching.

One important criterium must finally be discussed. Achieving the excitation of a precession mode requires the excitation field time dependence to comprise Fourier components of frequencies above the precession characteristic frequency. Success of the precessional strategy thus requires:

$$1/H (dH/dt) \gg \gamma_0 \sqrt{H.M_s} \quad (7)$$

In the experiments described in § 1.B (Figure 2), precession effects strongly dominate since $1/H (dH/dt) \approx 20$ GHz and $\gamma_0 \sqrt{H.M_s} \approx 3$ GHz.

II. PRECESSIONAL REVERSAL IN HIGH ANISOTROPY SYSTEMS

Two terms have been ignored so far in the Landau-Lifshitz equation: the magneto-crystalline anisotropy and exchange fields. In this section, hard material nanostructures are considered, and $\mathbf{H}_K = H_K \mathbf{z}$ is assumed to be higher than M_S . The effective perpendicular anisotropy $H_K - M_S$ is typically 0.1 to 1 T. \mathbf{H}_{exch} will be introduced in §II.C.

II.A. Adapting precessional strategy to high anisotropy systems

The uniform FMR mode of a soft platelet around the stable equilibrium position in zero applied field is given by $\omega_{UP} \approx \gamma_0 \sqrt{M_S H_A}$ [14], where H_A is small. The UP trajectory is very elliptical: the in-plane aperture angle is much greater than the out-of-plane angle. This provides a path for reversing the magnetization through a quasi easy-plane trajectory (section I).

The situation is very different for a hard platelet with high perpendicular anisotropy. The UP frequency in zero applied field is $\omega_{UP} = \gamma_0 (H_K - M_S)$, such that the intrinsic dynamics of the system is already faster than for a soft platelet (by a factor of about 2 with the parameters of this paper). But, as $(H_K - M_S)$ is much greater than any in plane anisotropies, the UP trajectory is nearly circular around the anisotropy axis, which does not provide an easy path for reversal. Considerably much higher transverse fields are required to pump these modes compared to a soft material. Following the arguments of § I.C.2, and considering that hard materials usually experience high damping, reversing the magnetization requires fields of the order of $(H_K - M_S)$.

Circumventing this difficulty requires to *favor* the pumping of *only one* transverse magnetization component to make the UP much more elliptical. This may be done by adding an additional term in the effective field, with a *different symmetry* from that of the anisotropy field. In the next subsection, we consider such an extra \mathbf{H}_X field in the (x) direction, with typical strength $\mu_0(H_K - M_S)/2$. In section II.C we will propose to use an exchange field \mathbf{H}_{exch} for this purpose. More general considerations on speed and energy cost will be given in section II.D.

II.B. Precessional reversal strategy in hard systems

Let us consider the state defined in step 1 of fig.3. The magnetization at rest (black arrow in Fig.3) is parallel to the effective field, i.e. the vector sum of an extra field \mathbf{H}_X along (x), an anisotropy field along (z) and a demagnetizing field along (-z).

To induce magnetization reversal, the external field \mathbf{H} (gray arrow in fig.3) is applied along the (x) direction. The Zeemann torque extracts \mathbf{M} from the (xz) plane at a rate $\gamma_0 M_S H \sin\phi$ (step 2). Precession is initiated and \mathbf{M} is sent towards the (xy) plane. The effective anisotropy field $(\mathbf{H}_K - \mathbf{M}_z)$ decreases as M_z as \mathbf{M} approaches the film plane. At step 3, magnetization is in the (xy) plane: $(\mathbf{H}_K - \mathbf{M}_z)$ vanishes and the precession proceeds around $(\mathbf{H}_X + \mathbf{H})$. However, the movement of \mathbf{M} slows down. The applied field can be possibly stopped at step 3: the *sole* extra field can finish the job until step 4, when M_z is strongly negative, and the anisotropy field has reset and stabilizes \mathbf{M} to a “reversed” position. However the movement is faster if the field \mathbf{H} is not switched off at step 3.

II.C. Micromagnetic illustration of the concept

One way to reach high enough values for this extra in-plane field H_X is to use exchange energy. This can be done for example by depositing a high perpendicular anisotropy alloy onto an antiferromagnetic buffer creating an in-plane exchange bias. In that case, the exchange field can reach typically 250 mT [18], which would be sufficient for our goal.

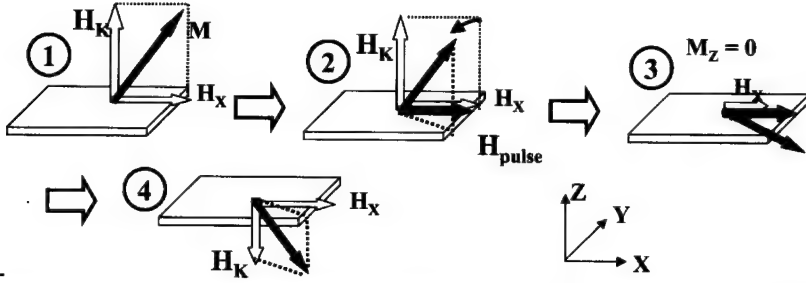


Figure 3 : Sketch of the precessional switching scenario of a hard platelet with perpendicular anisotropy subjected to an in-plane exchange field. Step 1: equilibrium configuration: \mathbf{M} is in the (xz) plane, making an angle ϕ with the (xy) plane. An extra field \mathbf{H}_K lies along (x) . Step 2: an in-plane field pulse parallel to \mathbf{H}_K tilts the magnetization out of the (xz) plane. Magnetization starts to precess about the effective field. Step 3: if the \mathbf{H}_K torque exceeds the anisotropy torque, magnetization proceeds with a precession around $\mathbf{H}_K + \mathbf{H}$. The applied field can be switched off as soon as \mathbf{M} crosses the xy plane. At $M_z(t)=0$, the sole \mathbf{H}_K torque exists and pushes \mathbf{M} further under the (xy) plane, while the anisotropy field resets to stabilize \mathbf{M} at an angle $-\phi$ with respect to (z) .

Such a high exchange field can also be found in a strong magnetization gradient. This occurs for instance in a Bloch domain wall, where the local exchange torque is of the order of the effective anisotropy torque. In the following, we will address this configuration.

Let us give an example of how a precessional strategy could be implemented on a nanostructure of perpendicular anisotropy, with non-uniform magnetization at equilibrium. In the Fig. 4 and 5, we report the calculated time evolution of $\langle \mathbf{M} \rangle$ in a system comprising a high anisotropy central nanostructure surrounded by a peripheral zone (the “matrix”) of weaker anisotropy. The fabrication of such a device will be discussed in §II.E.

The central $128 \times 64 \text{ nm}^2$ area possesses a high perpendicular anisotropy ($K=1.45 \times 10^6 \text{ J/m}^3$, $\mu_0(H_K - M_S) = 250 \text{ mT}$) while the complement of the $256 \times 128 \text{ nm}^2$ rectangle (the matrix) has a smaller anisotropy ($K=7.25 \times 10^5 \text{ J/m}^3$, $(\mu_0(H_K - M_S) = -770 \text{ mT})$. Magnetization is everywhere $\mu_0 M_S = 1.79 \text{ T}$. The easy axis is thus perpendicular to the film plane in the center of the cell, whereas shape anisotropy dominates in the surrounding matrix. The rectangular shape creates a S-like state [11] with an in-plane remanence mainly along the easy axis (Figure 5A). A domain wall separates the central part and the matrix. Because the matrix and the central part are exchange coupled through this wall, the central part feels an in-plane exchange field, which slightly tilts its magnetization away from the magneto-crystalline anisotropy axis (z) . With the parameters above the tilt angle is only 11° in the center.

We assume a film thickness of 14 \AA , a damping constant $\alpha=0.2$ [19], and an exchange stiffness of $3 \times 10^{11} \text{ J/m}$. Such parameters are compatible with those of Pt/Co/Pt sandwiches. At $t=0^+$, a 150 mT field step is applied along the long axis (x) of the platelet. This field is parallel to the magnetization of the matrix, such that \mathbf{M} will not evolve much in the matrix.

On the contrary, the precession induced by the Zeeman torque inside the central zone extracts its magnetization out of the (xz) plane.

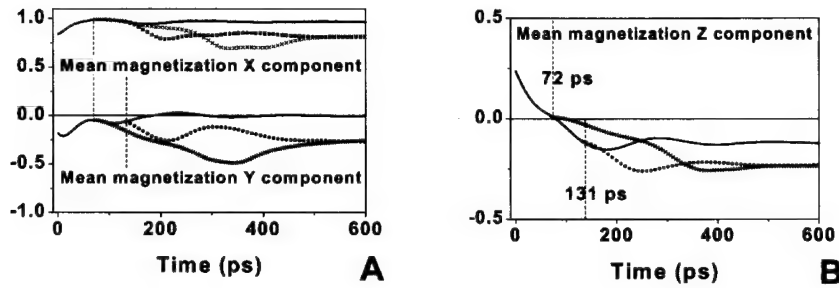


Figure 4 : Micromagnetic simulation of the precessional switching trajectory of a system comprising a $128 \times 64 \text{ nm}^2$ high anisotropy ($K=1.45 \times 10^6 \text{ J/m}^3$) nanostructure embedded in the middle of a $256 \times 128 \text{ nm}^2$ rectangle platelet with half anisotropy. Saturation magnetization is 1.79 T, film thickness is 1.4 nm. (A): X and Y components of the mean magnetization. (B): Z component of the mean magnetization. The 150 mT field pulse is stopped at 72 ps (after a 90° precession) in the curves with cross points, at 131 ps (after a 180° precession) in the curves with circular points, and is never stopped in the full line curves.

M_y grows first (Figure 5B) at the expense of M_z , and then the precession sends \mathbf{M} towards the platelet plane. At $t=72 \text{ ps}$, the mean magnetization lies in the platelet plane (Figure 4): \mathbf{M} has undergone a $\pi/2$ precession around the (x) axis. The precession is quicker in the domain wall, where the exchange torque is maximum, such that the z-component reverses first near the initial domain wall position (Figure 5C). This is further favored at the left and right domain walls surrounding the central part because there, an extra in-plane dipolar field along (x) is (constantly) generated by the matrix.

At $t=72 \text{ ps}$, the anisotropy field is zero, such that the precession speed comes solely from the weak external field and the exchange field. Note that this exchange field comes only from the y-component of \mathbf{M} and so is weaker than initially. This slows down the magnetization evolution, which corresponds to the inflexion point at $\langle M_z(t) \rangle = 0$ (Figure 4B, $t = 72 \text{ ps}$, full line curve).

Three scenarii can then be chosen:

(i) If the external field is maintained, the magnetization in the central part has fully switched after 131 ps (Figure 5D). A small ringing persists for some 100 ps longer (Figure 4), and the final state in constant applied field has negative M_z component, but M_y is zero (Figure 5E). If the field is removed at $t \gg 1 \text{ ns}$ (not shown), the system may evolve to any of the two S-states (M_y positive or negative) that are degenerate in energy. A crucial point is that the applied field is not strong enough to force the magnetization of the central part of the structure to be in the plane. This means that, as for the soft elements, switching can be obtained with fields *smaller* than the one obtained for a Stoner-Wohlfarth switching mechanism, at least within our scheme.

(ii) The post-reversal ringing can be avoided if the field is switched off at $t = 131 \text{ ps}$, i.e. after a π precession about the (x) axis. In that case, the pulse duration is matched to the first harmonic of the switching characteristic frequency, and ballistic switching is achieved. The final S-state of the matrix has the same chirality as the initial S-state, so the reversal is reversible.

(iii) In fact, the applied field can be already switched off at $\langle M_z(t) \rangle = 0$, i.e. at $t = 72 \text{ ps}$. The precession about the (x) axis continues, but the torque is solely due to the exchange field,

which is reduced compared to its initial value. The long-term ($t \geq 500$ ps) equilibrium state is the reversed magnetization state in the central high anisotropy area, and the initial S-state in the matrix. Meanwhile, a significant ringing of M_x and M_y is present (Figure 5F) during the slow, more regular evolution of M_z towards the reversed equilibrium state ($M_z < 0$).

II.D. Discussion

As formerly done for the soft elements, basic analytical considerations can give some useful insight into the critical parameters.

1. Requirements on the equilibrium exchange field

Let's first discuss the configuration of Fig.3. The field pushes initially (as $t \ll 1/\gamma_0 H$) the magnetization out of the film plane at a rate $M_y(t) = \gamma M_s H \sin \phi t$ (step 2 of Fig.3). Then, the effective field bends this movement. The projections of Eq.1 on the (x) and (z) axes give:

$$M_z(t) - M_z^0 = -\frac{1}{2} \gamma_0^2 M_s H \cdot t^2 (H + H_X) \sin \phi \quad (8)$$

$$M_x(t) - M_x^0 = \frac{1}{2} \gamma_0^2 M_s H \cdot t^2 (H_K - M_s) \sin \phi \quad (9)$$

In order to initiate a precession around (x), and not (z), we need to have: $(M_z^0 - M_z(t)) > (M_x^0 - M_x(t))$, i.e. $(H + H_X) \gg (H_K - M_s)$. So precessional switching may be achieved for moderate field H only if much energy is stored in H_X , i.e. in the exchange energy.

In the geometry of figure 3, the best compromise between large M_z signal (e.g. for a recording application), and cost in applied field H, is thus near $H_X \approx (H_K - M_s)/2$, which gives a tilt angle ϕ^0 at rest around 45 degrees. This is exactly the order of magnitude of H_X that we had proposed without justification in §II-A and §II-B.

For the configuration of figure 5 and §II-C, the condition equivalent to $H + H_X \geq (H_K - M_s)$ at moderate fields H is that the central area should not be much greater than the Bloch domain wall width, where exchange energy is stored. This is the case with our parameters, and one advantage of this geometry compared to that of figure 3 is that the central part can still remain nearly perpendicularly magnetized at rest. However, the reversal will be initially more efficient inside the domain wall (see Figure 5C), where the exchange field is maximal.

2. Conjecture on the switching time

In contrast to soft systems (I.C.1), an analytical estimate of switching time for high anisotropy systems may not be derived from simple energy considerations. The energy loss rate is too high in hard materials for energy conservation considerations to reasonably apply.

In addition, the remaining part of the initial Zeemann energy does not flow solely in the exchange energy but rather shares itself towards exchange and anisotropy energies, such that the exchange torque when $M_z(t)=0$ may only be calculated through full micromagnetic simulations.

As done in §I.C.1, it is worth studying magnetization fluctuations around the micromagnetic state of Figure 5E, i.e. long after the onset of a Heavyside step external field satisfying $H + H_X > H_K - M_s$ and thus aligning the magnetization in the (x) direction.

Again, the long term UP mode has a frequency which scales roughly with $\gamma_0 \sqrt{(H + H_X - (H_K - M_s))(H + H_X)}$ or equivalently $\gamma_0 \sqrt{(H - (H_K - M_s)/2)(H_K - M_s)}$, for the optimal "signal to speed" compromise. We anticipate that the characteristic reversal time is related to the latter frequency. Further calculations are in progress to confirm this point.

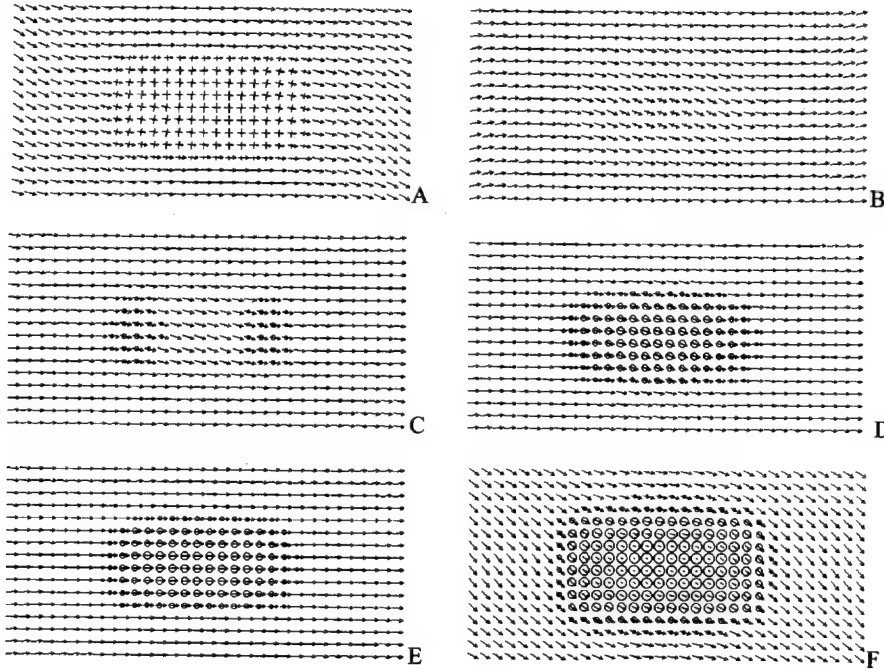


Figure 5 : Snapshots of the time-evolution of magnetization during precessional switching of the nanostructure defined in the text. The arrows stand for the in-plane magnetization. The circles or the crosses have sizes proportional to the out-of-plane (z) component of the magnetization (crosses for $M_z > 0$). (A) is the equilibrium state: the central, high anisotropy area has upwards perpendicular magnetization. The surrounding's magnetization points to the right. An in-plane 150 mT field along the long axis of the cell is applied on state A. States B, C, D and E are respectively snapshots after 60 ps, 72 ps, ($\pi/2$ precession angle), 132 ps (π precession angle) and 1 ns (equilibrium state in constant applied field). State F is the relaxed state after 300 ps, obtained if the field is suppressed 72 ps after its onset.

II.E. Possible fabrication routes

One way to fabricate the nanostructure of Figure 5A is to use light ion irradiation patterning [10] on a system with initial perpendicular anisotropy. For instance, 30 keV He^+ ion irradiation of Co-Pt multilayers with perpendicular magnetization easy axis was shown to be a powerful tool to tune their magnetic anisotropy. In these materials, ion-mixing at the Co/Pt interfaces gradually reduces the magnetic anisotropy energy in a controlled way, which first lowers the coercive force, then triggers an in-plane reorientation of the magnetization easy axis. Embedded hard magnetic nanostructures as small as 30 nm were demonstrated when the irradiation is performed through a mask directly patterned on the sample surface [20].

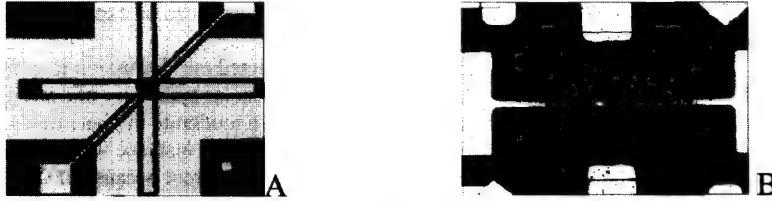


Figure 6 : Optical micrographs of prototype devices designed for broadband measurements of the precessional switching of a nanostructure with perpendicular anisotropy. (A) global 2x1.5 mm² view of the circuit. (B) Zoomed 200x150µm² image: magnetic Hall cross with 500 nm wide arms located above the 4µm wide stripline used to generate the field pulse. The faintly visible 100x100µm² square is a silica layer isolating the Hall cross from the pulse line.

One weakness of this approach is the intrinsically non-abrupt character of the transition between in plane and perpendicular magnetized areas. The transition width is comparable to a domain wall width, which will reduce the amount of exchange energy stored. Potentially more abrupt anisotropy transitions may be obtained following the technique developed in ref. [21]. The technology to fabricate the device studied in §II.C is thus certainly available.

Prototype devices are shown in Figure 6. The nanostructure will be irradiation-fabricated at the center of a Hall cross structure (Figure 6B), contacted to 4 coplanar stripes designed for Extraordinary Hall Effect measurement. The Hall cross is a Co/Pt multilayer with perpendicular magnetic anisotropy. The diagonal arms serve as DC current injection arms while the 50 µm wide vertical arms are 50 Ω coplanar waveguides that serve for the high frequency Hall voltage measurement. This cross is located above another 4µm wide coplanar waveguide that generates the fast rising in-plane magnetic field pulse. This pulse line is electrically isolated from the magnetic Hall cross by a silica layer (Figure 6B). First electrical characterizations indicate sufficient signal/noise ratio for high frequency magnetization dynamics measurement.

CONCLUSION

Through the derivation of approximate analytical expressions we have discussed the precessional switching of magnetization in soft and hard (perpendicularly magnetized) nanoplatelets. Fast, energy cost-efficient precessional switching was recently demonstrated in soft platelets [9, 11], and a similar result for hard platelets would be of high interest for application to for instance perpendicular hard disk recording. It may also become a crucial issue for the future of M-RAM technology, when largely sub-100 nm sizes will require high magnetic anisotropy to ensure thermal stability.

The main differences between soft and hard platelets lies in their damping coefficient α , and their effective field H_{eff}^0 near the stable equilibrium position. In soft platelets, α and H_{eff}^0 are weak, and H_{eff}^0 furthermore shows a strong easy plane symmetry. This enables fast (~150 ps) precessional reversal in moderate in-plane transverse applied fields.

On the contrary, hard platelets exhibit strong H_{eff}^0 , with nearly cylindrical symmetry around the perpendicular axis, together with a strong damping. So pumping of precessional modes will require high in-plane fields. We have shown that it is possible to bend this issue by adding an extra in-plane field H_x that breaks the cylindrical symmetry of H_{eff}^0 . We have further shown that H_x can be of exchange origin, and proposed a numerical example of realization, that

could be experimentally implemented. High reversal speeds can be expected, at fields as low as half of the perpendicular anisotropy field.

However, although in this paper we have restricted our discussion to exchange fields, we want to stress that the main concept of breaking the circular symmetry of a strong perpendicular anisotropy, in order to enable precessional switching in moderate in plane fields, holds a much more general validity. A similar effect could be obtained for instance with a tilted anisotropy axis, although analytical expressions would be slightly different because of the different dependences in \mathbf{M} orientation for Zeeman and anisotropy energies. A more elaborate treatment of these effects will be published in a forthcoming paper.

ACKNOWLEDGEMENTS:

The authors wish to thank Jacques Miltat and Harry Bernas for enlightening discussions. The work was supported in part by the NEDO contract "Nanopatterned magnets".

REFERENCES

1. *Spin Dynamics in Confined Magnetic Structures*, B. Hillebrands and K. Ounadjela (Springer, Berlin, 2001).
2. B. C. Choi et al., *Phys. Rev. Lett.* **86**, 728 (2001); W. K. Hiebert, G. E. Ballentine, and M. R. Freeman, *Phys. Rev. B* **65**, 140404(R) (2002)
3. R. H. Koch et al., *Phys. Rev. Lett.* **81**, 4512 (1998)
4. L. Landau, E. Lifshitz, *Phys. Z Sowjetunion* **8**, 153 (1953); T.L. Gilbert, *Phys. Rev.* **100**, 1243 (1955).
5. "Classical and quantum magnetization reversal studied in nanometer-sized particles and clusters", W. Wernsdorfer. To be publ. in *Advances in Chemical Physics* (Wiley Ed.), 2003.
6. Th. Gerrits, H. A. M. Van Den Berg, J. Hohlfeld, L. Bär, Th. Rasing, *Nat.* **418**, 6897 (2002)
7. H.W. Schumacher, C. Chappert, P. Crozat, R. C. Sousa, P. P. Freitas, J. Miltat, J. Fassbender, and B. Hillebrands, *Phys. Rev. Lett.* **90**(1), 017201 (2003).
8. S. Kaka and S. E. Russek, *Appl. Phys. Lett.* **80**, 2958 (2002).
9. H.W. Schumacher, C. Chappert, R. C. Sousa, P. P. Freitas, and J. Miltat, *Phys. Rev. Lett.* **90**(1) 017204 (2003).
10. C. Chappert, H. Bernas, J. Ferré, V. Kottler, J.P. Jamet, Y. Chen, E. Cambril, T. Devolder, F. Rousseaux, V. Mathet and H. Launois, *Science* **280**, 1919 (1998).
11. J. Miltat, G. Aburquerque and A. Thiaville in *Spin Dynamics in Confined Magnetic Structures*, edited by B. Hillebrands and K. Ounadjela (Springer, Berlin, 2001).
12. M. Bauer et al., *Phys. Rev. B* **61**(5) p3410 (2000)
13. Schumacher et al., *Appl. Phys. Letters* **80**, 3781 (2002)
14. C. Kittel, *Introduction to Solid State Physics*, 5th ed., Wiley, New York, 1976.
15. E. tC. tStoner tand tE. tP. tWohlfarth, *Philos. Trans. R. Soc. London, Ser. A* **240**, 599 (1948)
16. C-R. chang, J-S. Yang, *Phys. Rev. B* **54**(17) pp11957 (1996).
17. "Magnetization precession in confined geometry : physical and numerical aspects". PhD thesis of Gonçalo M. B. Albuquerque, Orsay, July 2002.
18. S. Maat, K. Takano, S.S.P. Parkin, E.E. Fullerton, *Phys. Rev. Lett.* **87**(8), 087202(2001)
19. Wall mobilities in similar Pt/Co systems gave $\alpha=0.2$. S. Lemerle, private communication.
20. T. Devolder et al., *Appl. Phys. Lett.* **74**, 22, p3383 (1999)
21. S.P. Li, W.S. Lew, J.A.C. Bland, L. Lopez-Diaz, C.A.F. Liaz, M. Natali, Y. Chen, *Phys. Rev. Lett.* **88**(8), 087202 (2002).

Inert Gas Condensation of Iron and Iron-Oxide Nanoparticles

C. Baker,¹ S. Ismat Shah,^{1,3,4} S.K. Hasanain,² B. Ali,² L. Shah,²
G. Li,³ T. Ekiert,³ and K.M. Unruh³

(1) Department of Materials Science and Engineering, University of Delaware, Newark, DE

(2) Department of Physics, Quaid-i-Azam University, Islamabad, Pakistan

(3) Department of Physics and Astronomy, University of Delaware, Newark, DE

(4) Fraunhofer Center for Manufacturing and Advanced Materials, Newark, DE

Abstract

An inert gas condensation technique has been used to prepare nanometer-sized particles of metallic iron by evaporation and agglomeration in a flowing inert gas stream. The resulting Fe nanoparticles were protected from complete oxidation either by the formation of a thin Fe-oxide surface passivation layer or by immersion in an oil bath. X-ray diffraction and transmission electron microscopy measurements indicated that the nanoparticles were typically between 10 and 20 nm in size, that the thickness of the Fe-oxide surface passivation layer was between 3 and 4 nm, and that the oil immersed samples exhibited a significant smaller volume fraction of Fe-oxides than did the surface passivated samples. Room temperature magnetization measurements were also carried out and the coercivity and saturation magnetization of the surface passivated and oil immersed samples determined. Although the coercivities and saturation magnetization values of both samples were very similar, the Fe/Fe-oxide samples exhibited a single component hysteresis loop while the Fe/oil samples exhibited a two component loop.

Introduction

Nanometer-sized Fe particles are pyrophoric and therefore must be protected from complete oxidation if they are to be exposed to atmospheric oxygen. The most common passivation procedure has been to form an Fe-oxide surface layer by slowly exposing the as-prepare nanoparticles to an oxygen containing environment.¹ Because the Fe-oxides are either antiferromagnetic (FeO, α -Fe₂O₃) or ferrimagnetic (γ -Fe₂O₃, Fe₃O₄),² however, the physical and chemical properties of these Fe/Fe-oxide nanoparticles reflect not only the properties of the Fe core but the properties of the passivation layer as well. For example, the hysteresis loops of these nanoparticles have often been observed to be shifted with respect to zero applied field when field cooled through the Néel temperature of the surface oxide due to an exchange coupling between the ferromagnetic core and the antiferromagnetic (or ferrimagnetic) surface oxide.³

Greater insight into the effects of finite size on the magnetic properties of small Fe particles, without the added complication of a core/shell exchange coupling, could be obtained by the study of particles passivated by a non-magnetic surface layer. Several schemes for achieving this have been reported in the literature including, for example, various chemical and physical methods for producing C, SiO₂, and Au coatings.⁴⁻⁶ An alternative approach involves immersing the Fe nanoparticles into an oil prior to their exposure to air. This procedure does not result in the formation of a passivation layer *per se*, but does allow the Fe/oil mixture to be handled in

ambient air without significant oxidation. This approach not only has the advantage of simplicity (no subsequent processing steps other than immersion are required) but also results in minimal structural distortion of the nanoparticle surface.

The primary motivation for this work was to compare the structural and magnetic properties of two sets of Fe nanoparticles that differed only in the manner in which they were protected from oxidation. By comparing the magnetic properties of nanometer-sized Fe particles passivated with an Fe-oxide to those without a surface oxide (or at least a minimal amount of oxide) our goal was to gain a better understanding of the conditions required for the study of homogeneous, ferromagnetic Fe nanoparticles.

Experimental

All of the Fe nanoparticles studied in this work were prepared by an inert gas condensation (ICG) technique.⁷ The procedure consisted of continuously feeding a high purity Fe wire toward a resistively heated Al_2O_3 coated W boat where it melted and evaporated. The resulting Fe vapor was entrained and cooled in a flowing stream of He gas where individual Fe atoms coalesced into small particles. These particles were deposited on a filter from which they were occasionally dislodged and collected in a removable container mounted to the bottom of the vacuum chamber. Fe/Fe-oxide nanoparticles were prepared by slowly exposing the collected Fe nanoparticles to a reduced pressure of atmospheric oxygen. Fe/oil samples were prepared by filling the collection container with vacuum pump oil and allowing the as-prepared Fe nanoparticles to settle into the oil as they were collected. In the latter instance, the oil immersed nanoparticles were subsequently filtered of excess oil to leave a thick Fe/oil residue.

The structure of both the Fe/Fe-oxide and Fe/oil samples was studied by x-ray diffraction (XRD) and transmission electron microscopy (TEM). In the former case, diffraction patterns were fit to a sum of two asymmetric Pearson VII functions representing the $\text{Cu K}_{\alpha 1}$ and $\text{Cu K}_{\alpha 2}$ components of the incident radiation. The resulting angular positions were used to obtain a best fit estimate of the lattice parameter while the width of the Fe (110) diffraction peak was used, in conjunction with the Scherrer formula, to estimate the mean particle size (after subtracting the measured natural line width in quadrature). Transmission electron microscopy samples were prepared by suspending a small quantity of the Fe nanoparticles in a volatile solvent, placing a small droplet onto a TEM grid, and allowing the solvent to evaporate. Both low magnification images and high magnification lattice images were obtained.

Magnetic properties measurements were carried out on disk shaped samples 4 mm in diameter and approximately 0.5 mm in thickness. A vibrating sample magnetometer (VSM) was used to measure the sample magnetization as a function of the applied field. The maximum applied field was 11 kOe and the law of approach to saturation was used to extrapolate the high field magnetization to its saturation value.⁸

The mass of the Fe nanoparticles in the Fe/oil samples was estimated based on the results of a series of XRD measurements on Fe/oil samples prepared from known amounts of (bulk) Fe powder mixed with the same oil used to protect the ICG prepared Fe samples. Fits to these data allowed a plot of the ratio of the Fe (110) peak area to the sum of the areas of the Fe (110) peak and the broad low angle oil scattering peak (see Fig. 1) as a function of the corresponding mass ratio to be constructed. A linear fit to these data (constrained to contain the origin) determined the proportionality constant between the peak areas and the mass ratios. This proportionality

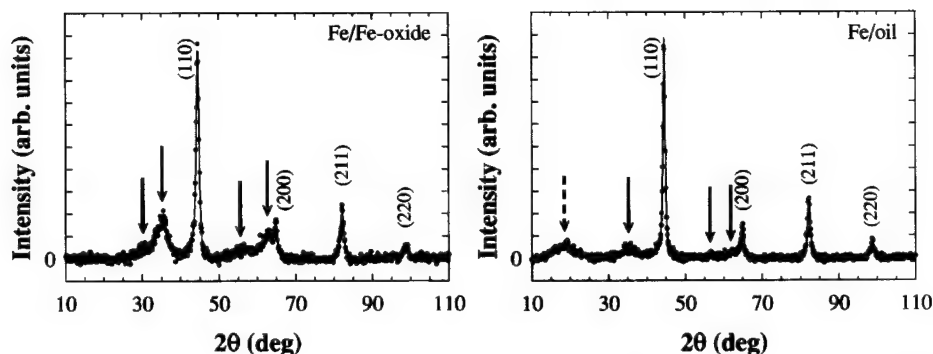


Figure 1: XRD patterns of Fe/Fe-oxide (left) and Fe/oil (right) samples. The solid lines are best fits to the data and the Miller indices of the metallic Fe phase have been indicated. The scattering peaks indicated by solid arrows probably correspond to γ -Fe₂O₃ as discussed in the text and the broad scattering peak indicated by a broken arrow in the Fe/oil sample arises from the oil.

constant was then used, in conjunction with the known total sample mass, to estimate the actual mass of the Fe nanoparticles in the Fe/oil samples.

Results and Discussion

Figure 1 shows typical XRD scattering patterns of Fe/Fe-oxide and Fe/oil samples, as well as the corresponding fits to the data. In both case the most intense scattering peaks arise from metallic Fe (indicated by their Miller indices) while the less intense peaks (indicated by solid arrows) probably arise from cubic γ -Fe₂O₃ although the cubic spinel Fe₃O₄ has a similar lattice parameter. The broad scattering peak centered at about 18 degrees (indicated by the broken arrow) in the Fe/oil sample arises from the oil used to protect the Fe nanoparticles. The best fit Fe lattice parameters of these two samples were $a=0.28707(3)$ nm and $a=0.28682(3)$ nm, respectively, for the Fe/Fe-oxide and Fe/oil samples; both of these values are slightly larger than the reported lattice parameter of bulk Fe ($a=0.28664$ nm) and may reflect some degree of oxygen incorporation into the Fe core.⁹ Likewise, the effective lattice parameter of the γ -Fe₂O₃ phase was determined to be $a=0.835(4)$ nm and $a=0.834(4)$ nm, consistent with the previously reported value of $a=0.8346$ nm (the lattice parameter of Fe₃O₄ is $a=0.8396$ nm).¹⁰ The corresponding Fe diameters of the Fe particle cores were $D=10.8(3)$ nm and $D=16.2$ nm. Based on a comparison of the area of the Fe (110) scattering peak to that of the most intense γ -Fe₂O₃ peak, the Fe/oil sample contains between 4 and 5 times less Fe-oxide than does the Fe/Fe-oxide sample.

Figure 2 shows a high magnification TEM lattice image taken from the Fe/Fe-oxide sample as well as a lower magnification image taken from an Fe/oil sample (higher magnification images were not taken because of the potential for contaminating the TEM sample space). For the Fe/Fe-oxide sample, it can be seen that the oxide layer surrounding the Fe is approximately 3 – 4 nm thick, and is crystalline in nature. The mean particle sizes estimated from the TEM images were in reasonable agreement with the corresponding values obtained from the Scherrer analysis of the XRD peak widths.

Figure 3 shows the room temperature hysteresis loops for the Fe/Fe-oxide and Fe/oil samples. The hysteresis loop of the Fe/Fe-oxide sample is characteristic of a single magnetic phase and exhibits a coercivity of $H_c=529$ Oe while the Fe/oil loop clearly exhibits two magnetic

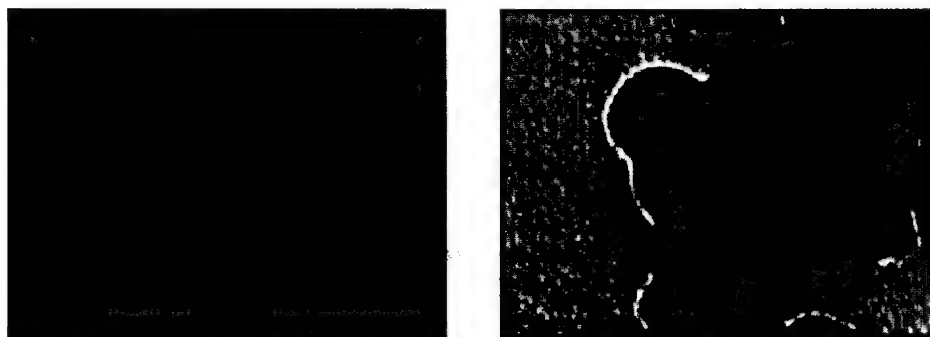


Figure 2: High resolution lattice image of Fe/Fe-oxide particle (left) and a low resolution image of Fe/oil coated particles. The particles shown in these images are not representative of average sized particles. Note the presence of the crystalline passivation layer surrounding the Fe core in the Fe/Fe-oxide image.

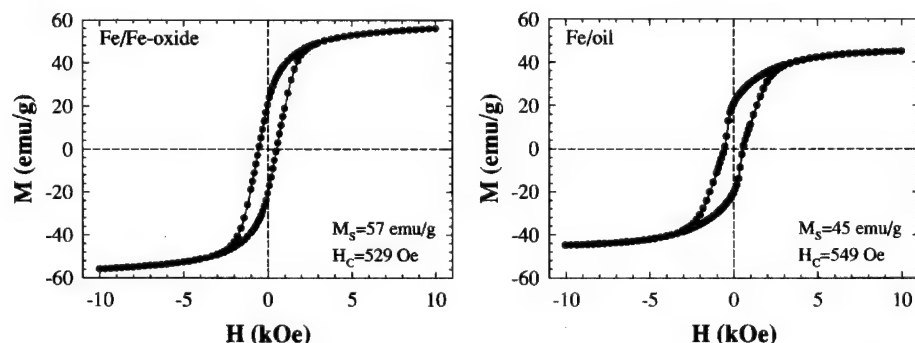


Figure 3: Room temperature hysteresis loops of Fe/Fe-oxide (left) and Fe/oil (right) samples. The saturation magnetization was determined based on an H^2 extrapolation of the measured high field magnetization using the total measured sample mass in the case of the Fe/Fe-oxide sample and the corrected sample mass as described in the text in the case of the Fe/oil sample.

components and a slightly larger coercivity of $H_c = 549$ Oe. The saturation magnetization of both samples was estimated using the law of approach to saturation taking the first term in the field dependent magnetization to be proportional to H^2 . Based on the total particle mass, this procedure yielded a saturation magnetization of $M_s = 57$ emu/g for the Fe/Fe-oxide sample and $M_s = 45$ emu/g for the Fe/oil sample (after correcting the total sample mass for the oil contribution as described above). Given the uncertainties in correcting for the oil mass in the Fe/oil samples, the difference between the saturation magnetization values of the Fe/Fe-oxide and Fe/oil samples is probably not significant. A more detailed analysis of the magnetization would require additional information as to the amount, density, and specific magnetizations of the individual Fe-oxide and Fe phases.

The Fe/oil samples contain less Fe-oxide per particle and one might have expected the magnetic properties of these particles to be less reflective of a two phase system (i.e. an Fe-oxide surface layer and an Fe core) and more reflective of nanometer-sized ferromagnetic Fe. Although the magnetic data shown in Fig. 3b provides some support for this expectation in the form of a

two component hysteresis loop, the coercivity and saturation magnetization values indicate a similar magnetic structure. In particular, the fact that the observed coercivity is significantly larger than the value $H_c \approx 0.64 K_f / M_s \approx 177$ Oe predicted by the simple Stoner-Wohlfarth magnetization reversal model for a collection of randomly oriented single domain particles, assuming that the magnetocrystalline anisotropy and saturation magnetization for a nanometer-sized Fe particle assume their bulk values of $K_f \approx 6 \times 10^4$ ergs/g and $M_s \approx 217$ emu/g,¹¹ suggests that both sets of samples are exchange coupled. Further evidence for an exchange coupled structure comes from an estimate of the effective magnetic anisotropy based on the law of approach to saturation. By fitting high field plots of $M_s(H)$ vs H^2 , or equivalently plots of χ vs H^3 , very similar values of $K_{eff}(\text{cubic}) \approx 2.3 \times 10^5$ erg/g or $K_{eff}(\text{uniaxial}) \approx 1.2 \times 10^5$ erg/g were obtained for the Fe/Fe-oxide and Fe/oil samples based on the assumption of either a cubic or a uniaxial anisotropy. Both values are significantly larger than the (cubic) anisotropy of bulk Fe.

Summary and Conclusion

We have developed a process in which Fe nanoparticles are synthesized by an IGC technique and protected from complete oxidation either by the formation of an Fe-oxide surface layer or by immersion in an oil. The magnetic behavior of the Fe/Fe-oxide and Fe/oil nanoparticles prepared in this way were then compared. Hysteresis loop measurements indicate that the presence of the Fe-oxide surface layer results in an exchange coupling between the surface moments and the moments of the entire Fe core in both samples, despite the significantly smaller amount of Fe-oxide present in the Fe/oil samples.

Acknowledgements

We are pleased to acknowledge Dr. C. Ni for his assistance with the TEM measurements. The work of SIS has been supported of the National Science Foundation through grant no. INT-0138151 and the work of KMU has been supported by AFRL DARPA METAMATERIALS contract no. F33615-01-2-2166.

References

1. See e.g. R.C. O'Handley, *Modern Magnetic Materials: Principles and Applications*, (John Wiley & Sons, Inc., New York, 2000).
2. See e.g. C.N.R. Rao and G.V. Rao, in *Transition Metal Oxides: Crystal Structure, Phase Transitions and Related Aspects* (NSRDS-NBS 49, 1974).
3. See e.g. W.H. Meiklejohn and C.P. Bean, *New Magnetic Anisotropy*, Phys. Rev. **105**, 904 (1957); J.F. Löffler, J.P. Meier, B. Doudin, J-P. Ansermet, and W. Wagner, *Random and Exchange Anisotropy in Consolidated Nanostructured Fe and Ni: Role of Grain Size and Trace Oxides on the Magnetic Properties*, Phys. Rev. B **57**(5), 2915 (1998); C. Prados, M. Multigner, A. Hernando, J.C. Sánchez, A. Fernández, C.F. Conde, and A. Conde, *Dependence of Exchange Anisotropy and Coercivity on the Fe-Oxide Structure in Oxygen-Passivated Fe Nanoparticles*, J. Appl. Phys. **85**(8), 6118 (1999). Two recent reviews on exchange coupled systems which contain many references can be found in J. Nogues and I.K. Schuller, *Exchange Bias*, J. Magn. Magn. Mater. **192**, 203 (1998) and A.E. Berkowitz and K. Takano, *Exchange Anisotropy – A Review*, J. Magn. Magn. Mater. **200**, 552 (1999).

4. S. Linderroth, L. Balcells, A. Laborta, J. Tajeda, P.V. Hendriksen, and S.A. Sethi, *Magnetization and Mössbauer studies of Ultrafine Fe-C particles*, J. Magn. Magn. Mater. **124**, 269 (1993).
5. E.E. Carpenter, *Iron Nanoparticles as Potential Magnetic Carriers*, J. Magn. Mag. Mater. **225**(1-2), 17 (2001).
6. T. Ibusuki, S. Kojima, O. Kitakami, and Y. Shimada, *Magnetic Anisotropy and Behaviors of Fe Nanoparticles*, IEEE Trans. Magn. **37**(4), 2223 (2001).
7. C.G. Granqvist and R.A. Buhrman, *Ultrafine Metal Particles*, -J. Appl. Phys. **47**(5), 2200 (1976).
8. S. Chikazumi, *Physics of Ferromagnetism*, (Clarendon Press, Oxford, 1997).
9. *Pearson's Handbook of Crystallographic Data for Intermetallic Phases*, edited by P. Villars and L.D. Calvert (American Society for Metals, Metals Park, Ohio, 1989).
10. T. Belin, N. Guigue-Millot, T. Caillot, D. Aymes, and J.C. Niepce, *Influence of Grain Size, Oxygen Stoichiometry, and Synthesis Conditions on the γ -Fe₂O₃ Vacancies and Lattice Parameters*, J. Solid State Chem. **163**, 459 (2002).
11. 14. E.C. Stoner and E.P. Wohlfarth, *A Mechanism of Magnetic Hysteresis in Heterogeneous Alloys*, Phil. Trans. Roy. Soc. London A **240**, 599 (1948).

Chemically Functional Alkanethiol Derivatized Magnetic Nanoparticles

David A. Fleming, Michael Napolitano, Mary Elizabeth Williams*
The Pennsylvania State University, Department of Chemistry,
152 Davey Laboratory, University Park, PA, 16802, U.S.A.

ABSTRACT

Chemically functional magnetic nanoparticles, comprised of an Fe core encased in a thin Au shell, have been prepared by sequential high temperature decomposition of organometallic compounds in a coordinating solvent. A novel approach to encapsulate the Fe core in Au has been developed. TEM analysis confirms that the nanoparticles are monodisperse (~20%) with average diameters of 8nm. The nanoparticles were subsequently functionalized with alkanethiolate ligands, which prevent aggregation, enable solubility in a range of solvents (both hydrophobic and hydrophilic), and permit subsequent derivatization (*e.g.*, via ligand exchange reactions). The functionalized particles are characterized using high-resolution transmission electron microscopy (HRTEM), X-ray powder diffraction (XRD) and ultraviolet-visible (UV-Vis) absorption spectroscopy.

We have utilized place-exchange to impart chemical functionality to the nanoparticles by attaching either (1) thiol-derivatized redox moieties (*e.g.*, ferrocene) or (2) alkanethiols with terminal reactive groups such as alcohols, amines and carboxylic acids. This paper presents our preliminary investigations of the voltammetry of the former class of these magnetic core/shell nanoparticles.

INTRODUCTION

The preparation and characterization of novel nanometer scale materials has led to an exponential increase in research activity concerned with examination of the fundamental properties and potential applications of these materials. Metal nanoparticles, for example, have been applied to innovative applications ranging from electronics¹ and optics² to DNA sensing³ and catalysis.⁴ The utility of magnetic nanoparticles has recently been described⁵ and demonstrated in a few cases for ultrahigh density information data storage,⁶ contrast agents in medical imaging technologies⁷, and 'spintronics'⁸ (*i.e.*, spin-based data transfer and storage). For example, Co and FePt nanoparticles have been shown to be useful for the preparation of highly ordered three-dimensional magnetic superlattices.⁹ There have been several demonstrations of the preparation of magnetic particles in the 10 nm – 2 μ m diameter range, comprised of either metal-coated polymeric beads or polymer-coated magnetic particles,¹⁰ which typically lack chemical functionality (*i.e.* synthetic reactivity) or whose electronic or magnetic properties have not been systematically examined. A critical need remains for the synthetic control of their size and composition, and extension of these materials to broader applications requires the design and synthesis of chemically *functional* magnetic nanoparticles.

Several strategies have been developed for the synthesis of magnetic nanoparticles, most notably those reported by Murray *et al.*, which rely on the thermal decomposition of small organometallic precursors in the presence of stabilizing ligands.¹¹ Using similar methods,

bimetallic particles of, for example, CoPt and FePt have been created, which are limited almost exclusively to alloys. Examples of non-alloyed, heterometallic nanoparticles include noble metal core/shell particles synthesized via citrate reduction¹² and semiconductor core/semiconductor shell materials.¹³ Shells on other particles, in particular magnetic nanoparticles, have yet to be widely reported. We have developed a synthetic strategy that relies on the surface passivation of ferromagnetic Fe particles with a shell Au. The Au shell prevents oxidation of the Fe core, while facilitating nanoparticle functionalization via well-known Au-thiol coupling chemistry. In this paper, we describe a route for the creation of Fe/Au core/shell nanoparticles by the high temperature decomposition of $\text{Fe}(\text{CO})_5$, followed by the subsequent addition of an Au shell via a transmetallation reaction.

Functionalization of *non*magnetic nanoparticles has been demonstrated by the covalent attachment of protective ligand monolayers; these studies have primarily investigated alkanethiolate attachment to Au,¹⁴ Ag,¹⁵ or Pt¹⁶ metal clusters, although many additional ligands have been utilized. Importantly, alkanethiolate monolayers (1) prevent irreversible particle aggregation, (2) impart solubility in solvents of varying polarity, and (3) can be used to create chemical functionality. A significant observation of these systems is that precipitation of the particles *prior* to monolayer protection results in irreversible aggregation.^{5a,17} By analogy, modification of the nanoscale magnetic particles requires *in situ* surface modification. Furthermore, ligand-exchange reactions permit the stepwise functionalization of the core/shell nanoparticles. To demonstrate our ability to prepare magnetic nanoparticles with bound reactive and functional groups, we have exchanged alkanethiolate ligands with alkanethiol-modified ferrocene chains, which impart redox activity. We use the well-known electrochemical signal of ferrocene to confirm nanoparticle substitution.

EXPERIMENTAL

Chemicals

Trioctylphosphine oxide (TOPO, Fluka), hexadecylamine (HDA), iron pentacarbonyl, diphenyl ether (DPE), n-butanol, chloroform and methylene chloride (Aldrich) were used as received. Tetrabutylammonium hexafluorophosphate (TBAPF₆, Fluka) was recrystallized from ethyl acetate. $\text{Au}(\text{acac})\text{PPh}_3$ ¹⁸ and ferrocene thiol¹⁹ were synthesized using literature procedures. Ultrapure water (18.2 M Ω) was purified by a Barnstead NANOpure water system.

Synthesis

In a typical synthetic preparation, a 100mL 3-neck flask was fitted with a condenser and thermometer and charged with 2.5 g (6.46 mmol) TOPO and 7 g (29 mmol) HDA. After thoroughly degassing the mixture, the temperature is raised to 250°C under argon. A solution of 0.625g (1.62 mmol) TOPO, 1.75g (7.25 mmol) HDA and 0.14mL (1.06 mmol) $\text{Fe}(\text{CO})_5$ is heated and injected into the TOPO mixture, and stirred for at least an additional 30 min. The temperature is lowered to 200°C, and a solution containing 0.139g (0.25 mmol) $\text{Au}(\text{acac})\text{PPh}_3$ in 10mL DPE is added dropwise. The solution is stirred for 30 min, cooled to ~120°C, 30 mL n-butanol is added, and the resulting black solution stirred for 24 hours.

The nanoparticles are isolated and purified by centrifugation (at least three times) from 50/50 ethanol/butanol, followed by dispersion in ethanol and collection on a permanent magnet (at least twice). The collected nanoparticles are dissolved in 2.5M decanethiol in chloroform, stirred for a minimum of 2 days, and collected via centrifugation. The decanethiol ligands are exchanged by stirring the nanoparticles in 32mM ferrocene thiol in chloroform for at least one week, producing a mixed monolayer.²⁰ Confirmation of removal of all excess ferrocene thiol is obtained from a lack of redox response of the decanted solutions during cyclic voltammetry; Fc content decreases with sequential centrifugation steps, and is below the limits of detection (*ca.* 10 nM) after three or four centrifugation cycles.

Measurements

TEM analysis was performed on a JOEL JEM 1200 EXII transmission electron microscope at the Penn State Biological Electron Microscopy Facility. XRD measurements were performed on a Philips PW3040-MPD X-Ray Diffractometer, and UV-Vis measurements were performed on a Cary 500 UV-Visible-Near IR spectrometer.

Cyclic voltammetry was performed using a CH Instruments Model CHI600A potentiostat interfaced with a personal computer. Pt microelectrodes (25 μ m diameter) were created by flame-sealing Pt microwire (Alfa Aesar) in glass capillaries. The sealed ends of the microelectrodes were bent to a 90° angle in the flame, and polished using fine grit sandpaper and sequentially smaller grades of alumina on fine nap polishing cloths (Buehler). The electrodes were sonicated briefly in ethanol prior to use. Pt and Ag wire were used as counter and reference electrodes, respectively. Sample solutions of functionalized particles (~1mg/ml) in 0.2M TBAPF₆ in chloroform were degassed, and the electrochemical cell sealed, to minimize oxygen contamination.

RESULTS AND DISCUSSION

Nanoparticle Characterization

The size and composition of the nanoparticles were confirmed using transmission electron microscopy (TEM); a representative TEM image of the synthesized Fe core/Au shell nanoparticles is shown in Figure 1A. Analysis shows that the as-prepared samples are relatively monodisperse (~20%) with an average size of 8.25 ± 1.8 nm. Darker, *ca.* 1 nm thick, rings around each particle are attributed to the Au shell, and have near-uniform thicknesses. The polydispersity of the core/shell particles is comparable to that of the Fe cores (prior to capping with Au), indicating that particle polydispersity arises during the initial Fe particle formation.

Further confirmation of nanoparticle structure is obtained from x-ray powder diffraction (XRD) spectra, such as in Figure 1B, which show peaks characteristic of the (111), (200), (220), (311), and (222) lattice planes of fcc Au. Due to similarities in lattice parameters, peaks corresponding to crystalline Fe are obscured by the Au peaks; however, no peaks for Fe oxides are observed as would be expected for Fe cores with protected surfaces. The magnetic character of the particles (evidenced by their attraction to the permanent magnet on which they are collected), taken together with the TEM and XRD data, confirms their Fe core/Au shell structures. High resolution TEM and energy dispersive x-ray spectroscopy studies are underway to gather additional and definitive evidence.

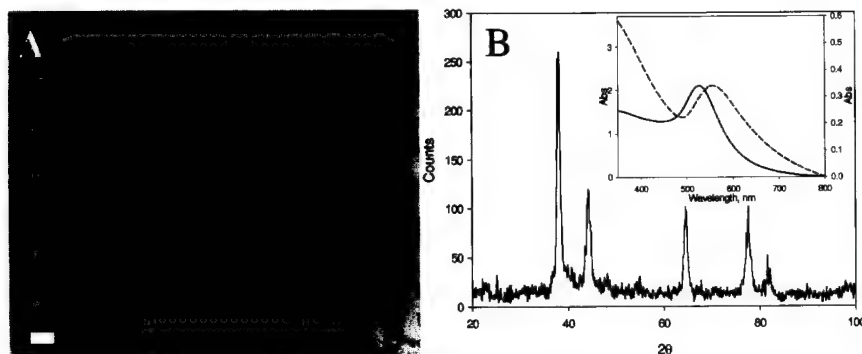


Figure 1. (A) TEM image of 8.25 ± 1.8 nm Fe@Au nanoparticles. Scale bar represents 20nm. (B) XRD spectra showing peaks (from left to right) for (111), (200), (220), (311), and (222) Au lattice planes. The Fe peaks are obscured by the Au (200), (220), and (222) peaks. The inset shows a typical UV-Vis spectrum of Fe@Au nanoparticles (dashed) versus to monometallic Au particles (solid) of similar size.

It is well established that metal nanoparticles possess a characteristic absorption in the visible region of the electromagnetic spectrum due to the surface propagation of free electrons in the metal. The energy of the surface plasmon band is a function of the metal, solvent, attached ligand, and size of the particle, thus is a sensitive measure of the dielectric properties of the nanoparticle. A typical UV-Vis spectrum of the Fe core/Au shell containing a decanethiol monolayer is shown in the inset of Figure 1B. The plasmon band of the Fe@Au nanoparticles appears at 555 nm, and is red-shifted in comparison with monometallic Au nanoparticles of similar size. The energy for the plasmon band may be shifted to lower energy by particle aggregation or due to electronic interaction of the Au shell with the Fe core. We do not observe any decreased solubility, and TEM images show individually isolated particles, so that the shifted plasmon peak cannot be a result of particle aggregation. It has been shown¹² for other core/shell nanoparticles that the energy of the plasmon absorbance of the shell can be dramatically effected by the size and dielectric properties of the core, and we infer that the Fe core causes a similar effect in our materials. Additional studies of the size and composition-dependent plasmon absorption of our alkanethiol stabilized Fe core/Au shell nanoparticles will be reported separately.

Electrochemical Measurements

There have been several reports of electrochemical studies of Au nanoparticles with redox-active ligands;²¹ we analogously attach alkanethiol-modified ferrocenes to the Au shell of our nanoparticles. Figure 2A shows a representative cyclic voltammogram of a solution of Fc-derivatized Fe core/Au shell nanoparticles, and the peak at 0.86 V (vs. Ag/Ag⁺) corresponds to the oxidation of nanoparticle-bound ferrocenes. The forward (oxidation) wave is nearly sigmoidal in shape, consistent with the microelectrode geometry and freely diffusing Fc-modified nanoparticles. However, upon reversing the potential sweep, the return (reduction)

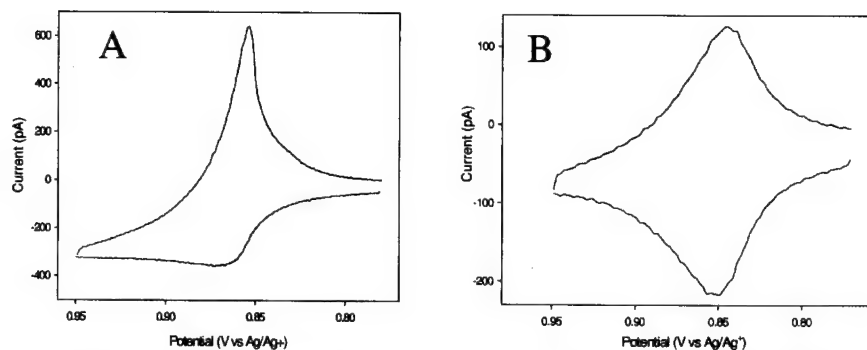


Figure 2. Cyclic voltammograms of (A) solution of Fc-functionalized nanoparticles and (B) microelectrode immersed in an electrolyte solution after nanoparticle adsorption. All voltammograms were performed using a potential scan rate of 20mV/s in 0.2M TBAPF₆ in methylene chloride at a 25 μ m diameter Pt electrode.

wave is sharp and Gaussian, evidence for adsorption of the nanoparticles on the microelectrode surface.

Nanoparticle adsorption was further examined (after these cyclic voltammograms) by removing the microelectrode and re-immersing it in a solution containing only electrolyte; Figure 2B shows a voltammogram of the microelectrode with adsorbed Fc-modified nanoparticles. The difference in potential between the anodic and cathodic peaks (ΔE_p) is 4 mV and the reduction current is five fold smaller. The shape of the redox wave in Figure 2B is consistent with surface-confined redox species on the working electrode.²² The surface coverage, calculated from the integrated current under the oxidation peak, is 1.9×10^{-9} mol/cm². This value is much larger than expected for a single adsorbed layer of nanoparticles, but because the number of ferrocenes per nanoparticle is not known, we are unable to estimate the thickness of the adsorbed particle layer.

CONCLUSIONS

Surface-protected Fe@Au nanoparticles have been synthesized using a novel high temperature approach, and their structure confirmed using TEM, XRD and UV-Visible spectroscopy. The nanoparticles were functionalized with electroactive Fc alkanethiolate ligands and their preliminary voltammetric behavior has been examined. The nanoparticles adsorb to the microelectrode surface, producing redox-active layers.

ACKNOWLEDGEMENTS

This work is funded in part by a grant from the American Chemical Society Petroleum Research Fund Type G grant. We are grateful for additional financial support from the Penn State Department of Chemistry and Eberly College of Science. We thank the Mallouk group for use of the XRD instrumentation.

REFERENCES.

1. Shipway, A. N.; Katz, E.; Willner, I. *Chem. Phys. Chem.* **2000**, *1*, 18-52.
2. For example, (a) Xia, Y.; Gates, B.; Yin, Y.; Lu, Y. *Adv. Mat.* **2000**, *12*, 693-712. (b) Haynes, C. L.; Van Duyne, R. P. *J. Phys. Chem. B.* **2001**, *105*, 5599-5611.
3. Recent examples include: (a) Taton, T. A.; Lu, G.; Mirkin, C. A. *J. Am. Chem. Soc.* **2001**, *123*, 5164-5165. (b) Dubertret, B.; Calame, M.; Libchaber, A. *J. Nat. Biotechnol.* **2001**, *19*, 365-370.
4. (a) Crooks, R. M.; Zhao, M. Q.; Sun, L.; Chechik, V.; Yeung, L. K. *Acc. Chem. Res.* **2001**, *34*, 181-190. (b) Somorjai, G. A.; Borodko, Y. G. *Catal. Lett.* **2001**, *76*, 1-5.
5. (a) Schmid, G. in *Clusters and Colloids, from Theory to Applications*; VCH Publishers: Weinheim, 1994. (b) Ji, T.; Lirtsman, V. G.; Avny, Y.; Davidov, D. *Adv. Mater.* **2001**, *13*, 1253-1256.
6. (a) Ross, C. *Annu. Rev. Mat. Sci.* **2001**, *21*, 203-235. (b) Tsunashima, S. *J. Phys. D – Appl. Phys.* **2001**, *34*, R87-R102. (c) Kirk, K. J. *Contemp. Phys.* **2000**, *41*, 61-78. (d) Weller, D.; Doerner, M. F. *Annu. Rev. Mat. Sci.* **2000**, *30*, 611-644.
7. (a) Reynolds, C. H.; Annan, N.; Beshash, K.; Huber, J. H.; Shaber, S. H.; Lenkinski, R. E.; Wortman, J. A. *J. Am. Chem. Soc.* **2000**, *122*, 8940-8945. (b) Goldstein, H.; Lumma, W.; Rudzik, A. *Annu. Rep. Med. Chem.* **1989**, *24*, 265-276.
8. Wolf, S. A.; Awschalom, D. D.; Buhrman, R. A.; Daughton, J. M.; von Molnar, S.; Roukes, M. L.; Chitchekanova, A. Y.; Treger, D. M. *Science*, **2001**, *294*, 1488-1495.
9. (a) Sun, S.; Fullerton, E. E.; Weller, D.; Murray, C. B. *IEEE Trans. Mag.* **2001**, *37*, 1239-1243. (b) Sun, S. H.; Murray, C. B.; Weller, D.; Folks, L.; Moser, A. *Science* **2000**, *287*, 1989-1992.
10. For example, (a) Burke, N. A. D.; Stover, H. D. H.; Dawson, F. P.; Lavers, J. D.; Jain, P. K.; Oka, H. *IEEE Trans. Mag.* **2001**, *37*, 2660-2662. (b) Caruso, F.; Spasova, M.; Susa, A.; Giersig, M.; Caruso, R. A. *Chem. Mater.* **2001**, *13*, 109-116.
11. Murray, C. B.; Sun, S.; Doyle, H.; Betley, T. *MRS Bull.* **2001**, *26*(12), 985-991.
12. Kim, Y.; Johnson, R. C.; Li, J.; Hupp, J. T.; Schatz, G. C. *Chem Phys Lett.* **2002**, *352*, 421-428.
13. Reiss, P.; Bleuse, J.; Pron, A. *Nano Lett.* **2002**, *2*, 781-784.
14. The original reports include (a) Brust, M.; Walker, M.; Bethell, D.; Schiffrin, D. J.; Whyman, R. *J. Chem. Soc., Chem. Commun.* **1994**, 801-802. (b) Brust, M.; Fink, J.; Bethell, D.; Schiffrin, D. J.; Kiely, C. J. *J. Chem. Soc. Chem. Comm.* **1995**, 1655-1656.
15. (a) He, S. T.; Yao, J. N.; Jiang, P.; Shi, D. X.; Zhang, H. X.; Xie, S. S.; Pang, S. J.; Gao, H. J. *Langmuir* **2001**, *17*, 1571-1575.
16. (a) Yee, C.; Scotti, M.; Ulman, A.; White, H.; Rafailovich, M.; Sokolov, J. *Langmuir* **1999**, *15*, 4314-4316.
17. Novak, J. P.; Nickerson, C.; Franzen, S.; Feldheim, D. L. *Anal. Chem.* **2001**, ASAP.
18. Uson, R.; Laguna, A. *Inorg. Synth.* **1998**, *26*, 85.
19. Chidsey, C. E. D.; Bertozzi, C. R.; Putvinski, T. M.; Muijsce, A. M. *J. Am. Chem. Soc.* **1990**, *112*, 4301-4306.
20. Ingram, R. S.; Hostetler, M. J.; Murray, R. W. *J. Am. Chem. Soc.* **1997**, *119*, 9175-9178.
21. (a) Ingram, R. S.; Murray, R. W. *Langmuir* **1998**, *14*, 4115-4121. (b) Hostetler, M. J.; Green, S. J.; Stokes, J. J.; Murray, R. W. *J. Am. Chem. Soc.* **1996**, *118*, 4212-4213.
22. Bard, A.; Faulkner, L. R. in *Electrochemical Methods: Fundamentals and Applications*, 2nd Edition. John Wiley & Sons, Inc.: New York, 2001.

Magnetic Properties of Ni Nanoparticles Embedded in Amorphous SiO₂

Fabio C. Fonseca¹, Gerardo F. Goya¹, Renato F. Jardim¹, Reginaldo Muccillo², Neftalí L. V. Carreño³, Elson Longo³, Edson R. Leite³

¹ Instituto de Física, Universidade de São Paulo, CP 66318, 05315-970, São Paulo, SP, Brazil

² Centro Multidisciplinar de Desenvolvimento de Materiais Cerâmicos CMDMC, CCTM-Instituto de Pesquisas Energéticas e Nucleares, CP 11049, 05422-970, São Paulo, SP, Brazil

³ Centro Multidisciplinar de Desenvolvimento de Materiais Cerâmicos CMDMC, Departamento de Química, Universidade Federal de São Carlos, CP 676, 13560-905, São Carlos, SP, Brazil

ABSTRACT

A modified sol-gel technique was used to synthesize nanocomposites of Ni:SiO₂ which resulted in Ni nanoparticles embedded in a SiO₂ amorphous matrix. Transmission electron microscopy TEM analysis were performed to study the structure and morphology of the magnetic powders. The Ni particles were found to have a good dispersion and a controlled particle size distribution, with average particle radius of ~ 3 nm. A detailed characterization of the magnetic properties was done through magnetization measurements $M(T,H)$ in applied magnetic fields up to ± 7 T and for temperatures ranging from 2 to 300 K. The superparamagnetic (SPM) behavior of these metallic nanoparticles was inferred from the temperature dependence of the magnetization. The blocking temperature T_B , as low as 20 K, was found to be dependent on Ni concentration, increasing with increasing Ni content. The SPM behavior above the blocking temperature T_B was confirmed by the collapse of M/M_S vs. H/T data in universal curves. These curves were fitted to a log-normal weighted Langevin function allowing us to determine the distribution of magnetic moments. Using the fitted magnetic moments and the Ni saturation magnetization, the radii of spherical particles were determined to be close to ~ 3 nm, in excellent agreement with TEM analysis. Also, magnetic hysteresis loops were found to be symmetric along the field axis with no shift via exchange bias, suggesting that Ni particles are free from an oxide layer. In addition, for the most diluted samples, the magnetic behavior of these Ni nanoparticles is in excellent agreement with the predictions of randomly oriented and noninteracting magnetic particles. This was confirmed by the temperature dependence of the coercivity field that obeys the relation $H_C(T) = H_{C0} [1 - (T/T_B)^{1/2}]$ below T_B with $H_{C0} \sim 780$ Oe.

INTRODUCTION

Nanosized superparamagnetic (SPM) particles of ferromagnetic metals as Fe, Co, and Ni have been extensively studied because of both the richness of their physical properties and a wide range of potential applications like catalysts, high density magnetic recording media, ferrofluids, and medical diagnostics [1,2]. Although they are easily obtained, a major point is the processing method used to produce such nanomaterials. In particular, several methods have been used to prepare Ni nanoparticles (NP) like evaporation [3], sputtering [4], high-energy ball milling [5], ion exchange, [6] and sol-gel [7,8]. However, metallic NP exhibit two main

problems: the control of particles size and the formation of an oxide layer surrounding the metallic particles. The control of particles size distribution (SD) and average size strongly depends on the parameters of the preparation method. Besides the processing technique used, an approach to assemble and maintain a nanostructured material is to host the metallic NP in an inorganic and non-magnetic matrix. The development of nanocomposites, in which metallic particles are embedded in a matrix, typically silica, can provide an effective way of tailoring a uniform SD and to control the dispersion of ultrafine particles [9].

In addition, these SPM particles have a high reactivity because of the very high surface area to volume ratio and can be easily environmentally degraded. Thus, as result of the processing method, an oxide surface layer can be formed leading to a shell-core morphology where an antiferromagnetic (AFM) oxide layer surrounds the ferromagnetic (FM) metallic NP. Such a morphology influences the magnetic properties due to the exchange interaction between the FM and AFM phases.

In the present study we focus on the magnetic characterization of high quality specimens of Ni nanoparticles embedded in amorphous silica prepared through a modified sol-gel precursor. Several physical characterizations performed on diluted samples of Ni:SiO₂, with Ni concentrations of ~ 1.5 and 5 wt%, indicated that they have average radius close to 3 nm, exhibit superparamagnetism (SPM), and are free from an oxide NiO layer.

EXPERIMENTAL

Nanocomposites of Ni:SiO₂ were synthesized by a modified sol-gel method using as start materials tetraethylorthosilicate (TEOS), citric acid, and nickel nitrate (Ni(NO₃)₂·6H₂O). The citric acid was dissolved in ethanol and the TEOS and the nickel nitrate were added together and mixed for homogenization during 15 min at room temperature. A citric acid/metal (Si+Ni) ratio of 3:1 (in mol) was used. Ethylene glycol was added to the citrate solutions, at a mass ratio of 40:60 in relation to the citric acid, to promote the polyesterification. The resulting polymer was pyrolysed in N₂ atmosphere at different temperatures and times: typically at 500 °C for 2 h. During the pyrolysis, the burn out of the organic material results in a rich CO/CO₂ atmosphere which promotes the reduction of the Ni-citrate, resulting in nanometric Ni particles. Here we concentrate our discussion in two diluted samples with ~ 1.5 and 5 Ni wt% which are referred in the text as samples S1 and S2, respectively. Further details of the preparation method employed are described elsewhere [7]. The structure and morphology of the magnetic powder were examined by high-resolution transmission electron microscopy (TEM) and X-ray diffraction (XRD) analysis. Magnetization measurements $M(T,H)$ in applied magnetic fields between ± 7 T and for temperatures ranging from 2 to 300 K, were performed in powders with a SQUID magnetometer.

RESULTS AND DISCUSSION

Figure 1 shows a Dark-Field (DF) TEM image of the S1 sample. It is observed that the Ni nanoparticles (bright spots in the photograph) are well dispersed in the amorphous matrix. DF-

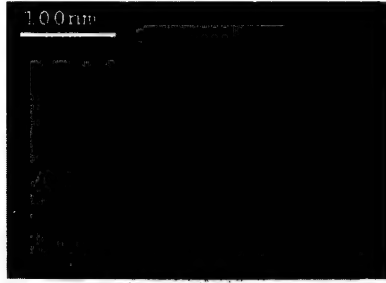


Figure 1. Dark-Field TEM image of the S1 specimen.

TEM analysis revealed that the Ni particles present an homogeneous particle SD, with a mean particle size of $r_{mT} \sim 3.3$ nm. The r_{mT} values are slightly higher but consistent with the average crystallite sizes determined from X-ray diffraction (XRD) data (not shown) through the Scherrer equation, as displayed in Table I. The particle SD's shown in Fig. 2 were built from TEM examinations by considering over than 400 particles. The log-normal SD's have distinct characteristics for the studied samples (Table I). For the sample S1, the median particle size $r_{0T} = 3.9$ nm is close to the mean particle size $r_{mT} = 4.2$ nm due to a small distribution width $\sigma_T = 0.35$ nm. The Ni richest sample S2 (not shown) revealed a SD with $r_{0T} = 2.3$ nm, $r_{mT} = 3.3$ nm, and a larger distribution width $\sigma_T = 0.84$ nm (see Table I).

Table I. Nanoparticles size distributions parameters^a.

Sample	log-normal L(x)					TEM analysis			XRD
	μ_0	r_0	μ_m	r_m	σ	r_{0T}	r_{mT}	σ_T	r_{XR}
S1	4.6	2.8	12	3.8	1.4	3.9	4.2	0.35	2.7
S2	5.1	2.9	17	4.4	1.6	2.3	3.3	0.84	2.3

^aMagnetic moment values in $\text{emu} \times 10^{17}$ and radii in nm.

The magnetic properties of these nanocomposites are also of interest. The temperature dependence of the magnetization $M(T)$, taken in zero-field-cooling (ZFC) and field-cooling (FC) conditions, exhibits clear features of SPM systems. These features are displayed in Figure 3 for both samples: (1) the ZFC curves are rounded at T_B , defined as the temperature of their maximum, indicating a blocking process of the small particles; and (2) a paramagnetic-like behavior above T_B . The value of T_B shifts from $T_B \approx 20$ K for the S1 sample to $T_B \approx 40$ K for the more concentrated S2 sample. This shift of T_B to higher temperatures is consistent with a higher metal content in sample S2.

Further evidence of the SPM behavior above T_B was inferred from hysteresis loops shown in the inset of Fig. 3. The M/M_S vs. H/T data, for $T > T_B$, resulted in a universal curve, a feature of the SPM response [10]. The magnetic moment distributions were fitted considering a log-normal weighted Langevin function (log-normal L(x)) [10]. From these fittings, the radius distributions of spherical particles were calculated using the saturation magnetization of bulk Ni at 300 K ($M_S = 521 \text{ emu/cm}^3$). The mean radii r_m were estimated to be 3.8 and 4.4 nm for samples S1 and S2, respectively, in excellent agreement with the ones obtained from TEM analyses.

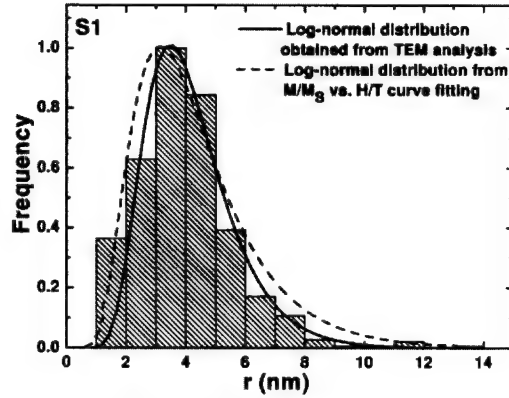


Figure 2. Histogram of the size distribution of Ni nanoparticles and log-normal fitting (solid line) for sample S1 determined from TEM analysis. Dashed line stands for the log-normal size distribution calculated from the log-normal Langevin $L(x)$ fitting for M/M_S vs. H/T curves (see text for details).

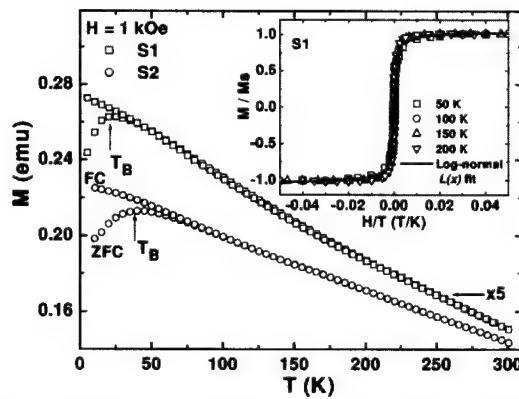


Figure 3. Temperature dependence of the magnetization for samples S1 and S2. Curves were taken in ZFC and FC processes at $H = 1$ kOe. The inset shows a universal M/M_S vs. H/T curve of the S1 specimen, for several temperatures.

A comparison between the log-normal SD's inferred by either TEM analysis and magnetic-data fitting for the more diluted sample S1 is shown in Fig. 2. The excellent agreement between the two log-normal SD's lends credence to our analysis and may be attributed to both a narrow SD and a negligible interaction between particles [10]. The same analysis, for the more concentrated specimen S2 (not shown) resulted in a poorer agreement, with r_0 being slightly higher than r_{OT} but close to r_{mT} (see Table I). Such a small discrepancy is certainly related to either a magnetic contribution arising from larger particles and weak dipolar interactions [10].

Turning now to the low temperature regime, Fig. 4 shows the hysteresis loops measured

at temperatures ranging from 3.5 to 200 K for sample S1. We remark that NiO/Ni composites exhibit exchange bias due to interfacial interaction between ferromagnetic Ni and antiferromagnetic AFM NiO [11]. This exchange interaction is evidenced through a shift of hysteresis loops along the field axis when the system is field-cooled below the ordering temperature of the AFM phase. Defining H_{C+} and H_{C-} as the coercive fields with decreasing and increasing fields, respectively, a measure of the symmetry of the $M(H)$ curves is given by $\Delta H_C = (H_{C+} + H_{C-})/2$. Previous works on Ni/NiO systems have reported values for the exchange bias field ΔH_C ranging from ~ 80 Oe in Ni/NiO nanowires [12], to ~ 700 Oe in partially oxidized Ni NP [13]. The hysteresis loops displayed in Fig. 4 clearly show that these loops are symmetric about zero field ($\Delta H_C \sim 1$ Oe) indicating the absence of particles with the shell-core NiO-Ni morphology. The data also indicate negligible contribution of isolated NiO nanoparticles, which would exhibit large loop shifts of up to ~ 10 kOe [14]. Thus, our magnetic data strongly suggest that the modified sol-gel method used for the synthesis of nanosized Ni metallic particles results in significantly less oxidized metallic particles than other techniques [12,13]. This result is in agreement with XRD analysis which revealed absence of extra phases in these samples.

The $H_C(T)$ values at different temperatures (Figure 4 (b)) reveal that coercivity develops appreciably below T_B in these samples. The coercivity for a system of randomly oriented and noninteracting particles is expected to follow the relation $H_C(T) = H_{C0} [1 - (T/T_B)]^{1/2}$ with $H_{C0} = 0.64K/M_S$ [15], where K is the anisotropy constant of bulk Ni, and M_S is the saturation magnetization. The above expression considers that the magnetization reversal takes place coherently, a situation that can be achieved when interparticle interactions are neglected [16]. Figure 4 (b) shows that this dependence is closely followed by both samples, supporting the picture of noninteracting particles, as previously observed in systems comprised of metallic and ferromagnetic NP [17]. Also, the extrapolation of $H_C(T)$ to 0 yields values of $T_B \sim 16$ and 27 K for samples S1 and S2, respectively, consistent with those obtained from $M(T)$ curves.

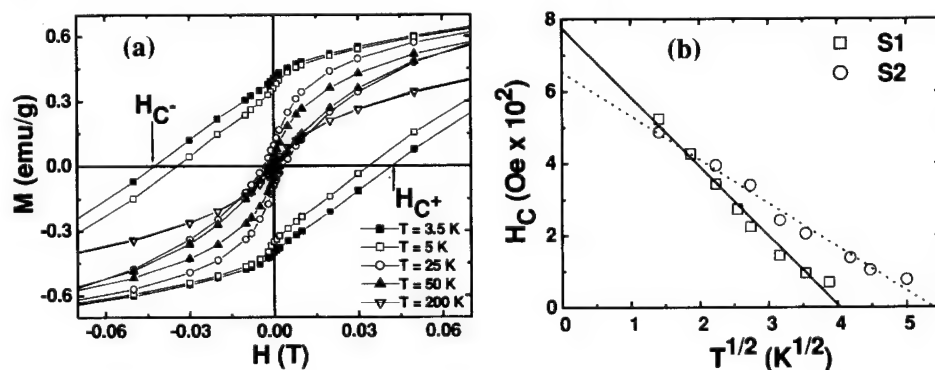


Figure 4. (a) Expanded view of hysteresis loops taken at 3.5, 5, 25, 50, and 200 K for the nanocrystalline Ni particles sample S1. H_{C+} and H_{C-} are defined in the text. (b) Temperature dependence of the coercivity H_C for samples S1 and S2. The Figure shows $H_C(T)$ to obey a $T^{1/2}$ dependence with H_{C0} of ~ 780 and 650 Oe for samples S1 and S2, respectively.

CONCLUSIONS

In summary, a modified sol-gel method to prepare high-quality Ni:SiO₂ nanocomposites has been developed. The obtained Ni-NP have mean radius of ~ 3 nm, narrow particle SD's, and exhibit SPM behavior above T_B (T_B < 40 K). The Ni-NP size distributions, determined from magnetic measurements, were in excellent agreement with those obtained from TEM analysis. Due to the absence of a shift along the field axis in M(H) curves below T_B and XRD data, we have also inferred that these Ni-NP are free from an oxide layer. The linear T^{1/2} dependence of the coercivity below T_B supports a picture of randomly oriented and noninteracting ferromagnetic nanoparticles in the samples studied.

ACKNOWLEDGMENTS

We are grateful to A. L. Brandl, J. Cesar, and M. Knobel for the program codes for distribution calculations. This work was supported in part by the Brazilian agency FAPESP under Grant Nos. 99/10798-0, 01/02598-3, 98/14324-0, and 01/04231-0. Three of us (R.F.J., G.F.G., and E.R.L.) are fellows of the CNPq.

REFERENCES

1. M. Ozaki, *Mater. Res. Bull.* XIV, 35 (1989).
2. H. Gleiter, *Nanostruct. Mater.* 1, 1 (1992).
3. T. Hayashi, T. Ohno, S. Yatsuya, R. Ueda, *Jap. J. Appl. Phys.* 16, 705 (1977).
4. A. Gavrin, C. L. Chien, *J. Appl. Phys.* 73, 6949 (1993).
5. E. M. González, M. I. Montero, F. Cebollada, C. de Julián, J. L. Vicent, J. M. González, *Europhys. Lett.* 42, 91 (1998).
6. J. S. Jung, W. S. Chae, R. A. McIntyre, C. T. Seip, J. B. Wiley, C. J. O'Connor, *Mater. Res. Bull.* 34, 1353 (1999).
7. E. R. Leite, N. L. V. Carreño, E. Longo, A. Valentini, and L. F. D. Probst, *J. Nanosci. Nanotechnol.* 2, 89 (2002).
8. C. Estournès, T. Lutz, J. Happich, T. Quaranta, P. Wissler, J. L. Guille, *J. Magn. Magn. Mater.* 173, 83 (1997).
9. C. A. Morris, M. L. Anderson, R. M. Stroud, C. I. Merzbacher, and D. R. Rolison, *Science* 284, 622 (1999).
10. F. C. Fonseca, G. F. Goya, R. F. Jardim, R. Muccillo, N. L. V. Carreño, E. Longo, and E. R. Leite, *Phys. Rev. B* 66, 104406 (2002).
11. J. B. D. Cullity, *Introduction to magnetic materials* (Addison-Wesley, Reading, Mass., 1972) Chap. 11.
12. M. Fraune, U. Rudiger, G. Guntherodt, S. Cardoso, and P. Freitas, *Appl. Phys. Lett.* 77, 3815 (2001).
13. Y. D. Yao, Y. Y. Chen, M. F. Tai, D. H. Wang, and H. M. Lin, *Mater. Sci. Eng.* A217, 837 (1996).
14. R. H. Kodama, S. A. Makhlof, and A. E. Berkowitz, *Phys. Rev. Lett.* 79, 1393 (1997).
15. R. M. Bozorth, *Ferromagnetism* (Van Nostrand, Princeton, N. J., 1956) Chap. 18, pag. 831.
16. E. C. Stoner and E. P. Wohlfarth, *Trans. Roy. Soc. (London)* A240, 599 (1948).
17. M. E. McHenry, S. A. Majetich, J. O. Artman, M. DeGraef, and S. W. Staley, *Phys. Rev. B* 49, 11358 (1994).

A Small Angle Polarized Neutron Scattering Investigation of Magnetic Correlations in Nanocrystalline $\text{Fe}_{89}\text{Zr}_7\text{B}_3\text{Cu}_1$

Enrico Agosti, Oscar Moze, John Cadogan¹, Kiyonori Suzuki^{1*}, Andre Heinemann² and Armen Hoell²

INFN - S³, Dipartimento di Fisica, Università degli Studi di Modena e Reggio Emilia, Italy.

¹School of Physics, University of New South Wales, Sydney, Australia.

²Berlin Neutron Scattering Centre, Hahn Meitner Institut, Berlin, Germany.

*now at The School of Physics and Materials Engineering, Monash University, Australia

ABSTRACT

The technique of small angle neutron scattering (SANS) is ideally suited for determining the length scale of magnetic correlations in nanocrystalline materials. The additional use of polarized neutrons also allows for a clear separation between magnetic and non-magnetic scattering. The temperature dependence of the SANS cross-section from a two-phase alloy, consisting of both amorphous and nano-crystalline parts, $\text{Fe}_{89}\text{Zr}_7\text{B}_3\text{Cu}_1$, has been measured in the temperature range from 293 to 500 K. The SANS measurements are accompanied by bulk magnetization and Mössbauer transmission data. In this range of temperatures, the magnetic contrast between the nanocrystalline and amorphous phases, which are both magnetic, changes dramatically. This phase contrast increases up to 380 K, which is the proposed decoupling temperature for the inter-granular exchange stiffness. Above this temperature, the contrast levels off slowly, being totally dominated by the decreasing magnetization of the nanocrystalline phase.

INTRODUCTION

Magnetic softness of exceptional quality is known to exist in both structurally amorphous and nanocrystalline systems. Two-phase Fe based nanocrystalline materials which consist of bcc nanocrystallites and a residual amorphous magnetic matrix are also excellent soft magnetic materials. The corresponding anisotropy energy of amorphous systems is based on the Random Anisotropy Model [1], a model which even accounts for the anisotropy in more structured nanocrystalline systems [2]. An extended model proposes a penetration of the Fe exchange field from the nanocrystal phase into the amorphous phase and partially describes the magnetic hardening present in such materials [3]. The dramatic increase with temperature near the Curie point of the amorphous phase has been accounted for in the framework of an extended two-phase Random Anisotropy Model [4]. The coercivity H_c is predicted, in the vicinity of the Curie point of the amorphous phase T_c^{am} , to vary as the -6^{th} power of the spontaneous magnetization of the amorphous phase. Above T_c^{am} , H_c is also very sensitive to the volume of the amorphous phase, V_{am} [5].

Small angle neutron scattering (SANS) allows density and magnetization fluctuations to be investigated on the length scales which occur in nanostructured magnets such as FINEMET [6]. In contrast to conventional SANS, use of polarized neutrons allows for a clear separation of magnetic from nuclear scattering [7]. Reported here is a direct determination of the temperature

dependence of the contrast between the magnetic nanocrystalline and amorphous phases in $\text{Fe}_{89}\text{Zr}_7\text{B}_3\text{Cu}_1$ by use of polarized SANS. The data show clear and unambiguous microscopic evidence, at a nanoscale level, for the magnetic decoupling between the two phases.

EXPERIMENTAL DETAILS

A sample of $\text{Fe}_{89}\text{Zr}_7\text{B}_3\text{Cu}_1$ was prepared in an argon atmosphere by a single roller melt spinner, sealed in evacuated quartz tubes (at a pressure of 10^{-3} Pa) and annealed for one hour at 745 K using a salt bath. The average grain size of the nanocrystalline particles, 12 nm, was determined by X-ray diffraction from the peak width of the bcc-(110) reflection. ^{57}Fe Mössbauer spectra were obtained using a conventional constant-acceleration spectrometer and a ^{57}Co Rh source. Coercivity was measured using a DC B - H loop tracer in the temperature range from 120 to 473 K. The volume fraction of the amorphous phase, approx. 60%, was evaluated from the Mössbauer spectra. Polarized Small Angle Neutron Scattering measurements were performed on the V4 instrument, located at the BENSCH BERII reactor, Hahn Meitner Institut, Berlin, Germany [8].

RESULTS AND DISCUSSION

The temperature dependence of H_c for $\text{Fe}_{89}\text{Zr}_7\text{B}_3\text{Cu}_1$ is displayed in figure 1. A decoupling between the two phases at a temperature of $T_c^{\text{am}} = 380$ K is inferred by assuming that the amorphous exchange interaction is Heisenberg like, with an associated critical exponent, $\beta = 0.36$ for the magnetization. In this context, the extended RMA model predicts that the temperature dependence of H_c varies as $(T_c^{\text{am}} - T)^{-6\beta}$ [4]. This variation of H_c is also displayed in figure 1.

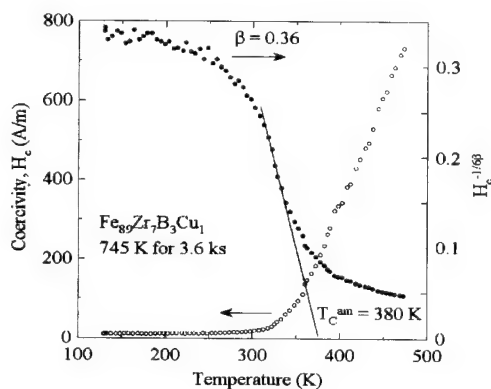


Figure 1. Temperature dependence of the coercivity field H_c for $\text{Fe}_{89}\text{Zr}_7\text{B}_3\text{Cu}_1$

A further estimate of the Curie point of the amorphous phase has been inferred by a least squares fitting analysis of the temperature dependence of the mean hyperfine field B_{hf} for the amorphous phase, obtained from the Mossbauer spectra, using the model of Handrich [9]. This is displayed in figure 2. Even though this method appears to underestimate the Curie point determined by the previous technique, lack of Mossbauer data above 300 K may account for this discrepancy.

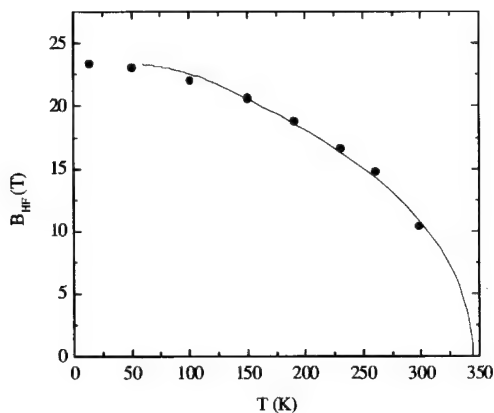


Figure 2. Temperature dependence of the measured mean hyperfine field B_{hf} for the amorphous phase of $\text{Fe}_{89}\text{Zr}_7\text{B}_3\text{Cu}_1$ (•) and the fitted dependence using the Handrich model (—).

In the limit of scattering at small angles, the neutron scattering amplitude for a particles i (nuclear or magnetic) of volume V_i , located at positions r_i , embedded in a homogeneous amorphous matrix is given by equation 1;

$$F(q) = \int dr \Delta\eta_i \exp(iq \cdot r_i) = \Delta\eta_i V_i f(qR) \quad (1)$$

where $\Delta\eta_i = \Delta\eta_{\text{particle}} - \Delta\eta_{\text{matrix}}$ is the amplitude contrast between particle and matrix scattering densities, \vec{q} is the neutron wave-vector transfer and $f(qR)$ is the particle form factor, a function which depends only on the shape of the particle with a nominal size R . For a system with a low fraction of independent scattering particles, the small angle scattering probability $I(q)$, when summed over all scattering centres, is directly proportional to the square of the scattering amplitude, as given by equation 2;

$$I(q) = F(q)^2 \quad (2)$$

The use of polarized neutron in a SANS experiment allows the separate *nuclear* and *magnetic* contributions to the scattering amplitude to be evaluated with more accuracy than by

use of conventional SANS [7]. The q -dependence of the *magnetic* contribution to $I(q)$ at 330 K is displayed below in figure. 3.

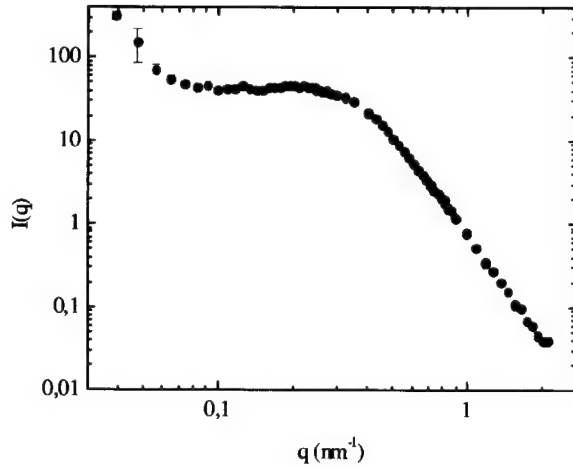


Figure 3. The q -dependence of the magnetic contribution to $I(q)$ for $\text{Fe}_{89}\text{Zr}_7\text{B}_3\text{Cu}_1$ at 330 K.

An extremely relevant aspect of the SANS technique is the relationship between the contrast $\Delta M = M_{\text{am}} - M_{\text{nano}}$ of the magnetic parts of the amorphous and nanocrystal phases and the magnetic scattering probability $I(q)$. This is given by the invariant quantity [10]:

$$c_p c_{\text{am}} V |\Delta M|^2 = 2\pi^2 \int_0^\infty q^2 I(q) dq \quad (3)$$

where c_p and c_{am} are the concentrations of particle and amorphous phases, respectively, for a sample volume V . The temperature dependence of the magnetic contrast has been determined in the range from 290 to 475 K. This is displayed in figure 4, together with the nuclear contrast, which has also been determined using equation (3) via the measured nuclear scattering probability. The error bars associated with the nuclear scattering are larger than their magnetic counterparts as the magnetic scattering is significantly larger than its nuclear counterpart. Use of conventional SANS would, however, preclude such a clear separation between the two types of scattering. As expected, the nuclear contrast displays no temperature dependence, whilst in the same temperature interval, the magnetic contrast increases up to 380 K, which is the proposed decoupling temperature for the inter-granular exchange stiffness. Above this temperature, the contrast levels off slowly as it is totally dominated by the slowly decreasing magnetization of the

nanocrystalline phase, M_{nano} . The behaviour of the magnetic contrast is very clear and unambiguous microscopic evidence for the decoupling.

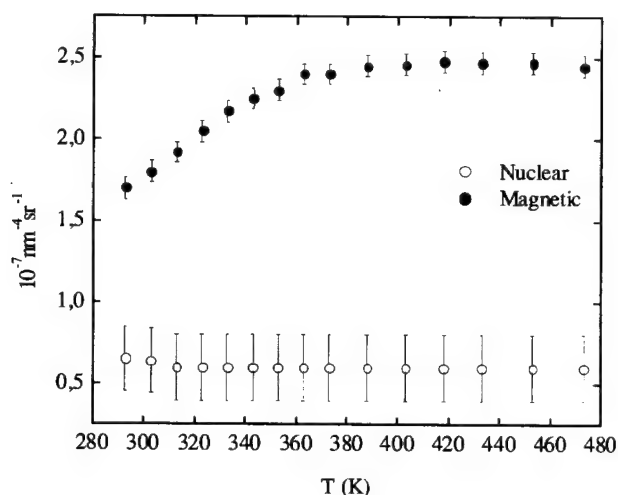


Figure 4. Temperature dependence of the magnetic and nuclear contrasts for $\text{Fe}_{89}\text{Zr}_7\text{B}_3\text{Cu}_1$.

The volume packing fraction of the Fe based nanocrystals, at approximately 40% is rather high in the system under investigation. This introduces significant interference effects between particles, a situation that is difficult to treat analytically [11]. However, SANS measurements are planned on samples with a much lower concentration of nanocrystalline grains in order to characterize in detail the length scale (or correlation length) over which magnetic fluctuations exist. What is clear from the present investigation is that the use of polarized SANS is a sensitive and unique structural probe for characterizing fluctuations in atomic and magnetic density in two-phase nanostructured magnets.

CONCLUSIONS

The technique of small angle neutron scattering (SANS) is ideally suited for determining the length scale of magnetic correlations in nanocrystalline materials. Polarized small angle scattering allows for a clear separation between magnetic and non-magnetic scattering in two-phase nanostructured magnets. The technique has been utilized to investigate the temperature dependence of the microscopic magnetic contrast between amorphous and nano-crystalline parts in $\text{Fe}_{89}\text{Zr}_7\text{B}_3\text{Cu}_1$, in the temperature range from 293 to 500 K. The decoupling temperature for the inter-granular exchange stiffness has been directly observed and compares well with that inferred from indirect bulk measurements.

ACKNOWLEDGMENTS

Research supported by the INFM Research Center – S³ (Nanostructures and Biosystems at Surfaces), University of Modena and Reggio Emilia, Italy and the Australian Research Council. This work was also carried out in the framework of the European Human Capital and Mobility Programme.

REFERENCES

1. R. Alben, J. J. Becker, and M. C. Chi, *J. Appl. Phys.* **49**, 1653 (1978).
2. G. Herzer, *IEEE Trans. Magn.* **25**, 3327 (1989).
3. A. Hernando, M. Vazquez, T. Kulik and C. Prados, *Phys. Rev. B*, **51**, 3581 (1995).
4. K. Suzuki and J. M. Cadogan, *Phys. Rev. B* **58**, 2730 (1998).
5. K. Suzuki and J. M. Cadogan, *J. Magn. Mag. Matls.* **203**, 229 (1999).
6. M. Ohnuma, J. Suzuki, S. Funahashi, T. Ishigaki, H. Kuwano, Y. Hamaguchi, *Materials Transactions, JIM*, **7**, 918 (1995).
7. A. Weidenmann, *J. Appl. Cryst.* **33**, 428 (2000).
8. U. Keiderling and A. Weidenmann, *Physica B* **213-214**, 895 (1995).
9. K. Handrich, *Phys. Stat Solidi* **32**, K55 (1969).
10. A. Guinier and G. Fournét, *Small-Angle Scattering of X-Rays*, Wiley, New York (1955).
11. A. Heinemann, H. Hermann, A. Weidenmann, N. Mattern, K. Wetzig, *J. Appl. Cryst.* **33**, J. Appl. Cryst, **33**, 1386 (2000).

Mössbauer Characterization of Iron Oxide Nanoclusters Grown within Aluminosilicate Matrices

Georgia C. Papaefthymiou¹, A. Bustamante Dominguez² and Rosa B. Scorzelli³

¹Department of Physics, Villanova University, Villanova, PA, USA.

²Facultad de Ciencias Físicas, Universidad Mayor de San Marcos, Lima, Peru.

³Centro Brasileiro de Pesquisas Físicas, Rio de Janeiro, Brasil.

ABSTRACT

Mössbauer spectroscopy uses the resonant absorption of nuclear radiation by ^{57}Fe to probe the electronic and internal magnetic structure of iron based magnetic materials. The technique has a characteristic measuring time of 10 ns enabling investigation of spin relaxation phenomena in nanoscale particles; and determination of their magnetic properties in the absence of externally applied magnetic fields. We report on Mössbauer studies of $\gamma\text{-Fe}_2\text{O}_3$ nanoparticles synthesized within hexagonally packed mesoporous MCM-41 aluminosilicate matrices with cylindrical pores of 2.5 nm diameter. Data analysis allowed differentiation of particle-matrix interfacial versus particle-core interior iron sites. Interfacial iron atoms experience large electric field gradients resulting in quadrupole splitting values of ΔE_q (surface) = (1.25 ± 0.05) mm/s, while core atoms exhibit smaller values of ΔE_q (core) = (0.73 ± 0.05) mm/s at room temperature. Similarly, differences were observed in the values of the internal hyperfine fields at low temperatures indicating reduced strength in the exchange interactions at the particle surface, with interfacial atoms experiencing internal fields H_{hf} (surface) = (458 ± 1) kOe reduced relative to the core H_{hf} (core) = (488 ± 1) kOe at 4.2 K. Particle/matrix interactions at the surface appear to perturb the electronic interactions deeper into the core than the magnetic exchange interactions.

INTRODUCTION

Porous matrices are ideal hosts for the dispersion of nanoclusters. Zeolitic and sol-gel derived molecular sieves and a variety of cross-linked and block co-polymers have been used to this purpose [1-4]. The matrices vary from micro- to meso-porous and from amorphous to highly ordered, affording nanocomposites with a wide range of physical properties. Nanotechnological applications, ranging from catalysis to novel electronic devices and magnetic media, drive the exploration of these advanced materials [5]. We have made use of hexagonally packed MCM-41 aluminosilicate matrices [6] for the production of well-organized nanocluster assemblies of Fe_2O_3 . By packing the nanoclusters within the host matrix the interfacial confinement environment is expected to lead to uniquely tailored morphology and magnetic behavior. In particular, the 1D-cylindrical pore channels of the hexagonally packed aluminosilicate matrices could afford the encapsulation of extremely elongated nanoparticles, leading to the production of magnetic nanorods or nanowires, as one of us and collaborators have previously reported [1]. Herewith, we present fundamental studies on the electronic and magnetic properties of the $\text{Fe}_2\text{O}_3/\text{AlSiO}_2$ nanocomposites based on Mössbauer spectroscopic measurements. Specifically, we address the characterization of the particle/matrix interfacial region and present a more thorough interpretation of Mössbauer results presented in [1]. Particle/matrix interactions impose large stress on the surface perturbing the electronic and magnetic interactions over a

finite shell of atomic lattice planes; they also appear to perturb the electronic interactions over a longer range from the particle surface than the magnetic exchange interactions.

MATERIALS AND METHODS

Mesoporous silica 25% doped with Al (AlSi-25) was synthesized from an inorganic siliceous precursor using organic cationic trimethylammonium surfactants as a supermolecular templating agent. Details of the synthesis and characterization of the resulting MCM-41 aluminosilicate matrix have been presented elsewhere [1]. The matrix had a narrow pore size distribution centered at about 2.5 nm pore diameter for the 1D-channels. Introduction of iron oxide within the pore structure of the matrix was achieved via evaporation/condensation of volatile $\text{Fe}(\text{CO})_5$. TEM bright field images of as prepared and 500 °C calcined $\text{Fe}_2\text{O}_3/\text{AlSi-25}$ nanocomposites indicated the presence of a hexagonally packed array with dark phase contrast inside the pores, corresponding to the iron oxide guest structure (Fig. 1). No particle agglomeration or sintering was observed after calcination in a tube oven under flowing oxygen for 3 hours at 500 °C. X-ray probe iron mapping and STEM images perpendicular to the hexagonally packed arrays (see reference [1]) indicated the presence of both spherical and elongated morphologies for the iron oxide particles.

We have used Mössbauer spectroscopy in order to examine the electronic and magnetic properties of the $\text{Fe}_2\text{O}_3/\text{AlSi-25}$ nanocomposites. Mössbauer spectroscopy [7] uses the resonant absorption of nuclear radiation by the ^{57}Fe -nucleus to probe the electronic and internal magnetic structure of iron based magnetic materials. This is accomplished by the determination of the electronic and magnetic hyperfine parameters at the iron site: isomer shift, δ , quadrupole splitting, ΔE_q , and hyperfine field, H_{hf} . Correlated values of all three Mössbauer parameters can be used for structural phase determination. This is particularly valuable in the study of nanostructures, as crystallites of nanometer size dimensions are not amenable to XRD structural determination, due to line broadening produced by the small particle diameter.

Mössbauer spectroscopy has a fast characteristic measurement time, $\tau_{\text{Möss}} = 10$ ns, which enables examination of dynamic and static magnetic properties of nanostructures over a convenient temperature range. This may be compared to routine macroscopic magnetization studies using Superconducting Quantum Interference Device (SQUID) magnetometers which have longer measurement times, $\tau_{\text{Mag}} = 10$ s to 100 s. Thus, Mössbauer blocking temperatures of

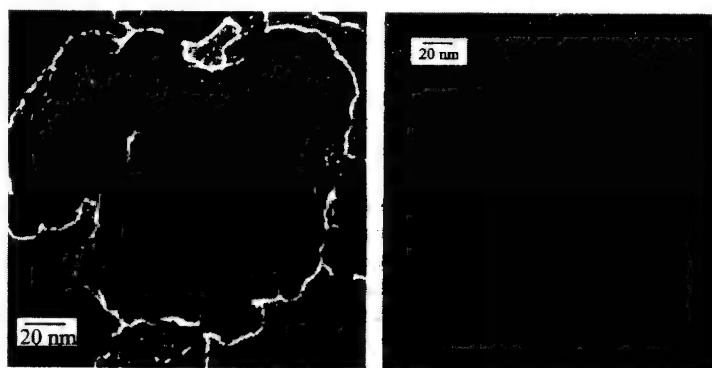


Figure 1. TEM micrographs of $\text{Fe}_2\text{O}_3/\text{AlSi-25}$ nanocomposites: (left) as prepared and (right) calcined at 500 °C.

magnetic nanostructures would be higher than those for SQUID measurements. Another important feature of the technique is that magnetic characterization is achieved in the absence of an externally applied field, obviating the need for zero-field extrapolation of the data.

Due to their extremely small size, nanometer size particles have a large fraction of surface to interior iron atoms. We have assumed a simple idealized core-shell model according to which the core is highly crystalline and uniformly magnetized, while the shell is somewhat amorphous with surface atom coordination severely distorted leading to large ligand-field splittings and iron spins strongly pinned at the surface [8]. Such surface atom coordination distortions would be reflected in ΔE_q and H_{hf} values for atoms at the particle-matrix interface versus those in the interior of the particle [9]. Mössbauer spectra were recorded for $4.2 \text{ K} < T < 300 \text{ K}$ using a continuous flow liquid helium cryostat. The experimental data were computer fitted to theoretical spectra using a non-linear, least-squares curve fitting procedure.

RESULTS AND DISCUSSION

Fitted Mössbauer spectra for the as-prepared sample are shown in Figure 2. The overall temperature profile is characteristic of magnetically ordered iron oxide particles [10] undergoing superparamagnetic relaxation processes due to thermally driven particle moment reversals [11]. The superparamagnetic relaxation time is given by $\tau_s = \tau_0 \exp(KV/kT)$, where T is the temperature, V the volume and K the magnetic anisotropy density of the particle; k is Boltzmann's constant and τ_0 is a temperature independent constant characteristic of the material.

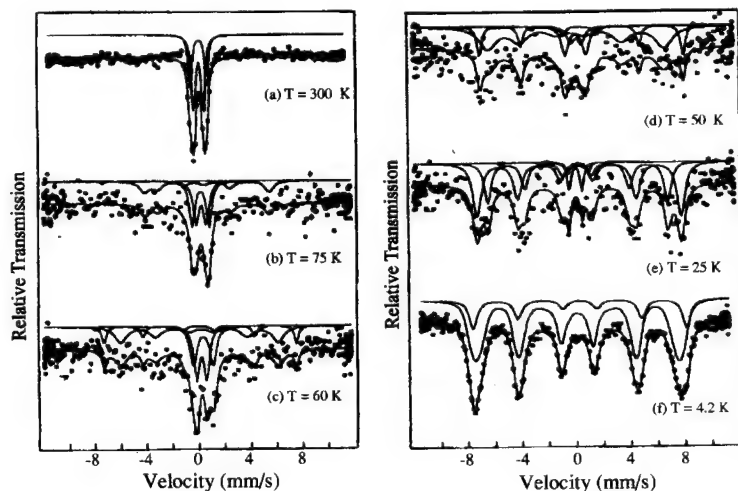


Figure 2. Mössbauer spectra of as-prepared $\text{Fe}_2\text{O}_3/\text{AlSi-25}$ nanocomposites. The solid line is a least-square fit to the experimental points, assuming a superposition of sites depicted by the theoretical spectra shown above the experimental data. The magnetic subcomponents were fitted to a distribution of magnetic hyperfine fields in order to simulate intermediate relaxation effects.

At low temperatures particle-moment reversals are slowed down revealing the internal magnetic order of the particle when $\tau_s > 10$ ns.

At room temperature, broad quadrupole doublets were obtained. The large absorption line-width necessitated fitting to the superposition of two unresolved doublets of similar isomer shift, but different quadrupole splittings (TABLE I). The values of ΔE_q 's reflect the degree of iron coordination distortion away from perfect octahedral or tetrahedral coordination. Thus, larger ΔE_q values were associated with the surface (shell) atoms; smaller ones with interior (core) atoms. The relative absorption intensity of shell vs. core atoms, determined by the ratio of the areas of absorption under the associated curves, gives the relative population of surface to core iron atoms within the assumption of similar recoil free-fractions [7]. Spectral fits at room temperature give A (shell) : A (core) = 40 : 60.

The six line magnetic spectra at low temperatures were also fit within the core-shell model to the superposition of two magnetic subsites with two internal hyperfine magnetic fields associated with core and shell iron atoms, respectively (TABLE I). The sharp discontinuity in the Fe-O-Fe superexchange paths of the magnetic lattice at the surface of the particle leads to a canted surface-spin structure with diminished strength of the magnetic exchange interactions at the surface. The contribution from surface atoms to the magnetic absorption spectral area was suppressed compared to that observed for the paramagnetic spectra at room temperature, resulting in A (shell) : A (core) = 20 : 80 at 4.2 K.

We have previously interpreted this reduction of surface to core ratio [1] as an indication of the presence of a frozen core spin-structure; while, surface spin fluctuations [12] still persisted at 4.2 K. That is, even though spins at the surface are canted relative to the magnetic easy axis of the core due to pinning forces at the surface, the lower magnetic fields observed at the surface could result in spin fluctuations about local easy axes being thermally accessible at lower temperatures than within the core where the observed internal hyperfine fields are 6% stronger. This, however, appears to be in contradiction to strong pinning at the surface. An alternative, and probably most likely interpretation, is that the discontinuity at the surface disturbs the

TABLE I. Mössbauer Parameters for Fe₂O₃/AlSi-25 Nanocomposite

Fe ₂ O ₃ /AlSi-25 Nanocomposite	T (K)	Isomer Shift ^{a,b} δ (mm/sec)		Quadrupole Splitting ^a ΔE_q (mm/sec)		Hyperfine Field ^a H_{hf} (kOe)	
		Surface	Core	Surface	Core	Surface	Core
As-prepared	300	0.33	0.33	1.25	0.73	---	---
	4.2	(0.45)	(0.45)	0	-0.026	458	488
Calcination at 300 °C	300	0.36	0.34	1.24	0.74	---	---
	4.2	(0.48)	(0.46)	0	-0.056	448	477
Calcination at 500 °C	300	0.39	0.35	1.10	0.81	---	---
	4.2	(0.51)	(0.47)	0	-0.132	442	488
Bulk γ -Fe ₂ O ₃ (A+B sites averaged)	298	0.35 ^c		0		496 ^d	

^aUncertainties in δ , ΔE_q and H_{hf} are ± 0.03 mm/sec, ± 0.05 mm/sec and ± 1.0 kOe, respectively.

^bIsomer shift is relative to metallic iron at room temperature; 4.2 K values were fixed at those obtained at room temperature + 0.12 mm/sec second-order Doppler shift. ^cReference [13]. ^dReference [14].

electric field gradients deeper into the core than the strength of the magnetic exchange interactions. Thus, the thickness of the shell derived from the quadrupolar spectra would appear larger than that derived from analysis of the magnetic spectra.

At intermediate temperatures, the spectra are more complex due to intermediate spin relaxation phenomena and the presence of a distribution of particle sizes. The relaxation profiles have been fitted to superpositions of paramagnetic and magnetic subcomponents. Intermediate relaxation processes have been simulated phenomenologically by introducing a distribution of hyperfine field values. The outer absorption magnetic field lines in Fig. 2 are observed to shift inward with increasing temperature, indicating that the average hyperfine fields decrease with increasing temperature. This is an indication that at low temperatures, where spin reversals are suppressed, the particle magnetization may still undergo collective magnetic excitations about its easy axis of magnetization [13].

The Mössbauer parameters of the as-prepared nanocomposite are consistent with maghemite ($\gamma\text{-Fe}_2\text{O}_3$). This phase identification is supported by: (i) the absence (or negligible) quadrupolar perturbation on the magnetic spectra and (ii) the values of the hyperfine fields observed. Hematite ($\alpha\text{-Fe}_2\text{O}_3$) exhibits a large quadrupolar perturbation of 0.12 mm/sec at 300 K and -0.22 mm/sec below the Morin transition [7]; and a saturation hyperfine field $H_{\text{sat}}=544$ kOe. In contrast, $\gamma\text{-Fe}_2\text{O}_3$ has zero quadrupolar perturbation and $H_{\text{sat}} = 527$ kOe. Furthermore, it is well known that $\alpha\text{-Fe}_2\text{O}_3$ is a canted antiferromagnet exhibiting weak bulk magnetization, while the present sample recorded a magnetization value of 57emu/g at 4.2 K in SQUID measurements (see reference [1]) consistent with ferrimagnetic $\gamma\text{-Fe}_2\text{O}_3$.

Furthermore, the phase of the iron oxide appeared to be stable at higher temperatures in transmission electron microscope and Mössbauer studies. Mössbauer parameters obtained for samples calcined for 3 hours in flowing oxygen at 300 and 500 °C are given in Table I. The small changes in parameter values observed appear to be consistent with increased particle crystallinity, due to atomic restructuring upon calcination at high temperatures.

CONCLUSION

Mössbauer spectroscopy affords structural, electronic and micromagnetic characterization of iron based, artificially structured magnetic materials. Spectral fitting procedures within a core/shell model hypothesis for this $\gamma\text{-Fe}_2\text{O}_3/\text{AlSi-25}$ nanocomposite allowed electronic and magnetic characterization of the embedded particle/matrix interfaces. Quadrupole splitting values at the surface increased by 37%, while magnetic field values decreased by 6%, relative to the interior; pointing to severe iron-ion coordination distortion at the surface and large surface stress or strain imposed by the supporting matrix. The core/shell model analysis yielded estimates of the fraction of atoms lying on the surface. Based on electronic measurements 40% of atoms lie on the surface, while internal magnetic field measurements yield a smaller number of only 20%. This is consistent with the hypothesis that the strength of the magnetic exchange interactions are modified to a lesser degree and over a shorter distance from the surface into the core as compared to the electronic interactions.

The observed distortions at the surface are consistent with the existence of large strains at the surface known to result in strong surface contributions to the magnetic anisotropy densities in small magnetic particles as compared to the bulk [15]. Even spherical particles of nanometer dimensions, lacking shape anisotropy, exhibit magnetic anisotropy constants two orders of magnitude larger than the corresponding bulk material [10]. Large distortions of the crystalline

lattice at the surface of the particle, as observed in this nanocomposite, originating from particle/matrix interfacial interactions could account for such effects. The same interactions and geometrical confinement of the particles within the aluminosilicate matrix could account for the increased stability of the particles at high temperatures.

ACKNOWLEDGEMENTS

The authors gratefully acknowledge Prof. J. Y. Ying and Dr. L. Zhang of MIT for the synthesis and TEM characterization of the $\gamma\text{-Fe}_2\text{O}_3/\text{AlSi-25}$ nanocomposites. G.C.P. acknowledges the Centro Brasileiro de Pesquisas Físicas and the NSF: DMR 0074537 for support. Figures 1 and 2 are reprinted with permission from reference [1]. Copyright 2001 American Chemical Society.

REFERENCES

1. L. Zhang, G. C. Papaefthymiou and J. Y. Ying, *J. Phys. Chem. B.*, **105**, 7414 (2001) and references there in.
2. L. Zhang, G. C. Papaefthymiou and J. Y. Ying, *J. Appl. Phys.*, **81**, 6892 (1997); L. Zhang, G. C. Papaefthymiou, R.F. Ziolo and J. Y. Ying, *Nanostr. Mater.* **9**, 185 (1997).
3. B. H. Sohn, R. E. Cohen and G. C. Papaefthymiou, *J. Mag. Mag. Mat.*, **182**, 216 (1998) and references there in.
4. S.R. Ahmed, S.B. Ogal, G.C. Papaefthymiou, R. Ramesh and P.Kofinas, *Appl. Phys. Lett.*, **80**, 1616 (2002)
5. G. C. Hadjipanayis, R. W. Siegel; Eds. *Nanophase Materials: Synthesis-Properties-Applications*; Kluwer: Boston, 1994; H. Gleiter, *Mater. Sci. Forum*, **67**, 189 (1995); C. L. Chien, *Ann. Rev. Mater. Sci.*, **129**, 25 (1995); D. L. Leslie-Pelecky and R.D. Rieke, *Chem. Mater.*, **8**, 1770 (1996); A.S. Edelstein R.C. Camarata, Eds. *Nanomaterials: Synthesis, Properties and Applications*, Institute of Physics Publishing: Bristol (1996)
6. C. T. Kresge, M. E. Leonowicz, W. J. Roth, J. C. Vartuli and J. S. Beck, *Nature*, **359**, 710 (1992).
7. N. N. Greenwood and T. C. Gibb, *Mössbauer Spectroscopy*; Chapman Hall: London, 1971.
8. J. M. D. Coey, *Phys. Rev. Lett.*, **27**, 1140 (1971).
9. G. C. Papaefthymiou, *Mat. Res. Soc. Symp. Proc.* **635** (2001) C2.4.1
10. J. L. Dormann and D. Fiorani; Eds. *Magnetic Properties of Fine Particles*; Elsevier: North-Holland, 1992.
11. L. Néel, *Ann. Geophys. (France)* **5**, 99 (1949); I.S. Jacobs and C.P. Bean, in *Magnetism III*, edited by G.T. Rado and H. Suhl (Academic Press, New York, 1963) p. 271; W.F. Brown Jr. *Phys. Rev.* **130**, 8061 (1963); A. Aharoni, *Phys. Rev. A* **135**, 447 (1964)
12. L.J. de Jongh and A.R. Miedema, *Adv. Phys.*, **1**, 23 (1974).
13. S. Mørup and H. Topsøe, *J. Appl. Phys.*, **11**, 63 (1976).
14. H. V. Kelly, V. J. Folen, M. Hass, W. N. Schreiner and G. B. Beard, *Phys. Rev.*, **122**, 1447 (1961).
15. E.C. Stoner, F.R.S. and E.P. Wohlfarth, *Phil. Trans. Roy. Soc. London*, **A240**, 599 (1948); reprinted in *IEEE Trans. Magn.*, **27**, 3475 (1991)

Half-Integer Spin Molecular Nanomagnets

David N. Hendrickson,^{1*} George Christou,^{2*} Wolfgang Wernsdorfer,³ Stephen O. Hill,⁴
Núria Aliaga-Alcade,² Sumit Bhaduri,² Rachel S. Edwards,⁴ Sheila M. J. Aubin,¹
and Ziming Sun¹

¹Department of Chemistry and Biochemistry-0358, University of California at San Diego, La Jolla, California 92093-0358, U.S.A.

²Department of Chemistry, University of Florida, Gainesville, Florida 32611-7200, U.S.A.

³L. Néel-CNRS, BP 166, 25 Avenue des Martyrs, 38042 Grenoble, Cedex 9, France.

⁴Department of Physics, University of Florida, Gainesville, Florida 32611, U.S.A.

ABSTRACT

Single-molecule magnets (SMM) are molecules that function as single-domain nanomagnets. SMMs have been characterized with a ground-state spin ranging from $S = 4$ to $S = 13$. A few SMMs have been identified that have half-integer spin ground states. [Cation][Mn₁₂O₁₂(O₂CR)₁₆(H₂O)₄] complexes, where R is some substituent, are SMMs that have either a $S = 19/2$ or $21/2$ ground state. Quantum tunneling of magnetization (QTM) is observed for these half-integer-spin Kramers [Mn₁₂]⁻ degenerate SMMs in zero external magnetic field, as well as for a class of $S = 9/2$ Mn₄ SMMs. The presence of QTM in zero external field is attributed to a transverse component of a nuclear spin field, dipolar interactions and intermolecular exchange interactions. The Landau-Zener method is used to measure the tunnel splitting as a function of transverse magnetic field for a single crystal of the $S = 9/2$ SMM [Mn₄O₃(OSiMe₃)(OAc)₃(dbm)₃]. Spin parity dependent QTM is established. The effect of a magnetic exchange interaction between two $S = 9/2$ Mn₄ SMMs upon QTM was studied for another compound. The hydrogen bonding and Cl...Cl contacts within a supramolecularly linked [Mn₄]₂ dimer lead to a weak antiferromagnetic exchange interaction between the two $S = 9/2$ SMMs. This interaction causes a shift (exchange bias) from zero field for the magnetic field at which QTM occurs.

INTRODUCTION

Single-molecule magnets (SMMs) are molecules that function as single-domain magnetic particles which, below their blocking temperature, exhibit the classical macroscale property of a

magnet, namely magnetization hysteresis [1,2]. SMMs owe their properties to a combination of a large ground state spin and an easy-axis-type anisotropy, which give a significant barrier to magnetization relaxation. SMMs thus represent a molecular approach to new nanoscale magnetic materials, offering all the advantages of molecular chemistry (room temperature synthesis, purity, solubility in many solvents, a well defined periphery of organic groups, and a crystalline ensemble of monodisperse units) as well as displaying the superparamagnetism of a mesoscale magnetic particle. They also display quantum tunneling of magnetization (QTM), indicating that they straddle the interface between the classical and quantum regimes [3,4]. SMMs have many potential applications, but these require that their properties be both understood and controlled, particularly QTM. The Mn_{12} SMMs have been the most thoroughly studied of the molecular nanomagnets [5,6]. Various derivatives have been prepared differing in the organic groups [7], and it has been discovered that the magnetic properties (including QTM) can be significantly altered. This is also possible by adding additional electrons, and both the $[\text{Mn}_{12}]^+$ ($S = 19/2$ or $21/2$) [8-13] and $[\text{Mn}_{12}]^{2-}$ ($S = 10$) [14,15] versions have been prepared [8-11]. Mn_4 SMMs with $S = 9/2$ have also been extensively studied [16-18].

EXPERIMENTAL DETAILS

Crystalline samples of the $[\text{Cation}][\text{Mn}_{12}\text{O}_{12}(\text{O}_2\text{CR})_{16}(\text{H}_2\text{O})_4]$ [8] ($R = \text{substituent}$), $[\text{Mn}_4\text{O}_3(\text{OSiMe}_3)(\text{OAc})_3(\text{dbm})_3]$ [19] and $[\text{Mn}_4\text{O}_3\text{Cl}_4(\text{O}_2\text{Cet})_3(\text{py})_3]$ [20] were prepared as reported previously. Magnetization measurements on one salt of the $[\text{Mn}_{12}]^+$ SMM were carried out on a few crystals oriented by means of a 5 T field and restrained in eicosane. A Quantum Design SQUID magnetometer was used. All magnetization measurements for the two Mn_4 SMMs were carried out on a single crystal using an array of micro-superconducting quantum interference devices (micro-SQUIDs) [21]. The high sensitivity allows one to study single crystals of SMMs on the order of 10-500 μm . The field can be applied in any direction by separately driving three orthogonal coils. Single crystal high-frequency electron paramagnetic resonance (HFEPRE) experiments were carried out using a cavity perturbation method, enabling high sensitivity measurements in the range from 20 to 200 GHz; the details of this technique are described elsewhere [22].

DISCUSSION

Kramers theorem [23] states that no matter how unsymmetric the crystal field is, a molecule possessing an odd number of electrons must have a ground state that is at least doubly degenerate, even in the presence of crystal fields and spin-orbit interactions. A magnetic field is needed to break the symmetry of a half-integer spin SMM and lead to tunneling. There have been several papers [24,25] addressing the fact that a molecule with a half-integer spin (such as $S = 19/2$) should not exhibit resonant magnetization tunneling in the absence of a magnetic field. For such a molecule, each pair of $\pm m_S$ levels in zero-field exhibits Kramers degeneracy. An $S = 19/2$ molecule should not be able to tunnel coherently between the $m_S = -19/2$ and $m_S = 19/2$ levels, or for that matter, between any m_S and $-m_S$ pair in the absence of a magnetic field.

$[\text{Mn}_{12}]^+$ single-molecule magnets

A few different half-integer SMMs with the composition [Cation][Mn₁₂O₁₂(O₂CR)₁₆(H₂O)₄] have been reported [8-13]. The [Mn₁₂]⁺ SMMs have either a $S = 19/2$ or a $S = 21/2$ ground state with axial zero-field splitting ($\hat{D}\hat{S}_z^2$) where $D = -0.4$ to -0.6 cm⁻¹. The single-crystal X-ray structure of [PPh₄][Mn₁₂O₁₂(O₂CEt)₁₆(H₂O)₄] (complex 1) has been reported [8]. Five small crystals (3 mm × 0.1 mm × 0.1 mm) of this $S =$

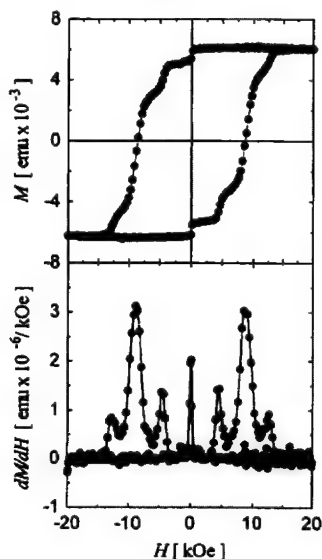


Figure 1. The top plot shows the magnetization hysteresis loop measured at 1.85 K for five crystals of [PPh₄][Mn₁₂O₁₂(O₂CEt)₁₆(H₂O)₄] oriented in an eicosane wax matrix. In the lower plot is shown the first derivative of the magnetization hysteresis loop.

19/2 complex were suspended in eicosane held at 40°C and the suspension introduced into a 5.5 T field, whereupon the five crystals were oriented with their easy axes parallel to the field. The eicosane was cooled to give a wax cube with the five crystals oriented with parallel easy axes. The magnetization versus external magnetic field data exhibit a hysteresis as shown in figure 1.

The sample of complex 1 was first saturated in a field of +2.0 T, and the field was then swept down to -2.0 T and cycled back to +2.0 T. Steps can clearly be seen on the hysteresis loop due to resonant QTM. As the field is decreased, the first step is seen at zero external field. Resonant tunneling occurs because the $-m_s$ levels on the right-hand side of the double well for magnetization reversal have the same energies as the $+m_s$ levels on the left. The most interesting feature on the hysteresis loop is the step seen at zero field. Since complex 1 has a $S =$

19/2 half-integer spin ground state, it should not be able to tunnel in zero magnetic field. Apparently, the explanation [9] for this step at zero field lies in the fact that several nuclei, particularly the ^{55}Mn with $I = 5/2$, have a nuclear spin. These nuclear spins give rise to a small internal magnetic field inside the molecule. A transverse component of this internal nuclear spin field leads to resonant QTM in zero external field. The suggestion that a nuclear spin field could play this important role was verified [26] by changing iron isotopes in the Fe8 SMM.

The effect of the cation on the properties of $[\text{Mn}_{12}]^-$ SMMs has been probed. An early suggestion [10] that a paramagnetic ($S = 1/2$) cation greatly increased the rate of QTM is apparently incorrect. More detailed studies [12,13] have shown that changing the cation from a diamagnetic one to a paramagnetic one while maintaining the same solid state structure does *not* affect the rate of QTM in the $[\text{Mn}_{12}]^-$ SMM.

[Mn₄] single-molecule magnets

There is a growing family of $S = 9/2$ SMMs that have the trigonal pyramidal $[\text{Mn}^{\text{IV}}\text{Mn}^{\text{III}}_3\text{O}_3\text{X}]^{6+}$ core where the X^- ligand is variously Cl^- , Br^- , N_3^- , OH^- , MeO^- , or Me_3SiO^- . There are several reasons why these Mn₄ complexes are particularly attractive for study as SMMs. Transverse interactions are such that both thermally activated and temperature-independent ground state (*i.e.*, $m_S = -9/2$ to $m_S = 9/2$) QTM can be observed for these $S = 9/2$

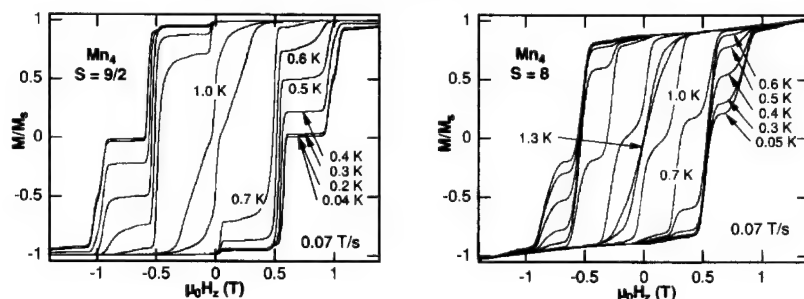


Figure 2. Magnetization hysteresis loops for a single crystal of (left plot) $[\text{Mn}_4\text{O}_3(\text{OSiMe}_3)(\text{OAc})_3(\text{dbm})_3]$ ($S = 9/2$, complex 2) and (right plot) $[\text{Mn}_4(\text{OAc})_2(\text{pdmH})_6](\text{ClO}_4)_2$ (complex 3) at different temperatures and a constant field sweep rate $dH_z/dt = 0.07$ T/s.

SMMs [12,13]. The $S = 9/2$ Mn₄ SMMs have served well to demonstrate for the first time two important phenomena: (1) the spin parity effect for a half-integer SMM; and (2) how magnetic exchange interactions between two SMMs in a crystal can dramatically affect the magnetic field at which resonant QTM occurs.

The spin parity effect was demonstrated [27] for the $S = 9/2$ SMM $[\text{Mn}_4\text{O}_3(\text{OSiMe}_3)(\text{OAc})_3(\text{dbm})_3]$ (complex 2) by measuring the tunneling splitting $\Delta_{m,m'}$ as a function of transverse magnetic field. The results for this $S = 9/2$ SMM were compared to those for two integer spin SMMs, $[\text{Mn}_4(\text{OAc})_2(\text{pdmH})_6](\text{ClO}_4)_2$ (complex 3) with $S = 8$ and the well

known Fe₈ SMM with $S = 10$. Figure 2 shows the magnetization hysteresis loops for single crystals of (left plot) $S = 9/2$ Mn₄ SMM complex 2 and (right plot) $S = 8$ Mn₄ SMM complex 3. Steps are observed on the hysteresis loops corresponding to resonant QTM. Thus, when the external field is adjusted so that the levels on the left and right side of the potential energy barrier are at equal energy, tunneling occurs and the rate of change of the magnetization increases to give a step. The tunnel splitting for a half-integer SMM is expected to be very sensitive to a transverse magnetic field: a small field will cause the tunnel splitting for a half-integer SMM to change dramatically from zero. On the other hand, the tunnel splitting of an integer spin SMM is expected to change much more gradually in response to a transverse field. The Landau-Zener model [28,29] describes the nonadiabatic transition between two states in a two-level system. When sweeping the longitudinal field H_z at a constant rate over an avoided energy-level crossing, the tunneling probability P is given in eqn. (1):

$$P_{m,m'} = 1 - \exp \left[\frac{-\pi \Delta_{m,m'}^2}{2\hbar g\mu_B |m-m'| \mu_0 (dH_z/dt)} \right] \quad (1)$$

, where m and m' are the quantum numbers of the avoided level crossing, dH_z/dt is the constant field sweep rate and \hbar is Planck's constant.

In figure 3 are given the plots of tunnel splitting versus magnitude of transverse magnetic field obtained for single crystals of complexes 2 ($S = 9/2$), 3 ($S = 8$) and the Fe₈ SMM ($S = 10$). It is clear that the response of the tunnel splitting with increasing transverse field is much more abrupt for the $S = 9/2$ complex than for the other two complexes. This is clear evidence for the spin parity effect. In the ideal case, $\Delta = 0$ would be expected for $H = 0$ in the case of this $S = 9/2$ SMM, however this is not found because of the influence of environmental degrees of freedom that can induce tunneling. For example, the Mn atoms have a nuclear spin of $I = 5/2$ and this leads to a small transverse magnetic field that is one form of an "environmental" effect.

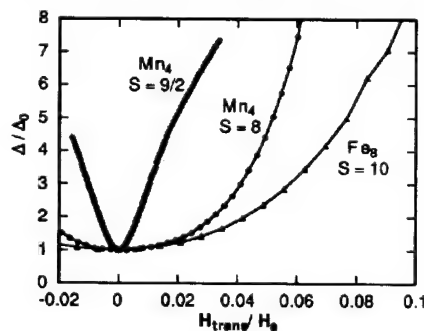


Figure 3. Tunnel splitting for three SMMs as a function of transverse field.

The tunnel splitting is normalized by $\Delta_0 = 1.9, 0.94$ and 0.28×10^7

K, and the transverse field is normalized by the anisotropy field $H_a = 2DS/g\mu_B = 4.6, 5.1$ and 4.0 T for complexes 2, 3 and the Fe₈ SMM, respectively.

Magnetic exchange-biased QTM can be demonstrated [30] for the $S = 9/2$ SMM complex 4, $[\text{Mn}_4\text{O}_3\text{Cl}_4(\text{O}_2\text{CEt})_3(\text{py})_3]$. In the crystal there is, in fact, a dimer formed by two of these $S = 9/2$ Mn_4 complexes. Six $\text{C-H}\cdots\text{Cl}$ hydrogen bonding contacts and one $\text{Cl}\cdots\text{Cl}$ contact support a weak antiferromagnetic exchange interaction ($J = -0.05$ K for $\hat{H} = -2K\hat{S}_1\cdot\hat{S}_2$) between the two $S = 9/2$ moieties in the $[\text{Mn}_4]_2$ dimer. As shown in figure 4, this weak intradimer exchange interaction leads to a profound change on the magnetic field at which QTM occurs. The first step for the $[\text{Mn}_4]_2$ dimer is seen at -0.33 T after saturation in a field of -1.2 T. Thus, the first step does not occur at zero field, but at -0.33 T; there is an exchange bias. When one $S = 9/2$ unit in the $[\text{Mn}_4]_2$ dimer tunnels from $m_S = -9/2$ to $m_S = 9/2$, the field at which this occurs is shifted from zero to -0.33 T. The field dependencies of all of the energy levels of the $[\text{Mn}_4]_2$ dimer can be calculated by diagonalizing the Hamiltonian matrix for the $[\text{Mn}_4]_2$ dimer. This explains not only the -0.33 T shift of the first step, but the several

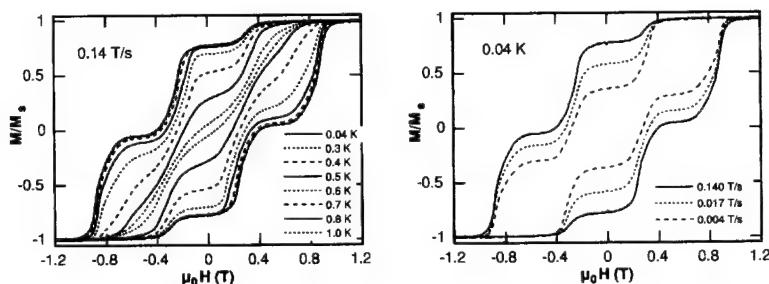


Figure 4. Magnetization (M) of $[\text{Mn}_4]_2$ (plotted as fraction of maximum value M_S) versus applied magnetic field ($\mu_0 H$). The resulting hysteresis loops are shown at different temperatures (left plot) and different field sweep rates (right plot). It is noted that the loops become temperature-independent below about 0.3 K, but are still sweep-rate-dependent owing to resonant QTM between discrete energy levels of the $[\text{Mn}_4]_2$ dimer.

other step features seen for this complex.

High-frequency EPR spectra obtained for the $[\text{Mn}_4]_2$ dimeric complex definitively confirm the above model for exchange biasing of QTM. The effective spin Hamiltonian for an isolated $S = 9/2$ SMM can be written as in eqn. (2):

$$\hat{H}_i = D\hat{S}_z^2 + (E\hat{S}_x^2 - \hat{S}_y^2) + g\mu_B\hat{B} \cdot \hat{S}_i + \hat{O}_4 + \hat{H}'_i \quad (2)$$

The first two terms represent the axial and rhombic zero-field interactions, respectively and the third term is the Zeeman interaction. The fourth term gauges fourth order zero-field interactions, whereas the last term \hat{H}'_i describes additional perturbations attributed to disorder, intermolecular

dipolar and exchange interactions. For the $[\text{Mn}_4]_2$ dimer the magnetic exchange interaction $-2J\hat{S}_1 \cdot \hat{S}_2$ couples two $S = 9/2$ units, each with their own Hamiltonian operators \hat{H}_1 and \hat{H}_2 to give for the dimer eqn. (3):

$$\hat{H} = \hat{H}_1 + \hat{H}_2 - 2J\hat{S}_1 \cdot \hat{S}_2 \quad (3)$$

where \hat{H}_1 and \hat{H}_2 are given by eqn. (2). For the $S = 9/2$ Mn_4 unit there are $(2S+1)$ energy levels; for the $[\text{Mn}_4]_2$ dimer there are $(2S+1) \times (2S+1)$ levels. Antiferromagnetic coupling in the $[\text{Mn}_4]_2$ dimer gives a $S_{\text{total}} = 0$ ground state that is degenerate: $(9/2, -9/2)$ and $(-9/2, 9/2)$ where (m_{S1}, m_{S2}) specifies the spin state level for the two SMMs in the $[\text{Mn}_4]_2$ dimer. The energies of the low lying states of the dimer are shown in figure 5 as a function of an external field. It can be seen that when a field is applied parallel to the z axis (easy axis) it can be increased to a value such that there is a crossing of the degenerate $(-9/2, 9/2)$ $(9/2, -9/2)$ levels and the $(-9/2, -9/2)$ level, thereby changing the ground state. Due to the exchange bias, the transition for one Mn_4 unit depends on the state of the other Mn_4 unit. Thus, the lowest-energy

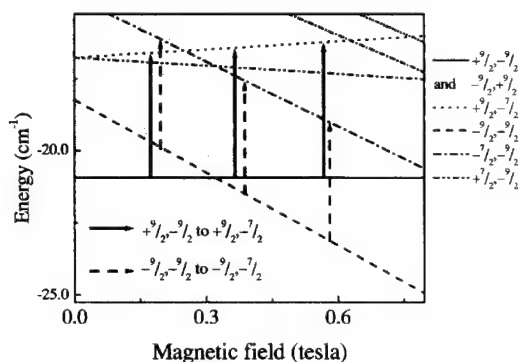


Figure 5. The low lying two-spin energy levels for the $[\text{Mn}_4]_2$ dimer plotted as a function of magnetic field. The most important levels have been labeled according to the scheme described in the text. The calculations of these levels ignored the transverse terms in eqns. (2) and (3).

transitions from the two ground states, *i.e.*, $(9/2, -9/2)$ to $(9/2, -7/2)$ and $(-9/2, -9/2)$ to $(-9/2, -7/2)$, have slightly different energies even though they both correspond to the same $-9/2$ to $-7/2$ transition for one Mn_4 unit.

Since many different frequencies can be employed in the HFEPR experiment, one can tune the ground state transition to the field region where the ground state level crossing occurs in figure 5. As can be seen in figure 6, a pronounced splitting is seen in the lowest-field resonance.

The splitting is due to the different energies of the respective $(9/2, -9/2)$ to $(9/2, -7/2)$ and $(-9/2, -9/2)$ to $(-9/2, -7/2)$ ground state transitions. As will be described in detail in a later publication [31], by following this exchange-bias split resonance through the exchange bias field region (~ 0.3 T), it is clear in figure 6 that the intensity smoothly transfers from one transition to the

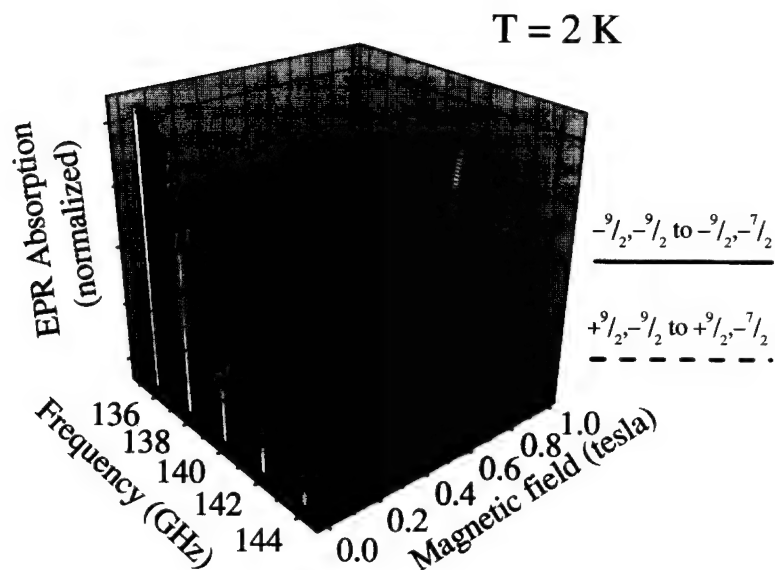


Figure 6. A 3D plot of the ground state transitions for the $[\text{Mn}_4]_2$ dimer over a narrow field and frequency range. A pronounced splitting is apparent, which is due to the different frequencies of the respective $(9/2, -9/2)$ to $(9/2, -7/2)$ and $(-9/2, -9/2)$ to $(-9/2, -7/2)$ ground state transitions.

other. This clearly establishes a change in the $[\text{Mn}_4]_2$ ground state at ~ 0.3 T. The exchange bias model is substantiated.

A very recent paper [32] has shown that the one-molecule tunnel picture of SMMs is not always sufficient to explain the tunnel transitions observed on magnetization hysteresis loops. Dipolar and weak superexchange interactions between molecules lead to two-molecule tunnel transitions such due to spin-spin cross relaxations.

CONCLUSIONS

Half-integer ground state single-molecule magnets, such as $[\text{Mn}_{12}]^+$ with $S = 19/2$ or $21/2$ and Mn_4 with $S = 9/2$, exhibit resonant quantum tunneling of magnetization in zero external magnetic field. The tunneling in these Kramers degenerate systems in zero external field is due to the presence of nuclear spins that create an internal magnetic field. A micro-SQUID array was used to demonstrate the presence of the spin parity effects for one $S = 9/2$ Mn_4 SMM. The tunnel splitting of this complex responds abruptly to the introduction of a transverse magnetic field, in contrast to the behavior seen for integer spin SMMs. A weak antiferromagnetic interaction between two $S = 9/2$ Mn_4 SMMs in a crystal is shown to bias the magnetic field at which QTM occurs for each $S = 9/2$ Mn_4 unit in the dimer.

ACKNOWLEDGMENTS

The authors thank the NSF for funding.

REFERENCES

1. G. Christou, D. Gatteschi, D. N. Hendrickson, and R. Sessoli, *MRS Bulletin* **25**, 66 (2000).
2. R. Sessoli, H.-L. Tsai, A. R. Schake, S. Wang, J. B. Vincent, K. Folting, D. Gatteschi, G. Christou, and D. N. Hendrickson, *J. Am. Chem. Soc.* **115**, 1804 (1993).
3. J. R. Friedman, M. P. Sarachik, J. Tejada, and R. Ziolo, *Phys. Rev. Lett.* **76**, 3830 (1996).
4. L. Thomas, F. Lioni, R. Ballou, D. Gatteschi, R. Sessoli, and B. Barbara, *Nature* **383**, 145 (1996).
5. M. Soler, P. Artus, K. Folting, J. C. Huffman, D. N. Hendrickson and G. Christou, *Inorg. Chem.* **40**, 4902 (2001).
6. D. N. Hendrickson, G. Christou, H. Ishimoto, J. Yoo, E. K. Brechin, A. Yamaguchi, E. M. Rumberger, S. M. J. Aubin, Z. Sun and G. Aromi, *Polyhedron* **20**, 1479 (2001).
7. S. M. J. Aubin, Z. Sun, H. J. Eppley, E. M. Rumberger, I. A. Guzei, K. Folting, P. K. Gantzel, A. L. Rheingold, G. Christou and D. N. Hendrickson, *Inorg. Chem.* **40**, 2127 (2001).
8. H. J. Eppley, H.-L. Tsai, N. de Vries, K. Folting, G. Christou and D. N. Hendrickson, *J. Am. Chem. Soc.* **117**, 301 (1995).
9. S. M. J. Aubin, S. Spagna, H. J. Eppley, R. E. Sager, G. Christou and D. N. Hendrickson, *J. Chem. Soc., Chem. Commun.* 803 (1998).
10. K. Takeda and K. Awaga, *Phys. Rev. B* **56**, 14560 (1997).
11. S. M. J. Aubin, Z. Sun, L. Pardi, J. Krzystek, K. Folting, L.-C. Brunel, A. L. Rheingold, G. Christou and D. N. Hendrickson, *Inorg. Chem.* **38**, 5329 (1999).
12. T. Kuroda-Sowa, M. Lam, A. L. Rheingold, C. Frommen, W. M. Reiff, M. Nakano, J. Yoo, A. L. Maniero, L.-C. Brunel, G. Christou and D. N. Hendrickson, *Inorg. Chem.* **40**, 6469 (2001).
13. T. Kuroda-Sowa, M. Nakano, G. Christou and D. N. Hendrickson, *Polyhedron* **20**, 1529 (2001).
14. M. Soler, S. K. Chandra, D. Ruiz, J. C. Huffman, D. N. Hendrickson and G. Christou, *Polyhedron* **20**, 1279 (2001).
15. W. Wernsdorfer, M. Soler, G. Christou and D. N. Hendrickson, *J. Appl. Phys.* **91**, 7146 (2002).

16. S. M. J. Aubin, M. W. Wemple, D. M. Adams, H.-L. Tsai, G. Christou, and D. N. Hendrickson, *J. Am. Chem. Soc.* **118**, 7746 (1996).
17. S. M. J. Aubin, N. R. Dilley, M. W. Wemple, M. B. Maple, G. Christou and D. N. Hendrickson, *J. Am. Chem. Soc.* **120**, 839 (1998).
18. S. M. J. Aubin, N. R. Dilley, L. Pardi, J. Krzystek, M. W. Wemple, L.-C. Brunel, M. B. Maple, G. Christou and D. N. Hendrickson, *J. Am. Chem. Soc.* **120**, 4991 (1998).
19. S. Bhaduri, M. Pink, K. Folting, W. Wernsdorfer, A. Sieber, H. U. Güdel, D. N. Hendrickson, and G. Christou, manuscript in preparation.
20. D. N. Hendrickson, G. Christou, E. A. Schmitt, E. Libby, J. S. Bashkin, S. Wang, H.-L. Tsai, J. B. Vincent, P. D. W. Boyd, J. C. Huffman, K. Folting, Q. Li and W. E. Streib, *J. Am. Chem. Soc.* **114**, 2455 (1992).
21. W. Wernsdorfer, T. Ohm, C. Sangregorio, R. Sessoli, D. Mailly and C. Paulsen, *Phys. Rev. Lett.* **82**, 3903 (1999).
22. M. Mola, S. O. Hill, P. Goy and M. Gross, *Rev. Sci. Instr.* **71**, 186 (2000).
23. H. A. Kramers, *Proc. R. Acad. Sci. Amsterdam* **33**, 959 (1930).
24. D. Loss, D. P. Di Vincenzo, G. Grinstein, D. Awschalom and J. F. Smyth, *Physica B* **189**, 189 (1993).
25. D. P. Di Vincenzo, *Physica B* **197**, 109 (1994).
26. W. Wernsdorfer, A. Caneschi, R. Sessoli, D. Gatteschi, A. Corina, V. Villar and C. Paulsen, *Phys. Rev. Lett.* **84**, 2965 (2000).
27. W. Wernsdorfer, S. Bhaduri, C. Boskovic, G. Christou and D. N. Hendrickson, *Phys. Rev. B* **65**, 180403 (2002).
28. L. Landau, *Phys. Z. Sowjetunion* **2**, 46 (1932).
29. C. Zener, *Proc. R. Soc. London, Ser. A* **137**, 696 (1932).
30. W. Wernsdorfer, N. Aliaga-Alcalde, D. N. Hendrickson and G. Christou, *Nature (London)* **416**, 406 (2002).
31. R. S. Edwards, S. Hill, S. Bhaduri, N. Aliaga-Alcalde, E. Bolin, S. Maccagnano, G. Christou and D. N. Hendrickson, in preparation.
32. W. Wernsdorfer, S. Bhaduri, R. Tiron, D. N. Hendrickson and G. Christou, *Phys. Rev. Lett.* **89**, 197201-1 (2002).

Defects, Tunneling, and EPR Spectra of Single-Molecule Magnets

Kyungwha Park^{1,2,3}, M. A. Novotny⁴, N. S. Dalal³, S. Hill⁵, P. A. Rikvold^{1,6}, S. Bhaduri⁷, G. Christou⁷, and D. N. Hendrickson⁸

¹School of Computational Science and Information Technology, Florida State University, Tallahassee, Florida 32306

²Department of Chemistry and Biochemistry, Florida State University, Tallahassee, Florida 32306

³Center for Computational Materials Science, Code 6390, Naval Research Laboratory, Washington DC 20375

⁴Department of Physics and Astronomy and the Engineering Research Center, Mississippi State University, Mississippi State, Mississippi 39762

⁵Department of Physics, University of Florida, Gainesville, Florida 32611

⁶Center for Materials Research and Technology and Department of Physics, Florida State University, Tallahassee, Florida 32306

⁷Department of Chemistry, University of Florida, Gainesville, Florida 32611

⁸Department of Chemistry and Biochemistry, University of California at San Diego, La Jolla, California 92093

ABSTRACT

We examine theoretically electron paramagnetic resonance (EPR) lineshapes as functions of resonance frequency, energy level, and temperature for single crystals of three different kinds of single-molecule nanomagnets (SMMs): Mn_{12} acetate, Fe_8Br , and the $S = 9/2$ Mn_4 compound. We use a density-matrix equation and consider distributions in the uniaxial (second-order) anisotropy parameter D and the g factor, caused by possible defects in the samples. Additionally, weak intermolecular exchange and electronic dipole interactions are included in a mean-field approximation. Our calculated linewidths are in good agreement with experiments. We find that the distribution in D is common to the three examined single-molecule magnets. This could provide a basis for a proposed tunneling mechanism due to lattice defects or imperfections. We also find that weak intermolecular exchange and dipolar interactions are mainly responsible for the temperature dependence of the lineshapes for all three SMMs, and that the intermolecular exchange interaction is more significant for Mn_4 than for the other two SMMs. This finding is consistent with earlier experiments and suggests the role of spin-spin relaxation processes in the mechanism of magnetization tunneling.

INTRODUCTION

Single-molecule magnets (SMMs) have recently been the focus of much attention because of the possibility of macroscopic quantum tunneling of their magnetizations [1, 2] and possible applications in magnetic storage devices and quantum computers

[3]. SMMs are composed of identical single-domain nanoscale molecules, comprised of a core of several transition-metal ions surrounded by many different species of atoms, and they have a large effective spin. The characteristics of SMMs are relatively weak exchange and dipolar interactions between molecules, a large zero-field energy barrier against magnetization reversal, and magnetization steps in their hysteresis loops, which indicate quantum tunneling despite the large spin values [4, 5, 6, 7, 8].

In this paper, we examine three different molecular magnets, which are briefly described in the following. The most extensively studied single-molecule magnet is $[\text{Mn}_{12}\text{O}_{12}(\text{CH}_3\text{COO})_{16}(\text{H}_2\text{O}_4)] \cdot 2\text{CH}_3\text{COOH} \cdot 4\text{H}_2\text{O}$ (abbreviated hereafter as Mn_{12}), which was first synthesized by Lis [9]. Each molecule in Mn_{12} has an effective spin of $S = 10$. It is a uniaxial system with a zero-field energy barrier against magnetization reversal of 65 K [5, 6, 7]. Another well-studied magnet is $[\text{Fe}_8\text{O}_2(\text{OH})_{12}(\text{tacn})_6]\text{Br}_8 \cdot 9\text{H}_2\text{O}$ (abbreviated as Fe_8) [10]. Each molecule in Fe_8 also has a spin of $S = 10$ with a magnetization-reversal barrier of 30 K [11, 12]. This is a biaxial system so exhibits oscillations in tunneling rates with transverse magnetic field [13]. Recently synthesized is $[\text{Mn}_4\text{O}_3(\text{OSiMe})_3(\text{O}_2\text{Cet})_3(\text{dbm})_3]$ (abbreviated as Mn_4). Each molecule in Mn_4 consists of two kinds of Mn ions with mixed valence: three Mn^{3+} ($S = 2$) and one Mn^{4+} ($S = 3/2$) are located in a distorted cubane structure and antiferromagnetically coupled to give a ground-state spin of $S = 9/2$. The approximate magnetization-reversal energy barrier is 13 K in zero field [14]. All three of these SMMs show clear magnetization steps in hysteresis loops below their blocking temperatures.

Recently, electron paramagnetic resonance (EPR) experiments [12, 14, 15, 16] on single crystals of these SMMs showed interesting results for the lineshapes as a function of EPR resonance frequency, energy levels involved in the EPR transitions, and temperature. The temperatures employed are in the 2–50 K range, and the frequencies are in the 40–190 GHz range. We focus on the case when the magnetic field is applied along the easy axis at fixed frequency. In this case, the measured linewidths are much broader than the homogeneous line broadening caused by the lifetimes of the energy levels, and the linewidths increase as lower energy levels are involved with the EPR transitions. Additionally, some interesting features have been observed in the temperature dependence of the linewidths and lineshapes of the EPR spectra [6, 12, 14, 15, 16]. These temperature dependences were different for different molecular magnets. In this paper, we summarize our theoretical understanding of the linewidths' dependence on frequency, energy level, and temperature for the three molecular magnets, Mn_{12} , Fe_8 , and Mn_4 . We also provide quantitative comparison of our calculated results with experimental data. The theoretical results on Mn_4 are preliminary and work on this system is still in progress.

MODEL

We start with a single-spin effective Hamiltonian considering embedded symmetry in each molecule and calculate the resonance linewidths using a density-matrix equation [17]. We find that an entirely single-spin picture cannot explain even qualitative trends in

the experimental data. Thus, it is inevitable to include many-body effects. As a simple start, we assume that the second-order uniaxial anisotropy parameter, D , and the g factor may not be the same for all molecules. The microscopic origin of the distribution in D has not yet been fully understood [18, 19]. In addition, each molecule may interact with the rest of the molecules through exchange and/or dipolar interactions. Details of the model and the technique are discussed in Refs. [15, 20, 21, 22]. This section is based in part on our earlier work [15, 20].

Since each molecule in Mn_{12} has approximate S_4 symmetry, the dominant single-spin Hamiltonian reads, with applied magnetic field along the easy magnetization axis (z axis),

$$\mathcal{H}_0 = -DS_z^2 - CS_z^4 - g\mu_B HS_z, \quad (1)$$

where $D = 0.55$ K, $C = 1.17 \times 10^{-3}$ K, and $g = 1.94$ [5]. The SMM Fe_8 has approximate D_2 symmetry, so the Hamiltonian reads

$$\mathcal{H}_0 = -DS_z^2 - E(S_x^2 - S_y^2) - g\mu_B HS_z, \quad (2)$$

where $D = 0.288$ K, $E = 0.043$ K, and $g = 2.0$ [12]. In our calculations for Fe_8 , we neglect the small E term because we are interested in the case with the applied field along the easy axis. The SMM Mn_4 has C_3 symmetry, so the Hamiltonian reads

$$\mathcal{H}_0 = -DS_z^2 - CS_z^4 - g\mu_B HS_z, \quad (3)$$

where $D = 0.632$ K, $C = 3.12 \times 10^{-3}$ K, and $g = 2.0$ [14].

We now introduce an interaction $V(t)$ between the spin system and an oscillating transverse magnetic field H_x with angular frequency $\omega \equiv 2\pi\nu$. The interaction of the spin system with the environment is governed by a time dependent density-matrix equation [17, 23]. The power absorption between the energy levels M_s and $M_s - 1$ from the oscillating field, up to first order in V_0 and near resonance (with a fixed value of D), is written as

$$\frac{d\mathcal{E}}{dt} = \frac{(\mathcal{E}_{M_s-1} - \mathcal{E}_{M_s})}{\hbar^2} |\langle M_s | V_0 | M_s - 1 \rangle|^2 \Delta(H) (\rho_{M_s} - \rho_{M_s-1}), \quad (4)$$

$$\Delta(H) \equiv \frac{\hbar^2 \gamma_{M_s-1, M_s}}{(g\mu_B)^2 (H - H_{\text{res}})^2 + (\hbar \gamma_{M_s-1, M_s})^2}, \quad (5)$$

$$H_{\text{res}} \equiv \frac{\hbar\omega - D(2M_s - 1) - C(4M_s^3 - 6M_s^2 + 4M_s - 1)}{g\mu_B}, \quad (6)$$

where V_0 is the strength of the interaction $V(t)$, \mathcal{E}_{M_s} is the energy of the level M_s , ρ_{M_s} is the population of the level M_s , $\Delta(H)$ is a Lorentzian lineshape function, and H_{res} is the resonance field for Mn_{12} and Mn_4 . (For Fe_8 there is no C term.) The ratio $\hbar \gamma_{M_s-1, M_s} / g\mu_B$ gives a linewidth due to the finite lifetime of any excited state. The linewidths determined by γ_{M_s-1, M_s} are on the order of several to several tens of gauss at the measured temperature (10 K for Fe_8 and Mn_4 and 25 K for Mn_{12}), and they

decrease with increasing M_s . (In our convention, $M_s = +10$ is the ground state with $H > 0$.) However, the measured linewidths *increase* with increasing M_s , and the order of magnitude of the widths is a couple of hundred to a thousand gauss. Additionally, the dramatic temperature dependence of the linewidths cannot be explained by homogeneous broadening alone.

To resolve this discrepancy, we include distributions in D and g , (called D -strain and g -strain effects, respectively) and intermolecular exchange and dipolar interactions. With Gaussian distributions in D and g , centered at the experimentally determined values and with small standard deviations σ_D and σ_g , we can average the power absorption (equation 4) over the distributions. To calculate the effect on the linewidths of the intermolecular exchange and dipolar interactions with fixed D and g , we use a multispin Hamiltonian [20, 21, 22]:

$$\mathcal{H}^{\text{tot}} = \sum_i [\mathcal{H}_{0i} + V_i(t)] + \mathcal{H}^{(1)}, \quad \mathcal{H}^{(1)} \equiv \mathcal{H}^{\text{dipole}} + \mathcal{H}^{\text{exch}}, \quad (7)$$

$$\mathcal{H}^{\text{dipole}} = \frac{1}{2} \sum_{jk} 'A_{jk} (\vec{S}_j \cdot \vec{S}_k - 3S_j^z S_k^z), \quad (8)$$

$$A_{jk} \equiv \left(\frac{\mu_0}{4\pi} \right) \frac{(g\mu_B)^2}{2r_{jk}^3} (3\zeta_{jk}^2 - 1), \quad (9)$$

$$\mathcal{H}^{\text{exch}} = \frac{1}{2} \sum_{jk} 'J_{jk} \vec{S}_j \cdot \vec{S}_k, \quad (10)$$

where \mathcal{H}_{0i} is the single-spin Hamiltonian for the i th molecule, the sum \sum_i runs over all molecules, and $V_i(t)$ is the interaction between the i th molecule and the oscillating transverse field. Here $\mathcal{H}^{\text{dipole}}$ is the dipolar interaction between the molecules, and ζ_{jk} are the direction cosines of the vector between molecules j and k (\vec{r}_{jk}) relative to the easy axis (z axis). The sum \sum_{jk} runs over all molecules, so that any two indices are not the same. $\mathcal{H}^{\text{exch}}$ is the isotropic exchange interaction between the spins of nearest-neighbor molecules, where the exchange coupling constant J_{ij} is J if the i th and j th spins are nearest neighbors and zero otherwise. Assuming that $\sum_i V_i(t)$ is much smaller than $\mathcal{H}^{(1)}$, which again is much smaller than $\sum_i \mathcal{H}_{0i}$, we neglect $\sum_i V_i(t)$ and treat $\mathcal{H}^{(1)}$ perturbatively. In a mean-field approximation, the sums of A_{jk} and J_{jk} (equations 9 and 10) can be separated from the spin operators.

Using the multispin Hamiltonian, we construct a probability density function for the resonance field. To compare with the measured linewidths, we calculate the second central moment of the resonance field, $\langle (H - \langle H \rangle)^2 \rangle$, to zero order in $\mathcal{H}^{(1)}/k_B T$. To explain the experimental data, we need to vary two parameters for the D -strain and g -strain effects, and to vary three parameters [20] for the contribution of the spin-spin interactions: $\sum_{ij} J_{ij}^2$, $\Gamma \equiv \sum_{ij} A_{ij}^2$, and $\Lambda \equiv \sum_{ij} J_{ij} A_{ij}$.

RESULTS AND DISCUSSION

We find that the uniaxial anisotropy parameter D is randomly distributed in all

three of the molecular magnets. This may be due to possible defects or imperfections in the the samples. For Mn_{12} and Mn_4 , the distribution in the g factor is also important, although this effect is not significant for Fe_8 . The spreads in D and g vary from sample to sample by 30–40%. The effect of the distribution in D on inhomogeneous broadening was observed in terahertz spectroscopy for Mn_{12} [24]. The temperature dependence of the linewidths is mainly caused by the spin-spin interactions. The dipolar field was measured in a millimeter-wave study of Fe_8 [25]. For Mn_4 , the intermolecular exchange interaction is stronger than the dipolar interaction, which is consistent with experiments on Mn_4 dimers [26] and monomers [27, 28]. For clarity, we discuss each SMM separately.

Fe_8

We find that for Fe_8 the distribution in D and the intermolecular exchange and dipolar interactions contribute to the linewidths. The distribution in D makes the linewidth increase with increasing energy level M_s , which can be seen from the resonance-field expression (equation 6). The intermolecular exchange and dipolar interactions make the linewidths increase with increasing M_s and with decreasing the resonance frequency ν . The reason is that the resonance field decreases with increasing M_s and with decreasing ν , which can be understood by equation 6. Combining the effect of the distribution in D with the exchange and dipolar interactions explains well the trend and the magnitude of the measured linewidths as functions of frequency and energy level [15].

Next we discuss the temperature dependence of the linewidths. The distribution in D alone cannot explain the interesting measured temperature dependence of the linewidths shown as symbols in figure 1 (a). The reason is that the linewidths caused by the distribution in D are only slightly temperature dependent due to the temperature dependence of the natural linewidths $\hbar\gamma_{M_s-1, M_s}/g\mu_B$ in equation 5. So this weak temperature dependence is monotonic and noticeable only for the small M_s (at most about 100 G at 30 K for $M_s = 3$) [20]. However, the linewidths caused solely by the exchange and dipolar interactions at fixed D and g vary significantly with temperature, as shown in figure 1 (b). For the ground state $M_s = 10$, the linewidths decrease with increasing temperature in the whole temperature range. For $M_s = 9, 8$, and 7 , the widths first increase sharply with temperature at low temperatures, and then decrease slowly with temperature at high temperatures. For $M_s = 6, 5, 4$, and 3 , the widths increase with increasing temperature in the whole range. This trend was also seen in the experimental linewidths, confirming that the exchange and dipolar interactions are crucial to understanding the temperature dependence of the linewidths. The calculated linewidths including the distribution in D and the spin-spin interactions are shown as curves in figure 1 (a). Here we use $\sigma_D \sim 0.0064 D$, $J = -7$ G, $\Gamma = 86$ G², and $\Lambda = -156$ G². The calculated linewidths agree with the measured linewidths except in the low-temperature range for large M_s transitions ($M_s = 10, 9, 8$). At present, we do not fully understand this discrepancy. We note that the quality of the fit that includes a small ferromagnetic exchange interaction is comparable with that without exchange interaction, because the exchange coupling constant is small compared with the linewidths[29].

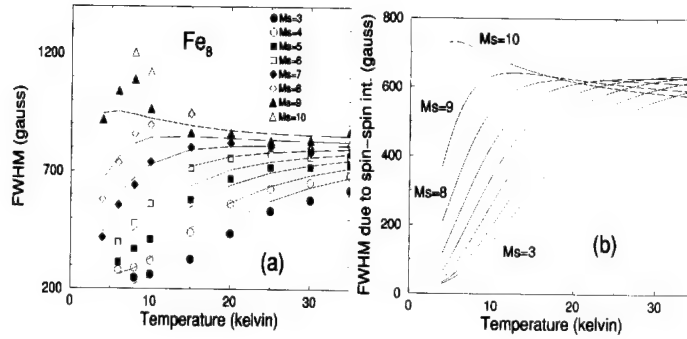


Figure 1: (a) Calculated (curves) and measured (symbols) FWHM vs temperature at $\nu = 116.9$ GHz for Fe_8 . Here the standard deviation of D , $\sigma_D \sim 0.0064D$, the exchange constant $J = -7$ G, $\Gamma = \sum_{ij} A_{ij}^2/N = 86$ G², and $\Lambda = \sum_{ij} J_{ij} A_{ij}/N = -156$ G². The solid curves, from bottom to top, correspond to $M_s = 3, 4, \dots, 9, 10$. (b) Calculated FWHM caused by the exchange and dipolar interactions only, shown vs temperature at $\nu = 116$ GHz for Fe_8 . Here $J = -7$ G, $\Gamma = 86$ G², and $\Lambda = -156$ G². Cited from Ref. [20].

Mn₁₂

We find that the inhomogeneous line broadening for Mn_{12} is due to the distributions in D and g , and to the dipolar interactions. The distribution in D contributes to the variation of the linewidth as a function of M_s and ν in the same way as for Fe_8 . The distribution in g makes the linewidths *decrease* with increasing M_s and decreasing ν , which is opposite to the effect of the distribution in D . The reason is that the resonance field decreases with increasing M_s and decreasing ν . The temperature dependence of the linewidths caused by only the distributions in D and g is very weak, so that it cannot explain the measured linewidths shown as symbols in figure 2 (a), which is similar to those for Fe_8 . The contribution of the dipolar interactions to the linewidths is shown as a function of temperature in figure 2 (b). Unlike for Fe_8 , the M_s dependence of the dipolar broadening does not decrease with increasing temperature (the curves are almost parallel as the temperature increases). Combining the three effects (distributions in D and g , and dipolar interactions), we find that the calculated linewidths agree well with the experimental data with $\sigma_D \sim 0.018D$, $\sigma_g \sim 0.002g$, and $\Gamma = 203$ G², as shown in figure 2 (a). Compared to the linewidths for Fe_8 , the relatively weak temperature dependence for Mn_{12} indicates that for Mn_{12} the dipolar broadening is overshadowed

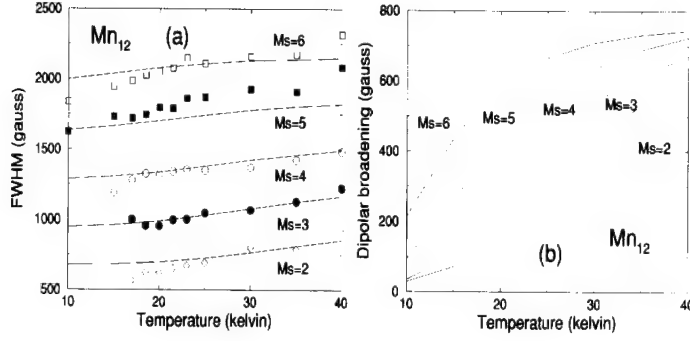


Figure 2: (a) Calculated (curves) and measured (symbols) FWHM vs temperature at $\nu = 189.123$ GHz for Mn_{12} . Here the D strain ($\sigma_D \sim 0.018D$), g strain ($\sigma_g \sim 0.002g$), and the dipolar interactions ($\Gamma = 203 \text{ G}^2$) are included in the calculated linewidths. (b) Calculated FWHM caused by the dipolar interactions only, shown vs temperature, at $\nu = 189.123$ GHz with $\Gamma = 203 \text{ G}^2$ for Mn_{12} . The examined temperature range for Mn_{12} is from 10 K to 40 K. Cited from Ref.[20].

by the effect of the distribution in D , which is three times as wide as for Fe_8 . With the same parameter values, we also check that the M_s and frequency dependence of the measured linewidths can be explained.

Mn_4

We find that for Mn_4 all of our considerations of the many-body effects - the distributions in D and g , and the intermolecular exchange and dipolar interactions - substantially affect the inhomogeneous broadening. One minor difference of this SMM from the other two SMMs is that the effect of the distribution in D disappears in the transition $M_s = 1/2 \rightarrow -1/2$ because the resonance field (equation 6) does not depend on D at this transition. To examine the temperature dependence of the linewidths caused solely by D -strain and g -strain, we used the same spin-phonon coupling parameters as for Mn_{12} [23] to obtain the order of magnitude of the lifetimes of the energy levels. As expected from the analysis of the two other SMMs, we also find that for Mn_4 the distributions in D and g do not significantly change the dependence of the linewidths on temperature.

Figure 3 (a) shows the calculated linewidths caused by the exchange and dipolar interactions only at fixed D and g versus temperature at $\nu = 138$ GHz. Here we use the exchange coupling constant $J = -40 \text{ G}$, two nearest neighbors along the easy axis (because the nearest-neighbor distance along this direction is half of the nearest-

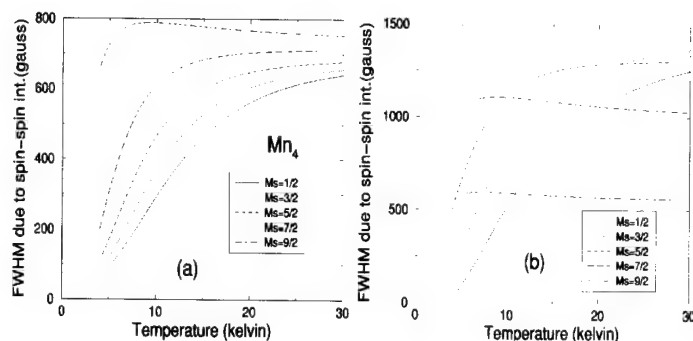


Figure 3: (a) Calculated linewidths due to the exchange and dipolar interactions only vs temperature at $\nu = 138$ GHz for Mn_4 . Here we use the exchange coupling constant $J = -40$ G, $\Lambda = \sum_{ij} J_{ij} A_{ij}/N = -1854.8$ G², and $\Gamma = \sum_{ij} A_{ij}^2/N = 344$ G². (b) The same linewidths as in (a) when the sign of J is flipped and the other parameter values are kept the same.

neighbor distance perpendicular to this direction), $\Lambda = \sum_{ij} J_{ij} A_{ij}/N = -1854.8$ G², and $\Gamma = \sum_{ij} A_{ij}^2/N = 344$ G². The negative sign in J means ferromagnetically coupled spins. If we assume the approximate lattice geometry as a tetragonal lattice and take the easy axis as the crystal c axis, then we know that the sign of Λ should be the same as that of J . We explore some other possibilities of combining the exchange with the dipolar interaction. For example, figure 3 (b) shows the linewidths due to positive J (antiferromagnetically coupled) and the dipolar interaction. With positive J , the linewidth for $M_s = 9/2$ is greatly reduced and the linewidth for $M_s = 1/2$ is appreciably enhanced. This feature is quite different from the broadening with negative J .

Figure 4 shows the calculated linewidths versus temperature at $\nu = 138$ GHz. Here we use $\sigma_D = 0.01D$, $\sigma_g = 0.004g$, $J = -40$ G, $\Lambda = -1854.8$ G², and $\Gamma = 344$ G². The calculated linewidths agree reasonably with the experimental data except for the transition $M_s = 1/2 \rightarrow -1/2$. Notice that the magnitudes of the values of J and Λ are greatly enhanced compared to those for Fe_8 . This suggests that Mn_4 has a stronger exchange interaction between molecules than Fe_8 . Our value for J is different by a factor of 2 from the experimentally extracted value, $J = -74$ G [27]. Therefore, our finding may support the proposed mechanism of spin-spin cross relaxation in Mn_4 [27].

With the same parameter values, we can explain the frequency dependence of the linewidths at $T = 10$ K shown in figure 5. Although there are substantial distributions in D and g , the widths are somewhat dependent on the frequency, which indicates that the spin-spin interactions are not completely overshadowed by the D -strain and g -strain effects as in Mn_{12} . But definitely the frequency dependence is stronger than for Mn_{12} but weaker than for Fe_8 .

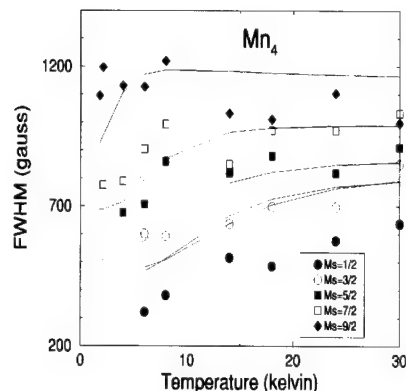


Figure 4: Calculated (curves) and measured (symbols) FWHM vs temperature at $\nu = 138$ GHz for Mn_4 . Here we use $\sigma_D = 0.01D$, $\sigma_g = 0.004g$, $J = -40$ G, $\Lambda = \sum_{ij} J_{ij}A_{ij}/N = -1854.8$ G², and $\Gamma = \sum_{ij} A_{ij}^2/N = 344$ G². The solid curves, from bottom to top, correspond to $M_s = 1/2, 3/2, \dots, 9/2$.

CONCLUSIONS

We investigated the EPR lineshapes as functions of resonance frequency ν , energy level M_s , and temperature T for the three different molecular magnets, Mn_{12} , Fe_8 , and Mn_4 , when the magnetic field is applied along the easy axis and the frequency is kept fixed. In our calculations, intermolecular exchange and dipolar interactions were included, as well as distributions in the uniaxial anisotropy parameter D and the g factor. We find that the distribution in D is present in all three SMMs but that the effect is strongest in Mn_{12} , and that the distribution in g contributes to the linewidths for Mn_{12} and Mn_4 . The spin-spin interactions are responsible for the interesting trend of the temperature dependent lineshapes for all three magnets. For Mn_4 , the exchange interaction is stronger than the dipolar interaction, which supports the conclusions derived from the earlier measurements[27]. The linewidths for the three magnets reveal different M_s , ν , and T dependences because of different contributions from the effects we are considering. Observation of EPR lineshapes could indicate which effects are dominant in a particular SMM, so that we may identify which mechanism leads to quantum tunneling.

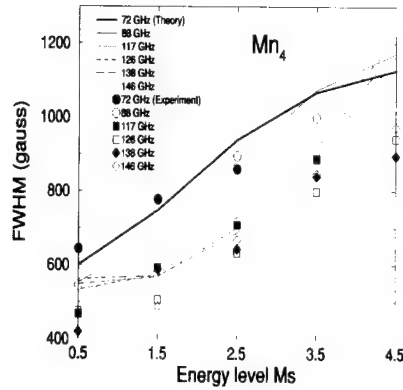


Figure 5: Calculated (curves) and measured (symbols) FWHM vs energy level M_s at $T = 10$ K for $\nu = 72, 88, 117, 126, 138$, and 146 GHz for Mn_4 . Here the values of σ_D , σ_g , J , Γ , and Λ are the same as those in figure 4.

ACKNOWLEDGMENTS

This work was funded by NSF Grant Nos. DMR-9871455, DMR-0120310, DMR-0103290, and DMR-0196430, Research Corporation (S.H.), and by Florida State University through the School of Computational Science and Information Technology and the Center for Materials Research and Technology.

REFERENCES

1. *Quantum Tunneling of Magnetization - QTM '94*, Vol. 301 of *NATO Advanced Study Institute, Series E: Applied Sciences*, edited by L. Gunther and B. Barbara (Kluwer, Dordrecht, 1995).
2. E. M. Chudnovsky and J. Tejada, *Macroscopic Quantum Tunneling of the Magnetic Moment*, Cambridge Studies in Magnetism, Vol. 4 (Cambridge University Press, Cambridge, 1998) and references therein.
3. M. N. Leuenberger and D. Loss, *Nature (London)* **410**, 789 (2001).
4. J. Villain, F. Hartman-Boutron, R. Sessoli, and A. Rettori, *Europhys. Lett.* **27**, 159 (1994).
5. A. L. Barra, D. Gatteschi, and R. Sessoli, *Phys. Rev. B* **56**, 8192 (1997).

6. S. Hill, J. A. A. J. Perenboom, N. S. Dalal, T. Hathaway, T. Stalcup, and J. S. Brooks, Phys. Rev. Lett. **80**, 2453 (1998).
7. J. A. A. J. Perenboom, J. S. Brooks, S. Hill, T. Hathaway, and N. S. Dalal, Phys. Rev. B **58**, 330 (1998).
8. I. Mirebeau, M. Hennion, H. Casalta, H. Andres, H. U. Güdel, A. V. Irodova, and A. Caneschi, Phys. Rev. Lett. **83**, 628 (1999).
9. T. Lis, Acta Crystallogr. B **36**, 2042 (1980).
10. K. Wieghart, K. Pohl, I. Jibril, and G. Huttner, Angew. Chem. Int. Ed. Engl. **23**, 77 (1984).
11. E. del Barco, J. M. Hernandez, J. Tejada, N. Biskup, R. Achey, I. Rutel, N. Dalal, and J. Brooks, Phys. Rev. B **62**, 3018 (2000).
12. S. Maccagnano, R. Achey, E. Negusse, A. Lussier, M. M. Mola, S. Hill, and N. S. Dalal, Polyhedron **20**, 1441 (2001).
13. A. Garg, Europhys. Lett. **22**, 205 (1993).
14. R. S. Edwards, S. Hill, S. Bhaduri, N. Aliaga-Alcade, E. Bolin, S. Maccagnano, G. Christou, and D. N. Hendrickson (unpublished).
15. K. Park, M. A. Novotny, N. S. Dalal, S. Hill, and P. A. Rikvold, Phys. Rev. B **65**, 014426 (2002).
16. S. Hill, S. Maccagnano, K. Park, R. M. Achey, J. M. North, and N. S. Dalal, Phys. Rev. B **65**, 224410 (2002).
17. K. Blum, *Density Matrix Theory and Applications*, 2nd edition (Plenum, New York, 1996).
18. E. M. Chudnovsky and D. A. Garanin, Phys. Rev. Lett. **87**, 187203 (2001); Phys. Rev. B **65**, 094423 (2002).
19. A. Cornia, R. Sessoli, L. Sorace, D. Gatteschi, A. L. Barra, and C. Daiguebonne, Phys. Rev. Lett. **89**, 257201 (2002).
20. K. Park, M. A. Novotny, N. S. Dalal, S. Hill, and P. A. Rikvold, Phys. Rev. B **66**, 144409 (2002).
21. M. McMillan and W. Opechowski, Can. J. Phys. **38**, 1168 (1960); *ibid.* **39**, 1369 (1961).
22. J. H. Van Vleck, Phys. Rev. **74**, 1168 (1948).

23. M. N. Leuenberger and D. Loss, Phys. Rev. B **61**, 1286 (2000); *ibid.*, **61**, 12200 (2000).
24. B. Parks, J. Loomis, E. Rumberger, D. Hendrickson, and G. Christou, Phys. Rev. B **64**, 184426 (2001).
25. A. Mukhin, B. Gorshunov, M. Dressel, C. Sangregorio, and D. Gatteschi, Phys. Rev. B **63**, 214411 (2001).
26. W. Wernsdorfer, N. Aliaga-Alcalde, D. N. Hendrickson, and G. Christou, Nature **416**, 406 (2002).
27. W. Wernsdorfer, S. Bhaduri, R. Tiron, D. N. Hendrickson, and G. Christou, Phys. Rev. Lett. **89**, 197201 (2002).
28. W. Wernsdorfer, S. Bhaduri, C. Boskovic, G. Christou, and D. N. Hendrickson, Phys. Rev. B **65**, 180403(R) (2002).
29. A. Abragam and B. Bleaney, *Electron Paramagnetic Resonance of Transition Ions* (Clarendon, Oxford, 1970).

Single Crystal High Frequency Cavity-based EPR Spectroscopy of Single Molecule Magnets

S. Hill,¹ R. S. Edwards,¹ S. I. Jones,¹ S. Maccagnano,¹ J. M. North,² N. Aliaga,³ E-C. Yang,⁴ N. S. Dalal,² G. Christou,³ D. N. Hendrickson⁴

¹Department of Physics, University of Florida, Gainesville, FL 32611-8440, USA

²Department of Chemistry, Florida State University, Tallahassee, FL 32310, USA

³Department of Chemistry, University of Florida, Gainesville, FL 32611-8440, USA

⁴Department of Chemistry and Biochemistry, University of California at San Diego, La Jolla, CA 92093, USA

ABSTRACT

We report high frequency electron paramagnetic resonance (EPR) investigations of a series of high spin (total spin up to $S = 10$) manganese and nickel complexes which have been shown to exhibit single molecule magnetism, including low temperature (below ~ 1 K) hysteresis loops and resonant magnetic quantum tunneling. A cavity perturbation technique enables high sensitivity oriented single crystal EPR measurements spanning a very wide frequency range (16 to 200+ GHz). Fitting of the frequency and field orientation dependence of EPR spectra allows direct determination of the effective spin Hamiltonian parameters. Studies on a range of materials with varying (approximately axial) site symmetries facilitates an assessment of the role of transverse anisotropy (terms in the Hamiltonian that do not commute with \hat{S}_z) in the magnetic quantum tunneling phenomenon.

INTRODUCTION

Single molecule magnets (SMMs) have stimulated considerable experimental and theoretical research interest since the discovery of resonant quantum tunneling of the magnetization (QTM) in Mn_{12} -acetate in 1996 [1]. Their main attraction is an intrinsic bistability which is realized via a large spin ground state (up to $26\mu_B$) and a significant axial (easy-axis) magnetocrystalline anisotropy [2,3]. This bistability has aroused great interest in terms of the use of SMMs in future molecular devices [4]. When grown as single crystals, the SMM unit is monodisperse—each molecule in the crystal has the same spin, orientation, magnetic anisotropy and structure. Thus, SMMs enable fundamental studies of properties intrinsic to magnetic nanostructures that have previously been inaccessible.

All of the SMMs of interest possess a dominant uniaxial magnetocrystalline anisotropy and, to lowest order, the effective spin Hamiltonian may be written

$$\hat{H} = D\hat{S}_z^2 + \mu_B \vec{B} \cdot \vec{g} \cdot \hat{S} + \hat{H}', \quad (1)$$

where D (< 0) is the uniaxial anisotropy constant, the second term represents the Zeeman interaction with an applied field B , and \hat{H}' includes higher order terms in the crystal field, as well as environmental couplings such as intermolecular dipolar and exchange interactions [1-7]. This Ising-type anisotropy is responsible for the energy barrier to magnetization reversal and the resulting magnetic bistability – factors which lead to magnetic hysteresis at sufficiently low temperatures [1-3]. Unlike bulk magnets, this hysteresis is intrinsic to each individual molecule – hence the term SMM. However, essentially all SMMs continue to exhibit slow magnetic

relaxation, even as $T \rightarrow 0$ K. This low temperature relaxation is due to quantum tunneling, whereby non-axially symmetric interactions in \hat{H}' cause the mixing of states of opposite magnetic polarity necessary for tunneling to occur [2,3].

One of the major goals in the design of future SMMs is to be able to control QTM so that it may be exploited for possible applications. For example, tunneling should be suppressed if one is to use SMMs for data storage applications, whereas an ability to switch coherent tunneling on and off could prove useful for quantum computation [4]. Tunnel rates depend on the degree of symmetry breaking (\hat{H}'), which is something which can be determined very precisely via single crystal EPR measurements [5-9]. However, the $(2S + 1)$ -fold quantum energy level structure associated with a large molecular spin S necessitates spectroscopies spanning a wide frequency range. Furthermore, large zero-field level splittings, due to the significant magnetocrystalline anisotropy (large $|D|$) and large total spin S , demand the use of frequencies and magnetic fields considerably higher (50 GHz to 1 THz, and up to 10+ tesla respectively) than those typically used by the majority of EPR spectroscopists. An important breakthrough, therefore, in the spectroscopy of SMMs has been the development of sensitive cavity perturbation techniques for carrying out multi-high-frequency (20 to 200+ GHz) EPR measurements on single crystals [5-10]. In particular, this technique leads to at least a three orders of magnitude improvement in detection sensitivity relative to conventional single-pass multi-high-frequency EPR techniques, which opens up many important new avenues for probing SMMs. Furthermore, as we shall demonstrate in this article, studies on oriented single crystals enable precise characterizations of weak interactions in \hat{H}' which turn out to be crucial as far as QTM is concerned.

The article is organized as follows: in the next section, we describe our experimental setup and procedures in detail, with emphasis on high-frequency EPR applications; this account of our technique expands upon an earlier article [10] which deals with the construction and characterization of cavity based microwave instrumentation for probing the electrodynamic response of conducting samples. We then provide a series of brief examples of the unique capabilities of this instrumentation, with emphasis on multi-frequency oriented single crystal measurements. This is followed by a short summary.

EXPERIMENTAL

Documented lack of resolution, sensitivity and/or various experimental artifacts have been known to affect most high frequency EPR investigations of SMMs to date. First of all, the low sensitivity usually limits possible studies to powder samples or aligned polycrystals, since single crystals are typically too small to detect a useful EPR signal. Even in the case of large polycrystalline samples, often only a few transitions are observed [11,12]. Furthermore, misalignment of polycrystals, stresses in pressed powders, or uncontrolled field-alignment of micro-crystallites in loose powders are all factors which may introduce unwanted experimental artifacts, particularly as far as EPR lineshape analyses are concerned. In addition, it is commonly stated that observed EPR lineshapes cannot be analyzed because they contain uncontrollable distortions caused by standing waves in the sample probe, which result in a mixing of the dissipative and reactive sample response [13,14,15]. As an example, it has been reported in [14] that the linewidths in Fe_8Br approximately scale as M_S^2 (where M_S is the spin projection of the state from which the transition is excited), whereas our earlier studies [5-9] have shown a dominant linear dependence of the linewidths on M_S , both for Fe_8Br and Mn_{12} -acetate.

As we will show in the following results section, measurements on single crystals are essential for studies of SMMs, as are several other unique aspects of our technique. For example, contrary to recent assertions [15], we are able to obviate essentially all instrumental artifacts that could influence/distort EPR line shapes. In addition, our ability to measure at many frequencies, temperatures and field orientations enables us to distinguish between many contributions to the EPR line widths and shapes. These include: inter-SMM and hyperfine dipolar fields; distributions in crystal field parameters; and spin-lattice interactions. Indeed, each of these effects have been discussed extensively in the QTM literature, *e.g.* dipolar fields [16], distributed crystal field parameters caused by dislocations [17,18] or solvent and ligand disorder [19], and hyperfine interactions [20].

The high degree of sensitivity required for single crystal measurements is achieved using a resonant cavity perturbation technique in combination with a broad-band Millimeter-wave Vector Network Analyzer (MVNA) exhibiting an exceptionally good signal-to-noise ratio; a detailed description of this instrumentation can be found in ref. [10]. The MVNA is a phase sensitive, fully sweepable (8 to 500+ GHz [10]), superheterodyne source/detection system. Several sample probes couple the network analyzer to a range of high sensitivity cavities (Q -factors of up to 25,000) situated within the bore of a 7 tesla superconducting magnet. The MVNA/cavity combination has been shown to exhibit a sensitivity of at least 10^9 spins. $G^{-1}.s^{-1}$, which is comparable with the best narrow-band EPR spectrometers. This, coupled with newly acquired sources and a split-pair magnet, enables single crystal measurements at any frequency in the range from 8 to 500 GHz, at temperatures down to 1.5 K (± 0.01 K), and for any geometrical combination of DC and AC field orientations up to 7 T (up to 45 T at the National High Magnetic Field Laboratory).

The use of a narrow band cavity offers many important advantages over non-resonant methods (see *e.g.* refs [5,8-10]). Careful consideration concerning the coupling of radiation to and from the cavity (via waveguide), combined with the ability to study very small samples, eliminates problems associated with standing waves in the sample probe [10]. This, in turn, eliminates a mixing of the dissipative and reactive responses of the sample under investigation and, when combined with a vector detection scheme, enables faithful extraction of the true EPR lineshapes (both the real and imaginary components), free from instrumental artifacts. One other notable feature of the superheterodyne scheme is its detection rate of 34 MHz; thus, there is no need for field modulation, unlike other high field EPR methods [13]. Consequently, the raw data displayed in this paper constitute pure absorption. Finally, the use of a cavity enables positioning of a single crystal sample into a well defined electromagnetic field environment, *i.e.* the orientations of the DC and AC magnetic fields relative to the sample's crystallographic axes are precisely known, and the DC field is very homogeneous over the tiny volume (< 1 mm³) of the sample. In this way, additional contributions to the EPR lineshapes are avoided due to, *e.g.* field inhomogeneities over the sample volume, or slight mis-alignments of crystallites, as may be the case for measurements on aligned powders.

In order to facilitate coupling between the spectrometer (MVNA) and the cavity, we have constructed various waveguide probes, optimized to work in various frequency bands up to about 200 GHz. Each probe consists of two waveguides for separately coupling the source and detector to the cavities. Composite waveguide materials (copper and gold plated stainless steel) are used both to minimize microwave losses and to maximize thermal isolation of the cold part of the probe. Rectangular and cylindrical cavities may be readily interchanged (at room temperature), as can the coupling to the cavity. A detailed description of the construction of these probes (with

detailed schematics), as well as extensive technical parameters associated with the cavities, are presented elsewhere [10]. Although the best results are usually achieved at the fundamental mode of a particular cavity (together with the appropriate coupling), exceptional results may also be achieved in over-moded cavities. In particular, high Q -factor cylindrical cavities permit measurements up to frequencies several times the fundamental mode frequency. Thus, broad band spectroscopy is possible, whilst maintaining many of the advantages of a narrow band cavity. The high Q -values (up to 10^4 at frequencies as high as 200 GHz) ensure well separated cavity modes which we can characterize with the MVNA prior to making a measurement; this procedure is described in more detail in ref. [10]. Furthermore, careful positioning of a tiny single crystal on the side walls of the cavity ensures that the sample sits in a magnetic field antinode for any mode of the cavity, as required for EPR. While these procedures have been extensively tested to frequencies on the order of 200 GHz, we have recently succeeded in extending measurements up to 300 GHz using low frequency (< 200 GHz) probes. However, for measurements above 200 GHz, a quasi-optical system is under construction which will be described in a future publication.

In order to enable in-situ rotation of the sample relative to the applied magnetic field, we utilize a split-pair magnet with a 7 T horizontal field and a vertical access. Smooth rotation of the entire rigid microwave probe, relative to the fixed field, is achieved via a room temperature stepper motor mounted at the neck of the magnet dewar; the stepper motor offers 0.01° angle resolution. The source and detector are bolted rigidly to the microwave probe; subsequent connection to and from the MVNA is achieved via flexible coaxial cables [10]. In this mode of operation, one can maintain optimal coupling between the spectrometer and the cavity containing the sample, whilst rotating the probe. As discussed in great detail in ref. [10], good coupling between the various microwave elements is essential in order to maintain a high sensitivity and a low noise level. Rotation of the entire rigid sample probe also ensures that the sample sits in a reproducible electromagnetic field environment for all measurements made on a particular mode of the cavity.

Temperature stabilization is achieved using a fully automated Quantum Design PPMS variable helium flow system; the control software for the PPMS also automates field sweeps and rotation of the sample probe. All of the data presented in this article were obtained by sweeping the magnetic field at a constant frequency, temperature and field orientation; however, it is also possible to sweep the temperature and field orientation. Fixed frequency measurements are then repeated at many different temperatures, frequencies and field orientations.

In the next section, we present data for the following SMM samples:

$[\text{Mn}_{12}\text{O}_{12}(\text{CH}_3\text{COO})_{16}(\text{H}_2\text{O})_4] \cdot 2\text{CH}_3\text{COOH} \cdot 4\text{H}_2\text{O}$ (Mn_{12} -acetate), $[\text{Mn}_4\text{O}_3\text{Cl}_4(\text{O}_2\text{Cet})_3\text{py}_3]_2$, and $[\text{Ni}(\text{hmp})(\text{R-OH})\text{Cl}]_4$ ($\text{R} = \text{Me}, \text{Et}$ and tBuEt). Details concerning the preparation of these materials are presented elsewhere [21-23]. The typical sizes of single crystals range from $1.4 \times 0.16 \times 0.16 \text{ mm}^3$ to $1.5 \times 1.5 \times 2.5 \text{ mm}^3$, and the shapes range from needles to flat platelets to distorted cubes. For many of the higher symmetry SMMs, fairly accurate alignment of the crystals can be achieved when mounting the samples in the cavity prior to cooling. For lower symmetry SMMs, in-situ rotation about several axes is usually required in order to locate the principle magnetic axes of the samples. Particular care is taken to avoid solvent loss, since this can affect both the quality of the data and, in some cases, this may even affect the underlying physics of the SMMs. The samples are removed from their mother liquor and transferred to the cavity in a matter of a few minutes; in some extreme cases, the samples are coated in a protective layer of grease immediately upon removing them from the mother liquor. The samples are then

cooled at about 10 K/min, initially under 1 atmosphere of helium gas; the pressure is only reduced at low temperatures. Silicone grease is used to secure samples within the cavity.

RESULTS

In this section, we give an overview of some of the recent data that have been obtained for several SMMs using the instrumentation described above. The first example involves the Mn_{12} -acetate spin $S = 10$ system, which was the first SMM and remains the most widely studied. The Mn_{12} molecule has a high S_4 symmetry and, therefore, exhibits very slow quantum relaxation at low temperatures. There has been a considerable effort to determine the symmetry breaking which is responsible for this tunneling. Recent studies clearly show that for a typical crystal, there is a distribution of tunnel splittings, *i.e.* there is a molecule-to-molecule variation in the magnitude of the transverse interactions responsible for the tunneling. It has long been assumed that the rhombic crystal field term (\hat{O}_4^2) in \hat{H}' (Eq. 1) is zero for Mn_{12} -acetate due to its S_4 site symmetry; for this reason, other sources of symmetry breaking are required in order to explain the QTM. While high-frequency EPR [13] and neutron studies [24] have provided convincing evidence for a fourth order single-ion transverse anisotropy (\hat{O}_4^4), such an interaction cannot explain many key experimental factors associated with the observed low-temperature hysteresis [25]. For this reason, recent theoretical and experimental efforts have focused on the possible role played by disorder [17-19,26].

Cornia *et al.* have proposed a model in which disorder in the solvent molecules surrounding the Mn_{12} molecule gives rise to a local transverse quadratic anisotropy [19], *i.e.* a local rhombic distortion. Such a disorder may be expected to result in several distinct species (isomers) of Mn_{12} -acetate, each having slightly different (*i.e.* a distribution) tunnel splittings caused by the slightly different solvent-disorder-induced rhombic terms in \hat{H}' . Such a model is quite appealing, since magnetic relaxation experiments clearly indicate a distribution in the tunnel splittings for Mn_{12} -acetate [26]. An alternative model proposed by Garanin and Chudnovsky involves a transverse quadratic anisotropy induced via dislocations [17,18]. The long range strains produced by these dislocations are predicted to result in very broad distributions of the tunnel splittings, indeed, probably much broader distributions than are observed experimentally [26]. While both disorder pictures can explain many aspects of the reported magnetic relaxation experiments, their respective spectroscopic signatures may be expected to be quite different.

Before presenting direct spectroscopic evidence for both quartic and quadratic transverse interactions in Mn_{12} -acetate, we should point out that our earlier investigations highlighted the significant effect that disorder has on EPR spectra obtained for fields parallel to the magnetic easy axis of the Mn_{12} molecule [5-9]. For this geometry, the spectra are most sensitive to diagonal terms in Eq. 1, *i.e.* $D\hat{S}_z^2$ and higher order terms such as $B_4^0\hat{O}_4^0$; these studies confirmed the existence of a significant D -strain (σ_D up to 2%) in Mn_{12} -acetate single crystals [5-9]. While these results hinted at the importance of disorder in the tunneling mechanism, they did not identify the transverse terms in Eq. 1 responsible for the tunneling. To do so, one has to measure spectra with the applied field transverse to the magnetic easy axis of the molecule. For this geometry, the EPR spectra exhibit maximum sensitivity to the transverse terms in \hat{H}' (Eq. 1). Indeed, spectra obtained as a function of angle within the hard plane of the molecule may be used to deconvolute several different contributions to the transverse anisotropy, as demonstrated by means of Figure 1.

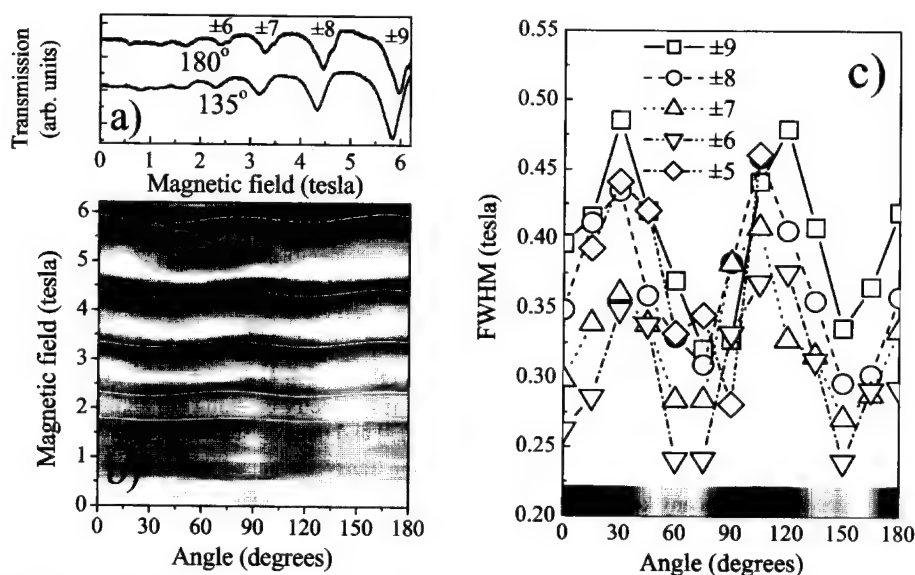


Figure 1. a) Two typical hard plane transmission spectra obtained for Mn₁₂-acetate (the in-plane field orientations are given in the figure); the frequency is 49.86 GHz, and the temperature is 15 K. The dips in transmission correspond to EPR absorptions between pairs of levels that evolve from the $\pm M_S$ levels (see labels) in zero field [8]. b) Contour plot of the angle dependence of the EPR absorption intensity (dark) for field rotations in the hard plane. The white lines are fits to the peak positions. c) Angle dependence of the EPR linewidths (FWHM) for the various transitions in a); see text for explanation of shaded region in the lower part of the figure.

The contour plot in Figure 1b demonstrates a pronounced four-fold pattern in the central positions (in field) of the EPR absorptions as a function of the orientation of the magnetic field within the hard plane of the molecule. This four-fold pattern is intrinsic to the Mn₁₂ molecule, and can be attributed to a quartic transverse zero-field interaction of the form $(\hat{S}_x^4 + \hat{S}_y^4)$ in \hat{H}' . Fits to the angle dependence (solid white curves) are consistent with a single value of the coefficient $B_4^4 = 3.2(1) \times 10^{-5} \text{ cm}^{-1}$. These fits also include a small two-fold correction, which is due to unavoidable misalignments of the sample's ($\sim 1^\circ$) easy axis with the field rotation axis; this effect is *not* related to any transverse zero-field interaction. Figure 1a shows raw transmission spectra obtained for two different orientations of the magnetic field within the hard plane. The $\psi = 135^\circ$ is extremely simple, showing nice symmetric EPR absorptions. On the other hand, the $\psi = 180^\circ$ spectrum exhibits a high field shoulder on each of the peaks. This splitting of the peaks for the hard plane spectra has been seen in several samples [8], and also by other groups [19]. Indeed, Cornia *et al.* have proposed that its origin is connected with the solvent disorder which leads to a local lowering of the symmetries of the Mn₁₂ molecules [19].

It is no coincidence that the angle separation is 45° between the clean trace and the trace exhibiting the shoulder in Figure 1a. This again signifies an effect with a four-fold symmetry, however, its origin is related to a disorder-induced two-fold rhombic distortion, as will be

explained below. The split double peaks ($\psi = 180^\circ$) are very similar to those observed by Cornia *et al.* [19], and their spacing of about 0.35 T also agrees. To emphasize the correlation between the shoulder and disorder, we plot the full width at half maximum (FWHM) of several of the peaks, as a function of ψ , in Figure 1c; ψ is merely a measure of the field orientation relative to a fixed arbitrary direction within the hard plane of the sample. The shaded strip at the bottom of Figure 1c signifies the strength of the observed shoulder seen in Figure 1a (darker implies stronger); the shoulder is most pronounced at angles slightly below the maxima in the linewidths.

Assuming that the fine structure (shoulder) and line broadening are due to local rhombic distortions, then the angle dependence has a natural explanation. The quadratic term in \hat{H}' has the form $E(\hat{S}_x^2 - \hat{S}_y^2)$, which produces a two-fold pattern for rotations in the hard plane. An intrinsic quadratic anisotropy of this form would produce shifts in the hard axis EPR peak positions, contrary to what is observed. However, in the case of Cornia's model (involving ligand disorder [19]) one expects equal numbers of molecules having positive and negative E . This is because the disorder involves an acetate ligand which can take four different positions (90° apart) about the z -axis of the molecule; a change in the sign of E merely corresponds to a 90° rotation of the hard axis. Thus, one expects overlapping two-fold patterns with a 90° phase shift, corresponding to molecules with their disorder-induced hard axes oriented at 90° to each other. The 90° phase shift results in line broadening rather than line shifts. What is more, the effect on the linewidths will exhibit a four-fold pattern, as opposed to a two-fold one, *i.e.* the S_4 symmetry is only broken locally, whereas EPR measures a global average of this disorder. Based on these studies, we estimate an E term associated with the disorder of about 0.01 cm^{-1} .

Studies for some other samples show additional fine structures. We believe this to be a consequence of a higher resolution in intrinsically cleaner samples, *i.e.* samples having intrinsically narrower EPR lines. Such multiple fine structures may signify additional configurations of the acetate ligands, all possible combinations of which have been discussed in ref. [19]. Indeed, it is likely that different ligand disorders will have different associated hard directions, and this might explain why the shoulders seen in Figure 1 are observed slightly away from the maxima in the linewidths. We note also, that there is an approximately 10° shift in the four-fold patterns observed in Figure 1b due to the intrinsic four-fold transverse interaction, and the disorder induced patterns seen in Figure 1c. Finally, temperature dependent measurements (not shown) provide the final confirmation that the splitting is due to distinct ground states, presumably different ligand isomers. Both components of the splitting persist to the lowest temperatures investigated, while the intensity in all of the excited state transitions vanishes as $T \rightarrow 0$, *i.e.* the shoulder in Figure 1a corresponds to a distinct ground state.

Next we turn to a manganese system in which the magnetic unit consists of a dimer of Mn_4 cubes, with the formula $[\text{Mn}_4\text{O}_3\text{Cl}_4(\text{O}_2\text{CEt})_3\text{py}_3]_2$ (denoted NA3 for short) [22]. Hysteresis experiments for this complex also show resonant QTM steps [27]. However, no tunneling is seen in zero-field – a behavior which is quite different from that observed for essentially all known monomeric SMMs [2]. Furthermore, the first tunneling transition is observed before one reaches zero-field on the down-sweeps of the hysteresis loops. Wernsdorfer *et al.* attribute these observations to antiferromagnetic intra-dimer magnetic interactions [27]; the magnitude of the effect suggests weak superexchange interactions via the $\text{Cl}\cdots\text{Cl}$ and $\text{C-H}\cdots\text{Cl}$ contacts between the two molecules within the dimer. This superexchange results in an antiferromagnetic exchange bias, whereby each half of the dimer acts as a field bias on its neighbor, resulting in a complete suppression of the zero-applied-field quantum tunneling resonance.

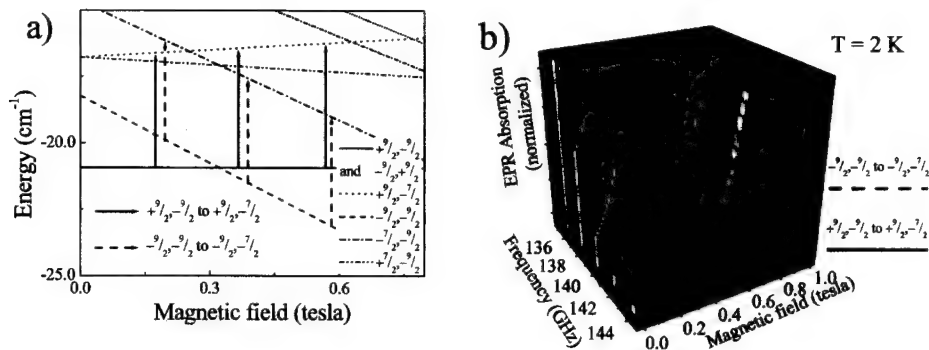


Figure 2. a) The low lying two-spin energy levels for the NA3 dimer plotted as a function of magnetic field; the most important levels have been labeled according to the scheme described in the main text. For simplicity, the calculations of these levels ignored the transverse terms in Eqs. 1 and 2. b) A 3D plot of the ground state transition(s) in NA3 obtained over a narrow field and frequency range; for clarity, the data correspond to Lorentzian fits to the original raw data. See main text for an explanation of the observed trends in the data.

In the case of two coupled SMMs, as is the case for NA3, the effective two-spin Hamiltonian is written as a sum [27]

$$\hat{H} = \hat{H}_1 + \hat{H}_2 + J\hat{S}_1 \cdot \hat{S}_2, \quad (2)$$

where \hat{H}_1 and \hat{H}_2 are given by Eq. 1; the cross term describes the superexchange coupling between the two molecules within the dimer, and J characterizes the strength of this coupling. This adds considerable complexity to the energy level diagram, resulting in $(2S + 1) \times (2S + 1)$ levels. For NA3, the antiferromagnetic coupling (positive J) results in a zero-field ground state comprised of the degenerate $(^{9/2}_{2}, ^{-9/2}_{2})$ and $(^{-9/2}_{2}, ^{9/2}_{2})$ levels, as shown in Figure 2a. However, application of a field ($\parallel z$) exceeding the exchange bias (~ 0.3 tesla) results in a crossing of the degenerate $(^{-9/2}_{2}, ^{9/2}_{2})/(^{9/2}_{2}, ^{-9/2}_{2})$ levels, and the $(^{-9/2}_{2}, ^{-9/2}_{2})$ level, thereby changing the ground state to the latter (see Figure 2a).

In terms of the EPR, the exchange coupling results in two distinct single-spin transitions from each two-spin state, *i.e.* (M_{S1}, M_{S2}) to $(M_{S1} + 1, M_{S2})$ or (M_{S1}, M_{S2}) to $(M_{S1}, M_{S2} + 1)$. However, more importantly, because of the exchange bias, the single-spin transitions now depend on the state of the other spin within the dimer. Thus, the first transitions from the two ground states, $(^{9/2}_{2}, ^{-9/2}_{2})$ to $(^{9/2}_{2}, ^{-7/2}_{2})$ and $(^{-9/2}_{2}, ^{9/2}_{2})$ to $(^{-9/2}_{2}, ^{-7/2}_{2})$, have slightly different energies even though they both correspond to the same $^{-9/2}_{2}$ to $^{-7/2}_{2}$ single-spin transition. This situation is illustrated in Figure 2a. It is also now possible to excite multi-spin EPR transitions within this coupling scheme [28], though this should represent a much weaker (higher order) process. Single crystal EPR measurements enable us to test the above hypotheses.

The easy axis spectra obtained for NA3 show many similarities to the easy axis data obtained for other monomeric manganese SMMs (see *e.g.* ref. [5]), including monomeric Mn₄ clusters, many examples of which have very similar single spin Hamiltonian parameters (S , D , *etc.*) to the dimer [29]. Based on the simple exchange bias scheme developed by Wernsdorfer *et al.* [27], we

have been able to estimate the axial crystal field parameters $D \approx -0.500 \text{ cm}^{-1}$ and $B_4^0 \approx -7 \times 10^{-5} \text{ cm}^{-1}$ for NA3; the details of this analysis will be published elsewhere [29].

The ability to measure at many different frequencies allows us to tune the ground state transition(s) to the field region where the ground state level crossing occurs in Figure 2a. In this field range, a pronounced splitting becomes apparent in the lowest field resonance, as shown in Figure 2b, *i.e.* the exchange bias has a significant effect on the EPR in this low field limit. The data in Figure 2b were obtained at 2 K so as to enhance the intensity of the ground state transition(s); thus no other transitions were observed at this low temperature. For clarity, the 3D plots in Figure 2b were made with Lorentzian fits to the data, rather than the raw data, because the signal-to-noise ratio varies considerably for the different frequencies employed. It is quite a remarkable experimental achievement to be able to make narrow band cavity measurements on such a small single crystal, and at 2 GHz intervals above 130 GHz. The splitting is due to the different energies of the respective $(^9/2, -^9/2)$ to $(^9/2, -^7/2)$ and $(-^9/2, -^9/2)$ to $(-^9/2, -^7/2)$ ground state transitions (see Figure 2a). This splitting is very robust, and is simply due to the exchange bias. By following the exchange-bias split resonance through the exchange bias field region ($\sim 0.3 \text{ T}$), it is apparent that the intensity transfers smoothly from the $(^9/2, -^9/2)$ to $(^9/2, -^7/2)$ transition to the $(-^9/2, -^9/2)$ to $(-^9/2, -^7/2)$ transition. This observation is consistent with the change in the ground state of the dimer at $\sim 0.3 \text{ T}$. Furthermore, the switch in intensity occurs in the correct sense according to Eqs. 1 and 2, *i.e.* the high field peak grows with increasing field, and vice versa. The intensities become roughly equal when the split resonance is centered about 0.3 T , in agreement with the exchange bias field determined by Wernsdorfer *et al* [27]. Therefore, these data provide substantial support for the exchange bias model.

Using a simple model which neglects transverse terms in Eq. 2, we can predict the expected splitting of the $(^9/2, -^9/2)$ to $(^9/2, -^7/2)$ and $(-^9/2, -^9/2)$ to $(-^9/2, -^7/2)$ ground state transitions. Surprisingly, the splitting should be twice the exchange bias field, yet we observe a substantially reduced value of about 0.2 T . However, this difference does not in any way invalidate the exchange bias model, which is based on the properties of the ground state. It merely tells us that we need to develop a more complete picture of the EPR, which involves excited levels as well; this is a work in progress.

The final example which we present concerns a series of SMMs based on tetranuclear nickel clusters with varying ligands, *e.g.* the complexes $[\text{Ni}(\text{hmp})(\text{MeOH})\text{Cl}]_4$, $[\text{Ni}(\text{hmp})(\text{EtOH})\text{Cl}]_4$ and $[\text{Ni}(\text{hmp})(\text{tBuEtOH})\text{Cl}]_4$, which we call MeOH, EtOH and tBuEtOH for short [23]. Each complex has been predicted to have a spin $S = 4$ ground state, and an easy-axis type anisotropy. Recent low-temperature ($< 1 \text{ K}$) hysteresis experiments have shown that the magnetic moments associated with each of these SMMs *do* exhibit resonant QTM [23]. However, in the first two complexes, the expected zero-field QTM resonance is shifted considerably away from $B = 0$; this behavior may again be attributed to an appreciable intermolecular exchange bias effect [27,28]. The existence of significant inter-SMM exchange interactions in these nickel based SMMs is not unexpected since the intermolecular Cl---Cl contact distances are rather short (~ 4.8 to 6 \AA). Through systematic variations of the ligands, it is possible to tune these exchange effects, *e.g.* by varying the Cl---Cl contact distance from $\sim 4.9 \text{ \AA}$ in the MeOH and EtOH complexes, to $\sim 6 \text{ \AA}$ in the tBuEtOH complex.

Figure 3a shows raw field sweeps for each of the three complexes; in each case, the field is roughly aligned with the easy axis, the frequency is approximately 190 GHz , and the temperature is 10 K . Data obtained for the tBuEtOH complex are the easiest to interpret. A series of more-or-less evenly spaced double peaks is observed, with the intensity decreasing for successive pairs of

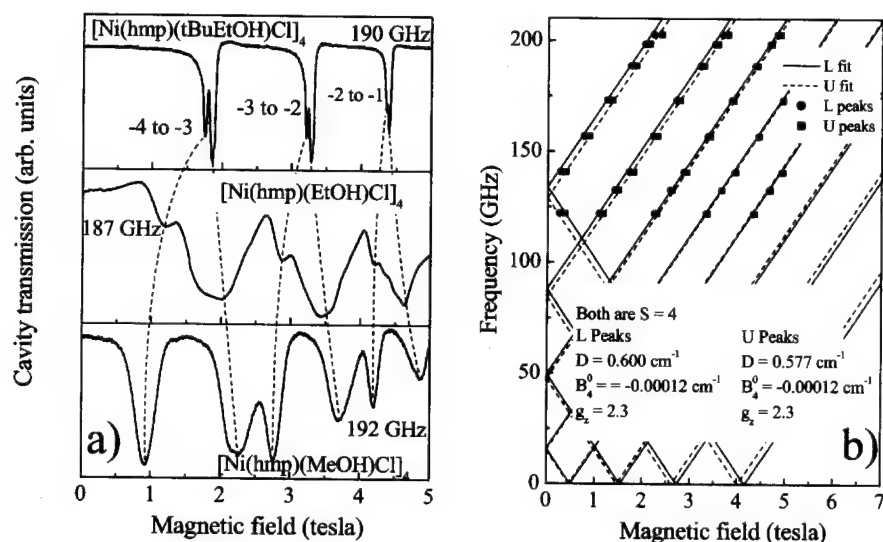


Figure 3. a) Raw EPR spectra for three different Ni_4 SMMs, obtained with the field \sim parallel to the easy axes; the temperature is 10 K, and the frequencies are indicated in the figure. In the top panel, the resonances are labeled according to the M_S quantum numbers involved in the transitions. Each peak shows a splitting which increases from top to bottom; the dashed lines indicate how the peaks evolve from one complex to the next. b) Separate fits to Eq. (1) for the lower (L) and upper (U) peaks within each split doublet for the tBuEtOH complex. These fits confirm the $S = 4$ ground state and yield the diagonal components of the effective spin Hamiltonian. Similar fits (not shown) were obtained for the EtOH and MeOH complexes.

peaks. One possible interpretation of the splitting involves the existence of two species of molecule within the crystal, with slightly different crystal field parameters. Separate fits to the $S = 4$ Hamiltonian (Eq. 1) for the lower (L) and upper (U) split peaks are shown in Figure 3b. Although the fits are excellent, such an interpretation is inconsistent with X-ray studies which indicate that all molecules are crystallographically identical (with S_4 site symmetry) and that no disorder associated with the ligands exists. Careful angle dependent studies rule out crystal twinning or sample mis-alignment as a possible explanation for the splitting.

EPR spectra for the EtOH and MeOH complexes reveal considerably broader absorptions and dramatically enhanced splittings. Assignments of the peaks were determined from their temperature dependence (not shown), and from similar fits to the one shown in Figure 3b for the tBuEtOH complex. The evolution of the peaks for the three complexes is shown in Figure 3a by dashed lines, and assignments in terms of the M_S quantum numbers are given in the top panel. In every case, fits to the $S = 4$ Hamiltonian for the L and U peaks are surprisingly good (not shown), yielding the following parameters: $D_L = -0.715 \text{ cm}^{-1}$, $D_U = -0.499 \text{ cm}^{-1}$, $B_4^0 = -2 \times 10^{-4} \text{ cm}^{-1}$ and $g_z = 2.24$ for the MeOH complex; $D_L = -0.673 \text{ cm}^{-1}$, $D_U = -0.609 \text{ cm}^{-1}$, $B_4^0 = -1.2 \times 10^{-4} \text{ cm}^{-1}$ and $g_z = 2.20$ for the EtOH complex. Transverse terms have been

determined from powder spectra and from the same procedure as shown for Mn_{12} -acetate in Figure 1b. The dominant contribution to the ground state tunnel splitting is the quartic $B_4^4\hat{O}_4^4$ crystal field term ($B_4^4 \approx 4 \times 10^{-4} \text{ cm}^{-1}$ for the tBuEtOH complex), which leads to a strong interaction between the $M_S = \pm 4$ ground states, and to fast relaxation in zero field (ground state tunnel splitting $\sim 12 \text{ MHz}$).

While an explanation for the EPR splittings in terms of crystallographically distinct Ni_4 species cannot be ruled out in the case of the EtOH and MeOH complexes (their structures are each composed of two inter-penetrating diamond lattices), it is interesting to note that the magnitudes of the splittings scale roughly with the expected strength of the exchange interactions, as determined both from the Cl---Cl contact distances and from the relative magnitudes of the exchange bias effects observed from hysteresis experiments; the MeOH complex shows an appreciably larger exchange bias effect than the EtOH complex, while the tBuEtOH complex shows no measurable exchange bias [23]. The EPR line widths and shapes are also considerably broader and more complex for the two SMMs that show a clear exchange bias effect. We note that EPR line broadening due to intermolecular exchange interactions is well documented in other SMMs [6,7], and EPR line splittings may also be expected on the basis of a simple dimer model which includes the effects of exchange between pairs of SMMs (see above). Although further investigations are needed to determine the precise origin of the splitting, it should be noted that the ability to distinguish between exchange and disorder effects will only likely be possible through single crystal measurements of the kind reported here.

SUMMARY AND CONCLUSIONS

We have described a unique cavity perturbation technique that enables high sensitivity oriented single crystal EPR measurements spanning a very wide frequency range (16 to 200+ GHz). We also present a series of brief examples of the unique capabilities of this instrumentation, with emphasis on multi-frequency oriented single crystal measurements. In particular, these studies enable precise characterizations of weak transverse interactions which turn out to be crucial as far as the quantum tunneling is concerned in SMMs.

ACKNOWLEDGEMENTS

We thank Andrew Kent and Wolfgang Wernsdorfer for stimulating discussion. Funding is provided by the National Science Foundation (DMR 0103290 and DMR0196430) and by Research Corporation.

REFERENCES

- [1] J. R. Friedman, M. P. Sarachik, J. Tejada, and R. Ziolo, *Phys. Rev. Lett.* **76**, 3830 (1996); L. Thomas, F. Lioni, R. Ballou, D. Gatteschi, R. Sessoli, B. Barbara, *Nature (London)* **383**, 145 (1996).
- [2] G. Christou, D. Gatteschi, D.N. Hendrickson, and R. Sessoli, *MRS Bulletin*, **Volume 25**, No. 11, 66 (2000).
- [3] E. M. Chudnovsky, J. Tejada, *Macroscopic Quantum Tunneling of the Magnetic Moment*, (Cambridge University Press, Cambridge, 1998).
- [4] Michael N. Leuenberger and Daniel Loss, *Nature* **410**, 789 (2001).

- [5] S. Hill, S. Maccagnano, K. Park, R. M. Achey, J. M. North, and N. S. Dalal, *Phys. Rev. B* **65**, 224410 (2002).
- [6] K. Park, M. A. Novotny, N. S. Dalal, S. Hill, and P. A. Rikvold, *Phys. Rev. B* **65**, 014426 (2002).
- [7] Kyungwha Park, M.A. Novotny, N.S. Dalal, S. Hill, P.A. Rikvold, *Phys. Rev. B* **66**, 144409 (2002).
- [8] S. Hill, J. A. A. J. Perenboom, N. S. Dalal, T. Hathaway, T. Stalcup, and J. S. Brooks, *Phys. Rev. Lett.* **80**, 2453 (1998).
- [9] S. Maccagnano, R. Achey, E. Negusse, A. Lussier, M.M. Mola, S. Hill, and N.S. Dalal, *Polyhedron* **20**, 1441 (2001).
- [10] M. Mola, S. Hill, M. Gross, and P. Goy, *Rev. Sci. Instrum.* **71**, 186 (2000).
- [11] A. A. Mukhin, V. D. Travkin, A. K. Zvezdin, S. P. Lebedev, A. Caneschi and D. Gatteschi, *Europhys. Lett.*, **44** (6), 778 (1998).
- [12] A. Mukhin, B. Gorshunov, M. Dressel, C. Sangregorio and D. Gatteschi, *Phys. Rev. B* **63**, 214411 (2001).
- [13] A-L. Barra, D. Gatteschi, and R. Sessoli, *Phys. Rev. B* **56**, 8192 (1997).
- [14] A-L. Barra, D. Gatteschi, R. Sessoli, *Chem-Eur. J.* **6**, 1608 (2000)
- [15] R. Blinc, P. Cevc, D. Arčon, N. S. Dalal and R. M. Achey, *Phys. Rev. B* **63**, 212401 (2001).
- [16] J. F. Fernández, F. Luis, and J. Bartolomé, *Phys. Rev. Lett.* **80**, 5659 (1998).
- [17] E. M. Chudnovsky and D. A. Garanin, *Phys. Rev. Lett.* **87**, 187203 (2001).
- [18] D. A. Garanin and E. M. Chudnovsky, *Phys. Rev. B* **65**, 094423 (2002).
- [19] A. Cornia, R. Sessoli, L. Sorace, D. Gatteschi, A. L. Barra, C. Daiguebonne, *cond-mat/0112112* (unpublished).
- [20] N. V. Prokofev and P. C. E. Stamp, *Phys. Rev. Lett.* **80**, 5794 (1998).
- [21] T. Lis, *Acta Cryst. B* **36**, 2042 (1980).
- [22] D. N. Hendrickson, G. Christou, E. A. Schmitt, E. Libby, J. S. Bashkin, S. Wang, H.-L. Tsai, J. B. Vincent, P. D. W. Boyd, J. C. Huffman, K. Folting, Q. Li, and W. E. Streib, *J. Am. Chem. Soc.* **114**, 2455 (1992).
- [23] E-C Yang, W. Wernsdorfer, S. Hill, R. S. Edwards, M. Nakano, S. Maccagnano, L. N. Zakharov, A. L. Rheingold, G. Christou, D. N. Hendrickson, in-preparation.
- [24] I. Mirebeau, M. Hennion, H. Casalta, H. Andres, H. U. Güdel, A. V. Irodova, and A. Caneschi, *Phys. Rev. Lett.* **83**, 628 (1999).
- [25] J. R. Friedman, M. P. Sarachik, and R. Ziolo, *Phys. Rev. B* **58**, R14729 (1998).
- [26] E. del Barco, A. D. Kent, E. Rumberger, D. Hendrickson, and G. Christou, to appear in *Europhys. Lett.*; *cond-mat/0209167*.
- [27] W. Wernsdorfer, N. Aliaga-Alcalde, D. N. Hendrickson, G. Christou, *Nature* **416**, 406-409 (2002).
- [28] W. Wernsdorfer, S. Bhaduri, R. Tiron, D.N. Hendrickson, G. Christou, *Phys. Rev. Lett.* **89**, 197201 (2002).
- [29] R. S. Edwards, S. Hill, S. Bhaduri, N. Aliaga-Alcade, E. Bolin, S. Maccagnano, G. Christou, and D. N. Hendrickson, *Polyhedron* (Elsevier, in press).

QUANTUM COMPUTING: FROM BRAGG REFLECTIONS TO DECOHERENCE ESTIMATES

Peter Pfeifer and Chen Hou
Department of Physics, University of Missouri
Columbia, MO 65211, U.S.A.

ABSTRACT

We give an exposition of the principles of quantum computing (logic gates, exponential parallelism from polynomial hardware, fast quantum algorithms, quantum error correction, hardware requirements, and experimental milestones). A compact description of the quantum Fourier transform to find the period of a function—the key step in Shor's factoring algorithm—illustrates how parallel state evolution along many classical computational paths produces fast algorithms by constructive interference similar to Bragg reflections in x-ray crystallography. On the hardware side, we present a new method to estimate critical time scales for the operation of a quantum computer. We derive a universal *upper* bound on the probability of a computation to fail due to decoherence (entanglement of the computer with the environment), as a function of time. The bound is parameter-free, requiring only the interaction between the computer and the environment, and the time-evolving state in the absence of any interaction. For a simple model we find that the bound performs well and decoherence is small when the energy of the computer state is large compared to the interaction energy. This supports a recent estimate of minimum energy requirements for quantum computation.

INTRODUCTION

A quantum computer puts to use the fact that a quantum particle, such as an electron passing through a double-slit apparatus or an atom or molecule traversing a matter-wave interferometer [1], can be in two different locations at the same time. By equating different locations—as a paradigm, we take an electron in the lowest orbit or in an excited orbit of an atom—to binary digits 0 and 1, one may interpret the time-evolving state of the particles as executing several computations at the same time. One set of locations at a given time describes the result of one computation. Thus one atom can do two computations at once; two atoms can do four; three atoms can do eight. The challenge is to coerce the atoms to follow trajectories that amount to meaningful computations and to read out a definite result from the multitude of computations occurring in parallel. The control of trajectories is the hardware part of the challenge; the design of useful trajectories—algorithms that are superior to classical algorithms—is the software part of the challenge.

This paper is a comprehensive survey of both aspects. It illustrates in terms of explicit case studies the key components of a quantum computer, namely, the design of a computational trajectory (Shor's algorithm), the trajectory's superior performance (exponential parallelism), and the reliable operation of the computer vis-à-vis decoherence, with emphasis on analogies to familiar physical phenomena. The case studies apply regardless of whether the computer is implemented in terms of nuclear spins, ion traps, cavity quantum electrodynamics, superconducting currents, or spintronics. General references are [2-9].

QUANTUM VERSUS CLASSICAL COMPUTATION

A classical computer manipulates strings of N classical bits, (n_1, \dots, n_N) with $n_j = 0$ or 1 ($j = 1, \dots, N$), in such a way that intermediate states of the computation are also strings of classical bits. A quantum computer manipulates states of N two-level atoms or any other two-level entities, $|n_1, \dots, n_N\rangle$ with $n_j = 0$ if the j -th atom is in the ground state and $n_j = 1$ if it is in the excited state, in such a way that intermediate states are superpositions of the states $|n_1, \dots, n_N\rangle$. The 2^N states $|n_1, \dots, n_N\rangle$ ("computational basis") are product states in which each atom is either in the ground state or excited state, and n_j is called the value of the j -th qubit ("quantum bit"); they represent the strings of classical bits. The superpositions include states in which an atom no longer has a sharp value of n_j (indefinite bit value), and states in which an atom no longer exists in a state separate from the other atoms (entangled state); both have no classical counterpart.

A quantum computation starts with a product state $|n_1, \dots, n_N\rangle$, lets the state evolve according to the Schrödinger equation, $i\hbar \frac{d}{dt}|\psi(t)\rangle = H(t)|\psi(t)\rangle$, with initial condition $|\psi(0)\rangle = |n_1, \dots, n_N\rangle$ and time-dependent Hamiltonian $H(t)$ driving the coupled atoms, and ends with the measurement of the values of the qubits of the state $|\psi(t)\rangle$. The Hamiltonian generates the unitary time-evolution operator $U(t)$ which takes the initial state into the final state,

$$|\psi(t)\rangle = T \exp\left(-i/\hbar \int_0^t H(s) ds\right) |\psi(0)\rangle = U(t) |\psi(0)\rangle \quad (1)$$

with T the time-ordering operator. The measurement transforms $|\psi(t)\rangle$ into the output state $|n'_1, \dots, n'_N\rangle$ with probability $|\langle n'_1, \dots, n'_N | \psi(t) \rangle|^2$. The output is probabilistic because quantum measurements are so. The computation $|n_1, \dots, n_N\rangle \mapsto |\psi(t)\rangle$ is a unitary transformation, hence reversible; the readout $|\psi(t)\rangle \mapsto |n'_1, \dots, n'_N\rangle$ is a projection ("collapse of the wave function"), hence irreversible. Thus, to perform a specific computation, one must drive the atoms with a specific Hamiltonian; to read out the result, one must send the atoms through a series of state detectors.

A quantum computer is more powerful than a classical computer for two reasons. (i) The quantum state space is much larger than the classical state space: N qubits can be in an infinite number of different states (any point on the unit sphere of the complex Hilbert space spanned by the 2^N basis vectors $|n_1, \dots, n_N\rangle$); N classical bits can only be in 2^N different states (the points where the 2^N coordinate axes intersect the unit sphere, Fig. 1). If the expansion coefficients of the superpositions can be controlled with accuracy ϵ ($\epsilon \ll 1$), the sphere hosts $O(\epsilon^{-(2^N-1)})$ distinct states. Thus a quantum computer can store and access an exponentially large number of states compared to a classical computer. (ii) The quantum computer operates in a massively parallel way: if the initial state is the uniform superposition of all basis states,

$$|\psi(0)\rangle = 2^{-N/2} \sum_{n_1, \dots, n_N=0,1} |n_1, \dots, n_N\rangle, \quad (2)$$

the time evolution computes simultaneously $U(t)|n_1, \dots, n_N\rangle$ for all 2^N possible inputs $|n_1, \dots, n_N\rangle$ by linearity of $U(t)$. The matrix element $\langle n'_1, \dots, n'_N | U(t) | n_1, \dots, n_N \rangle$ is the probability amplitude that the computation converts the input $|n_1, \dots, n_N\rangle$ into the output $|n'_1, \dots, n'_N\rangle$, along all possible classical computational paths in parallel (Feynman's path integral). A classical computation can follow only a single path. The aim is to choose $U(t)$ so that computational paths of no interest

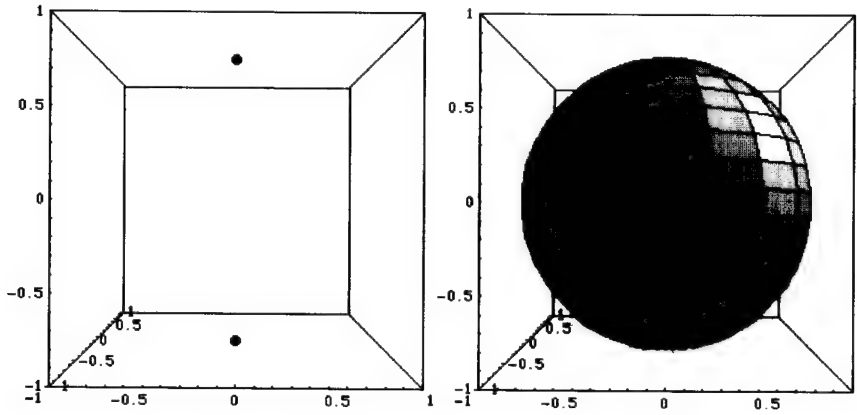


Figure 1. A classical bit can be in state $|0\rangle$ or $|1\rangle$ (left). A quantum bit can be in any superposition $a|0\rangle + b|1\rangle$, where the complex numbers a and b satisfy $|a|^2 + |b|^2 = 1$ (right). The states are shown as expectation values of the spin vector.

cancel each other by destructive interference, and paths of interest add constructively (selection of relevant computations by quantum interference, Fig. 2).

Any computation $U(t)$, also called a quantum circuit, can be approximated by sequential application of a finite set of unitary transformations that operate on only one or two qubits. An example for such a “universal set of quantum logic gates” is

$$H_j = (|0_j\rangle\langle 0_j| + |0_j\rangle\langle 1_j| + |1_j\rangle\langle 0_j| - |1_j\rangle\langle 1_j|)/\sqrt{2} \quad (\text{“Hadamard gate”}), \quad (3)$$

$$T_j = |0_j\rangle\langle 0_j| + e^{i\pi/4}|1_j\rangle\langle 1_j| \quad (\text{“}T\text{ gate”}), \quad (4)$$

$$C_{jk} = |0_0\rangle\langle 0_0| + |0_1\rangle\langle 0_1| + |1_0\rangle\langle 1_1| + |1_1\rangle\langle 1_0| \quad (\text{“controlled-not gate”}), \quad (5)$$

where $|n_j\rangle\langle n'_j|$ acts only on qubit j , and $|n_j n_k\rangle\langle n'_j n'_k|$ only on qubits j and k . They correspond to the logic gates in a classical computer, but are reversible (the classical ‘and’ and ‘exclusive or’ gates are irreversible). The Hadamard gate transforms the states $|0_j\rangle$ and $|1_j\rangle$ into the superpositions $(|0_j\rangle \pm |1_j\rangle)/\sqrt{2}$; the T gate shifts the phase of the excited state relative to the ground state by $\pi/4$; and the controlled-not gate flips the “target” qubit k if and only if the “control” qubit j is in the excited state. The three gates are the analog of an optical beam splitter, phase shifter (refractive medium), and conditional mirror, respectively. Only the Hadamard gate creates multiple computational paths; the other two transform a single basis state into a single basis state. To approximate a general $U(t)$ to within accuracy ϵ requires $O(4^N N^2 [\ln(4^N N^2/\epsilon)]^\alpha)$ gates, where $\alpha \approx 2$ (Solovay-Kitaev theorem [6]) and the leading factor 4^N is set by the number of matrix elements of $U(t)$. For special computations, however, often a much smaller number of gates, independent of ϵ , suffices, as we shall see in the next section.

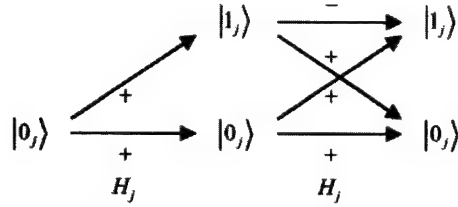


Figure 2. Application of the Hadamard gate to state $|n_j\rangle$ creates two computational paths, one leading to $|0_j\rangle$ with probability amplitude $1/\sqrt{2}$, the other to $|1_j\rangle$ with amplitude $(-1)^{n_j}/\sqrt{2}$. Application of the Hadamard gate twice to $|0_j\rangle$ creates four paths, leading to $|0_j\rangle$ with amplitude $[(+1)(+1) + (+1)(+1)]/2$, and to $|1_j\rangle$ with amplitude $[(+1)(+1) + (+1)(-1)]/2$ (cancellation of trajectories leading to $|1_j\rangle$).

AN EXPLICIT EXAMPLE—FINDING THE PERIOD OF A FUNCTION

A widely used class of encryption systems for public transmission of sensitive data (RSA public key cryptosystem [10]) derive their security from the difficulty of factoring a large, publicly transmitted integer. The fastest known classical algorithm factors an N -bit number in time $O(2^{\text{const} \times N^{1/3} (\ln N)^{2/3}})$. Shor's celebrated quantum algorithm [11, 12] for the same task requires only time $O(N^2 (\ln N) (\ln \ln N))$. The key task in Shor's algorithm is to find the period r of a periodic function $f(x)$ related to the number to be factored, and the tool used to determine the period is the discrete Fourier transform. The values of the Fourier variable at which the transform does not vanish yield the period, just as in x-ray diffraction from a crystal the scattered wave vectors at which the x-ray intensity is nonzero yield the crystal periodicity (Bragg reflection at wave vectors equal to a reciprocal lattice vector).

The discrete Fourier transform assigns to a given complex-valued function $f(x)$ (not necessarily periodic) the function

$$\hat{f}(y) = 2^{-N/2} \sum_{x=0}^{2^N-1} e^{2\pi i xy/2^N} f(x), \quad (6)$$

where both x and y run through the integers $0, 1, \dots, 2^N - 1$. Its quantum computation reads

$$\sum_{y=0}^{2^N-1} \hat{f}(y) |y_1, \dots, y_N\rangle = U(t) \sum_{x=0}^{2^N-1} f(x) |x_1, \dots, x_N\rangle, \quad (7)$$

$$U(t) |x_1, \dots, x_N\rangle = 2^{-N/2} \sum_{y=0}^{2^N-1} e^{2\pi i xy/2^N} |y_1, \dots, y_N\rangle, \quad (8)$$

$$x = x_1 2^{N-1} + x_2 2^{N-2} + \dots + x_N 2^0, \quad (9a)$$

$$y = y_1 2^{N-1} + y_2 2^{N-2} + \dots + y_N 2^0. \quad (9b)$$

Equation (8) defines the operator $U(t)$ in terms of the computational basis; (9) is the binary expansion of the summation variables in (7, 8); and Eq. (7) is established by substitution of (6) and (8). The sums in (7), running over the whole basis, completely describe the function and its Fourier transform. The implementation of $U(t)$ in terms of logic gates is given by

$$\begin{aligned}
U(t)|x_1, \dots, x_N\rangle &= 2^{-N/2} \sum_{y=0}^{2^N-1} e^{2\pi i xy/2^N} |y_1, \dots, y_N\rangle \\
&= 2^{-N/2} \prod_{j=1}^N (|0_j\rangle + e^{2\pi i 0 x_{N-j+1} x_{N-j+2} \dots x_N} |1_j\rangle) \\
&= R(H_1 B_{1,2} B_{1,3} \dots B_{1,N})(H_2 B_{2,3} B_{2,4} \dots B_{2,N}) \dots (H_{N-1} B_{N-1,N})(H_N)|x_1, \dots, x_N\rangle.
\end{aligned} \tag{10}$$

The first line recalls the action of $U(t)$ on a basis state; the second line shows that the result is a product state, not an entangled state (the binary fractions $0.x_{N-j+1}x_{N-j+2}\dots x_N$ arise from the expansion of $xy/2^N$); and the third line expresses the product in terms of successive applications of the Hadamard gate, the controlled-phase-shift gate,

$$B_{jk} = |0_j 0_k\rangle\langle 0_j 0_k| + |0_j 1_k\rangle\langle 0_j 1_k| + |1_j 0_k\rangle\langle 1_j 0_k| + e^{2\pi i 2^{k-j}} |1_j 1_k\rangle\langle 1_j 1_k|, \tag{11}$$

and the qubit reversal operator, $R|n_1, \dots, n_N\rangle = |n_N, \dots, n_1\rangle$ (implemented by reading the qubits in reverse order), on the original basis state.

Equation (10) is the quantum fast Fourier transform. It is an explicit example for the decomposition of a quantum circuit into a product of one- and two-qubit operations and shows that the transform, without any approximation, can be carried out with only $N(N+1)/2$ operations. This is much less than the Solovay-Kitaev bound and much less than the $O(2^N N)$ operations in the classical fast Fourier transform. The N Hadamard gates create 2^N classical paths along which the state $|x_1, \dots, x_N\rangle$ evolves in parallel.

The period r is obtained by measuring the qubits of state (7). The measurement yields the output state $|y_1, \dots, y_N\rangle$ with probability

$$|\langle y_1, \dots, y_N | \psi(t) \rangle|^2 = |\hat{f}(y)|^2. \tag{12a}$$

If r divides 2^N , the probability is

$$|\hat{f}(y)|^2 = \frac{2^N}{r^2} \left| \sum_{x=0}^{r-1} e^{2\pi i xy/2^N} f(x) \right|^2 = 0 \quad \text{if } y/2^N = 0, 1/r, 2/r, \dots, (r-1)/r, \tag{12b}$$

$$|\hat{f}(y)|^2 = 0 \quad \text{else,} \tag{12c}$$

from (6). Thus as advertised, only "good" y 's, related to r , remain. Outcomes unrelated to r occur with probability zero, by virtue of destructive interference. The good y 's yield r as the largest denominator of the reduced fractions $y/2^N$, as y runs through all outcomes $|y_1, \dots, y_N\rangle$. The largest denominator from m distinct outcomes ($m \ll r$) equals r with probability better than $1 - (1 - 0.561/\ln \ln r)^m$ (prime number theorem), so even a period as large as 2^{100} is found with a success rate better than 99% from only 33 distinct outcomes. If r does not divide 2^N , destructive interference is not perfect, and the measurements with high probability yield y 's satisfying $y/2^N = 0, 1/r, 2/r, \dots, (r-1)/r$ approximately. In this case, r is found from a slightly more involved analysis, but still with only $O(\ln N)$ Fourier transforms and measurements. This gives the period in time $O(N^2 \ln N)$. With this efficiency, it turns out that the bottleneck in Shor's algorithm is the computation of $f(x)$, i.e., the preparation of the initial state $\sum_x f(x)|x_1, \dots, x_N\rangle$, which we have suppressed here. The determination of the period, including the preparation of the initial state, requires time $O(N^2(\ln N)(\ln \ln N))$.

Table I. Exponential parallelism of the quantum Fourier transform from polynomial hardware. The second line is often expressed as that the quantum computer can do 2^N classical computations simultaneously. The abbreviations in the last column stand for 'effort' and 'payoff'.

	Number	Eq.	Effort/payoff
Logic gates acting on $ \psi(0)\rangle$	$N(N+1)/2$	(10)	Polynomial e.
Classical bit strings processed at once in $ \psi(t)\rangle$	2^N	(7)	Exponential p.
Classical paths followed at once in $ \psi(t)\rangle$	2^{2N}	(10)	Exponential p.
Distinct constructive interference events from $ \psi(t)\rangle$	$2^N r$	(12)	Exponential p.
Repeated computations of $ \psi(t)\rangle$ needed to find r	$O(\ln N)$	—	Logarithmic e.

Table I summarizes the algorithm in terms of parallel computing and interference of computational paths. The number of distinct constructive interference events increases with increasing period r , just as in x-ray diffraction the number of Bragg reflections increases with increasing size of the unit cell. The degree of entanglement of computational states varies in the opposite direction: If f is zero everywhere except at position x , then f has period $r = 2^N$, the initial state is a product state by $|\psi(0)\rangle = |x_1, \dots, x_N\rangle$, and so is the final state $|\psi(t)\rangle$ by (10). In this case, neither the initial nor final state is entangled. If $f(x) = 2^{-N/2}$ for all x , then f has period $r = 1$, the initial state equals the state (2), and the final state is $|\psi(t)\rangle = |0, \dots, 0\rangle$. In this case, the initial state is maximally entangled, and the final state is not entangled. This suggests that the smaller the period, the more entangled are relevant states in the computation.

OTHER FAST QUANTUM ALGORITHMS

Factoring integers can be reduced to finding integer solutions of Pell's equation, $x^2 - ay^2 = 1$, where a is a positive non-square integer; but a converse is not known. So it is of interest that a quantum algorithm exists also for Pell's equation. The algorithm is due to Hallgren [13] and finds the solution in polynomial time as in Shor's algorithm, instead of exponential time as on a classical computer.

Other quantum algorithms that outperform classical algorithms by orders of magnitude are: Grover's algorithm for "finding a needle in a haystack" (search of an item in a database of 2^N items in $O(2^{N/2})$ instead of $O(2^N)$ steps); estimation of the median and mean of 2^N items to precision ε in $O(N/\varepsilon)$ instead of $O(N/\varepsilon^2)$ steps; search of the minimum of a function sampled at 2^N points in $O(2^{N/2})$ instead of $O(2^N)$ steps; search of two distinct pre-images giving the same image of a two-to-one function sampled at 2^N points, in $O(2^{N/3})$ instead of $O(2^{N/2})$ steps; the Deutsch-Jozsa algorithm to determine if 2^N numbers are either all 0 ("constant function"), or half are 0 and half are 1 ("balanced function"), in one instead of up to $2^{N-1} + 1$ steps; and various allocation tasks and game-theoretic strategies.

Quantum algorithms for solving complex physical problems in polynomial time instead of exponential time include [9]: path integration with respect to Wiener measure; quantum random walks; simulation of the quantum baker's map; quantum lattice-gas model for the time-dependent Schrödinger equation of many-body systems; and the dynamical sign problem in fermionic systems.

QUANTUM ERROR CORRECTION

Noise from imperfect computer operation poses no fundamental barrier to large-scale computations. A quantum error-correction code encodes the N "logical qubits" into N' "carrier qubits" ($N' > N$), runs the carrier qubits through a group of accordingly encoded logic gates, transforms the noisy state by appropriate projection operators ("syndrome measurements") and unitary operators ("recovery of original carrier qubits") into an error-corrected state, and feeds the state into the next group of gates. Such periodic error correction prevents accumulation of errors in the state ("quantum Zeno effect"). At the end of the computation, the carrier qubits are decoded. The encoding spreads the state of the N logical qubits over all N' carrier qubits so that when the syndromes are measured, no information about the state of the logical qubits is revealed ("noiseless" or "decoherence-free" subspaces): the projections preserve superpositions of the logical qubits, and the state of the carrier qubits is highly entangled even if the logical-qubit state is not. Remarkably, a discrete set of corrections can correct a continuum of errors. For a code to correct any error on any M carrier qubits, a necessary condition is

$$N' \geq 4M + N \quad (13)$$

(Knill-Laflamme bound), and a sufficient condition for large N is

$$N/N' < 1 - 2 \left[-x \log_2 x - (1-x) \log_2 (1-x) \right]_{x=2M/N'} \quad (14)$$

(Gilbert-Varshamov bound). E.g., a code exists which encodes one logical qubit ($N = 1$) into 5 carrier qubits ($N' = 5$) and corrects any error on any one carrier qubit ($M = 1$) with 16 pairs of syndrome measurements and recovery operations (equality in the Knill-Laflamme bound).

Different codes require different encoding of gates, and of interest are encodings for which an error in an input carrier qubit or the gate operation propagates only to a small number of output carrier qubits. Specifically, an encoded gate is called fault-tolerant if a failure with probability p of any single component (e.g., one of the 10 "wires" feeding two logical qubits, each encoded by 5 carrier qubits, into a controlled-not gate) introduces an error in two or more carrier qubits in any logical output qubit with probability cp^2 at most, with c a constant and p small. Such a gate, when followed by error correction with $M = 1$, yields an error-free output with probability $1 - cp^2$, i.e., reduces the error probability from p to cp^2 if $p < 1/c$. Fault-tolerant Hadamard, T , and controlled-not gates exist with $c \approx 10^4$ and $d \approx 10^2$, where d is the number of operations on carrier qubits needed to encode and error-correct the gate. By hierarchical fault-tolerant encoding of all gates, a computation involving L gates can be carried out to within accuracy ε using only $O(L[\ln(L/\varepsilon)]^{\log_2 d})$ operations on carrier qubits, if $p < 1/c$ (threshold theorem for quantum computation). Thus, if the noise in individual carrier qubits is low enough, $p < 1/c \approx 10^{-4}$, arbitrarily large computations can be performed because the overhead for error correction grows only polynomial-logarithmically with the size of the computation, L .

EXPERIMENTAL STATE OF THE ART AND HARDWARE REQUIREMENTS

A remarkable array of experimental realizations of quantum computing devices and algorithms have been achieved to date. Current record holders with respect to the number of qubits

that can be controlled and prepared in well-defined states include, in the different categories of experimental implementation:

(i) 7-qubit nuclear magnetic resonance devices (NMR): three ^1H and four ^{13}C nuclei in *trans*-crotonic acid, each in the spin up or down state, with a total of twelve 2-qubit gates driven by radio-frequency pulses, preparing the "Schrödinger-cat state" $(|0000000\rangle + |1111111\rangle)/\sqrt{2}$ and converting it into the state $|0000000\rangle$ [14]; and five ^{19}F and two ^{13}C nuclei in a custom-made molecule, fully implementing, with a sequence of 300 radio-frequency pulses, Shor's algorithm to factor the number 15 [15];

(ii) a 4-qubit ion-trap device (IT): four $^9\text{Be}^+$ ions in a linear electromagnetic trap, each in one of two hyperfine Zeeman levels and driven by Raman transitions [16];

(iii) a 3-qubit device based on cavity quantum electrodynamics (CQED): three Rb atoms, each in one of two Rydberg states (principal quantum numbers 49, 50, and 51) and coupled to a cavity mode with zero or one photon, driven by microwave pulses [17]; and

(iv) 1-qubit devices based on macroscopic persistent-current states in superconductors [18].

Computations carried out, in addition to Shor's algorithm, include: Grover's algorithm on a 2-qubit NMR device (1998/99); dynamics of quantum harmonic and anharmonic oscillators on a 2-qubit NMR device (1999); the Deutsch-Jozsa algorithm on a 5-qubit NMR device (2000); finding the order of a permutation on a 5-qubit NMR device (2000); correction of any one-qubit error on a 5-qubit NMR device (2001); noiseless encoding of one logical qubit in a 3-qubit NMR device (2001); quantum lattice-gas treatment of the diffusion equation and Burgers equation on a 2-qubit NMR device (2002); quantum baker's map on a 3-qubit NMR device (2002); protection of an IT qubit from decoherence (two $^9\text{Be}^+$ ions encoding one qubit (2001)); controlled-not gate on a 2-qubit IT device (one $^9\text{Be}^+$ ion implementing a motional and an internal-state qubit (2002)); and Grover's algorithm in a 5-"qubit" classical optical cavity, demonstrating that the algorithm requires no entanglement (2002).

Any experimental realization faces three challenges:

(i) The device must be able to control the state of each qubit separately, while allowing neighboring qubits to interact with each other for the operation of two-qubit gates. Control of individual qubits is achieved by different chemical shifts in NMR, laser beams driving ions spatially separated by tens of μm in IT, and pulses addressing successive atoms traveling at spatial separation of several cm in CQED. Qubits interact via spin-spin coupling in NMR, a shared phonon state of the ions (excitation of the center-of-mass mode) in IT, and electric dipole coupling between each atom and the cavity mode in CQED.

(ii) The system must be switchable, so that interactions executing a prescribed sequence of gate operations (Hamiltonian $H(t)$) can be turned on and off by external control. Switching is done by magnetic field pulses in NMR, and laser pulses in IT and CQED.

(iii) The computer must be well isolated from the environment so that the decoherence time t_d , the time at which the computer and the environment depart significantly from a product state (entanglement of the computer with the environment), is long compared to t_g , the time it takes to operate a single gate. At time t_d , a generic qubit state $a|0\rangle + b|1\rangle$ will have degraded into the mixture $|a|^2|0\rangle\langle 0| + |b|^2|1\rangle\langle 1|$ (density matrix), which no longer contains the interference terms necessary for quantum computation. Good isolation is provided by long spin-spin and spin-lattice relaxation times in NMR ($t_d = 10^{-2} - 10^8$ s, $t_g = 10^{-6} - 10^{-3}$ s), long-lived hyperfine levels and stable trap and laser operation in IT ($t_d = 10^{-1} - 10^0$ s, $t_g = 10^{-7} - 10^{-5}$ s), and the low spontaneous emission rate of Rydberg states and low photon escape rate from the cavity in CQED ($t_d = 10^{-3} - 10^0$ s, $t_g = 10^{-5} - 10^{-4}$ s).

DECOHERENCE ESTIMATES

The condition $t_g < t_d$ is a challenge because the computer must be a weakly open system for time t_g , but a strongly closed system for time t_d . The condition $p < 1/c$ in the threshold theorem for quantum computation is even more demanding. To see this, let $|\psi_i(t)\rangle$ be the state of the computer and environment interacting with each other, starting from a product state at $t = 0$; and let $|\psi_n(t)\rangle$ be the same state, but noninteracting (product state at all times):

$$|\psi_i(t)\rangle = T \exp\left(-\frac{i}{\hbar} \int_0^t \{H_c(s) + H_e(s) + V(s)\} ds\right) |\psi_c(0)\rangle |\psi_e(0)\rangle, \quad (15)$$

$$|\psi_n(t)\rangle = \left[T \exp\left(-\frac{i}{\hbar} \int_0^t H_c(s) ds\right) |\psi_c(0)\rangle \right] \left[T \exp\left(-\frac{i}{\hbar} \int_0^t H_e(s) ds\right) |\psi_e(0)\rangle \right]. \quad (16)$$

Here $H_c(t)$, $H_e(t)$, and $V(t)$ is the Hamiltonian of the computer, environment, and interaction between the two, respectively; and $|\psi_c(0)\rangle$ and $|\psi_e(0)\rangle$ is the initial state of the computer and environment, respectively. Suppose now the overlap ("fidelity"),

$$F(t) := \langle \psi_i(t) | \psi_n(t) \rangle, \quad (17)$$

decays exponentially with time. The decay constant is the inverse of the decoherence time, $F(t) = e^{-t/t_d}$, and the threshold condition requires the failure probability p to satisfy

$$p = 1 - F^2(t_g) = 1 - e^{-2t_g/t_d} < 1/c, \quad (18)$$

which gives the condition $t_g < t_d/(2c)$ for large c . Thus the computer must remain isolated from the environment for about 10^4 gate operations for sustained computations. Present devices can execute about 300 operations [15] and are far from this goal.

One may seek to reduce t_g and use (18) to estimate how short t_g should be for the threshold theorem to kick in. But for short times, the fidelity does not decay exponentially, and Eq. (18) is not appropriate. Also, the fidelity evolves differently if a gate is switched rapidly instead of slowly, which further limits the validity of (18). It is therefore of interest that a universal bound for the fidelity exists which suffers from none of these limitations. The bound reads

$$F(t) \geq F_-(t) := \cos\left(\min\left\{\hbar^{-1} \int_0^t \Delta(s) ds, \pi/2\right\}\right), \quad (19)$$

$$\Delta(s) := \sqrt{\langle \psi_n(s) | V^2(s) | \psi_n(s) \rangle - \langle \psi_n(s) | V(s) | \psi_n(s) \rangle^2}, \quad (20)$$

valid for all t . It requires only the knowledge of the product state (16) and interaction $V(s)$. The energy uncertainty $\Delta(s)$ is easy to evaluate compared to the task of computing the fidelity from (15-17). The bound is a "worst-case" decoherence estimate: if $F_-(t)$ is close to 1, so is $F(t)$ by $F(t) \leq 1$, and decoherence is *guaranteed* small. $F_-(t)$ equals 1 at $t = 0$, decreases with increasing t (the more slowly, the weaker the interaction), and reaches zero (trivial bound) when the integral exceeds $\pi\hbar/2$. The time τ at which $F_-(t)$ has dropped to the value $1/e$, $\hbar^{-1} \int_0^\tau \Delta(s) ds = 1.19$, gives a lower bound for the decoherence time, $\tau \leq t_d$ (Fig. 3). A particularly appealing form of inequality (19) is the *upper* bound

$$p(t) \leq \sin^2 \left(\min \left\{ \hbar^{-1} \int_0^t \Delta(s) ds, \pi/2 \right\} \right) \quad (21)$$

for the probability of the quantum computation $|\psi_c(t)\rangle$ (first factor in (16)) to “fail” after time t due to imperfect isolation, $p(t) := 1 - F^2(t)$. The term “fail” is short for the interacting state to give possibly different results than the noninteracting state. The bound (21) estimates the failure probability rigorously, at any point in time, and without reference to gate-switching and decoherence times (parameter-free decoherence estimate), unlike (18).

The result (19) is an application of the variational principle of Pfeifer and Fröhlich [19] (see also [20]) which states that if $|\psi(t)\rangle$ is a solution of the time-dependent Schrödinger equation with Hamiltonian $H(t)$ and $|\psi_i(t)\rangle$ is a trial state with $|\psi_i(0)\rangle = |\psi(0)\rangle$, then

$$|\langle \psi(t) | \psi_i(t) \rangle| \geq \cos \left(\min \left\{ \hbar^{-1} \int_0^t \left\| (1 - |\psi_i(s)\rangle\langle\psi_i(s)|) (H(s) - i\hbar \frac{d}{ds}) |\psi_i(s)\rangle \right\| ds, \pi/2 \right\} \right). \quad (22)$$

The norm under the integral tracks the amount by which the trial state does not satisfy the Schrödinger equation. For the choice $H(t) = H_c(t) + H_e(t) + V(t)$, $|\psi(t)\rangle = |\psi_i(t)\rangle$, and $|\psi_i(t)\rangle = |\psi_n(t)\rangle$, the norm reduces to $\Delta(s)$, whence (19).

To explore the performance of (19), we have computed (22) numerically for a model system. The system is a particle in a step potential in one dimension, which splits an incoming wave packet into a transmitted and reflected wave packet, similar to a Hadamard gate. But here the potential models the interaction of the computer and environment. The initial state is a Gaussian wave packet. The trial state is a Gaussian wave packet with position and momentum equal to the classical motion across the potential step, neglects the reflected wave packet, but includes the spreading of the transmitted packet (“quasi-free particle”). Table II maps the computer dynamics onto the wave-packet dynamics. Figure 4 shows the result for incident kinetic energy 100 times the energy of the potential step, and initial wave-packet width 1/10 of the initial distance from the step. It is a sample from 15 computations, varying in initial energy and width. When the wave packet reaches the step and splits into a large-amplitude transmitted and small-amplitude reflected component, the overlap drops from 1.000 to 0.997; when the transmitted component is well separated from the reflected component, the overlap rises back to 1.000. In comparison, the

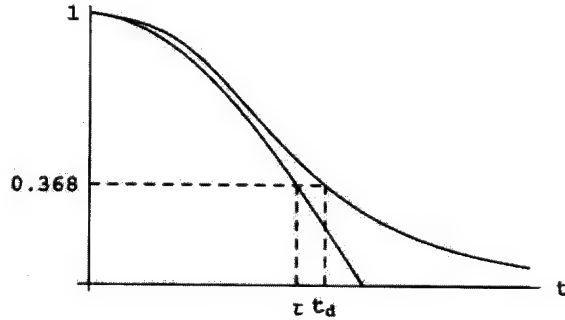


Figure 3. Lower bound τ for the decoherence time t_d (schematic). The upper curve is $F(t)$, assumed to obey $F(t) = e^{-t/t_d}$ for large t (definition of t_d); the lower curve is $F_-(t)$.

Table II. Wave-packet model (WP) of the dynamics of a quantum computer (QC).

	QC	WP
Isolated computer: • Hamiltonian • State	$H_c(t) + H_e(t)$ $ \psi_n(t)\rangle$	Quasi-free particle $ \psi_i(t)\rangle$
Nonisolated computer: • Hamiltonian • State	$H_c(t) + H_e(t) + V(t)$ $ \psi_i(t)\rangle$	Particle in step potential $ \psi(t)\rangle$
Fidelity: • Lower bound • Lower bound = 1 if • Lower bound ≈ 1 if	Eq. (19) $V(t) = 0$ Energy of $ \psi_n(0)\rangle$ is large	Eq. (22) Potential step = 0 Traversal of step is fast

lower bound drops to 0.95 when the wave packet reaches the step, and remains at that value because the integral in (22) accumulates all departures of the trial state from the exact state: a temporary departure produces a permanent drop. The bound does not drop further because the trial state is asymptotically exact on the far side of the step. Thus the bound performs very well. It performs well whenever the wave packet traverses the step fast, i.e., the arrival time at the step is long and the residence time at the step is short.

Fast traversal of the step translates into a large energy of the computer state compared to the interaction energy. Thus the probability of a gate to fail at time t_g , $p(t_g)$, is small if the energy supplied to switch the gate, E_g , is large: $(\partial p / \partial E_g)_{t_g} < 0$. This agrees with the recent estimate, $p \sim \hbar / (t_g E_g)$, of the smallest achievable failure probability, or minimum energy required to switch the gate, under isolation [21]. Our result is a first step to extend the estimate to the case where the computer is not isolated.

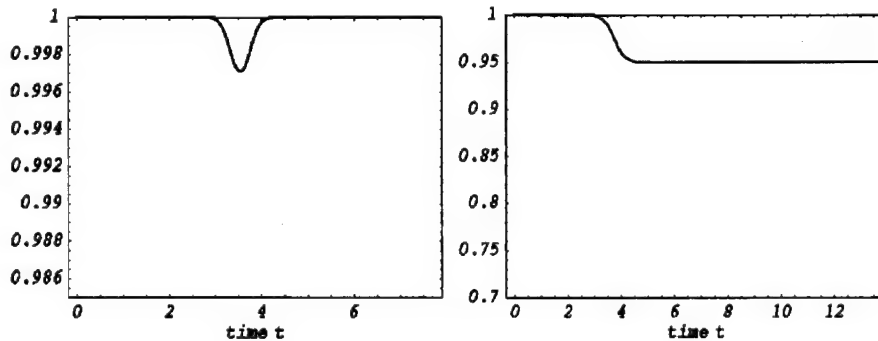


Figure 4. Numerical evaluation of inequality (22). Left: overlap of the exact state and the trial state [left-hand side of (22)]. Right: lower bound of the overlap [right-hand side of (22)]. Time is in units of $\hbar/(\text{energy of the potential step})$.

CONCLUSIONS

We have reviewed quantum computing as an interplay of deterministic time evolution and probabilistic measurement outcomes, constructive and destructive interference, open and closed system dynamics, and theory and experiment. We have developed an inequality, Eq. (21), which decomposes the failure probability of the computer, due to imperfect isolation, into a part that maintains coherence, $|\psi_a(s)\rangle$, and the part that causes decoherence, $V(s)$. The inequality reduces the estimation of failure probabilities to a computationally easy problem for a wide range of computer designs. In an exploratory model computation, we find that the failure probability can be made small by making the energy stored in the computer large. This suggests there may be a variety of ways, to be uncovered yet, to minimize decoherence at given $V(s)$.

REFERENCES

1. B. Brezger et al., Phys. Rev. Lett. **88**, 100404 (2002).
2. P. Pfeifer, in *McGraw-Hill Yearbook of Science and Technology 2002* (McGraw-Hill, New York, 2001), pp. 294-298.
3. G.P. Berman, G.D. Doolen, R. Mainieri, and V.I. Tsifrinovich, *Introduction to Quantum Computers* (World Scientific, Singapore, 1998).
4. J. Gruska, *Quantum Computing* (McGraw-Hill, New York, 1999).
5. A.O. Pittenger, *An Introduction to Quantum Computing Algorithms* (Birkhäuser, Boston, 2000).
6. M.A. Nielsen and I.L. Chuang, *Quantum Computation and Quantum Information* (Cambridge University Press, Cambridge, 2000).
7. C. Macchiavello, G.M. Palma, and A. Zeilinger (eds.), *Quantum Computation and Quantum Information Theory* (World Scientific, Singapore, 2001).
8. Special issue "Experimental Proposals for Quantum Computation," Fortschr. Phys. **48**, 769-1138 (2000).
9. Special issue "Quantum Computation for Physical Modeling," Comput. Phys. Comm. **146**, 277-344 (2002).
10. D. Gottesman and H.-K. Lo, Phys. Today **53** (11), 22 (2000).
11. P. Shor, in *Proceedings of the 35th Annual Symposium on the Foundations of Computer Science*, edited by S. Goldwasser (IEEE Computer Society, Los Alamitos, CA, 1994), pp. 124-134.
12. A. Ekert and R. Jozsa, Rev. Mod. Phys. **68**, 733 (1996).
13. S. Hallgren, in *Proceedings of the 34th Annual ACM Symposium on Theory of Computing*, edited by J. Reif (ACM Press, New York, 2002), pp. 653-658.
14. E. Knill, R. Laflamme, R. Martinez, and C.-H. Tseng, Nature **404**, 368 (2000).
15. L.M.K. Vandersypen et al., Nature **414**, 883 (2001).
16. C.A. Sackett et al., Nature **404**, 256 (2000).
17. A. Rauschenbeutel et al., Science **288**, 2024 (2000).
18. A.J. Leggett, Science **296**, 861 (2002); D. Vion et al., *ibid.*, 886; Y. Yu et al., *ibid.*, 889.
19. P. Pfeifer and J. Fröhlich, Rev. Mod. Phys. **67**, 759 (1995).
20. P. Pfeifer, Phys. Rev. Lett. **70**, 3365 (1993); **71**, 306 (1993).
21. J. Gea-Banacloche, Phys. Rev. Lett. **89**, 217901 (2002).

AUTHOR INDEX

- Agosti, Enrico, 219
 Ali, B., 201
 Aliaga-Alcade, Núria, 231, 253
 Aliev, F.G., 81, 133
 Alldredge, Lisa Berndt, 127
 Aubin, Sheila M.J., 231

 Baker, C., 201
 Barthélémy, A., 145
 Belmeguenai, M., 189
 Bhaduri, Sumit, 231, 241
 Bowen, M., 145

 Cadogan, John, 219
 Carreño, Neftalí L.V., 213
 Chappert, C., 189
 Christou, George, 231, 241, 253
 Colliex, C., 145
 Contour, J.-P., 145

 Dalal, N.S., 241, 253
 Devolder, T., 189
 Dittrich, Rok, 183
 Dominguez, A. Bustamante, 225
 Doudin, B., 139, 169

 Ebert, Jörg, 89
 Edwards, Rachel S., 231, 253
 Ekiert, T., 201
 Entel, Peter, 101

 Fert, A., 145
 Fidler, Josef, 25, 183
 Fleming, David A., 207
 Fonseca, Fabio C., 213
 Forster, Hermann, 183
 Fried, Tcipi, 151
 Fujii, Tatsuo, 55

 Ghafari, Mohammad, 89
 Goya, Gerardo F., 213
 Guerrero, R., 133

 Hahn, Horst, 89
 Hasanain, S.K., 201
 Heinemann, Andre, 219

 Heinrich, B., 67
 Hendrickson, David N., 231, 241, 253
 Herper, Heike C., 101
 Hill, Stephen O., 231, 241, 253
 Hoell, Armen, 219
 Horing, Norman J.M., 157
 Hou, Chen, 265
 Hübner, W., 43

 Imhoff, D., 145

 Jardim, Renato F., 213
 Jones, David E., 75
 Jones, S.I., 253

 Katz, David, 151
 Kawano, Shinji, 49
 Kayano, Masakazu, 55
 Kirschner, Markus, 25
 Kiwi, Miguel, 1

 Lederman, D., 37
 Leite, Edson R., 213
 Li, G., 201
 Liou, S.-H., 139
 Longo, Elson, 213
 Loutts, George B., 75

 Maccagnano, S., 253
 Markovich, Gil, 151
 Martinez, J.L., 81, 133
 Maurice, J.-L., 145
 Millo, Oded, 151
 Misra, A., 13
 Moodera, J., 133
 Morales, Erie H., 37
 Mourokh, Lev G., 157
 Moze, Oscar, 219
 Muccillo, Reginaldo, 213

 Nakagawa, Takashi, 49
 Nakanishi, Makoto, 55
 Napolitano, Michael, 207
 Neamtu, Jenica, 95
 North, J.M., 253
 Novotny, M.A., 241

Nowak, U., 13	Stahl, Branko, 89
Oh, D.Y., 61	Suess, Dieter, 25, 183
Oshiki, Mitsumasa, 175	Sun, Ziming, 231
Ovchenkov, Y.A., 169	Suzuki, Kiyonori, 219
Ovtchenkov, E., 139	Suzuki, Y., 127, 189
	Szunyogh, Laszlo, 101
Pailloux, F., 145	Tachibana, Takeshi, 49
Papaefthymiou, Georgia C., 225	Takada, Jun, 55
Park, J.K., 61	Takada, Yukio, 49
Park, Kyungwha, 241	Takemura, Yasushi, 163
Pfeifer, Peter, 265	Tanaka, Atsushi, 175
Poddar, Pankaj, 151	Tsiantos, Vassilios, 183
Pryadun, V.V., 133	
Qian, X., 43	Unruh, K.M., 201
	Urban, R., 67
Rakhimov, Rakhim R., 75	Usadel, K.D., 13
Redepenning, J., 169	
Rikvold, P.A., 241	Villar, R., 81, 133
	Volmer, Marius, 95
Sadai, Makoto, 55	
Schad, R., 81	Wang, Yikuan, 37
Scholz, Werner, 183	Weinberger, Peter, 101, 107
Schrefl, Thomas, 25, 183	Wernsdorfer, Wolfgang, 231
Schulthess, T.C., 31	Williams, Mary Elizabeth, 207
Schumacher, H.W., 189	Wizansky, Tommer, 151
Scorzelli, Rosa B., 225	Woltersdorf, G., 67
Shah, L., 201	
Shah, S. Ismat, 201	Yamamoto, Takao A., 49
Sharoni, Amos, 151	Yang, C.-S., 139
Shimada, Takeshi, 49	Yang, E.-C., 253
Shirakashi, Jun-ichi, 163	Yuan, L., 139
Smirnov, Anatoly Yu., 157	
Sokolov, A., 139	Zhang, Chunjuan, 169

SUBJECT INDEX

- ab initio calculations, 43, 101, 107
- annealing, 89
- antiferromagnet/ferromagnet bilayers, 25, 31, 37
- carbon dissolution, 61
- chromium dioxide, 139
- CoPt thin film, 61
- CoSrTiO₃, 145
- Coulomb blockade, 169
- CPP transport, 101, 107
- crystal-field effect, 43
- current perpendicular to the plane, 175
- damping, 67
- decoherence, 265
- domain walls, 81
- doped manganites, 127
- double quantum wires, 157
- EELS, 145
- electron paramagnetic resonance (EPR), 75, 241, 253
- exchange bias, 13, 25, 31, 37
- Fe on W(100) and W(110) substrate, 43
- Fe/Au nanoparticle, 207
- Fe/Cr, 81
- ferromagnetic
 - resonance, 67
 - single-electron transistor, 163
- FeZrBCu, 219
- GMR, 89, 101
- Green's function, 157
- half-metal, 139, 151
- Hall effect, 95
- HRTEM, 145
- ilmenite, 55
- inert gas condensation, 201
- interdiffusion, 37
- interface magnetism, 31
- inter-granular exchange stiffness, 219
- IrMn, 25
- iron-
 - chromium, 81, 101
 - oxide, 151, 201, 225
- Kubo-Greenwood, 101
- LSMO, 127
- macroscopic tunneling, 231
- magnetic
 - multilayers, 13, 81, 95, 107
 - giant magnetoresistance, 89, 101
 - nanostuctures, 133, 183, 189
 - quantum tunneling, 253
 - response, 157
 - storage, 189
 - tunnel junctions, 133, 145, 169
- magnetite nanocrystals, 151
- magnetoresistance, 95, 127, 139, 175
- manganese, 231
 - dopant, 75
- MCM-41 aluminosilicate matrix, 225
- memory effect, 139
- micromagnetics, 13, 25, 183
- minimum energy path, 183
- MnPt, 37
- molecular beam epitaxy, 67
- Mössbauer, 225
- nanoparticles, 133, 201, 207, 213, 225
- neutron diffraction, 49
- non-resonant microwave absorption, 75
- nonstoichiometry, 55
- perpendicular anisotropy, 189
- polarized small angle neutron scattering, 219

precessional switching, 189

quantum

computing, 265

tunneling, 241

Rietveld analysis, 49

single-molecule magnets, 231, 241,
253

sol-gel, 213

spin(-)

injection, 1

dependent tunneling, 75, 133,
139, 145

superparamagnetism, 213

superposition, 265

thiols, 169

training effect, 25

transmission electron microscopy,
207

tunnel

junctions, 133, 139, 145, 169

magnetoresistance, 107, 145, 163

tunneling spectroscopy, 151

Verwey transition, 151

voltammetry, 207

x-ray reflectometry, 89

yttrium aluminates, 75

Z-type hexagonal barium ferrite, 49